ICRR ANNUAL REPORT 2017
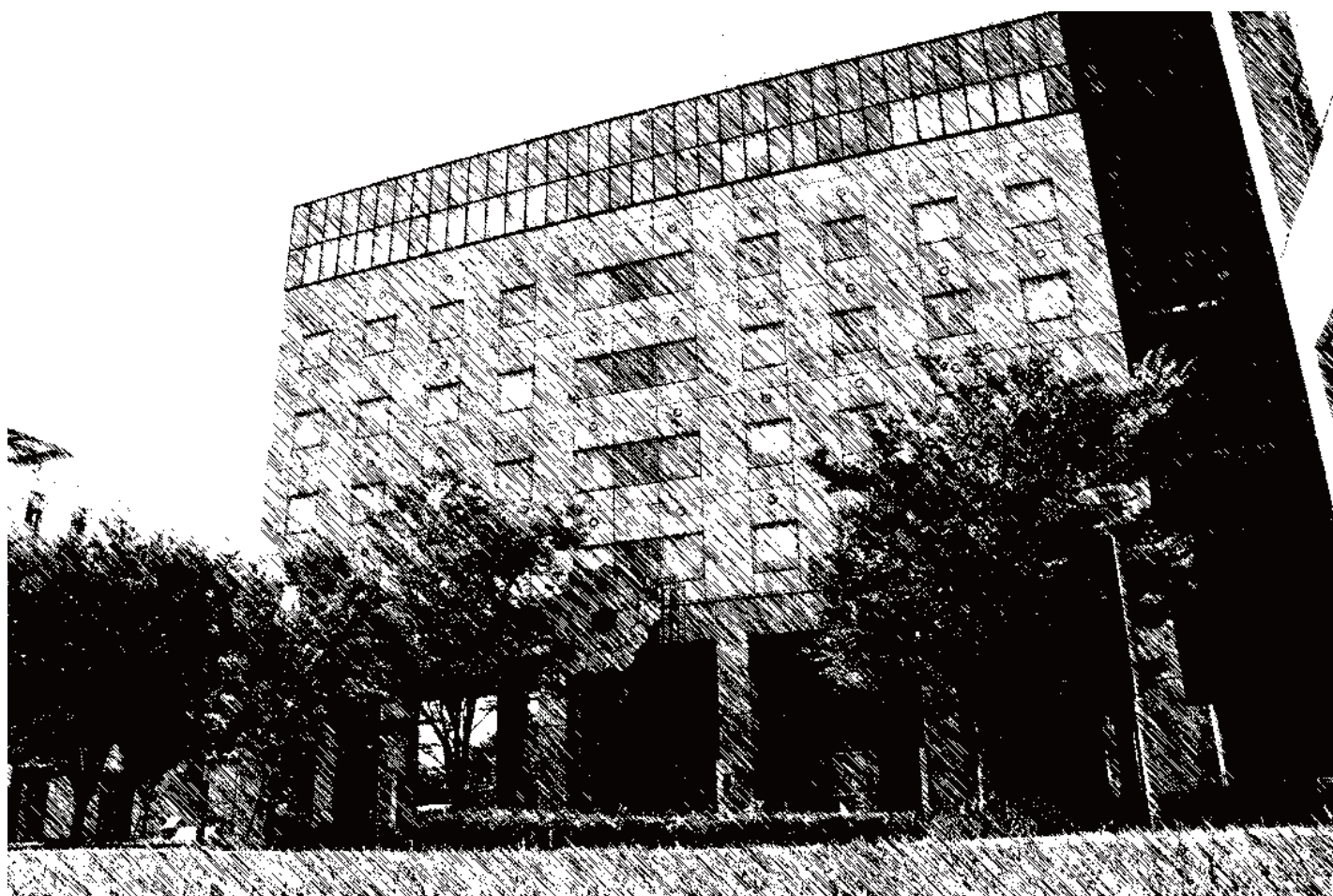
INSTITUTE

FOR

COSMIC RAY RESEARCH

THE UNIVERSITY OF TOKYO

ANNUAL REPORT
(APRIL 2017 – MARCH 2018)

ICRR
Institute for Cosmic Ray Research
University of Tokyo

TABLE OF CONTENTS

PREFACE

This report summarizes the scientific activities of the Institute for Cosmic Ray Research (ICRR) of the University of Tokyo in the Japanese FY 2017.

ICRR is an inter-university research institute for studies of cosmic rays. The headquarters of ICRR is located in Kashiwa, Chiba prefecture, Japan. In order to promote various cosmic-ray-related studies efficiently, ICRR has three research divisions; Neutrino and Astroparticle division, High Energy Cosmic Ray division, and Astrophysics and Gravity division. ICRR have four observatories in Japan; Kamioka Observatory (Kamioka underground, Gifu prefecture), Norikura Observatory (2770 meters above sea level, Mt. Norikura, Gifu prefecture), Akeno Observatory (Yamanashi prefecture), and KAGRA Observatory (Kamioka underground, Gifu prefecture), together with 1 research center; Research Center for Cosmic Neutrinos (Kashiwa, Chiba prefecture). In addition, there are two major experimental facilities outside of Japan. They are located in Utah in USA, and Yangbajing in Tibet, China. The La Palma island in Spain is also recognized as an important site for the ICRR activities.

Many researchers from various Japanese institutions as well as those from overseas are involved in the research programs of ICRR. It should be noted that most of the scientific outputs from this institute are the results of the collaborative efforts by many scientists from various institutions. In order to produce outstanding results, it is very important to carry out an experiment by an international collaboration composed of top-level researchers all over the world. Hence, most of the experimental collaborations that ICRR is involved are international ones. For example, the number of collaborators in the Super-Kamiokande experiment is about 160; about a half of them are from abroad (USA, Korea, China, Poland, Spain, Canada, Italy, France and United Kingdom).

Many exciting scientific activities of ICRR are described in this report. For example, the Super-Kamiokande and T2K (which uses Super-Kamiokande as the far detector) experiments have been continuously producing impressive results on neutrino oscillation physics. The neutrino oscillation studies by the Super-Kamiokande experiment were recognized by the 2015 Nobel Prize in Physics.

Some of the other recent highlights are mentioned here: KAGRA is under construction and plans to begin the observation run in the fall of 2019. The highest energy cosmic ray experiment TA (Telescope Array) has observed indication that the highest energy cosmic rays arrive from a particular direction of the sky, which may suggest the birth of a new research field, the highest energy cosmic ray astronomy. ICRR joins the CTA project, which is a global TeV gamma ray astronomy project. ICRR is contributing substantially to the construction of Large-Sized Telescopes (LST) of the CTA-North observatory.

As an inter-university research institute, ICRR is reviewed by the top-level researchers in the field. Furthermore, future projects of ICRR are evaluated by a committee composed of top-level researchers from various nearby fields. The report from the ICRR Future Project Evaluation Committee was released in October 2017. The Committee evaluated various possible future projects of ICRR. Several projects have been recommended highly. Among them, Hyper-Kamiokande, which is the next generation neutrino detector, has been recommended as the top priority ICRR future project. ICRR is working hard toward the realization of Hyper-Kamiokande.

We hope that this report is useful for the understanding of the current research activities of ICRR. Finally, we appreciate the strong support of our colleagues in this research field, the University of Tokyo and the Japanese Ministry of Education, Culture, Sports, Science and Technology. They are indispensable for the continuing, and exciting scientific outcome of ICRR.
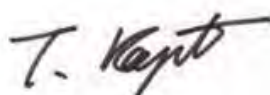
Takaaki Kajita,
Director,
Institute for Cosmic Ray Research,
The University of Tokyo

The ICRR building at Kashiwa, Chiba, Japan.
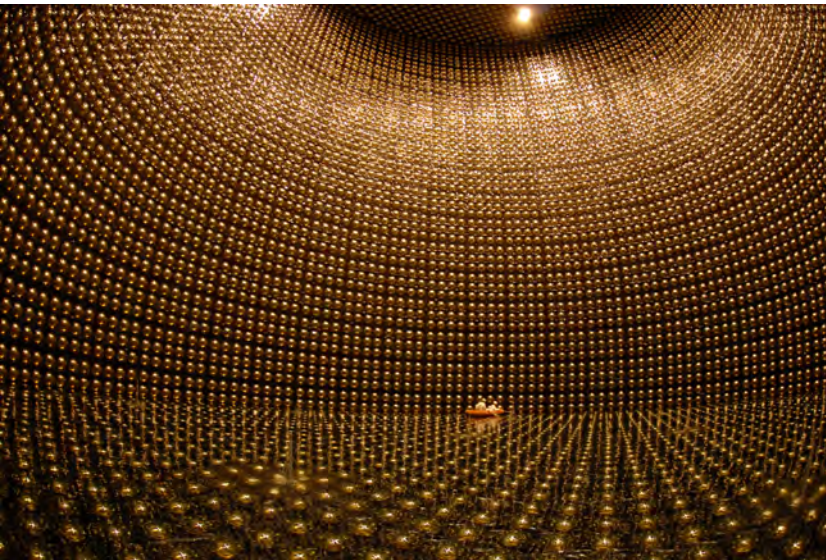
The Super-Kamiokande detector (the photo was taken during pure water fill in 2006).
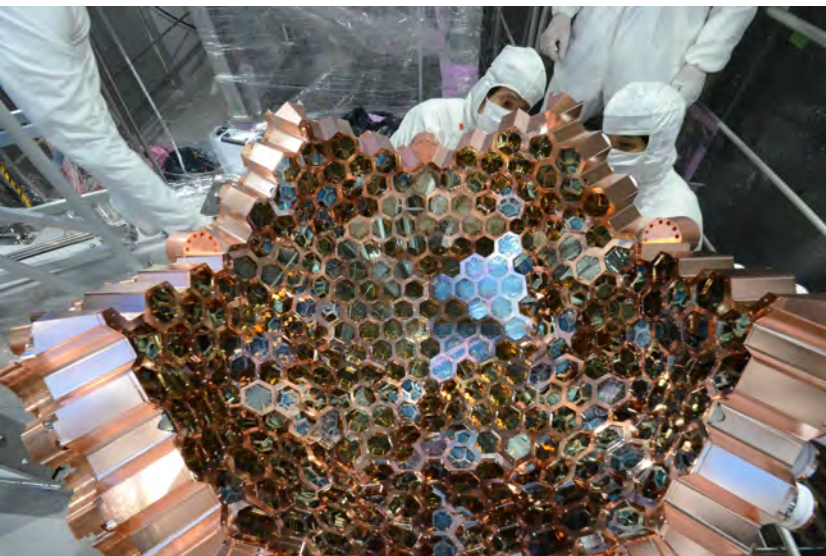
The XMASS detector (the photo was taken during the refurbishment work in 2013).
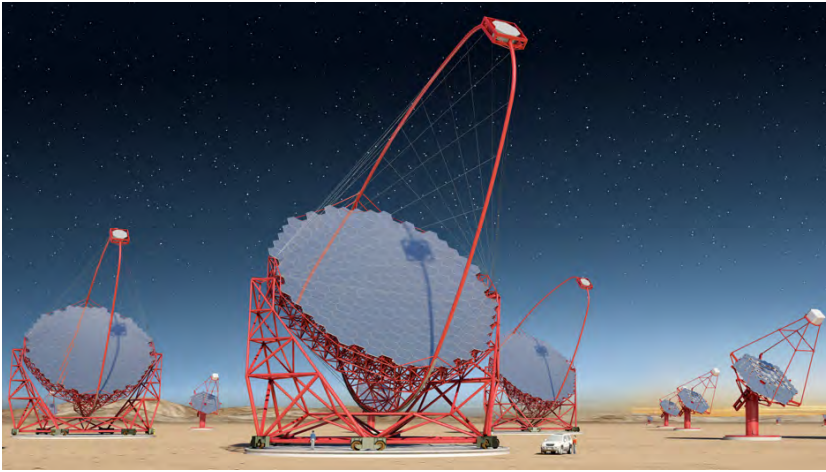
Artist view of the CTA observatory. CTA consists of three types of telescopes, Large Size Telescopes (23m diameter), Mid Size Telescopes (12m) and Small Size Telescopes (4m), and covers the broad energy band from 20GeV to 100TeV.

Tibet-III air shower array (37000 m^2) at Yangbajing, Tibet (4300 m in altitude).
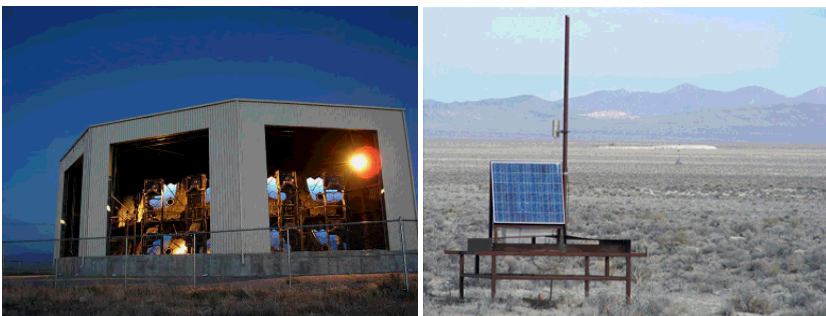
Air fluorescence telescopes (left) and a scintillator surface detector (right) of the Telescope Array experiment in Utah, USA to explore the origin of extremely high energy cosmic rays.

KAGRA X-arm tunnel.

A public lecture co-organized with the Institute for the Physics and Mathematics of the Universe (Kavli IPMU).

Organization
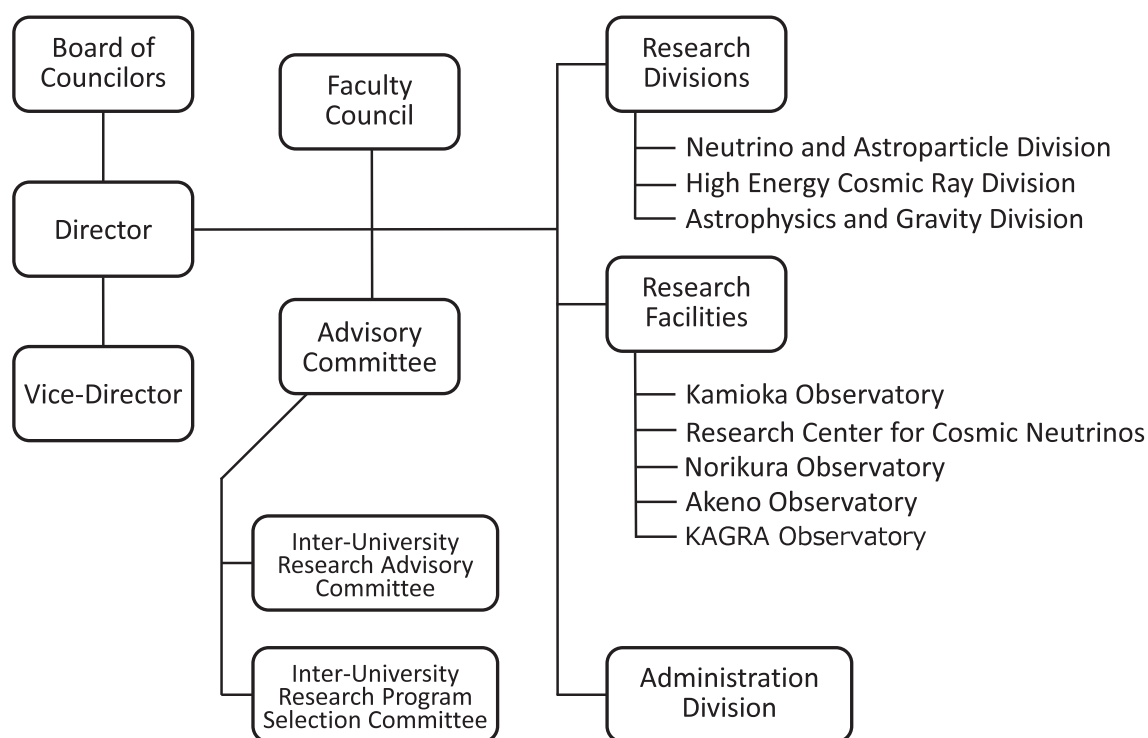
Number of Staff Members (As of May 1, 2017)

	Scientific Staff	Technical Staff	Research Fellows	Administrators and Secretaries	Total
Neutrino and Astroparticle Div.	26	4	3	18	51
High Energy Cosmic Ray Div.	16	10	2	2	30
Astrophysics and Gravity Div.	14	6	7	8	35
Administration	0	0	0	19	19
Total	56	20	12	47	135

FY 2011-2017 Budget

	2011	2012	2013	2014	2015	2016	2017
Personnel expenses	653 000	658 000	687 000	706 000	684 000	683 000	779 000
Non-personnel expenses	1 400 000	1 172 000	1 095 000	1 282 000	1 595 000	1 288 000	1 514 000
Total	2 053 000	1 830 000	1 782 000	1 988 000	2 279 000	1 971 000	2 293 000

(in 1 000 yen)

RESEARCH DIVISIONS

Neutrino and Astroparticle Division

Overview
Super-Kamiokande
T2K Experiment
XMASS Experiment
Hyper-Kamiokande

High Energy Cosmic Ray Division

Overview
Cherenkov Cosmic Gamma-Ray Group
TA: Telescope Array Experiment
Tibet ASγ Project
ALPACA Project
High Energy Astrophysics Group
Other Activities

Astrophysics and Gravity Division

Overview
Gravitational Wave Group
    KAGRA Project
Observational Cosmology Group
Theory Group
    Particle Phenomenology
    Particle Cosmology

NEUTRINO AND ASTROPARTICLE DIVISION

Overview

This division aims to study particle physics with prime interests in physics of neutrinos and proton decay, and astroparticle physics with the use of underground experimental facilities.

The Super-Kamiokande (SK) detector is a 50 kton water Cherenkov detector using 11,129 50 cm-diameter photomultipliers (PMTs) for its inner detector and 1,885 20 cm-diameter PMTs for its outer detector. The data taking of SK started in April 1996 and 20th anniversary was celebrated in 2016. The neutrino oscillations in atmospheric neutrinos were discovered in 1998 and thereby it was demonstrated that neutrinos have a finite mass. In 2001, the accurate measurements of the ^{8}B solar neutrino flux by SK and SNO discovered that neutrino oscillations are the solution of the solar neutrino problem beyond doubt. These findings became the research achievement for which the Nobel Prize in Physics was awarded in 2015. After the epoch-making discoveries, precise measurements of atmospheric neutrinos and solar neutrinos have been performed and they unraveled various phenomena of neutrino oscillations. The evidence of tau neutrino appearance in atmospheric neutrinos was confirmed in 2013 and atmospheric neutrino anomaly has been finally concluded. The indication of day-night asymmetry of the solar neutrino flux, which is expected from the matter effect of neutrino oscillations, was reported in 2014. At present, the most interesting subjects in those observations are the determination of neutrino mass hierarchy using atmospheric neutrinos and the consistency check of solar(ν_e) and reactor($\bar{\nu}_e$) oscillations.

A high intensity neutrino beam experiment using the J-PARC accelerator (T2K) was started in 2009. The T2K experiment uses the SK detector as the far detector. Search for leptonic CP violation and the high precision measurement of oscillation parameters are main physics subjects in T2K. An indication of electron neutrino appearance was found in June 2011, and later the electron appearance has been established with greatly improved significance. Since 2014, anti-neutrino beam data also have been taken in order to search for CP violation.

The search for nucleon decay is another important subject at SK because it gives a direct evidence for the Grand Unified Theories (GUTs). SK gives the current best limit which strongly constrains various GUT models.

If a supernova happens in our galaxy, thousands of neutrino interactions are expected at SK and they will reveal detailed mechanism of the supernova explosion. SK is the only detector in the world which can identify the direction of the supernova neutrinos. So, SK has been operated almost all the time with small dead time and if a supernova is observed at SK, we will send burst information to astronomers as soon as it is detected. In addition, SK aims to observe supernova relic neutrinos, which is an accumulated supernova burst neutrinos from the beginning of the universe. For this purpose, it

is planned to add 0.1% of gadolinium into the Super-K tank (called SK-Gd project) in order to tag neutrons for $\bar{\nu}_e$ detection. A feasibility study for the SK-Gd project is being performed using a 200 ton tank which mimics the Super-K detector.

Another activity of the Neutrino and Astroparticle division is a multi-purpose experiment using liquid xenon aiming at the detection of cold dark matter, neutrino absolute mass using neutrinoless double beta decay, and low energy solar neutrinos. A 800 kg liquid xenon detector was constructed in an experimental hall near the SK site, and searches for dark matter interactions and rare phenomena in liquid xenon have been running in the last several years.

The Hyper-Kamiokande (Hyper-K or HK) experiment is proposed as a joint project of the university of Tokyo and KEK by combining a next generation underground water Cherenkov detector and upgraded J-PARC neutrino beam. The Hyper-K detector is an order of magnitude larger in detector fiducial mass than Super-K and has discovery potential of leptonic CP violation and proton decays. The detector construction has been endorsed by the ICRR future project committee's report in March 2017. Hyper-K has been selected as one of the seven large scientific projects in the Roadmap of the Japanese Ministry of Education, Culture, Sports, Science and Technology (MEXT) in 2017. We are eagerly waiting for the approval by the Japanese government.

SUPER-KAMIOKANDE

[Spokesperson : Masayuki Nakahata
(Kamioka Observatory, ICRR, The University of Tokyo)]

Search for nucleon decay

Proton decays and bound neutron decays (nucleon decays in general) is the most dramatic prediction of Grand Unified Theories (GUTs) in which three fundamental forces of elementary particles are unified into a single force. Super-Kamiokande (SK) is the world's largest detector to search for nucleon decays. Various nucleon decay modes have been looked for, but we have found no significant signal excess so far.

A proton decay into one charged lepton and one neutral pion ($p \rightarrow e^+\pi^0$, $p \rightarrow \mu^+\pi^0$) is one of the benchmark decay modes which have large detection efficiency. The results has been updated since the published paper [1] with 365 kton·year exposure. There ware no candidates observed for $p \rightarrow e^+\pi^0$ with 0.6 expected background. One event which is the same event reported in the previous report and no new event observed for $p \rightarrow \mu^+\pi^0$ mode. That is consistent with

0.7 expected background. The lower limits of proton for these modes were calculated as 2.0×10^{34} and 1.2×10^{34} years, respectively. A proton decay into K^+ and ν is suggested by GUTs collaborated with Supersymmetry theories (SUSY-GUTs). No candidates observed in 365 kton·year data and lifetime limit was estimated as 8.2×10^{33} year.

In addition to searching for $\Delta B=1$ decays such as proton decay, Super-Kamiokande data can be used to search for decays where $\Delta B=2$. One type of $\Delta B=2$ decay is dinucleon decay, where two nucleons in an oxygen atom decay together. We searched for 10 dinucleon and proton decay modes which are characterized by a two-body final state with no hadrons. For example, our search included the dinucleon decay mode $pp \rightarrow e^+ e^+$, and the proton decay mode $p \rightarrow e^+ \gamma$. We use Super-Kamiokande data from April 1996 to April 2018, with a total exposure of 365 kton·years.

The eight dinucleon decay modes studied were: $pp \rightarrow e^+ e^+$, $pp \rightarrow e^+ \mu^+$, $pp \rightarrow \mu^+ \mu^+$, $nn \rightarrow e^+ e^-$, $nn \rightarrow e^+ \mu^-$, $nn \rightarrow e^- \mu^+$, $nn \rightarrow \mu^+ \mu^-$ and $nn \rightarrow \gamma\gamma$. The two proton decay modes studied were: $p \rightarrow e^+ \gamma$ and $p \rightarrow \mu^+ \gamma$.

The three columns of Figure 1 show the scatter plots of invariant mass versus total momentum for signal Monte Carlo (100,000 simulated events for each mode), 2000 years of atmospheric background Monte Carlo (500 years for each of the four SK periods) and combined data for all SK periods. Signal Monte Carlo is plotted for three of the dinucleon decay modes ($pp \rightarrow e^+ e^+$, $pp \rightarrow e^+ \mu^+$, and $pp \rightarrow \mu^+ \mu^+$) and for the two proton decay modes ($p \rightarrow e^+ \gamma$ and $p \rightarrow \mu^+ \gamma$). In the top row, the events plotted are those which have passed the following cuts: the event is fully contained in the SK fiducial volume, the event has two e-like rings and zero decay electrons. In the middle row, the events plotted are those which have passed the following cuts: the event is fully contained in the SK fiducial volume, the event has an e-like and a mu-like ring and ≤ 1 decay electron. In the bottom row, the events plotted are those which have passed the following cuts: the event is fully contained in the SK fiducial volume and the event has two μ-like rings.

For the proton decay searches, as in the $p \rightarrow e^+ \pi^0$ analysis a two-box analysis is applied and an additional neutron tagging cut is applied since those modes have a significant number of expected background events. As seen in the rightmost column of the middle row of Figure 1, there are two candidate events for the $p \rightarrow \mu^+ \gamma$ decay mode which is consistent with 0.7 expected background. Figure 2 shows the summary of the lower lifetime limits for each of the decay modes to the 90% confidence level, including systematic uncertainties. For all 10 modes these are the most stringent limits in the world.

Bibliography

[1] K. Abe *et al.* [Super-Kamiokande Collaboration], Phys. Rev. D **95**, 012004 (2017).

[2] C. McGrew *et al.* [IMB Collaboration], Phys. Rev. D **59**, 052004 (1999).

[3] C. Berger *et al.* [Frejus Collaboration], Z.Phys. C **50**, 385-394 (1991).
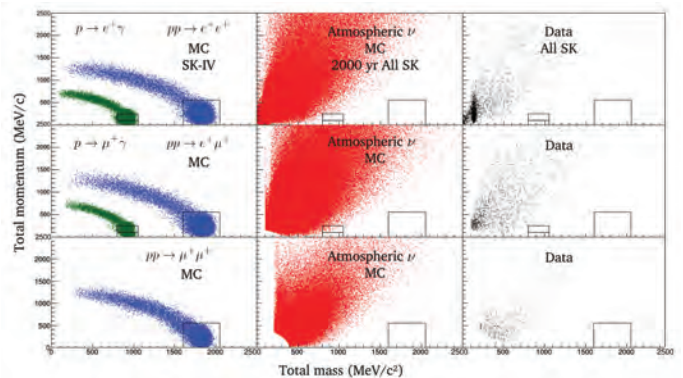
Fig. 1. Reconstructed total mass vs total momentum for $pp \rightarrow e^+ e^+, e^+ \mu^+, \mu^+ \mu^+$ and $p \rightarrow e^+ \gamma, \mu^+ \gamma$. Left, middle, and right figures show signal MC, background MC, and data, respectively.
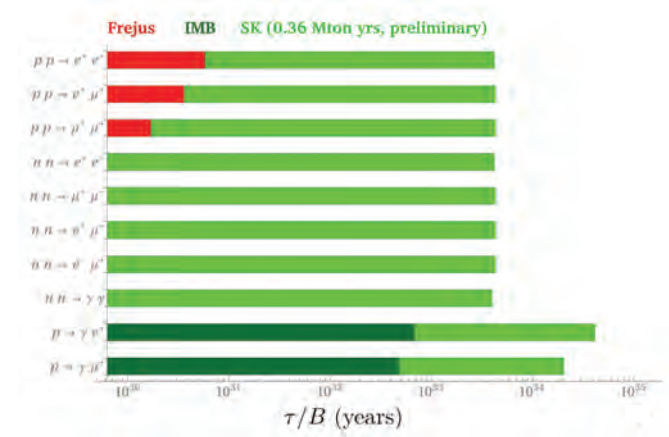
Fig. 2. Summary of lifetime limits for eight dinucleon decay modes and two proton decay modes. Red corresponds to results of Frejus [3], dark green shows IMB[2], and light green shows results of this study.

Atmospheric neutrinos

Atmospheric neutrinos are produced from the decays of secondary particles produced in the collision of primary cosmic rays with nuclei in the atmosphere. Atmospheric neutrinos have several remarkable features:

- The flavor ratio, $(\nu_\mu + \bar{\nu}_\mu)/(\nu_e + \bar{\nu}_e)$ is 2 (> 2 for above few GeV)

- Zenith angle distribution is up/down symmetry above a few GeV

These features are realized without neutrino oscillations, and provide a useful constraint in the study of these neutrinos. Super-Kamiokande has been observing atmospheric neutrinos since 1996 and has accordingly made several important

measurements, including the discovery of neutrino oscillations [1, 2].

Three flavor oscillations and the neutrino mass hierarchy

The SK atmospheric neutrino data are described at leading order by two-flavor $\nu_\mu \rightarrow \nu_\tau$ oscillations with maximal mixing ($\theta_{23}=\pi/4$). However, sub-leading contributions via $\nu_\mu \rightarrow \nu_e$ oscillations induced by the mixing angle θ_{13} as well as the "solar" mixing parameters ($\Delta m_{12}^2, \theta_{12}$) provide the ability to probe currently unknown aspects of the standard neutrino oscillation paradigm, such as the existence of leptonic *CP* violation and the neutrino mass ordering (hierarchy). Understanding these open questions may bring important insight into larger questions, such as the origin and evolution of today's matter-dominated universe.

Several sub-leading oscillation effects are expected to appear in atmospheric neutrinos:

- Resonant enhancement of $\nu_\mu \rightarrow \nu_e$ oscillations due to the effects of matter is expected to occur at energies between 2 and 10 GeV and will manifest as an excess of upward-going electron-like events (e-like) in the atmospheric sample.

- This enhancement exists for either ν_e or $\bar{\nu}_e$ depending on the mass hierarchy. Therefore the mass hierarchy can be probed by understanding the relative amount of neutrino and antineutrino interactions in the detector.

- The combination of the solar oscillation parameters and the octant of $\sin^2 \theta_{23}$, may enhance or suppress the event rate, and to some extent alter the spectral shape, of Sub-GeV electron-like data the due to the $\nu_\mu \leftrightarrow \nu_e$ oscillations they induce.

- The standard oscillation paradigm includes a *CP*-violating factor, δ_{cp}, which is expected to induce several sub-dominant oscillation effects in many of the SK atmospheric neutrino samples, even if CP is conserved.

Super-Kamiokande has studied the effects of these oscillations on atmospheric neutrino data separated into fully-contained (FC) events, partially-contained (PC) events, and upward-going muon topologies. Fully-contained events are characterized by a primary interaction vertex that is located inside the 22.5 kton fiducial volume of the detector and whose visible particles stop within the inner detector. On the other hand, though the primary vertex position of PC events is within the fiducial volume, they are characterized by having at least one charged particle escaping the inner detector and depositing light in the outer detector. In most cases the escaping particle is a muon. Upward-going muons originate from high energy muon-neutrino interactions in the rock surrounding the detector. Since all other particles are lost to interactions in the rock, only the muon is penetrating enough to reach the detector and be identified. The FC sample is separated into electron-like and muon-like (μ-like) subsamples by applying a particle identification algorithm to the most energetic Cherenkov ring of each event. Since PC and upward-going events are predominantly produced by muon neutrinos,

no particle identification is applied. Though SK cannot distinguish on an event-by-event basis neutrino and antineutrino interactions, statistical separation of multi-GeV electron-like subsamples is performed to improve sensitivity to the mass hierarchy. A likelihood method designed to enhance the kinematic differences between neutrino and antineutrino interactions is applied to separate events into ν_e-like and $\bar{\nu}_e$-like subsamples.

The atmospheric neutrino data accumulated in four period of Super-Kamiokande (5,326 days in total) have been analyzed. Zenith angle distributions for six data subsamples are shown in Figure 3. An oscillation analysis considering all mixing parameters from the PMNS framework, including the *CP*-violating term, δ_{cp}, and the effects of the earth's matter on neutrino propagation, has been performed assuming that θ_{13} is constrained to the measured value from reactor neutrino experiments, $\sin^2 \theta_{13}=0.0219$, with its uncertainty included as systematic error in the analysis. Figure 4 shows the $\Delta\chi^2$ distribution as a function of neutrino mixing parameters, θ_{23}, δ_{cp}, and mass squared difference (Δm_{32}^2 or Δm_{13}^2) . Comparing the minimum absolute χ^2 values between fits to the normal and inverted hierarchy hypotheses indicate that the Super-K data have a weak preference for the normal mass hierarchy, $\Delta\chi^2 = \chi_{NH}^2 - \chi_{IH}^2$ = -4.33. In order to improve sensitivity to the mass hierarchy the analysis has been extended to include external constraints from the T2K experiment. A model of the T2K experiment based on atmospheric neutrino MC reweighted to the beam spectrum and incorporating publicly available data and systematic error information was used for this analysis [4, 5]. Data samples created from this model are analyzed simultaneously with the atmospheric neutrino data including relevant systematic error correlations. In this fit the normal hierarchy preference is strengthened to $\Delta\chi^2 = -5.27$. The best fit oscillation parameters and minimum χ^2 values from these analyses are shown in Table 1. For the range of parameters allowed by these analyses at the 90% C.L. the inverted hierarchy is rejected by between 81.9% and 96.7% when SK data are fit by themselves and by between 91.9% and 94.5% when the data are fit with constraints from T2K.

Tau neutrino appearance search

The deficit of the muon neutrinos observed in the Super-K data is predominantly explained by the oscillation of the original muon neutrinos into tau neutrinos. For this reason, the direct detection of tau neutrinos is important to confirm the standard three-flavor neutrino oscillation scheme.

Super-Kamiokande collaboration previously published a measurement of atmospheric tau neutrino appearance consistent with three-flavor neutrino oscillation with data collected in SK-I through SK-III [6]. The analysis has been updated to use fitting technique and includes new data from the SK-IV period for a total livetime of 5,326 days.

The ν_τ signal is characterized by an isotropic distribution of hadrons produced when the τ lepton emerging from the original neutrino interaction decays. Background events are mainly are result of charged current CC ν_μ and ν_e interactions which produce multiple hadrons. We employ a neural network (NN) technique to help distinguish CC ν_τ events from back-
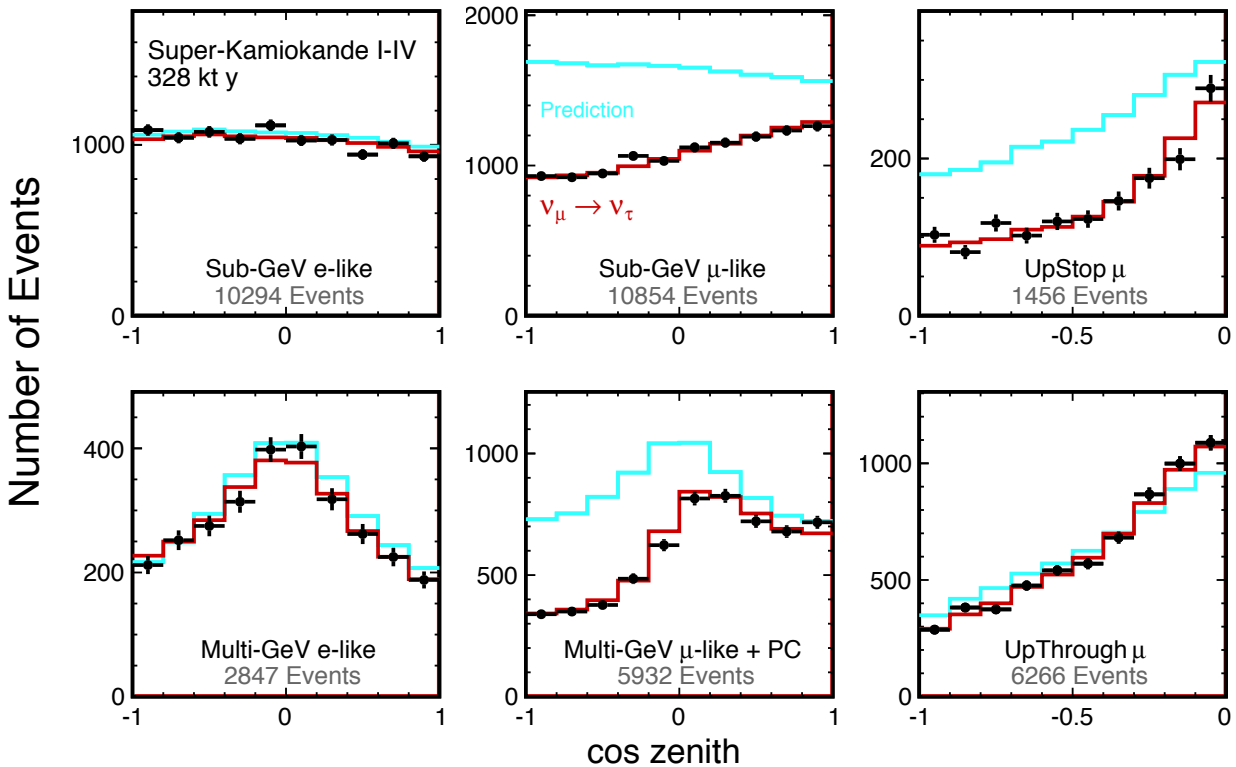
Fig. 3. Zenith angle distributions of SK atmospheric neutrino data. The horizontal axis indicates the cosine of the reconstructed zenith angle ($\cos\theta = -1$ corresponds to the upward-going direction). The data are shown by the black points with error bars and the MC predictions without oscillations and with two flavor $\nu_\mu \rightarrow \nu_\tau$ oscillations are shown by the blue and red lines, respectively.

Fit	Hierarchy	$\sin^2\theta_{23}$	$|\Delta m^2_{32,31}|\ [\times 10^{-3}\ \mathrm{eV}^2]$	δ_{CP}
SK only	NH	$0.588^{+0.031}_{-0.064}$	$2.50^{+0.13}_{-0.20}$	$4.18^{+1.41}_{-1.61}$
	IH	$0.575^{+0.036}_{-0.073}$	$2.50^{+0.08}_{-0.37}$	$4.18^{+1.52}_{-1.66}$
SK+T2K	NH	$0.550^{+0.039}_{-0.057}$	$2.50^{+0.05}_{-0.12}$	$4.88^{+0.81}_{-1.48}$
	IH	$0.550^{+0.035}_{-0.051}$	$2.40^{+0.13}_{-0.05}$	$4.54^{+1.05}_{-0.97}$

Table 1. Best fit oscillation parameters obtained by the three flavor oscillation analysis. Fits are conducted for both the normal (NH) and inverted (IH) hierarchy assumptions for the atmospheric neutrino data ("SK only") and including constraints from the T2K experiment("SK+T2K"). All fits are performed assuming $\sin^2\theta_{13}$=0.0219, which is taken from PDG.

ground events. Seven kinematic variables are sampled from simulated signal and background events to build and train the NN before applying it to the data.

To estimate the amount of tau neutrino events in the data, we employ a two-dimensional unbinned maximum likelihood fit. Two dimensional probability density functions (PDFs) are constructed for both the signal and background as a function of the NN output and the cosine of the zenith angle of each event. The PDFs for each event is a combination of that for background and signal:

$$PDFs = PDFs_{bg} + \alpha \times PDFs_{tau} + \sum_i \varepsilon_i \cdot PDFs_{sys},$$

where the last term represents the change of the PDFs due to systematic error effects. The likelihood is calculated as the product of PDFs for each events and the parameters α and ε_i's are adjusted to maximize the likelihood.

Figure 5 shows the zenith angle distribution of tau-like (NN output > 0.5) and non-tau-like (NN output < 0.5) samples after fitting (left side). The NN output distributions for upward- ($\cos(\Theta) < -0.2$) and downward-going ($\cos(\Theta) > 0.2$) events are shown in the right panels. Relative to the expectation for standard three-flavor neutrino oscillations the fitted number of tau events in the data is $\alpha = 1.47 \pm 0.32$(stat+syst.). This corresponds to a statistical significance 4.6σ to reject the no-tau-appearance hypothesis.
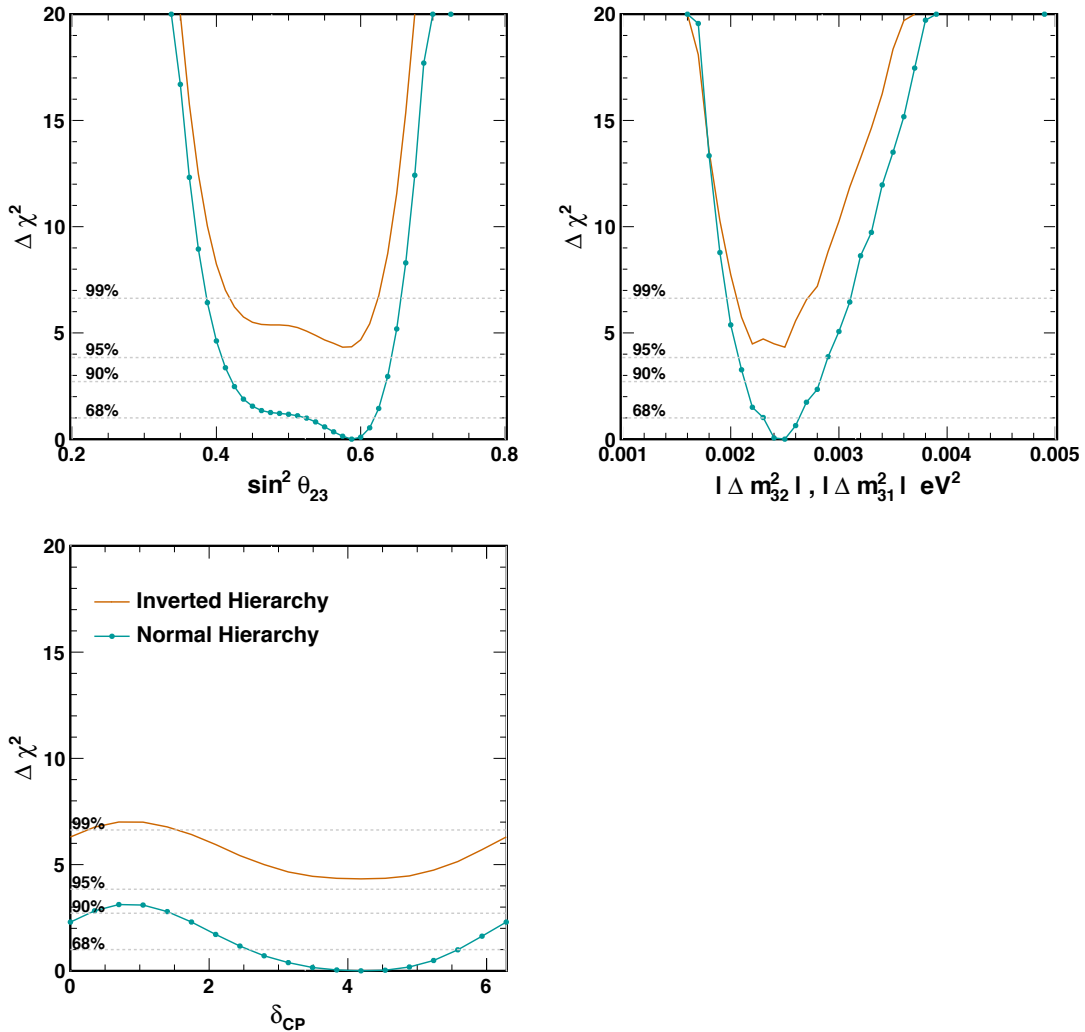
Fig. 4. The $\Delta\chi^2$ as a function of $\Delta m^2_{23,31}$, $\sin^2\theta_{23}$, and δ_{cp}. Fits to the normal (blue) and inverted (orange) hierarchy hypotheses are shown.

As a result of this observation of tau neutrino appearance, we have produced the first atmospheric neutrino flux-averaged measurement of the tau neutrino cross section. The measured result is $(0.94 \pm 0.20) \times 10^{-38} \mathrm{cm}^2$ for energies between 3.5 GeV and 70 GeV. This result agrees with the predictions of the Standard Model at the 1.5σ level and is consistent with previous accelerator-based measurements.

Indirect WIMP searches

Weakly Interacting Massive Particles (WIMPs) are GeV/c^2-scale particles which have only gravitational and weak interactions, making them an ideal dark matter candidate. Though direct dark matter detection experiments search for the elastic scattering interactions of these proposed particles with ordinary baryonic matter, it is also possible that WIMPs decay or self-annihilate into Standard Model particles which can then be detected to give indirect evidence for WIMPs. If WIMPs become trapped in the gravitational potential of a massive system, such as the center of the Milky Way, the earth, or the sun, their density may become sufficient for large numbers of these particles to annihilate into particles

which then decay into neutrinos. Such neutrinos would pass undeflected through the galaxy (or solar or terrestrial medium) before being detected at Super-K.

The atmospheric neutrino data are binned in both lepton momentum and either the reconstructed angle to the galactic center, the earth core, or to the sun to search for the presence of an extra neutrino signal from those directions. The analysis proceeds by separately assuming annihilation into each of $\nu\bar{\nu}$, $b\bar{b}$, $t\bar{t}$, and W^+W^- with 100% branching fraction. For each assumed WIMP mass the expected neutrino energy distribution emerging from the decay chains of these particles is computed and used to define the signal spectrum at Super-K. Super-Kamiokande collaboration previously published the results from the sun [7]. The searches for a WIMP signal from the galactic center and Earth have been updated to use 5,326 days of data including SK-IV data up through 2016. No evidence for a neutrino signal on top of the atmospheric neutrino background has been found in either case, but Super-K continues to provide the most stringent limits below WIMP masses of 100 MeV/c^2 among indirect search experiments using neutrinos. Limits on the product of self-annihilation cross section

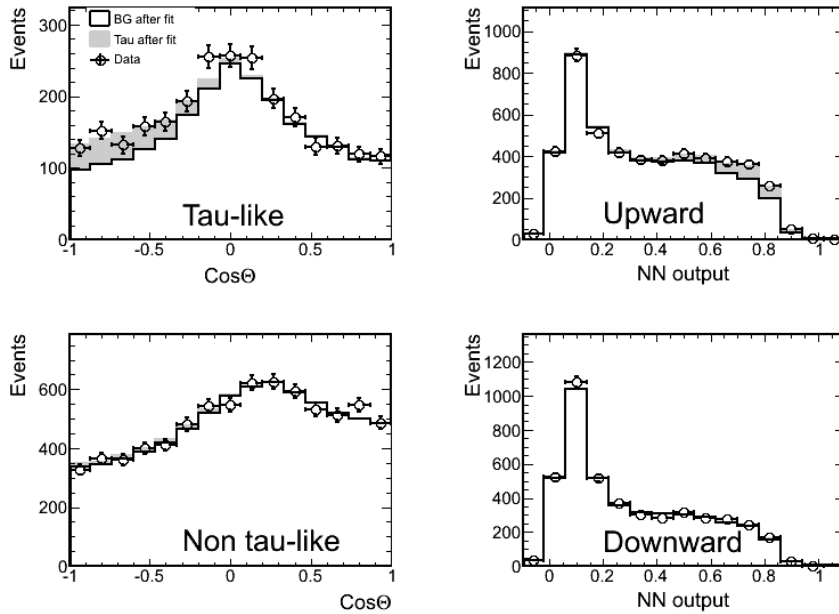Fig. 5. (Left) Zenith angle distribution of tau-like (NN output < 0.5) and non-tau-like (NN output > 0.5) samples after fitting. (Right) NN output distribution for upward ($\cos(\Theta) < -0.2$) and downward ($\cos(\Theta) > 0.2$) events. Shaded histograms show CC tau events components for best fitted parameters.

and relative velocity, and and WIMP-nucleon scattering cross sections are shown in Figure 6.

Bibliography

[1] Y. Fukuda *et al.* [Super-Kamiokande Collaboration], Phys. Rev. Lett. **81** 1562 (1998).

[2] Y. Fukuda *et al.* [Super-Kamiokande Collaboration], Phys. Rev. Lett. **81**, 1562 (1998) [arXiv:9807003 [hep-ex]].

[3] P. Adamson *et al.* [MINOS Collaboration], Phys. Rev. Lett. **112**, 191801 (2014) [arXiv:1403.0867 [hep-ex]].

[4] K. Abe *et al.* [T2K Collaboration], Phys. Rev. Lett. **112**, 181801 (2014) [arXiv:1403.1532 [hep-ex]].

[5] K. Abe *et al.* [T2K Collaboration], Phys. Rev. Lett. **112**, 061802 (2014) [arXiv:1311.4750 [hep-ex]].

[6] K. Abe *et al.* [Super-Kamiokande Collaboration], Phys.Rev.Lett **110**, 181802 (2013), [arXiv:1206.0328 [hep-ex]].

[7] K. Choi *et al.* [Super-Kamiokande Collaboration], Phys. Rev. Lett. **114**, no. 14, 141301 (2015) [arXiv:1503.04858 [hep-ex]].

[8] M.G. Aartsen *et al.* [IceCube Collaboration], [arXiv:1705.08103 [hep-ex]].

[9] R.Bernabei *et al.* [DAMA Collaboration], Eur. Phys. J. C **56**, 333 (2008)

[10] C. Savage *et al.*, J. Cosmol. Astropart. Phys. **04**, 010 (2009)

[11] A. Albert *et al.* [ANTARES Collaboration], arXiv:1602.06792 [hep-ex].

[12] M.G. Aartsen *et al.* [IceCube Collaboration], Eur. Phys. J. C **77**, 82 (2017) [arXiv:1609.01492 [astro-ph.HE]].

Solar Neutrinos

Introduction

Solar neutrinos are produced by the nuclear fusion reaction, $4p \rightarrow \alpha + 2e^+ + 2\nu_e$, in the core of the Sun. Electron neutrinos (ν_e) produced in the Sun are so called pp, pep, ^{7}Be, ^{8}B and hep neutrinos[1], whose fluxes had been predicted by the standard solar model [1]. Their energy distributes from $\sim$0.1 MeV to $\sim$20 MeV as shown in the left of Figure 7. Because of its high energy, ^{8}B solar neutrino can be easily detected in many solar neutrino experiments.

Solar neutrino flux measurements from Super-Kamiokande (SK) [2] and the Sudbury Neutrino Observatory (SNO) [3] have provided direct evidence for solar neutrino flavor conversion. However, there is still no clear evidence that this solar neutrino flavor conversion is indeed due to neutrino oscillations and not caused by any other mechanism.

The current interesting physics motivation of the solar neutrino observation with the SK detector [4] is to search for a matter effect, which is so called Mikheyev-Smirnov-Wolfenstein (MSW) effect [5, 6]. The MSW effect leads to a resonant conversion of the higher energy solar neutrinos within the Sun and results in an about 30% level of the survival probability above a few MeV as shown in the left of Figure 7, which is so called "Up-turn".

Current experimental data among solar neutrino experiments is not enough to demonstrate the "Up-turn" of the
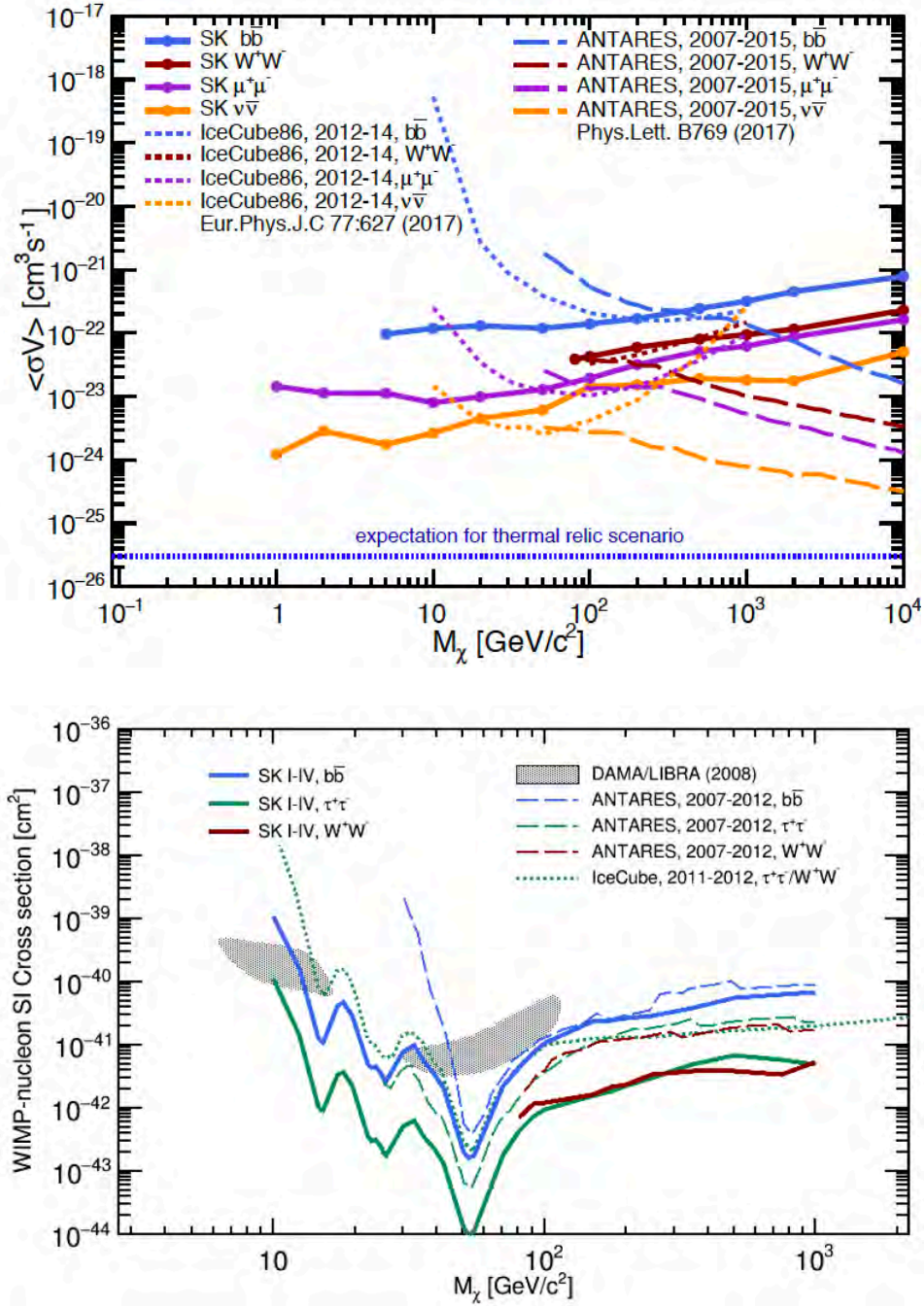
---

*[1] As well as CNO neutrinos

Fig. 6. The 90% C.L. upper limits on the product of dark matter self-annihilation cross section and the relative velocity of the dark matter particles in the galactic center (upper) and the 90% C.L. upper limit on the WIMP-nucleon spin independent cross section in the earth core (lower). These limits are calculated assuming WIMP annihilation into $\tau^+\tau^-$, $b\bar{b}$, and W^+W^- each with 100% branching fraction. Limits and allowed regions from other experiments are also shown [8, 9, 10, 11, 12].

MSW prediction assuming the large mixing angle parameters because the survival probability in the transition region, which is placed between the vacuum oscillation dominant region (below a few MeV) and the matter oscillation dominant region (above 5 MeV), has never been measured precisely.

SK searches for the "Spectrum up-turn" by measuring the recoil electron energy spectrum since the recoil electron energy spectrum reflects the survival probability of the electron neutrinos produced in the Sun. Therefore, the measurement of the energy spectrum in the transition region using SK is important to test the MSW effect as well as several alternative theoretical models to explain the current experimental results, such as sterile neutrinos [7, 8], mass-varying neutrinos [9], non-standard interactions [10, 11] and so on.

In addition, due to the matter effect in the interior of the Earth, electron flavor neutrinos are regenerated as shown in
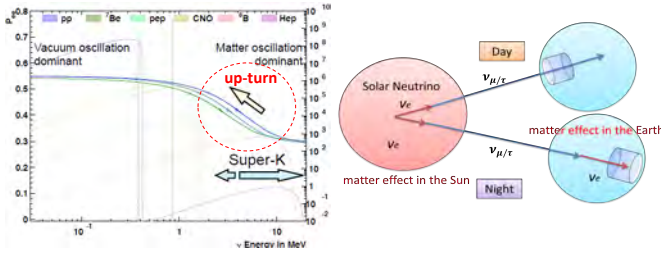
Fig. 7. Left: Several predictions of the survival probability of electron neutrinos emitted from the Sun as well as the fluxes of each solar neutrino; Right: The visual explanation of the day/night flux asymmetry.

the right of Figure 7. It is expected that the neutrino flux in night is larger than that in day by about a few % level depending on the neutrino oscillation parameters. In 2014, SK reported an indication of the terrestrial matter effects by about 2.7σ [12].

For the both physics targets, it is required to precisely detect the ^{8}B solar neutrino event with the high detection efficiency and to carefully reduce the measurement uncertainties. To satisfy those requirements, several calibration source (or devices) have been used in SK. For example, the electron LINAC [13], which generates electron with uniform energy, and the deuterium-tritium neutrino generator, which generates ^{16}N radioisotopes [14], are used to determine the energy scale and both energy and angle resolution. In addition, Ni-Cf calibration source [15] is used to estimate the resolution of the reconstructed position and the detection efficiency of the low energy neutrino-like event.

In 2016, the Super-Kamiokande collaboration released a paper about the solar neutrino analysis results [16]. In this annual report, the updated results, expect for the day/night flux asymmetry measurement, are presented using data taken through the end of March, 2017 (SK-IV 2,645 days data set). The total livetime throughout the different phases of SK [2, 17, 18] is 5,480 days.
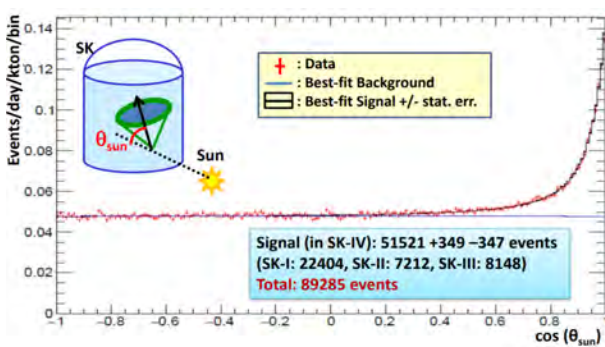
^{8}B solar neutrino flux measurement

Fig. 8. The solar angle distribution in SK-IV. The horizontal axis shows the cosine of the solar angle $\cos\theta_{Sun}$ and the vertical axis shows the number of the observed events. The red points shows the observed data, the black (blue) histogram shows the best-fit (background-shape).

The SK detector observes solar neutrinos via the elastic scattering between the solar neutrino and the electron in pure water. In case of ν-e interaction, the direction of the recoil electron is highly correlated with the direction of the incident neutrino. Figure 8 shows the distribution of cosine between the reconstructed direction of observed recoil electrons and the direction of the Sun. Using 2,645 days data in SK-IV, more than 50,000 events are observed over the background. Adding the solar neutrino events observed in other phases, the total number of the solar neutrino events reaches about 90,000 events so far. Based on this data, the ^{8}B solar neutrino flux is determined to be $(2.355\pm0.033)\times10^6$ /cm^2/sec assuming a pure electron neutrino flavor content. The ratio between the SK result and the SNO NC current flux (5.25×10^6 /cm^2/sec) [19] becomes 0.4486 ± 0.0062.

Although the standard solar model predicts the production rate of solar neutrinos in the core of the Sun, it does not consider periodical activities of the Sun, for example, the rotation of the Sun, the variation of the sun spots on the surface of the Sun and the modulation of the solar magnetic fields. When a periodic signal of solar neutrinos is observed, this leads to a further improvement of the standard solar model.

The solar activity cycle is the 11 years periodic change of sun spots releasing the magnetic flux at the surface of the Sun. The number of the sun spots strongly correlated with the solar activity cycle. If the neutrino has large magnetic moment, the magnetic field inside the Sun would cause precession of the neutrino spin [20, 21]. Therefore, the evaluation of stability of the observed solar neutrino flux is important in order to understand the solar activity as well as properties of neutrinos.

Since the SK has observed solar neutrinos for more than 20 years, this long term observation covers nearly 2 solar activity cycles. Figure 9 shows the SK yearly flux measured throughout the different phases of SK together with the corresponding sun spot number (Source: WDC–SILSO, Royal Observatory of Belgium, Brussels [22]).
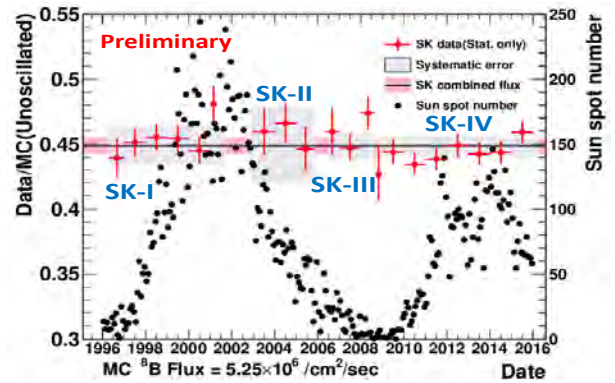
Fig. 9. The ratio of ^{8}B solar neutrino flux in SK over the SNO's NC current flux from 1996 to 2015. The red points show the yearly flux measured by SK (statistical uncertainty only), the gray bands show the systematic uncertainties for each SK phase, the black-horizontal line shows the combined measured flux with the uncertainty drawn as the red horizontal band. The back points show the sun spot number provided by [22].

Using the present data, the χ^2 is calculated with the total experimental uncertainties as $\chi^2 = 15.52/19$ d.o.f., which corresponds to a probability of 68.9%. The SK solar rate measurements are fully consistent with a constant solar neutrino

flux emitted by the Sun.

Periodic modulation search

In order to search for an unexpected periodic signal of solar neutrinos, we had performed a periodic search analysis using SK-I 1,496 days data set [23]. In the past analysis, we used 5-days binning flux data sample whose energy range is from 4.5 MeV to 19.5 MeV in the recoil electron kinetic energy and applied Lomb-Scargle method to the 5-days sample. Finally, we reported that no significant periodic signal was found.

On the other hand, other researches pointed out that the periodic signal at $\sim$9.42 year^{-1} was observed using the same data set [24, 25]. Their analysis used the generalized Lomb-Scargle method [26] which deals the measurement asymmetric uncertainty properly.

We performed the re-analysis of the SK-I 1,496 days data set [2] and the analysis of the SK-IV 1,664 days data set [16] using the generalized Lomb-Scargle method. The analysis condition is summarized in Table 2.

Table 2. The summary of the periodic signal analysis.

SK phase	SK-I	SK-IV
Livetime	1,496 days [2]	1,664 days [16]
Analysis method	Generalized Lomb-Scargle method	
Binning	5-days	
Energy range	4.5–19.5 MeV (Recoil electrons)	

Figure 10 shows the result of the periodic signal search using the generalized Lomb-Scargle method. The maximum peak at $\sim$9.42 year^{-1} is found in SK-I data sample while no significant peak is seen around that frequencies in SK-IV data sample.
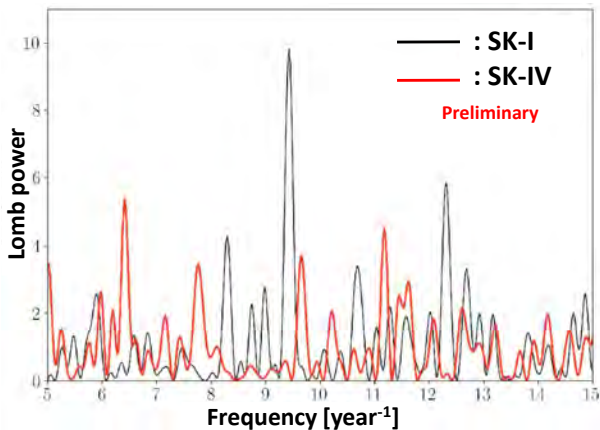

Fig. 10. The results of the periodic analysis using the generalized Lomb-Scargle method. The black (red) line shows Lomb power of SK-I (SK-IV) as a function of frequency in unit of year^{-1}. The range of the frequency is from 5 year^{-1} to 15 year^{-1}.

The updated analysis using the data set of SK-II, SK-III and recent SK-IV 2,645 days sample will be performed soon.

Energy spectrum analysis

Because of the installation of new front-end electronics for SK-IV [27], the improvements of the water circulation system and the upgrade of calibration methods [15], solar neutrino interactions as well as the background event in multi-MeV regions has been well understood in SK-IV. Owing to these upgrades above, SK has achieved the lowest background (induced by radioisotopes in pure water, especially ^{214}Bi) among all SK phases [28]. Finally, the energy threshold in SK-IV have been lowered at 3.5 MeV in recoil energy kinetic energy (SK-I: 4.5 MeV, SK-III: 4.0 MeV) and this enables SK to measure the solar neutrino energy spectrum with high sensitivity. In addition, on May 2015, the trigger threshold was changed from 34 observed PMT signals within 200 nsec to 31 hits [29, 30]. Because of this lower threshold, the detection efficiency between 3.5 MeV and 4.0 MeV was improved from $\sim$86% to $\sim$100%. This improvement leads the further reduction of the statistics uncertainty below 5 MeV in SK-IV.

Although an energy of the incident neutrino is not directly measured in the SK detector, the neutrino energy spectrum can be extracted from the recoil electron energy spectrum in SK. The energy spectrum of recoil electrons are extracted using an extended maximum likelihood fit [16].

The number of expected solar neutrino interactions without the neutrino oscillations is estimated by using the MC simulation considering the cross section of the ν-e elastic scattering, recoil electron kinematics, the response of the SK detector (PMT and electronics) and the performance of the SK detector (energy scale, energy resolution and so on). After the MC production above, the number of the observed solar neutrino interactions is compared with the expected number of events, thus the survival probability of the electron neutrino produced in the Sun is obtained. Then, a parametrized polynomial function centered at 10 MeV, which was developed by SNO [19], is used in order to discuss the survival provability[2]:

$$P_{ee}(E_\nu) = \sum_{i=0}^{n \leq 3} c_i \left(\frac{E_\nu}{\text{MeV}} - 10 \right)^i \qquad (2)$$

Figure 11 shows the energy spectrum obtained among all SK phases, its best-fits and the prediction of the MSW up-turn assuming the current oscillation parameters described in the next section.

Figure 12 shows the combined energy spectrum from SK-I to SK-IV with the predictions of the MSW effect assuming the current oscillation parameters described later. It is noted that all SK phases are combined without regard to energy resolution or systematic uncertainties in Figure 12, but those uncertainties are taken into account in the χ^2 calculation between the data and the prediction. Comparing χ^2 between the data (black) and the predictions (green or blue), the energy spectrum of SK is consistent within $\sim$1σ with the MSW up-turn for the solar best-fit parameters (green in Figure 14) and marginally consistent within $\sim$2σ with the MSW up-turn for KamLAND best-fit parameters (blue in Figure 14).

---

[2] If c_1 is small when $n = 2$ or $n = 3$, we can convert this polynomial function into an exponential function:

$$P_{ee}(E_\nu) = e_0 + \frac{e_1}{e_2} \left[\exp\left\{ e_2 \left(\frac{E_\nu}{\text{MeV}} - 10 \right) \right\} - 1 \right] \qquad (1)$$
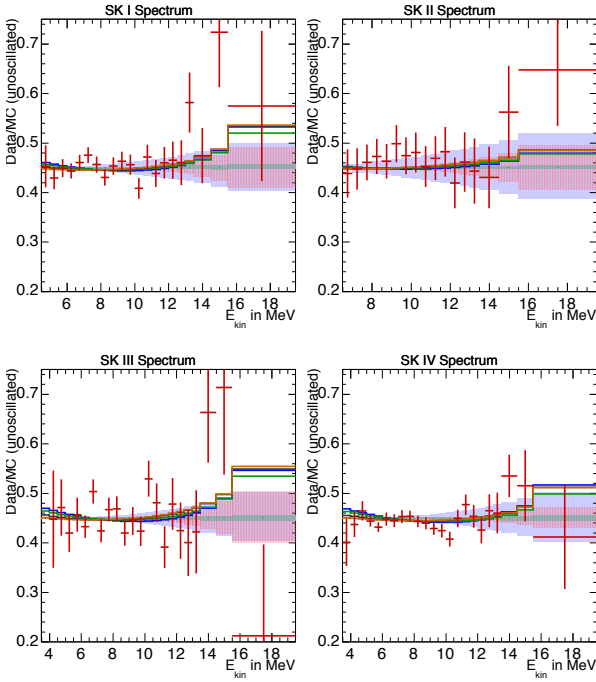
Fig. 11. SK-I, II, III and IV recoil electron spectra divided by the nonoscillated expectation. The green (blue) line represents the best-fit to SK data using the oscillation parameters from the fit to all solar (solar plus KamLAND) data. The orange (black) line is the best-fit to SK data of a general exponential or quadratic (cubic) P_{ee} survival probability. Error bars on the data points give the statistical plus systematic energy-uncorrelated uncertainties while the shaded purple, red, and green histograms give the energy-correlated systematic uncertainties arising from energy scale, energy resolution, and neutrino energy spectrum shift.
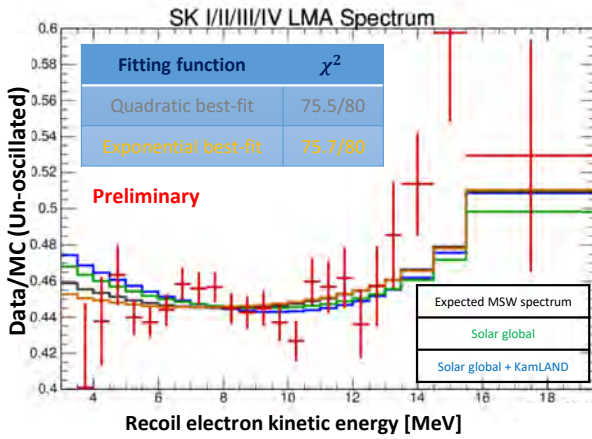

Fig. 12. The energy spectrum combining SK-I through SK-IV as a function of the recoil electron energy. The red points show the ratio of the data to the expected flux using a non-oscillated ^{8}B solar neutrino spectrum. The green (blue) curve shows the expected energy spectrum assuming the MSW effect inputting oscillation parameters of solar global (solar plus KamLAND).

Neutrino oscillation analysis

The oscillation analysis was conducted using the results from SK [2, 17, 18, 16], SNO [19], radiochemical solar neutrino experiments [31, 32, 33] and Borexino [34, 35, 36] as well as the anti-neutrino measurement by KamLAND

[37, 38]. Figure 13 shows the allowed contour measured by SK as well as KamLAND. SK uniquely selects the large mixing angle MSW region by more than 3σ and SK significantly contributes to the measurement of the solar angle θ_{12}. The SK energy spectrum and day/night data favors a lower Δm_{21}^2 value than KamLAND's by more than 2σ.

When combining with results from the other solar neutrino experiments, the mixing angle is determined to be $\sin^2\theta_{12} = 0.309 \pm 0.014$ and the mass difference is determined to be $\Delta m_{21}^2 = 4.83^{+1.24}_{-0.60} \times 10^{-5}$ eV^{-2} as shown in Figure 14. Adding the KamLAND result, the oscillation parameters are determined as $\sin^2\theta_{12} = 0.309^{+0.013}_{-0.012}$, $\Delta m_{21}^2 = 7.49^{+0.19}_{-0.18} \times 10^{-5}$ eV^2. These parameters are mostly determined by the solar neutrino oscillation fit and further precise measurements are required in future.
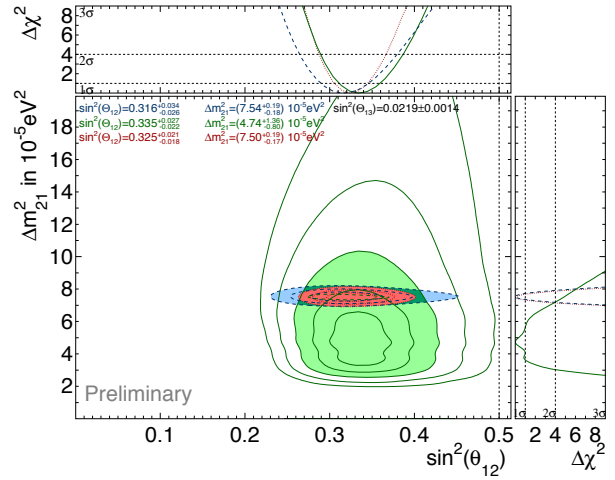
Fig. 13. The allowed contours for Δm_{21}^2 vs. $\sin^2\theta_{12}$ from the SK combined analysis (green) as well as the allowed region from KamLAND (blue). The combined allowed region is shown in red.
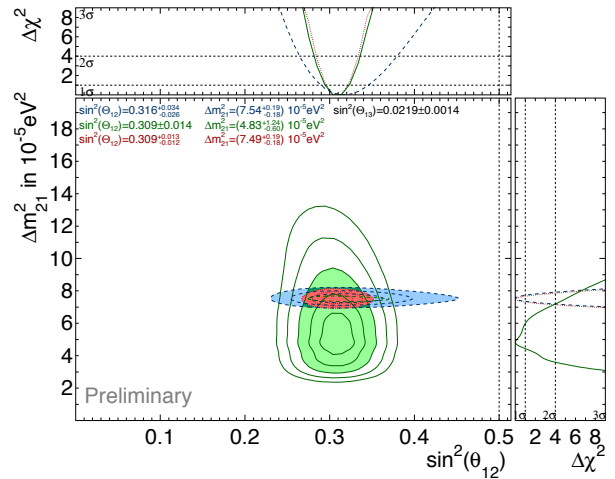

Fig. 14. The allowed contours for Δm_{21}^2 vs. $\sin^2\theta_{12}$ from all solar neutrino data (green solid line). The allowed contour from KamLAND is also shown in blue. The combined allowed region is shown in red.

In summary, Super-Kamiokande has precisely measured

the ^{8}B solar neutrino flux, its time variation and recoil electron spectrum. Using 5,480 days data, about 90,000 solar neutrino interactions are extracted over the background. SK has stably measured the solar neutrino flux for more than 20 years. No significant correlation between the observed solar neutrino flux and the sun spot number is found. In order to search for a periodic modulation of the solar neutrino flux, we applied the generalized Lomb-Scargle method to the SK flux measurement data. The maximum peak at $\sim$9.42 year^{-1} is found in SK-I data while no peak is seen around that frequencies in SK-IV. In addition, the energy spectrum of SK is consistent within $\sim$1σ with the MSW up-turn for the solar best-fit parameters and marginally consistent within $\sim$2σ with the MSW upturn for KamLAND best-fit parameters. In the solar neutrino oscillation analysis combined with the KamLAND result, the oscillation parameters are determined as $\Delta m_{21}^2 = 7.49^{+0.19}_{-0.18} \times 10^{-5}$ eV^2, $\sin^2 \theta_{12} = 0.309^{+0.013}_{-0.012}$.

Bibliography

[1] John N. Bahcall and Roger K. Ulrich, Rev. mod, Phys. **60**, 297 (1988).

[2] J. Hosaka *et al.*, Phys. Rev. D **73**, 112001 (2006).

[3] Q.R. Ahmad *et al.*, Phys. Rev. Lett. **87**, 071301 (2001).

[4] Y. Fukuda *et al.*, Nucl. Instrum. Meth. A **501**, 418 (2003).

[5] S.P. Mikheyev and A. Y. Smirnov, Sov. Jour. Nucl. Phys. **42**, 913 (1985).

[6] L. Wolfenstein, Phys. Rev. D **17**, 2369 (1978).

[7] P.C. de Holanda and Yu, Smirnov, Phys. Rev. D **69**, 113002 (2004).

[8] P.C. de Holanda and Yu, Smirnov, Phys. Rev. D **83**, 113011 (2011).

[9] V.Barger *et al.*, Phys. Rev. Lett. **95**, 211802 (2005).

[10] A. Friedland *et al.*, Phys. Rev. B **594**, 347 (2004).

[11] O.G. Miranda *et al.*, J. High Energy Phys. **10** 008 (2006)

[12] A. Renshaw *et al.*, Phys. Rev. Lett. **112**, 091805 (2014).

[13] M. Nakahata *et al.*, Nucl. Instrum. Meth. A **421**, 113 (1999).

[14] E. Blaufuss *et al.*, Nucl. Instrum. Meth. A **458**. 636 (2001).

[15] K. Abe *et al.*, Nucl. Instrum. Meth. A **737**, 253 (2014).

[16] K. Abe *et al.*, Phys. Rev. D **94**, 052010 (2016).

[17] J.P. Cravens *et al.*, Phys. Rev. D **78**, 032002 (2008).

[18] K. Abe *et al.*, Phys. Rev. D **83**, 052010 (2011).

[19] B. Aharmin *et al.*, Phys. Rev. C **88**, 025501 (2013).

[20] A. Cisneros, Astrophys. Spa. Sci **10**, 87 (1971).

[21] M.B. Voloshin, M. Vystoskii and L.B. Okun , Sov. Phys. JTEP **64**, 446 (1986).

[22] WDC-SILSO, Royal Observatory of Belgium, Brussels. http://www.sidc.be/silso/datafiles

[23] J. Yoo *et al.*, Phys. Rev. D **68**, 092002 (2003).

[24] P.A. Sturrock and J.D. Scargle, Sol. Phys. **237**, 1 (2006).

[25] S. Desai and D.W. Liu, Astropart. Phys. **82**, 86 (2016).

[26] M. Zechmeister and M. Kürster, A&A **496**, 577 (2009).

[27] H. Nishino *et al.*, Nucl. Instrum. Meth. A **610**, 710 (2009).

[28] Y. Nakano, J. Phys. Conf. Ser. **888**, 012191 (2017).

[29] S. Yamada *et al.*, IEEE Trans. Nucl. Sci. **57**, 428 (2010).

[30] Y. Nakano, PhD thesis, The Univ. of Tokyo (2016).

[31] R. Davis, Jr., D. S. Harmer, and K. C. Hoffman *et al.*, Phys. Rev. Lett. **20**, 1205 (1968).

[32] J.N. Adburashitov *et al.*, Phys. Rev. C **80**, 015807 (2009).

[33] M. Altmann *et al.*, Phys. Lett. B **616**, 174 (2005).

[34] G. Bellini *et al.*, Phys. Rev. Lett. **107**, 141302 (2011).

[35] G. Bellini *et al.*, Phys. Rev. D **82**, 033006 (2010).

[36] G. Bellini *et al.*, Phys. Rev. Lett. **707**, 051302 (2012).

[37] S. Abe *et al.*, Phys. Rev. Lett **100**, 221803 (2008).

[38] A. Gando *et al.*, Phys. Rev. D **88**, 033001 (2013).

Supernova neutrinos

In 1987, the observation of supernova 1987a by Kamiokande and IMB etc, opened the neutrino astronomy. This observation confirmed that the energy released by neutrinos is about several$\times 10^{53}$ergs. However, the core collapse supernova (ccSN) mechanism is not yet fully understood. Super-Kamiokande (SK) would be able to detect several thousand neutrino events if a ccSN happened near the center of our galaxy. Such an observation would enable us to investigate in detail the mechanics of the ccSN explosion.

On average, 1-2 ccSNe per century are expected in our galaxy and therefore we must be prepared for these events. An online program called SNWATCH searches for time clustered events [1]. Events with total energy greater than 7 MeV and vertex position within the 22.5-kton fiducial volume in SK are selected. Cosmic ray muons and their subsequent decay electron events are removed. For each selected event, a 20-second time window is opened backwards in time, and the number of selected events in the window, N_{clus}, is counted. A variable D that identifies the dimension of the vertex distribution is computed. It is an integer number from 0 to 3, corresponding to point-, line-, plane- and volume-like distributions, respectively.

When $N_{clus} \geq 60$ and $D = 3$ a prompt SN warning is generated including an automatic phone-calling and emails to experts. Then, the experts check whether it is a real supernova signal or not by looking at various plots which are uploaded to a secured site accessible from the Internet. These alarms are usually due to the accidental coincidence of two cosmic ray induced clusters. We have supernova drills several times per year. So far, no real supernova neutrino burst signal has been observed at SK.

In a drill, the SNWATCH conveners and the executive committee members meet via TV conference system, and discuss to make a decision for a prompt announcement (within 1 hour) to outside researchers and the press. We practice this drill as if a real supernova happened. We also have SK shift training by illuminating an LD in the SK detector a few times every month. SK shift members are notified by a dummy alarm that SNWATCH makes when the LD is illuminated. The shift members then call to the SNWATCH experts and give a report. The SK collaborators will be ready for the real supernovae through the drill and the training.

Another searches conducted at SK are those for neutrinos from Supernova Relic Neutrinos (SRNs). The SRN signal is the diffuse supernova neutrino background from all the past core collapse supernovae in the universe. This signal has never been detected, but it is expected to be detectable in the 16-30 MeV energy region, which is the gap between the energy ranges of solar neutrinos and atmospheric neutrinos. Our published result [2] utilizes SK-I, II and SK-III data with analysis energy threshold of 16 MeV. A maximum likelihood search was performed in multiple regions of the Cherenkov angle distribution to extract the most accurate flux limit. The obtained flux limit is between 2.7 and 3.0 $\bar{v}cm^{-2}s^{-1}$ (positron energy > 16 MeV), which in fact depends on the shape of the neutrino spectrum assumed. This result currently provides the world's best limit on SRN flux. (Figure 16).

In SK-IV, a new result of the SRN search using the neutron tagging technique was also published [3]. In this analysis, neutrons from inverse beta decay (IBD) reactions ($\bar{v}_e, p \rightarrow e^+, n$) are captured on hydrogen. After a neutron is captured, a single 2.2 MeV gamma is emitted. Thus, by detecting the prompt positron signal and the delayed 2.2 MeV gamma signal, we can reduce backgrounds, most of which are not accompanied by neutrons.

Figure 15 shows the energy spectrum of prompt signal, the time difference between a prompt signal and a delayed signal, and the detection efficiency of SRN for each energy bin. Figure 16 shows the obtained flux limit comparing with other results. The neutron detection efficiency is very low because of the low energy of the gamma from the neutron capture on hydrogen (to compare the 2.2 MeV gamma with the analysis kinetic energy threshold for solar neutrino of 3.5 MeV). However, we with this method we could obtain the world best limit below 16 MeV. This result shows a high potential of neutron tagging techniques, which can be a strong tool for SRN detection.

Bibliography

[1] Abe, K. et al., Astropart. Phys. 81, 39 (2016)
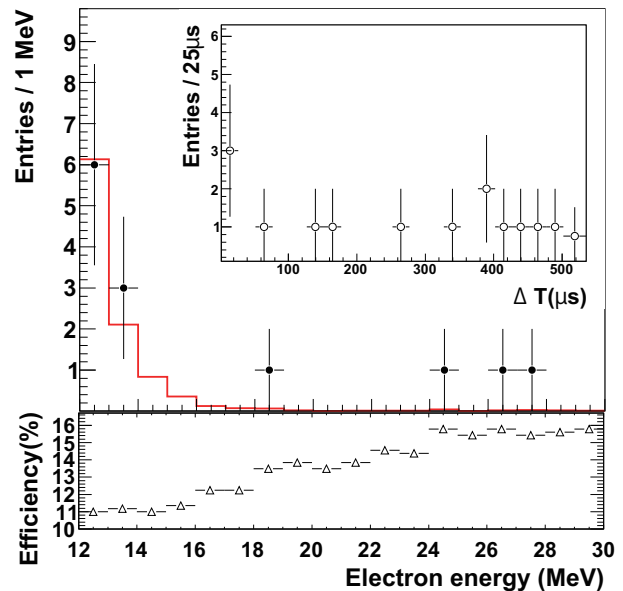
Fig. 15. Energy spectrum of prompt signals (points). The red histogram shows the expected accidental background. The plot embedded in the upper right shows the timing difference for the delayed candidates. The bottom figure shows the detection efficiency of SRN for each energy bin; the jumps at 18 MeV and 24 MeV are due to energy-dependent spallation cuts. Errors are statistical only.
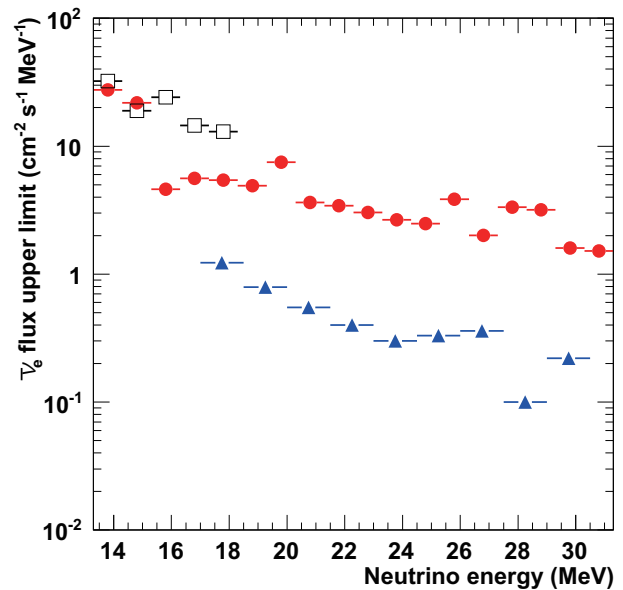
Fig. 16. Model-independent SRN 90% C.L. upper limits as a function of neutrino energy for SK-IV (solid circle). For comparison, both KamLAND result (open square) and previous SK result (solid triangle) are also shown.

[2] K.Bays et al., Phys. Rev. D 85, 052007 (2012)

[3] H.Zhang et al., Astropart. Phys. 60, 41 (2015)

R&D for the gadolinium project

As mentioned above, although at SK a few SRN events a year are expected, SRNs have not been detected yet because of the large backgrounds that constrain our search. The main goal of our research is to reduce these backgrounds and be able to detect SRNs. The observation of SRNs in general or

Fig. 17. In the new cavern, the 200-ton tank (a) with currently 240 photomultipliers installed, the Gd pre-mixing and pre-treatment 15-ton tank (b), the selective filtration system (d), Gd removal resins (c) for test and a device to measure the water transparency (e) have been installed.

neutrinos from distant supernovae in particular, would give us some information about the universe, for example the core collapse rate from SRNs, and about the neutrino itself too, for example its lifetime.

As shown in the previous section, the current SK detector can only detect positrons efficiently but not neutrons. In order to achieve a high detection efficiency for neutrons, it is proposed to add 0.2% of gadolinium (Gd) sulfate by mass into SK. Since Gd has a neutron capture cross section of 49.000 barns (about 5 orders of magnitude larger than that of protons) and emits a gamma cascade of 8 MeV, neutrons could be easily detected at SK (in space, vertices within tens of cm and in time, with the neutron capture delayed about 20 μsec).

EGADS (Evaluating Gadolinium's Action on Detector Systems) project was funded in 2009. The main motivation of EGADS is to show that by adding Gd, SK will be able to detect anti-neutrinos using the delayed coincidence technique, while keeping all its capabilities in the other analyses like solar and atmospheric neutrinos. Since then, a new hall near the SK detector has been excavated and a 200-ton tank with its ancillary equipment has been installed, see Fig.17, to mimic the conditions at SK. Of special importance is the selective water filtration system, that filters out water impurities while keeping the Gd in the water.

From January 2010 to July 2011 we circulated pure water through the 200-ton tank and proved that our water system is stable and achieves a high water quality. In 2013, from February 6th to April 20th, the 200-ton tank has been stepwise loaded with Gd sulfate until the final 0.2% concentration was reached. Two values are monitored at three different depths: the Cherenkov light left after travelling 15 m (LL15) in water and the Gd concentration. Both values confirmed that we can achieve and maintain a good water quality and that Gd sulfate homogeneously and quickly dissolves in the 200-ton tank.

In summer 2013, we installed 240 photomultipliers and the data taking started from September without Gd and with a DAQ based on old SK ATM modules.

After the water quality became good and stable, detector calibrations were performed. In April 2015, the target concentration of 0.2% $Gd_2(SO_4)_3$ was achieved. Figure 18 shows the time variation of LL15. The blue band in the figure shows typical values for SK-III and SK-IV. As shown in the figure, the transparency of 0.2% $Gd_2(SO_4)_3$ water is within the SK range. In addition to the good water transparency, no Gd loss has been detected since the EGADS detector reached the final concentration until it was emptied again after about 2 years and 5 months.

Detailed studies have evaluated the impact on current analyses at SK. These studies show that current analyses will be basically unharmed after adding Gd in SK and all other tests and studies conducted have shown no showstoppers. As a consequence, the SK collaboration decided in spring 2015 to approve the SuperK-Gd project. The SK tank has been opened for refurbishment work from April 1st.

In June 2017 we installed new electronics at EGADS. The old ATM modules were changed for the SK QBEEs and a new DAQ system installed. Several SN tests have demonstrated that EGADS can now detect and process all events during a galactic SN (including a close SN like Betelgeuse). Additionally, we are developing a dedicated SN watch for EGADS that reconstructs every event. It will look for IBD, including the neutron captures on Gd which reduces backgrounds and allows EGADS to look for SN in the far end of our galaxy. This will enable us to instantly and autonomously detect a galactic SN and report to local experts and neutrino and astronomy community. This will be specially useful during the SK refurbishment work from April 1st 2018.

T2K EXPERIMENT

[Spokesperson : Tsuyoshi Nakaya] Kyoto University

The Tokai to Kamioka (T2K) experiment [1] is a long baseline neutrino oscillation experiment: a man-made beam of neutrinos is used to do precise studies of the oscillations of neutrinos. Accelerated protons are used to produce the neutrino beam in the J-PARC center in the Ibaraki prefecture, which then travel 295 km to reach the Super-Kamiokande (Super-K) detector in the Gifu prefecture where they can be detected after oscillations. A complex of near detectors located 280 meters away from the proton target is used to monitor the neutrino beam, and constrain systematic uncertainties on the neutrino fluxes and interactions. T2K was the first long baseline experiment to use the off-axis beam technique [2]: the beam is not aimed directly at Super-K, but in a direction making a 2.5° angle with the far detector direction. This gives increased sensitivity to neutrino oscillations while reducing the backgrounds by producing a narrow band neutrino beam centered on the energy corresponding to the first maximum of the $\nu_\mu \to \nu_e$ oscillation probability.

T2K realized the first observation of the appearance of a flavor of neutrinos through oscillation by detecting electron neutrinos in a beam of neutrinos produced in the muon flavor [3]. After achieving this milestone, the experiment has been using its ability to produce a beam of either neutrinos
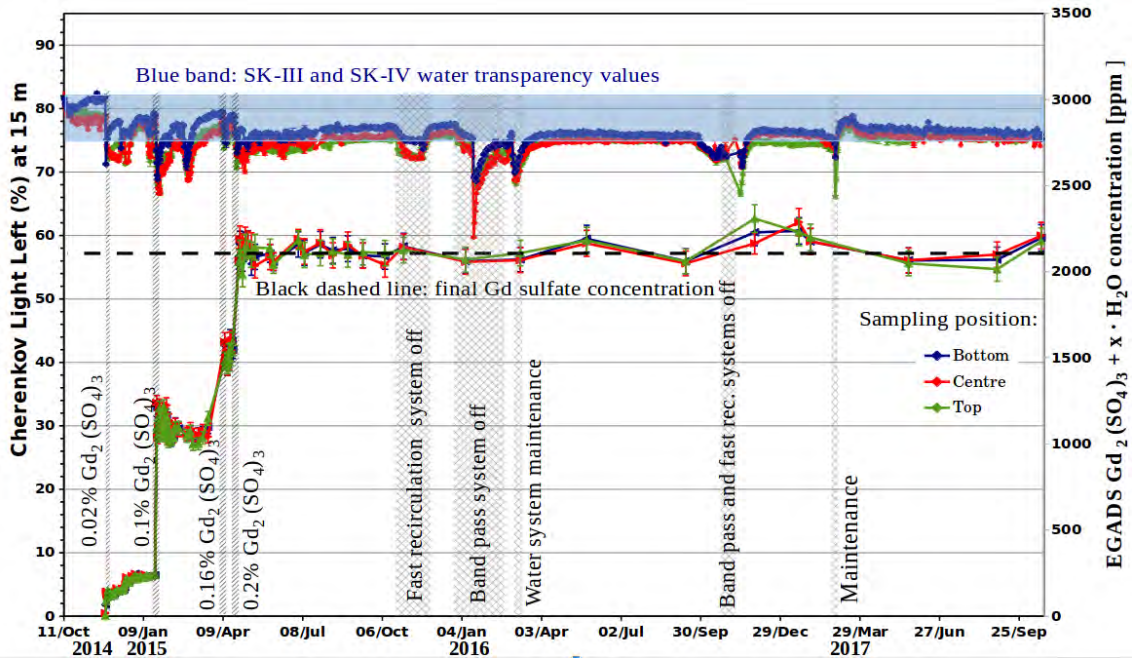
Fig. 18. Cherenkov light left at 15 m for Gd loaded water. The horizontal blue band are the typical values for SK-III and SK-IV. The vertical lines shows the injection dates where we also indicate the concentration (% in mass) in the 200-ton tank. The black dashed line shows the final expected concentration.

or anti-neutrinos to compare the oscillations of neutrinos and their antiparticles. This allows to study the main remaining open questions in neutrino oscillations (CP symmetry and ordering of the neutrino mass states) by looking at the differences between the oscillations $\nu_\mu \to \nu_e$ and $\bar{\nu}_\mu \to \bar{\nu}_e$. At the same time, T2K's physics goals include the precise measurement of the neutrino oscillation parameters θ_{23} and Δm^2_{32} through a precise study of the pattern of disappearance of the muon neutrinos in conjunction with the data used to study the oscillation to the electron flavor. The experiment additionally performs searches for physics beyond the standard model, such as oscillations due to sterile neutrinos and CPT violation. Finally, the near detectors are used to perform a wide range of neutrino and anti-neutrino cross-section measurements.

In J-PARC, protons are accelerated to 30 GeV by a series of three accelerators, and hit a 1.9 interaction-length graphite target. The collisions produce hadrons, in particular charged pions and kaons, which are focused by three electromagnetic horns. The hadrons then go through a 96m long decay tunnel where they decay in flight into neutrinos. A beam dump at the end of the decay tunnel stops the remaining hadrons, while high energy muons (5 GeV/c or higher) can pass through this beam dump and are measured to provide a first, indirect monitoring of the neutrino beam. The horns can be used either with a positive current (ν-mode), in which case the beam is mainly made of ν_μ, or with a negative current ($\bar{\nu}$-mode) which gives a mainly $\bar{\nu}_\mu$ beam.

The near detectors are separated into two groups. On the axis of the beam, the INGRID detector, made of fourteen identical modules is used to monitor the beam direction and rate stabilities. Each module is made of an succession of iron plates to provide large target mass (7.1 tons per module) alter-

nating with scintillator planes for detection. Using the number of events reconstructed in each module, the beam direction can be measured daily with better than 0.4 mrad accuracy. Located in the direction of Super-K, the off-axis detector ND280 is made of several detectors located inside a 0.2T magnet. The higher precision of those off-axis detectors allow to do more detailed measurements of the unoscillated neutrino beam. In neutrino oscillation analyses, the ND280 is used to provide information on the ν_μ and $\bar{\nu}_\mu$ unoscillated spectra directed at SK, constrain the dominant backgrounds, and constrain the combination of flux and interaction cross sections.

The far detector, Super-K, is a 50 kton water Cherenkov detector, shielded from atmospheric muons by 1000 m of rock, or 2700 meters-water-equivalent (m.w.e.) mean overburden. To select events corresponding to the T2K beam, Super-K is synchronized via GPS to the J-PARC beamline. Hit information within $\pm 500 \mu s$ from the beam arrival timing are used for T2K data analysis. Events where only one ring was reconstructed (corresponding to one charged particle above Cherenkov threshold) are used in oscillation analysis. Those events are separated into muon-like and electron-like events based on the light pattern of this ring, and additional selection cuts are applied to produce samples enriched in certain interaction modes.

To study neutrino oscillations, the data observed at the far detector are compared to the predictions of the three-flavor oscillation model for different values of the oscillation parameters. To this end, a model of the experiment is constructed: the fluxes of the different flavors of neutrinos reaching the detectors are predicted by a series of simulations, and the interactions of ν and $\bar{\nu}$ in the detectors are simulated using the NEUT Monte Carlo event generator [9]. First, the flux and

Table 3. T2K data taking periods and integrated numbers of protons on target (POT) used in the far detector analysis.

Run Period	Dates	$\times 10^{20}$ POT	
		ν	$\overline{\nu}$
Run 1	Jan.2010 - Jun.2010	0.32	–
Run 2	Nov.2010 - Mar.2011	1.11	–
Run 3	Mar.2012 - Jun.2012	1.60	–
Run 4	Oct.2012 - May.2013	3.60	–
Run 5	May.2014 - Jun.2014	0.24	0.51
Run 6	Oct.2014 - Jun.2015	0.19	3.55
Run 7	Feb.2016 - May.2016	0.48	3.50
Run 8	Oct.2016 - Apr.2017	7.17	–
Run 9	Oct.2017 - May.2018	0.20	8.79
Total	**Jan.2010 - May.2018**	**14.94**	**16.35**

Fig. 19. 90% confidence regions for $\sin^2(\theta_{23})$ and Δm_{32}^2 in ν mode (corresponding to 7.482×10^{20}POT) and $\overline{\nu}$-mode (corresponding to 7.471×10^{20}POT). Normal hierarchy is assumed. 90% confidence regions obtained by SK [12] and MINOS [13] for $\overline{\nu}$ are also shown. The best fit in the case $\sin^2(\theta_{23}) > 0.5$ is also displayed for comparison with the MINOS result.

properties of the proton beam reaching the target are measured by the proton beam line monitors. Interactions of the protons in the graphite target and production of secondary hadrons are then simulated using the FLUKA package [6]. Measurements from hadron production experiments, in particular NA61/SHINE [7], are used to tune this part of the simulation and the out-of-target interactions. The propagation and decay in flight of the hadrons in the decay tunnel are then simulated using the GEANT3 and GCALOR [8] packages. The predictions from this model are compared to the data observed in the near detectors to tune the predictions for the far detector by constraining the model parameters. The result of this near detector fit provides the initial values and uncertainties of the flux and interaction model parameters used in the far detector analysis to measure parameters describing neutrino oscillations.

T2K started collecting physics data in January 2010, and has now completed its 9th run, accumulating a total of 1.51×10^{21} protons on target (POT) in ν-mode and 1.65×10^{21} POT in $\overline{\nu}$-mode. The details of the data used in the far detector analysis (slightly lower due to data quality cuts) can be found in table 3. Over this period, the event rates and the beam direction were found to be consistent with the expectations and stable by the measurements of the muon monitor and the on-axis near detector. In particular, the beam direction remained stable well within the $\pm$1mrad target. During run 9, stable operation at 485 kW was achieved, and operation at more than 500 kW was successfully demonstrated.

Updated $\overline{\nu}_\mu$ disappearance measurement

In the standard three flavor oscillation picture, the survival probability in vacuum is identical for muon neutrinos and antineutrinos. For the neutrino energies used by T2K, matter effects do not significantly affect this symmetry. Any difference in the oscillations could therefore be interpreted as possible CPT violation and/or evidence of nonstandard interactions [4, 5]. T2K presented a first measurement of muon antineutrino disappearance in 2016 [10], where the parameters describing the disappearance of $\overline{\nu}_\mu$ were found to be in agreement to the ones measured for the disappearance of ν_μ by T2K. An updated measurement was presented in 2017 [11]
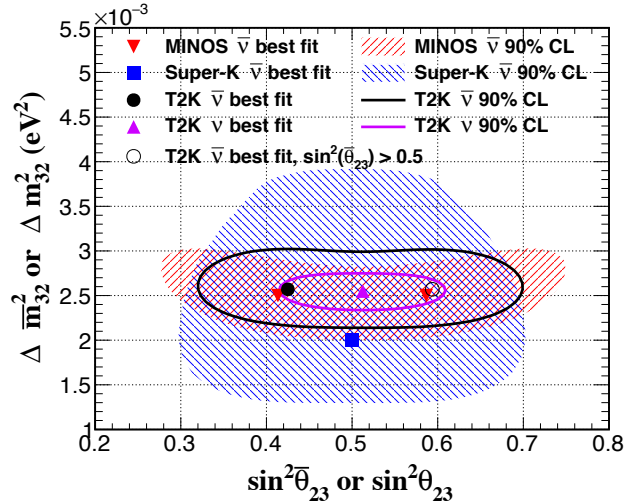
using larger statistics and a substantial improvement to the analysis procedure.

The analysis allowed the antineutrino oscillation parameters for $\overline{\nu}_\mu$ disappearance to vary independently from those describing neutrino oscillations, i.e., $\theta_{23} \neq \overline{\theta}_{23}$ and $\Delta m_{32}^2 \neq \Delta \overline{m}_{32}^2$, where the barred parameters govern antineutrino oscillations. All other parameters were assumed to be the same for neutrinos and antineutrinos since the muon like samples cannot constrain them. δ_{CP} was fixed to 0 as it has a negligible impact on the disappearance spectra at T2K, and θ_{13} value was constrained using the measurements by the reactor experiments. Finally, the data from ν-mode and $\overline{\nu}$-mode are analyzed together in a simultaneous fit, as the main uncertainty on the background to measure $\overline{\theta}_{23}$ and $\Delta \overline{m}_{32}^2$ in $\overline{\nu}$-mode is the size of the neutrino background, which depends on the values of θ_{23} and Δm_{32}^2.

Using data corresponding to an exposure of 7.48×10^{20} and 7.47×10^{20} protons on target (POT) for neutrinos and antineutrinos respectively, the best fit values obtained for the parameters describing neutrino oscillations assuming normal hierarchy are $\sin^2(\theta_{23}) = 0.51$ and $\Delta m_{32}^2 = 2.53 \times 10^{-3}$eV^2/c^4 with 68% confidence intervals of $0.44 - 0.59$ and $2.40 - 2.68$ ($\times 10^{-3}$eV^2/c^4) respectively. For the antineutrino parameters, the best fit values are $\sin^2(\overline{\theta}_{23}) = 0.42$ and $\Delta \overline{m}_{32}^2 = 2.55 \times 10^{-3}$eV^2/c^4 with 68% confidence intervals of $0.35 - 0.67$ and $2.28 - 2.88$ ($\times 10^{-3}$eV^2/c^4) respectively. In Fig. 19, the 90% confidence regions obtained for the parameters describing the disappearance of muon neutrinos and antineutrinos are compared. The confidence regions obtained in the two cases are compatible, and no evidence for new physics was found in this comparison. This measurement of $\overline{\theta}_{23}$ and $\Delta \overline{m}_{32}^2$ is also consistent with the results obtained by the SK and MINOS collaborations.
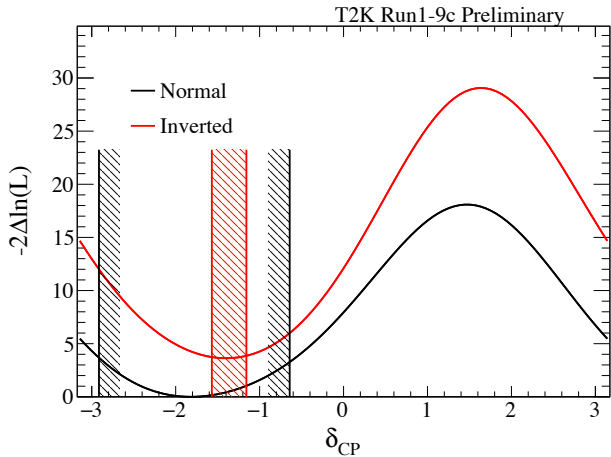
Fig. 20. Results of the fit of T2K run 1-9c data for δ_{CP} with 2σ confidence intervals obtained using the Feldman-Cousins method. The value of θ_{13} was constrained using measurements by reactor experiments.
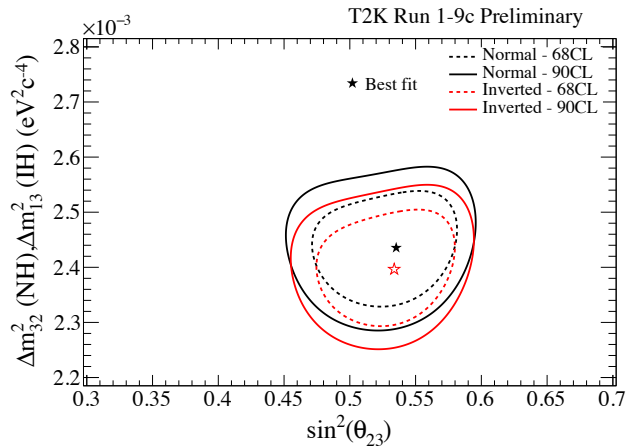

Fig. 21. 68% and 90% CL regions obtained for the atmospheric parameters using T2K run 1-9c data. The value of θ_{13} was constrained using measurements by reactor experiments.

Updated combined analysis of ν and $\bar{\nu}$ oscillations

In the first half of 2017, T2K published results excluding for the first time the conservation of CP symmetry in neutrino oscillations at 90% CL [14, 15]. We then presented new results during the summer 2017 [16] with the additional data collected during run 8 (for a total exposure of 14.7×10^{20}POT in ν-mode and 7.6×10^{20}POT in $\bar{\nu}$-mode) and a number of improvements in the analysis. First, the model describing neutrino interactions was improved both in terms of modelization of the interactions, and of parameterization of their uncertainties. The second significant change is a major update of the far detector analysis, with the use of a new event reconstruction algorithm, giving better particle identification capabilities, and improved vertex and momentum resolution. Taking advantage of the increased precision of this new algorithm, the selection cuts for the fiducial volume were optimized to increase sensitivity, and a new likelihood cut was introduced for the disappearance samples to reduce the background coming from neutral current single pion interactions. With those improvements and additional data, we found a 2σ CL interval of (-2.98, -0.60) for δ_{CP}: the conservation of CP symmetry in neutrino oscillation was excluded with 2σ significance for the first time. At the beginning of the summer 2018, we presented updated results [17] including data collected during the first half of the run 9. The 2σ CL interval for δ_{CP} was found to be of similar size, and slightly shifted: (-2.914, -0.642), confirming the 2σ exclusion of the conservation of CP symmetry obtained the summer before. The results of the data fit for δ_{CP} and the atmospheric parameters can be seen on figures 20 and 21 respectively.

Measurement of $\bar{\nu}_\mu$ and ν_μ charged current inclusive cross sections and their ratio

T2K presented a measurement at a peak energy ~ 0.6 GeV of the charged current inclusive (CCINC) $\nu_\mu + N$ cross section and first CCINC measurements of the $\bar{\nu}_\mu + N$ cross section and their ratio of the $\nu_\mu + N$ over the $\bar{\nu}_\mu + N$ cross section [18]. These ν_μ and $\bar{\nu}_\mu$ measurements are important to understand their impact on future searches for CP violation and to test neutrino cross section models, and were performed using the Pi0 detector (P0D) and the Time Projection Chambers (TPC) tracking sub-detectors in the off-axis near detector complex (ND280). Using a dataset corresponding to an exposure of 1.624×10^{20} POT in ν-mode and 0.43×10^{20} POT in $\bar{\nu}$-mode, we have measured charged current inclusive events, in a restricted phase space of $\theta_\mu < 32°$ and $p_\mu > 500$ MeV/c, the flux averaged cross sections (cm^2 per nucleon) and ratio of cross sections, as:

$$\sigma(\bar{\nu}_\mu) = (0.900 \pm 0.029(\text{stat}) \pm 0.088(\text{syst})) \times 10^{-39}$$

$$\sigma(\nu_\mu) = (2.410 \pm 0.021(\text{stat}) \pm 0.231(\text{syst})) \times 10^{-39}$$

$$R(\frac{\sigma(\bar{\nu}_\mu)}{\sigma(\nu_\mu)}) = 0.373 \pm 0.012(\text{stat}) \pm 0.015(\text{syst})$$

The $\bar{\nu}_\mu$ inclusive cross section and the ratio R results are the first published measurements at ν_μ and $\bar{\nu}_\mu$ flux energies below 1.5 GeV. Although the current uncertainty on the different model combinations is relatively large, we expect future higher statistics comparisons will be valuable for model discrimination.

First measurement of the ν_μ charged-current cross section on a water target without pions in the final state

At the energies of the T2K beam line, the main neutrino interaction process is charged-current quasi-elastic (CCQE) interactions ($\nu_\mu + n \rightarrow \mu^- + p$). Because these neutrino interactions occur within nuclear targets and not on free nuclei, additional nuclear effects and final state interactions can modify the composition and kinematics of the particles that are observed to be exiting the interaction. The active target regions of the ND280 near detector are primarily composed of plastic scintillator, but the far detector is water based. One of the dominant remaining uncertainties for oscillation analysis is due to potential differences between the oxygen and carbon cross sections that are not currently well constrained by

the ND280 detector. The ND280 detector also contains water targets, and T2K presented the first differential measurement of the charged-current interaction cross section of ν_μ on water with no pions in the final state (CCQE-like), reported in doubly differential bins of muon momentum and angle [19].

The analysis used events where a single track was reconstructed in the P0D, on a dataset corresponding to an exposure of 5.52×10^{20} POT in ν-mode. The flux-averaged total cross section in a restricted region of phase space was found to be $\sigma = (0.95 \pm 0.08(\text{stat}) \pm 0.06(\text{det syst}) \pm 0.04(\text{model syst}) \pm 0.08(\text{flux syst})) \times 10^{-38} \text{cm}^2/\text{nucleon}$. This is significantly higher than the predictions obtained with the neutrino interaction generators NEUT (resp. GENIE) of 0.66 (resp. $0.68) \times 10^{-38} \text{cm}^2/\text{nucleon}$, primarily due to the disagreement between data and MC in the high-angle regions, which cover a large portion of the reduced phase space. Another comparison to the Martini et al. [20] CCQE prediction with and without interactions on correlated pairs of nucleons (2p2h) prefers the 2p2h contribution. A comparison to the SuSAv2 model predictions [21, 22] also generally agrees with the data within errors, though the data points tend to be lower than the model in the more forward regions.

Bibliography

[1] K. Abe *et al.* (T2K Collaboration), Nucl. Instrum. Meth. A **659**, 106 (2011)

[2] D. Beavis, A. Carroll, I. Chiang, *et al.*, Long Baseline Neutrino Oscillation Experiment at the AGS (Proposal E889), 1995. Physics Design Report, BNL 52459.

[3] K. Abe *et al.* (T2K Collaboration), Phys. Rev. Lett. **112**, 061802 (2014)

[4] A. Kostelecky and M. Mewes, Phys. Rev. D **85**, 096005 (2012)

[5] O. G. Miranda and H. Nunokawa, New J. Phys. **17**, 095002 (2015)

[6] T. Bhlen *et al.*, Nucl. Data Sheets **120**, 211 (2014)

[7] N. Abgrall et al. (NA61/SHINE Collaboration), Eur. Phys. J. C **76**, 84 (2016).

[8] C. Zeitnitz and T. A. Gabriel, Proceedings of International Conference on Calorimetry in High Energy Physics (World Scientific, Corpus Christi, Texas, 1992), ISBN 9789810213039, pp. 394-404.

[9] Y. Hayato, Acta Phys. Pol. B **40**, 2477 (2009)

[10] K. Abe *et al.* (T2K Collaboration), Phys. Rev. Lett. **116**,181801 (2016)

[11] K. Abe *et al.* (T2K Collaboration), Phys. Rev. D **96**,011102(R) (2017)

[12] K. Abe et al. (Super-Kamiokande Collaboration), Phys. Rev. Lett. **107**, 241801 (2011)

[13] P. Adamson et al. (MINOS Collaboration), Phys. Rev. Lett. **108**, 191801 (2012)

[14] K. Abe *et al.* (T2K Collaboration),Phys. Rev. Lett. **118**, 151801 (2017)

[15] K. Abe *et al.* (T2K Collaboration), Phys. Rev. D **96**, 092006 (2017)

[16] M. Hartz (on behalf of the T2K collaboration), T2K Neutrino Oscillation Results with Data up to 2017 Summer, KEK special seminar Aug. 4th 2017

[17] M. Wascko (on behalf of the T2K collaboration), T2K Status, Results, and Plans, Presentation at the Neutrino 2018 conference

[18] K. Abe *et al.* (T2K Collaboration), Phys. Rev. D **96**, 052001 (2017)

[19] K. Abe *et al.* (T2K Collaboration), Phys. Rev. D **97**, 012001 (2018)

[20] M. Martini, M. Ericson, G. Chanfray, and J. Marteau, Phys. Rev. C **80**, 065501 (2009).

[21] J. E. Amaro, M. B. Barbaro, J. A. Caballero, T. W. Donnelly, A. Molinari, and I. Sick, Phys. Rev. C **71**, 015501 (2005).

[22] G. D. Megias, J. E. Amaro, M. B. Barbaro, J. A. Caballero, and T. W. Donnelly, Phys. Rev. D **94**, 013012 (2016).

XMASS EXPERIMENT

[Spokesperson : Shigetaka Moriyama]
Kamioka Observatory, ICRR, the University of Tokyo

Introduction

The XMASS project is designed to detect dark matter, neutrinoless double beta decay, and $^7\text{Be}/pp$ solar neutrinos using highly-purified liquid xenon (LXe) scintillator in an ultra-low radioactivity environment [1]. The advantages of using LXe are a large amount of scintillation light yield, scalability of the size of the detector mass, an easy purification to reduce internal radioactive backgrounds (BGs), and a high atomic number ($Z = 54$) to shield radiations from outside of the detector. As the first stage of the XMASS project (XMASS-I), the detector with $\sim$830 kg of LXe was constructed. Its construction started in April 2007 and completed in September 2010. After completion of the detector, commissioning data was taken from December 2010 to May 2012. We published results from a search for light weekly interacting massive particle (WIMP) dark matter [2] and a search for solar axions [3], both using 6.7 live days of data collected with the full LXe volume and with a lower energy threshold. We also performed searches for inelastic WIMP-nucleon scattering on ^{129}Xe [4], bosonic super-WIMPs [5], and two-neutrino double electron

capture on ^{124}Xe [6], using 165.9 live days of data with a restricted target mass of 41 kg at the central region of the detector. We also studied a possibility to detect galactic supernova neutrinos via coherent elastic neutrino-nucleus scattering [7].

During the commissioning data-taking, we found that a majority of events at low energy originated from radioactive contamination in the aluminum seal of the photomultiplier tube (PMT) window. In order to reduce the BGs, detector refurbishment was conducted. The contaminated parts of PMTs were covered by copper rings and plates in order to stop scintillation lights and radiations caused by its contamination. PMTs were cleaned by acid and copper parts were electropolished in order to remove possible surface contamination. After a year of detector refurbishment, data-taking resumed in November 2013 and is continuing for more than four years till now.

In the following sections, we report the latest physics results from the XMASS data collected after the refurbishment.

The XMASS-I detector

XMASS-I is a single phase LXe scintillator detector located underground (2700 m water equivalent) at the Kamioka Observatory [8]. Fig. 22 shows a schematic drawing of the XMASS-I detector. It contains ∼830 kg of LXe in an active region. The volume is viewed by 630 hexagonal and 12 cylindrical Hamamatsu R10789 PMTs arranged on an 80 cm diameter pentakis-dodecahedron support structure. A total photocathode coverage of more than 62% is achieved. The spherical arrays of PMTs are arranged in a double wall vessel made of oxygen free high conductivity (OFHC) copper. The waveforms in each PMT are recorded with CAEN V1751 waveform digitizers with 1 GHz sampling rate and 10 bit resolution. The detector is calibrated regularly with a ^{57}Co source inserted along the central vertical axis of the detector. By the data taken with the ^{57}Co source at the center of the detector volume, the photoelectron (PE) yield was determined to be ∼14 PE/keV. Two different energy scales were used: keV$_{ee}$ represents an electron equivalent energy, and keV$_{nr}$ denotes the nuclear recoil energy.

In order to shield the LXe detector from external gammas, neutrons, and muon-induced BGs, the copper vessel was placed at the center of a $\phi 10$ m × 10.5 m cylindrical tank filled with pure water. The water tank is equipped with 72 Hamamatsu R3600 20-inch PMTs to provide both an active muon veto and passive shielding against these BGs. XMASS-I is the first direct detection dark matter experiment equipped with such an active water Cherenkov shield. The LXe and water Cherenkov detectors are hence called an Inner Detector (ID) and an Outer Detector (OD), respectively.

Dark matter search in a fiducial volume [9]

WIMPs are one of the well-motivated dark matter candidates and are thought to be observable through nuclear recoils in the target material. A number of experimental searches have been carried out, however, no indication of such a signature has been observed yet. Considering the latest experimental constraints on the WIMP-nucleon cross section, the detectors have to have a low energy threshold, ultra-low BG, and a large target mass.
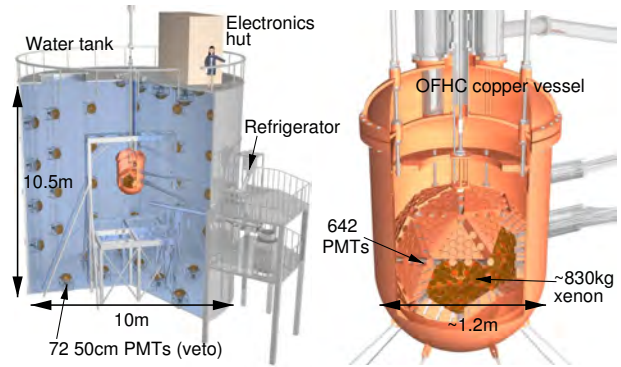

Fig. 22. Schematic drawing of the XMASS-I detector.

We performed a search for WIMP dark matter in a fiducial volume using 705.9 live days of data collected between November 2013 and March 2016. The event vertex was reconstructed with two different methods: one based on hits' timing and the other based on the PE distribution. The reconstructed radial positions by these methods are referred to as $R(T)$ and $R(PE)$, respectively. The position resolution of $R(T)$ is worse than that of $R(PE)$ since traveling time of the scintillation light across the detector volume is not much larger than the scintillation time constant or PMT timing response. However, requiring $R(T) < 38$ cm eliminated some surface events that were often mis-reconstructed by the PE-based reconstruction. Then, a fiducial volume containing 97 kg of xenon was established by requiring $R(PE) < 20$ cm. The event rate after the selection was $(4.2 \pm 0.2) \times 10^{-3}$ event/day/kg/keV$_{ee}$ around 5 keV$_{ee}$ with the signal efficiency of 20%.

In order to extract the WIMP signals, the amount of BG and its systematic error were evaluated from a detailed detector simulation verified by various detector calibrations. The assumed radioactive BG was classified as either RIs dissolved in the LXe, ^{210}Pb in the detector's inner surface, or RIs in other detector material.

For the RIs in the LXe, ^{222}Rn, ^{85}Kr, ^{39}Ar, and ^{14}C are considered. The ^{222}Rn amount was measured to be 10.3 ± 0.2 μBq/kg using the ^{214}Bi-^{214}Po coincidence. The ^{85}Kr contamination was found to be 0.30 ± 0.05 μBq/kg by the β-γ coincidence in its decay. The ^{39}Ar and ^{14}C concentrations were evaluated by the spectrum fitting in a larger fiducial volume of $R(PE) < 30$ cm in the 30–250 keV$_{ee}$ energy range where no contribution from possible WIMP-induced nuclear recoils appear. The ^{210}Pb contamination at the detector surface was evaluated by α-ray events extracted from the full volume of the LXe detector. The α-ray events were selected based on their shorter scintillation decay time. Then, the ratio of the maximum number of PEs on a single PMT to the total number of PEs in the event was used to discriminate α-ray events originating from the PMT's quartz window surface, the copper surface, or the bulk of the copper. The estimated concentration of ^{210}Pb in the copper bulk was 25 ± 5 mBq/kg, which was consistent with the measured value of 17–40 mBq/kg with a low-BG α-ray counter [10]. The RIs in other detector material were evaluated by the spectrum fitting using the full volume of the LXe detector. All the detector components except for the
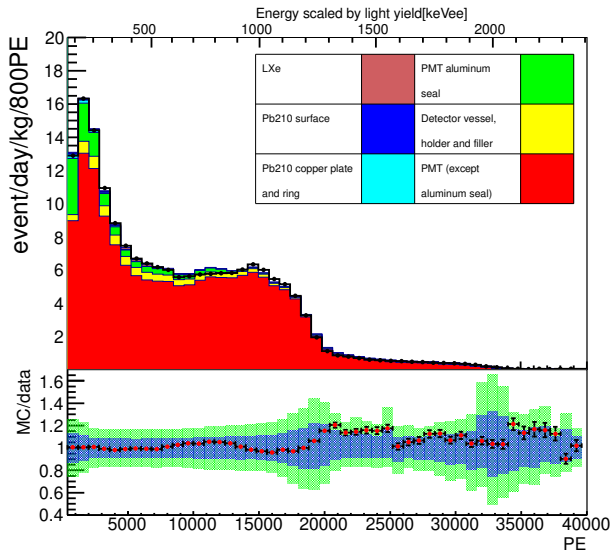
Fig. 23. Number of PE spectra in the full volume of data and the best–fit simulation. The black line represents the data and each colored histogram is a different BG RI. In the bottom plot, the ratio of the best-fit simulation to the data is shown as a red points. The blue and green bands indicate the $\pm 1\sigma$ and $\pm 2\sigma$ systematic uncertainties, respectively.

copper and the LXe were assayed with high-purity germanium (HPGe) detectors and the results of these measurements were used as initial values and their uncertainties as constraints for the full volume spectrum fit. The spectrum above ~ 400 PE was fit to determine the activities of the RIs. Fig. 23 shows a comparison of the full volume spectrum and the expected BG spectrum corresponding to the best-fit. The γ-rays from the PMTs were the largest BG source in the full volume data.

Fig. 24 shows the expected BG spectrum in the fiducial volume. The dominant contribution comes from ^{210}Pb in the bulk of the copper and the RIs in the PMTs. The size of the systematic uncertainty is also shown in the figure. The largest contribution comes from the uncertainty of the detector geometry such as gaps between the copper plates, the roughness of the copper rings, and the copper reflectivity.

To search for the WIMP dark matter signal in our fiducial volume data, we performed a chi-square fitting of the observed energy spectrum with the expected signal and BG spectra in the 2–15 keV$_{ee}$ energy range The best-fit result was obtained in the case of no existence of a WIMP signal, with χ^2/NDF=8.1/12. Fig. 25 shows the energy spectrum of the data and the best-fit BG estimate with the $\pm 1\sigma$ systematic error band. All the remaining events are consistent with our BG evaluation. Hence, the 90% confidence level (CL) upper limit on the spin-independent WIMP-nucleon cross section was derived as a function of mass between 20 GeV/c^2 and 10 TeV/c^2 as shown in Fig. 26. Our lowest limit is 2.2×10^{-44} cm^2 for a 60 GeV/c^2 WIMP.

Dark matter search by annual modulation [11]

The count rate of dark matter signal is expected to modulate annually due to the relative motion of the Earth around the Sun. The relative velocity of the Earth to the dark mat-
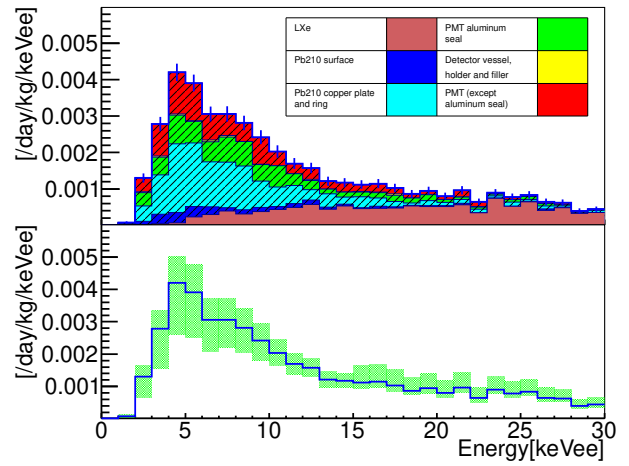
Fig. 24. Expected BG energy spectrum in the fiducial volume. The top figure illustrates a breakdown of the BG while the bottom figure shows the same energy spectrum with systematic error evaluation.
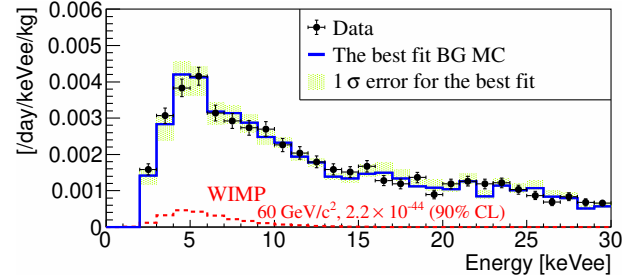
Fig. 25. Data spectrum (filled dots) overlaid with the best-fit BG estimate (blue) with the $\pm 1\sigma$ error band (green). The expected 60 GeV/c^2 WIMP spectrum (red) at a WIMP-nucleon cross section of 2.2×10^{-44} cm^2 is also shown.

ter distribution becomes maximal in June and minimal in December. The annual modulation would be a strong signature for dark matter. The DAMA/LIBRA experiment observed annual modulation of event rate at a 9.3σ significance in 1.33 ton·year of data collected over 14 annual cycles with 100–250 kg of NaI(Tl). However, the interpretation of the result as
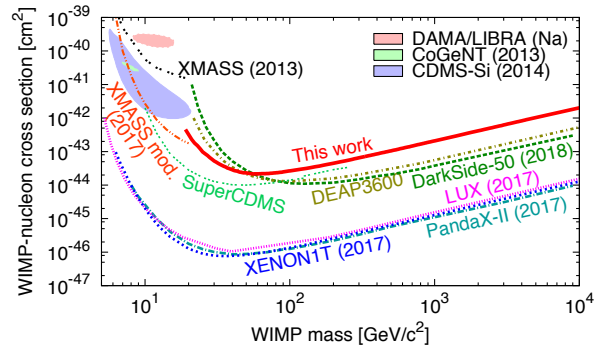
Fig. 26. Spin-independent WIMP-nucleon cross section as a function of the WIMP mass. The red solid curve represents the 90% CL limit obtained from the XMASS fiducial volume data.

a dark matter signature is in question because of tension with other direct detection experiments.

In 2016, we published an annual modulation search for dark matter using 359.2 live days of data collected between November 2013 and March 2015, and a small negative amplitude was found with p-values of 0.014 or 0.068 for two different analyses [12]. This time we included more than one year of additional data collected until July 2016, which resulted in a total of 800.0 live days. This analysis used the full 832 kg LXe volume as target and the total exposure became 1.82 ton·year which was larger than DAMA/LIBRA. The energy threshold in this analysis was 1.0 keV$_{ee}$ or 4.8 keV$_{nr}$.

To obtain the annual modulation amplitude from the data, the least squares method was used. The data set was divided into 63 time-bins with roughly 15 days of real time each. The data in each time-bin were further divided into energy-bins with a width of 0.5 keV$_{ee}$. All energy- and time-bins were fitted simultaneously and the effects of the systematic uncertainties were taken into account in the chi-square by the pull method. We performed two analyses, one assuming WIMP interactions and the other independent of any specific dark matter model.

In the case of the WIMP analysis, the expected count rate in the i-th energy and j-th time bin is expressed as:

$$R_{i,j}^{ex}(\alpha,\beta) = \int_{t_j-\frac{1}{2}\Delta t_j}^{t_j+\frac{1}{2}\Delta t_j} \left(\varepsilon_{i,j}^b(\alpha) \cdot (B_i^b t + C_i^b) \right.$$
$$\left. + \sigma_{\chi N}\varepsilon_{i,j}^s(\alpha)\left(A_i^s(\beta)\cos\frac{2\pi(t-\phi)}{T}\right) + C_i^s(\beta)\right) dt , \quad (3)$$

where t_j and Δt_j are the time-bin's center and width, respectively. To account for changing BG rates due to long-lived isotopes such as ^{60}Co and ^{210}Pb, we modeled the BG time variation using a linear function with the slope B_i^b and the constant C_i^b. $\varepsilon_{i,j}^b(\alpha)$ and $\varepsilon_{i,j}^s(\alpha)$ are the relative efficiencies for BG and signal, respectively, and the parameter α represents their systematic uncertainty. $A_i^s(\beta)$ and $C_i^s(\beta)$ are the modulation amplitude and the unmodulated component of the signal, respectively, and the parameter β represents their systematic uncertainty. Since the WIMP mass m_χ determines the recoil energy spectrum, $A_i^s(\beta)$ and $C_i^s(\beta)$ become a function of the WIMP mass. $\sigma_{\chi N}$ is the WIMP-nucleon cross section. The modulation period T is fixed to one year and the phase ϕ is fixed to 152.5 days when the Earth's velocity relative to the dark matter distribution is expected to be maximal.

The best fit for an 8 GeV/c^2 WIMP had χ^2/NDF=2357/2314 and $\sigma_{\chi n} = (-0.7^{+1.0}_{-1.7}) \times 10^{-41}$ cm^2. Since we found no significant signal, a 90% CL exclusion limit on the spin-independent WIMP-nucleon cross section was set for each WIMP mass as shown in Fig. 27. The $\pm 1\sigma$ and $\pm 2\sigma$ bands represent the expected 90% CL exclusion sensitivity estimated using 10,000 dummy samples including systematic uncertainties. The obtained upper limit was 1.9×10^{-41} cm^2 at 8 GeV/c^2, and the result excludes the 3σ DAMA/LIBRA allowed region.

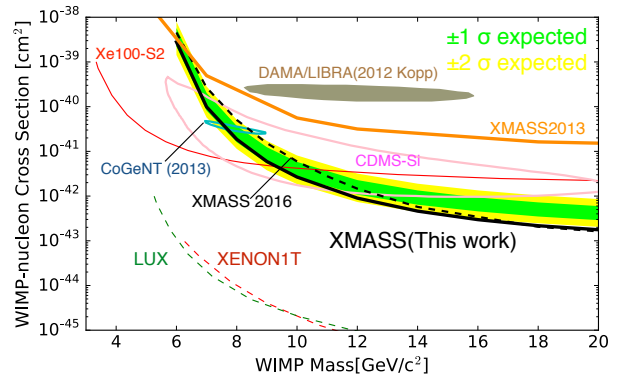For the model independent analysis, the expected count

Fig. 27. Limits on the spin-independent WIMP-nucleon cross section as a function of WIMP mass. The black solid curve shows the XMASS 90% CL exclusion limit from the annual modulation analysis. The $\pm 1\sigma$ and $\pm 2\sigma$ bands represent the expected 90% CL exclusion sensitivity.

rate is estimated as:

$$R_{i,j}^{ex}(\alpha,\beta) = \int_{t_j-\frac{1}{2}\Delta t_j}^{t_j+\frac{1}{2}\Delta t_j} \left(\varepsilon_{i,j}^s(\alpha)A_i^s(\beta)\cos\frac{2\pi(t-\phi)}{T} \right.$$
$$\left. + \varepsilon_{i,j}^b(\alpha)(B_i^b t + C_i^b) \right) dt , \quad (4)$$

where the free parameters C_i and A_i are the unmodulated count rate and the modulation amplitude at i-th energy bin, respectively. In the fitting procedure, the energy range between 1.1 and 20 keV$_{ee}$ was used. The modulation period T and phase t_0 were again fixed to one year and 152.5 days, respectively.

The observed count rate after cuts as a function of time in the energy region between 1.0 and 3.0 keV$_{ee}$ is shown in Fig. 28. In the figure, the data points are corrected for by relative efficiency based on the best-fit parameters instead of the fitting function. Fig. 29 shows the best-fit amplitudes as a function of energy after correcting for the efficiency. The efficiency was evaluated from the simulation of electrons with a flat energy spectrum uniformly distributed in the sensitive volume. The $\pm 1\sigma$ and $\pm 2\sigma$ bands represent the expected sensitivity on the modulation amplitude derived from the same dummy samples mentioned above. A hypothesis test was also done using the χ^2 difference between the modulation hypothesis and the null hypothesis ($\chi_0^2 - \chi_1^2$). It gave a p-value of 0.11 for the null hypothesis in the 1.0–20 keV$_{ee}$ energy range.

To be able to test any model of dark matter, we evaluated the constraints on the positive and negative amplitudes separately. The 90% confidence level upper limits on the positive and negative amplitudes a_{up} were calculated by the relations $\int_0^{a_{up}} G(a)da / \int_0^\infty G(a)da = 0.9$ and $\int_{a_{up}}^0 G(a)da / \int_{-\infty}^0 G(a)da = 0.9$, respectively, where $G(a)$ is the Gaussian distribution with the mean and sigma of the amplitude obtained from the fit. We obtained positive and negative upper limits at 0.96×10^{-2} and -1.5×10^{-2} events/day/kg/keV$_{ee}$ in the 1.0–1.5 keV$_{ee}$, respectively, and the limits become stricter at higher energy.

We make direct comparisons with other experiments by the modulation amplitude of the count rate. The DAMA/LIBRA experiment obtained the modulation ampli-
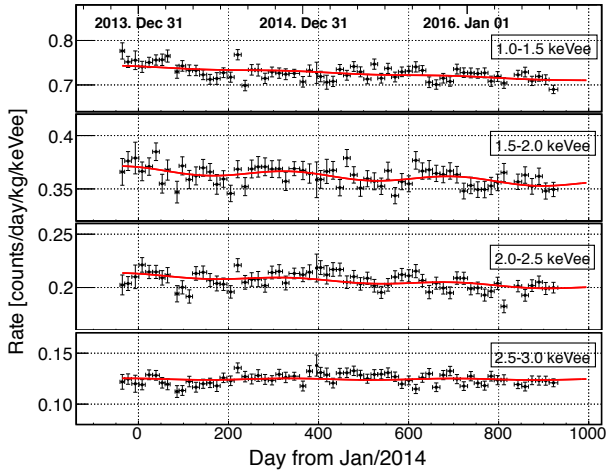
Fig. 28. Observed count rate as a function of time in the 1.0-3.0 keV$_{ee}$ energy range after correcting for relative efficiency. The error bars show the statistical uncertainty. The red solid curves represent the best-fit result for a model-independent analysis.

tude of $\sim 2 \times 10^{-2}$ events/day/kg/keV$_{ee}$ in the 2.0–3.5 keV$_{ee}$ energy range. The XENON100 experiment reported the amplitude of $(1.67 \pm 0.73) \times 10^{-3}$ events/day/kg/keV$_{ee}$ in the 2.0–5.8 keV$_{ee}$ energy range. We estimated a 90% CL one-sided upper limit of 2.9×10^{-3} events/day/kg/keV$_{ee}$ for their result. XMASS obtained the positive upper limits at $(1.3$–$3.2) \times 10^{-3}$ events/day/kg/keV$_{ee}$ in the same energy region and gave more stringent constraint above 3.0 keV$_{ee}$.

A frequency analysis was also conducted to find any periodicity in the energy range between 1 and 6 keV$_{ee}$ where significant amplitudes were observed by DAMA/LIBRA. To calculate the significance of the signal, we used the χ^2 difference ($\chi_0^2 - \chi_1^2$) for each periodicity with NDF=11 (10 amplitudes + 1 phase) as a test statistics.

To demonstrate the sensitivity to find modulation with a particular period, we used dummy samples with a simulated input signal. The energy dependence of the amplitude of this simulated input signal was assumed to be the same as the expected sensitivity band in Fig. 29, and the signal strength with different periodicities was chosen to reproduce the $\chi_0^2 - \chi_1^2$ of about 30 ($\sim 3\sigma$ significance) at T=365.24 days. We tested the sensitivity using these dummy samples with an artificial periodicity of T= 30, 40, 50, 100, 365.24, 500, and 700 days. The dummy samples with T=50 days and longer periods show the $\chi_0^2 - \chi_1^2$ of about 30, however, shorter periods lose significance as the time-bin width was about 15 days in this analysis. Therefore, we tested only for periods between 50 days and 600 days in the data. We also found that the time-dependent systematic error in the relative efficiency affects the significance for T=365.24 days and longer periods.

Fig. 31 shows the result from the observed data together with the expected $\pm 1\sigma$ and $\pm 2\sigma$ local significance bands from the dummy samples without any modulation signal. To take into account the "look elsewhere effect," we calculated the global significance as indicated in the figure. No significant periodicity was found between 50 and 600 days.
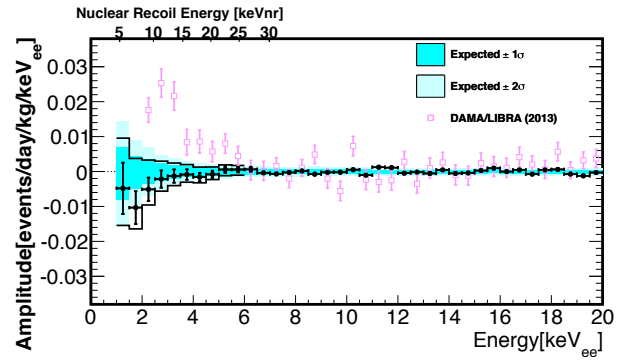
Fig. 29. Observed modulation amplitude as a function of energy for the model independent analysis (circle). The solid lines represent the XMASS 90% positive (negative) upper limits on the modulation amplitude. The $\pm 1\sigma$ and $\pm 2\sigma$ bands represent the expected sensitivity on the amplitude. The DAMA/LIBRA result (square) is also shown.
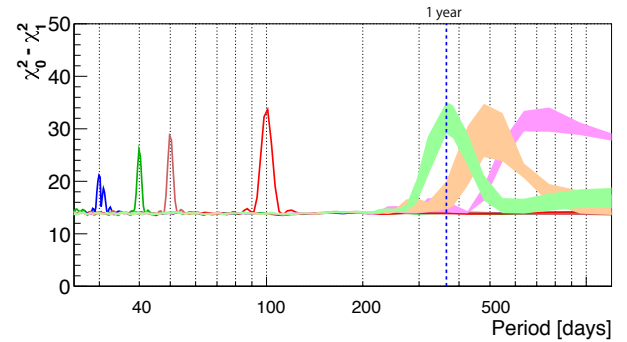
Fig. 30. The mean χ^2 difference, $\chi_0^2 - \chi_1^2$, as a function of period for dummy samples with an artificial periodicity of T= 30, 40, 50, 100, 365.24, 500, and 700 days. The width of the bands reflects the time-dependent systematic error.

Search for two-neutrino double electron capture [13]

Double electron capture (ECEC) is a rare nuclear decay mode where two orbital electrons of an atom are simultaneously capture by a nucleus of the atom. Measurement of its two-neutrino mode (2νECEC) would provide a new reference for the calculation of nuclear matrix elements while observa-
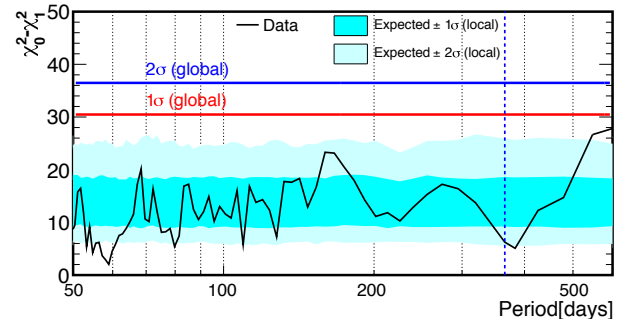
Fig. 31. The χ^2 difference, $\chi_0^2 - \chi_1^2$, as a function of period for the observed data in the 1–6 keV$_{ee}$ energy range. The expected bands for the local $\pm 1\sigma$ and $\pm 2\sigma$ significance and lines for the global 1σ and 2σ significance are also shown.

tion of its neutrinoless mode (0νECEC) would be evidence for lepton number violation and the Majorana nature of the neutrino. Natural xenon contains ^{124}Xe (abundance 0.095%) and ^{126}Xe (0.089%), which can undergo ECEC. The predicted half-lives of ^{124}Xe 2νECEC are spread over a wide range between 10^{20} and 10^{24} years depending on the models used for calculating the corresponding nuclear matrix element and the effective value of the nucleus' axial current coupling constant g_A. The half-life of ^{126}Xe is expected to be much longer than that of ^{124}Xe since its Q-value is smaller.

In the case of the simultaneous capture of two K-shell electrons with emission of two neutrinos (2ν2K), the observable energy comes from atomic X-rays and/or Auger electrons. The total energy deposition in the detector is 63.6 keV, which is twice of the binding energy of a K-shell electron in a tellurium atom. Previously, we performed a search for 2ν2K on ^{124}Xe with a fiducial xenon mass of 41 kg (containing 39 g of ^{124}Xe) using 132.0 live days of data collected between December 2010 and May 2012 and set the most stringent lower limit on the half-life, $T_{1/2}^{2\nu 2K}(^{124}\mathrm{Xe}) > 4.7 \times 10^{21}$ years at 90% CL [6]. This time, we conducted an improved search using a new data set taken between November 2013 and July 2016. The total live time amounts to 800.0 days and the fiducial xenon mass was enlarged to 327 kg (containing about 311 g of ^{124}Xe).

After the fiducial volume selection, the largest source of BG in the relevant energy range is $β$-rays coming from radioactive impurities in the LXe. ^{222}Rn emanates from the detector's surface and contaminates the LXe. Thus, its daughters, ^{214}Bi and ^{214}Pb, become one of the major sources of $β$-ray BG. ^{214}Bi can be tagged using the ^{214}Bi-^{214}Po delayed coincidence ($T_{1/2} = 164$ μs). To remove the ^{214}Bi events, events whose time difference from the subsequent event (dT_{post}) is less than 1 ms are rejected from the 2ν2K signal sample. The events with 0.015 ms $< dT_{\mathrm{post}} < 1$ ms is referred to as the ^{214}Bi sample and is used to constrain the ^{214}Bi and ^{214}Pb BGs.

We also developed a novel method for discriminating the 2ν2K signal from the $β$-ray BG using LXe scintillation time profiles. The scintillation decay time for electron induced events increases from 28 ns to 48 ns as the kinetic energy of an electron increases from 3 keV to 1 MeV [14]. In the case of the 2ν2K or $γ$-ray events, the X-ray or $γ$-ray is converted into multiple low-energy electrons in the LXe; this shortens the effective scintillation decay time by a few ns from that of an event caused by a single electron with the same deposited energy. The particle-identification parameter $β$CL is defined as

$$\beta \mathrm{CL} = P \times \sum_{i=0}^{n-1} \frac{(-\ln P)^i}{i!} , \qquad (5)$$

where n is the total number of single-PE pluses after truncating the first 20 ns, $P = \prod_{i=0}^{n-1} \mathrm{CL}_i$, and CL_i (i=0, 1, 2, …, $n-1$) is the CL of each pulse timing under the assumption that the event is caused by a $β$-ray. The probability-density function of the pulse-timing distribution for a $β$-ray event including its energy and position dependences is modeled from measurements in the ^{214}Bi data sample in the 30–200 keV$_{\mathrm{ee}}$ energy range. Fig. 32 shows distributions of the variable $β$CL for the ^{214}Bi sample in the 30–200 keV$_{\mathrm{ee}}$ energy range along

with the ^{241}Am 59.5 keV $γ$-ray events. While the $β$-ray events in the ^{214}Bi sample are distributed between 0 and 1, the distribution of the 59.5 keV $γ$-ray events in the ^{241}Am sample peaks at $β$CL = 0. Events with $β$CL less than 0.05 are classified as the $β$-depleted sample, and the rest is referred to as the $β$-enriched sample. 42% of the 2ν2K signal events are selected in the $β$-depleted sample, while only 6% of the $β$-ray events from the ^{214}Bi decay in this energy range remain. Thus, the signal-to-noise ratio is improved by a factor of 7 by this selection.

To extract the 2ν2K signal from the observed data, the energy spectra for the $β$-depleted samples, $β$-enriched samples, and ^{214}Bi samples from four periods are simultaneously fitted to the expected signal and BG spectra. The energy range from 30 to 200 keV$_{\mathrm{ee}}$ is used for fitting. The data set was divided into four periods depending on the detector conditions to account for period-dependent BG components and systematic uncertainties. Fig. 33 shows the closeup energy spectra between 30 and 100 keV$_{\mathrm{ee}}$ for the $β$-depleted samples overlaid with the best-fit 2ν2K signal and BG spectra. The peak found at 67.5 keV$_{\mathrm{ee}}$ is attributable to the ^{125}I decay. The ^{125}I is produced from ^{125}Xe and ^{125m}Xe created by thermal neutron capture on ^{124}Xe outside the water shield. In the spectrum fitting, the event rate of the ^{125}I decay is constrained by the thermal neutron flux in the Kamioka mine which has been measured to be (0.8-1.4)$\times 10^{-5}$ /cm^2/s.

We made a profile scan of χ^2 as a function of the inverse of the ^{124}Xe 2ν2K half-life. As a result, no significant signal was found and we set the 90% CL lower limit on the half-life $T_{1/2}^{2\nu 2K}(^{124}\mathrm{Xe}) > 2.1 \times 10^{22}$ years. The fact that we do not observe significant excess above BG allows us to give a constraint on 2ν2K on ^{126}Xe in the same manner: $T_{1/2}^{2\nu 2K}(^{126}\mathrm{Xe}) > 1.9 \times 10^{22}$ years at 90% CL. Fig. 34 shows a comparison of the experimental 90% CL exclusion limits on ^{124}Xe 2ν2K half-life overlaid with the theoretical calculations for comparison. The present result gives a lower limit stronger by a factor 4.5 over our previous result, and gives the most stringent experimental constraint reported to date.

Search for solar Kaluza-Klein axion [15]

In theories of the large extra dimensions, axions could propagate in the extra dimensions beyond the 4-dimensional spacetime, and would acquire Kaluza-Klein (KK) excitations, which could be observed as particles with heavier masses in the standard spacetime. The KK axions can be produced in the Sun via the Primakoff effect ($γZ \to aZ$) and the photon coalescence mechanism ($γγ \to a$). While most of the produced KK axions escape from the solar system, a small fraction is gravitationally trapped in the orbits around the Sun and accumulated over the age of the Sun. They decay into two photons inside the terrestrial detector. The expected number density of the trapped KK axions n_a as a function of the distance from the Sun r has been calculated by L. Di Lella and K. Zioutas, and is fitted well by r^{-4}. The distance between the Earth and the Sun as a function of time $r(t)$ is written as

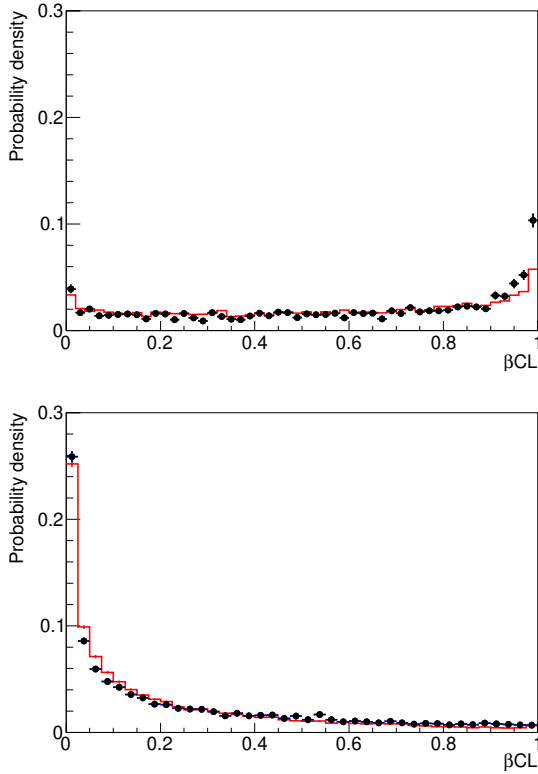$$r(t) = a \left(1 - e \cos \frac{2\pi(t - t_0)}{T} \right) \qquad (6)$$

Fig. 32. The particle-identification parameter βCL for the ^{214}Bi β-ray events in the energy range from 30 to 200 keV$_{\text{ee}}$ (top) and the ^{241}Am 59.5 keV γ-ray events (bottom). The distributions of the observed data (black points) and the simulated events (red curves) are normalized to the unit area.
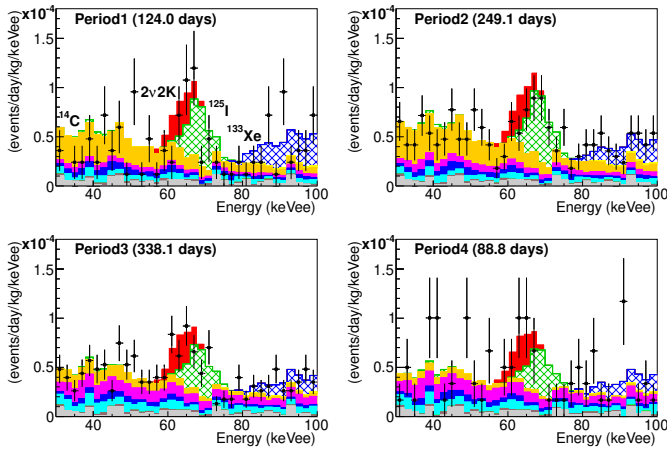

Fig. 33. Closeup figures of energy spectra between 30 and 100 keV$_{\text{ee}}$ for the β-depleted samples. The observed spectra (points) are overlaid with the best-fit 2ν2K signal and BG spectra (colored stacked histograms).

where $a = 1.496 \times 10^8$ km $= 215.0 R_\odot$ and $e = 0.0167$ are the semimajor axis and the eccentricity of the Earth's orbit, respectively. Here, t is a date in one year, and T represents one year; t_0 represents the date when the Earth is at perihelion. Thus, the expected number of events shows annual modulation depending on the distance from the Sun. Fig. 35 shows
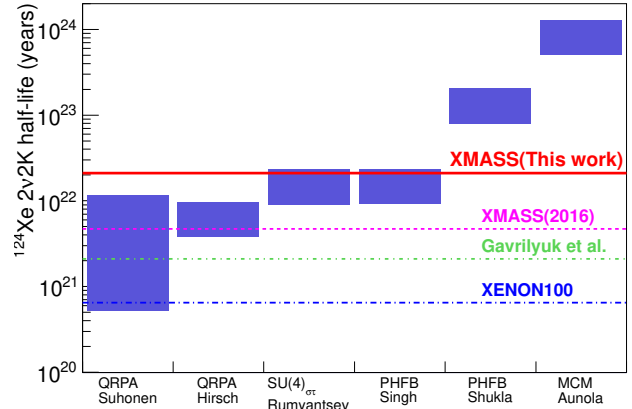

Fig. 34. Comparison of the experimental 90% CL exclusion limits on the ^{124}Xe 2ν2K half-life overlaid with the theoretical calculations. For the theoretical predictions, the reported 2νECEC half-lives are converted to 2ν2K half-lives, divided by the branching ratio for the two electrons being captured from the K-shell, P_{2K}=0.767. The lower and upper edges of the bands correspond to $g_A = 1.26$ and $g_A = 1$, respectively.

the expected energy spectra by the trapped solar KK axion at the perihelion and the aphelion. Here, the number of extra dimensions $n = 2$, the number of extra dimensions axion can propagate $\delta = 2$, and the fundamental scale $M_F = 100$ TeV are assumed.

We have searched for the decay of these solar KK axions using 832 kg×359 days of the XMASS-I data by annual modulation. The expected count rate is calculated as

$$R_{i,j}^{\text{ex}} = \int_{t_j - \frac{1}{2}\Delta t_j}^{t_j + \frac{1}{2}\Delta t_j} [C_i + \xi (A_i - \beta L_i) \\ \times \left(\cos \frac{2\pi(t - t_0)}{T} + \frac{5}{2} e \cos^2 \frac{2\pi(t - t_0)}{T} \right)] \, dt \quad (7)$$

where t_j and Δt_j are the time-bin's center and width, respectively. We have C_i and A_i as the constant term and the expected amplitude of the event rate in the ith energy-bin, respectively. A_i corresponds to half of the residual event rate in Fig. 35, and L_i, which is associated with the penalty term β, accounts for the uncertainty stemming from the nonlinearity of the scintillation efficiency on A_i.

The χ^2 fitting was performed in the energy range between 3 and 22 keV$_{\text{ee}}$, excluding the range between 14 and 17 keV$_{\text{ee}}$. This exclusion avoids systematic effects associated with the end of the range over which the Cherenkov cut is applied. Fig. 36 shows the event rate modulation and the best fit result for the expected event rate. No significant amplitude excess is found, and therefore a 90% confidence level exclusion limit is set on the KK axion-photon coupling $g_{a\gamma\gamma}$ as a function of the KK axion number density $\bar{n}_a$ as shown in Fig. 37. As a bench mark, the proposed solar KK axion model ($g_{a\gamma\gamma} = 9.2 \times 10^{-14}$ GeV^{-1}, $\bar{n}_a = 4.07 \times 10^{13}$ m^{-3}) is also shown. This is the first experimental constraint for the KK axion.
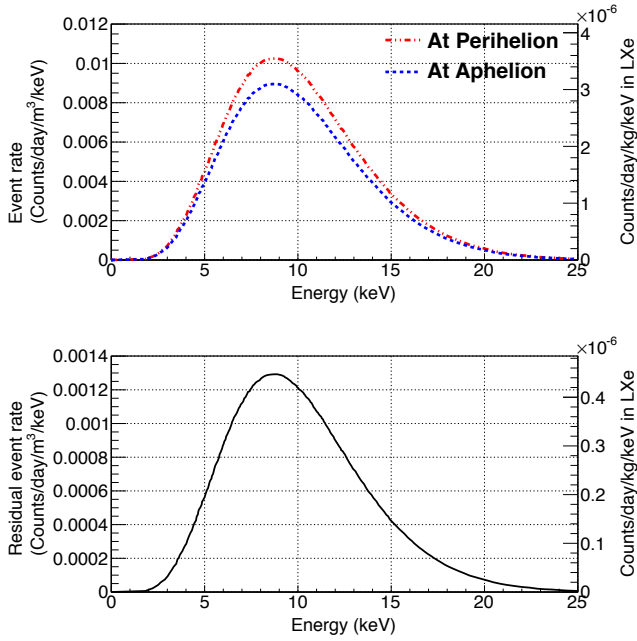
Fig. 35. Expected energy spectra of the sum of the two photons by the decay of the trapped KK axions at the perihelion and the aphelion. The curve in the lower panel shows the expected residual event rate (difference between the perihelion and the aphelion).

Bibliography

[1] Y. Suzuki *et al.*, hep-ph/0008296.

[2] K. Abe *et al.* (XMASS Collaboration), Phys. Lett. B **719** (2013) 78.

[3] K. Abe *et al.* (XMASS Collaboration), Phys. Lett. B **724** (2013) 46.

[4] H. Uchida *et al.* (XMASS Collaboration), Prog. Theor. Exp. Phys. (2014) 063C01.

[5] K. Abe *et al.* (XMASS Collaboration), Phys. Rev. Lett. **113** (2014) 121301.

[6] K. Abe *et al.* (XMASS Collaboration), Phys. Lett. B **759** (2016) 64.

[7] K. Abe *et al.* (XMASS Collaboration), Astropart. Phys. **89** (2017) 51.

[8] K. Abe *et al.* (XMASS Collaboration), Nucl. Instrum. Meth. A **716** (2013) 78.

[9] K. Abe *et al.* (XMASS Collaboration), arXiv:1804.02180 [astro-ph.CO].

[10] K. Abe *et al.* (XMASS Collaboration), Nucl. Instrum. Meth. A **884** (2018) 157.

[11] K. Abe *et al.* (XMASS Collaboration), Phys. Rev. D **97** (2018) 102006.

[12] K. Abe *et al.* (XMASS Collaboration), Phys. Lett. B **759** (2016) 272.
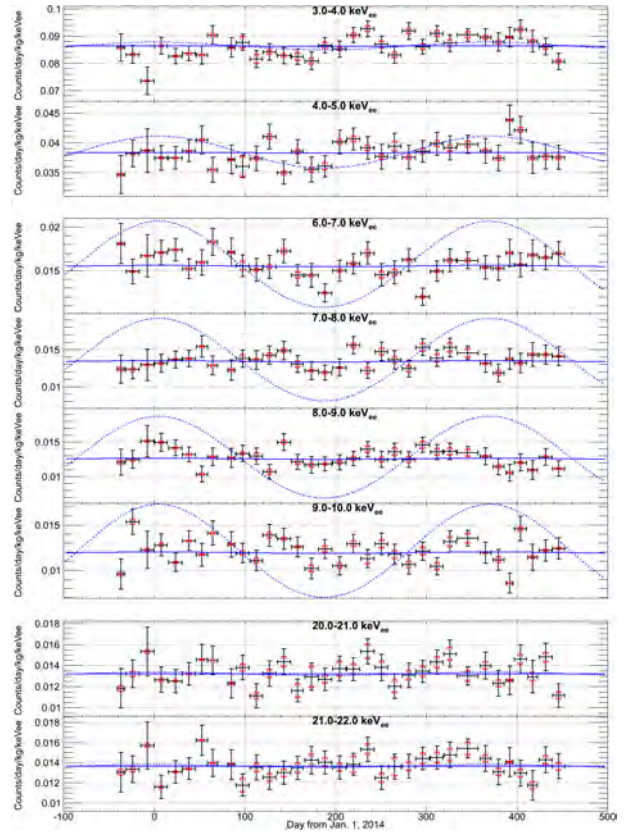
Fig. 36. Time variation of the observed event rate in representative energy-bins. The black points with error bars show the observed event rate for each period with statistical error. The red error bars show the systematic errors. The blue solid curves show the best fit result of the expected event rate variation. The blue dotted curves show the 20 times enhanced expected amplitudes of 90% CL upper limit.

Fig. 37. 90% confidence level exclusion limit on the KK axion-photon coupling as a function of the mean KK axion number density.

[13] K. Abe *et al.* (XMASS Collaboration), Prog. Theor. Exp. Phys. **2018** (2018) 053D03.

[14] H. Takiya *et al.* (XMASS Collaboration), Nucl. Instrum. Meth. A **834** (2016) 192.

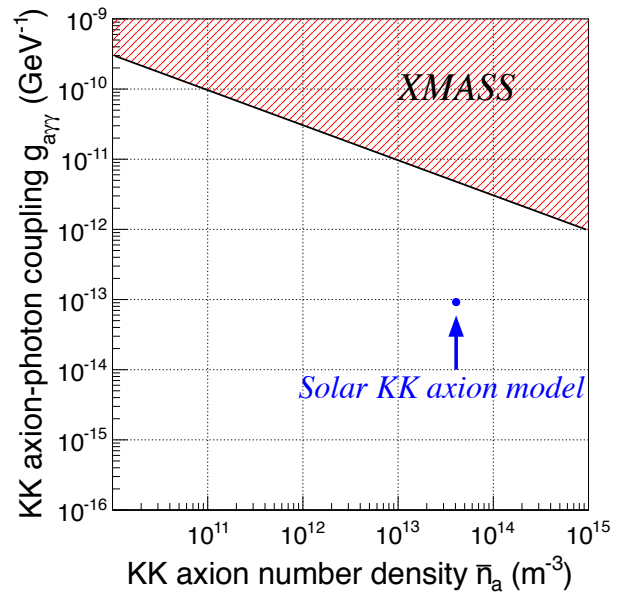[15] N. Oka *et al.* (XMASS Collaboration), Prog. Theor. Exp. Phys. **2017** (2017) 103C01.

HYPER-KAMIOKANDE

[Project Leader: Masato Shiozawa
(Kamioka Observatory, ICRR, The University of Tokyo)]

Introduction

The Hyper-Kamiokande (Hyper-K or HK) experiment is proposed as a joint project of the university of Tokyo and KEK by combining a next generation underground water Cherenkov detector and upgraded J-PARC (Japan Proton Accelerator Research Complex, Ibaraki, Japan) neutrino beam. In FY2016 ICRR and KEK have set first priority to the Hyper-K and upgrade of J-PARC for the project. This project is selected as one of top 28 important large research projects in the "Masterplan 2017" by the Science Council of Japan.

Figure 38 shows a schematic view of the Hyper-K cylindrical detector with 60 m in height and 74 m in diameter. The water mass is 0.258 million metric tons, with an order of magnitude larger fiducial mass of 0.187 million metric tons than Super-K. It provides an enormous potential to discover leptonic charge-parity (CP) violation by observing neutrino and anti-neutrino beams from J-PARC. A search for nucleon decays is an important subject to explore new paradigm beyond the standard model of particle physics. Hyper-K will also have far better capabilities to observe atmospheric neutrinos, solar neutrinos, and neutrinos from other astronomical sources than those of predecessor experiments.
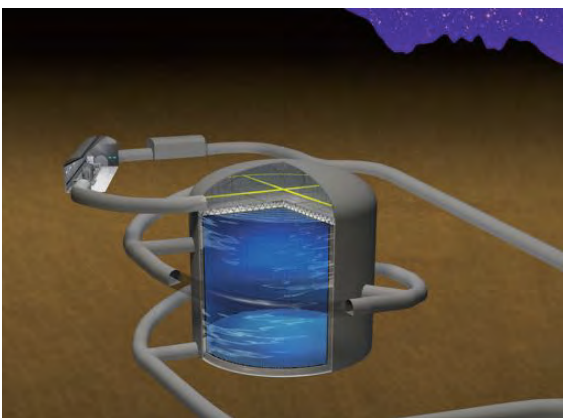

Fig. 38. Schematic view of the Hyper-K water tank.

The Hyper-K international proto-collaboration consists of about 300 researchers from 77 institutes in 15 countries. Technical details were published as a design report in May 2018 with various physics reaches[1]. The detector technology has been developed based upon the successful Super-K experiment. The candidate site has been pinned down by geological surveys. In conclusion the feasibility study has been completed and the project is technically ready to start construction. The international group aims to start the detector construction in 2018 and to start its operation in 2026.

Photosensors

A Cherenkov light in a ultra pure water is detected by 40,000 newly developed photomultiplier tubes (PMTs), R12860 by Hamamatsu Photonics K.K., with 40% photo-coverage. It was significantly upgraded from the R3600 PMT used in Super-K due to an improved dynode structure using a box-and-line type and optimized curvature glass as shown in Fig. 39.

Fig. 39. New 50 cm photomultiplier tube with a box-and-line dynode (R12860, Hamamatsu Photonics K.K.).

The peak quantum efficiency is about 30%, that is 1.4 times higher than that of the Super-K PMT. In total, the new PMT achieved twice higher single photon detection efficiency because the photoelectron collection efficiency was also greatly improved. The timing and charge resolutions at single photoelectron also becomes much better as 1.1 ns and 35% which can be compared with 2.1 ns and 53% of the Super-K PMT, respectively. These outstanding improvements enhance Hyper-K detector performance and its physics reaches.

Moreover, pressure tolerance was improved up to the 125 m water depth in order to fit the 60 m depth of the detector water. To prevent a chain reaction of imploding PMTs caused by the unlikely event of a single PMT implosion, every PMT in the Hyper-K water tank will be housed in the shockwave prevention cover. The prototype cover consists of an acrylic front window and a stainless steel backside cover with conical shape. In addition, we study two alternative designs. One is a stainless steel tubelike-shaped cover, and another is a resin-made monolithic cover. Acrylic front window is commonly used in both design. These alternative designs are studied to reduce weights and / or production costs.

To evaluate the performance of the prototype cover, a mock test simulating the event of a photosensor implosion in Hyper-K was carried out in a deep vertical shaft at Kami-Sunagawa town, Hokkaido. First prototype was tested from February to March 2016, and improved prototype and alternative two designs were tested in March 2018 (Fig. 40)..

We successfully established the prototype in 80m depth, and we proved the concept of tubelike-shaped cover and resin-
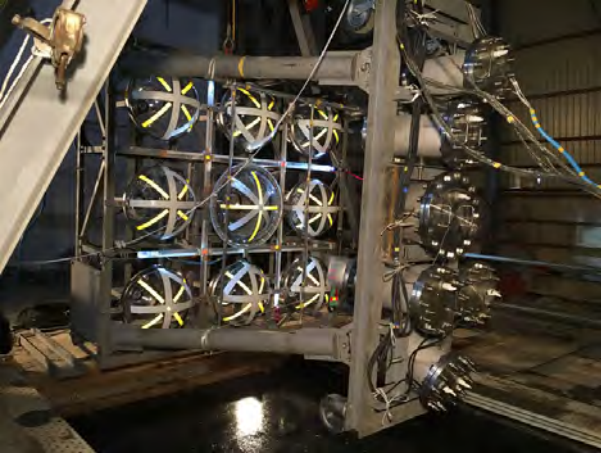
Fig. 40. The strength test setup of the PMT protective covers. The test was carried out in a deep vertical shaft located at Kami-Sunagawa town, Hokkaido. The events at a water depth of 60-80 m of an artificial implosion of the center bulb, with and without the protective cover, have been measured by using monitors such as pressure gauges and high-speed cameras.

Fig. 41. Top view of reflection imaging by seismic prospecting at altitude of 483 m above sea level. Asterisks (*) indicate the reflection positions where reflection happens which indicate faults, fracture zone, and open cracks in the bedrock. Blue dashed lines indicate the location of known faults. The red dashed rectangles denotes a selected candidate region for Hyper-K cavern. Dashed circle indicates the size of the Hyper-K cavern.

Fig. 42. Rock class distribution obtained by combining the results of seismic tomography, reflection imaging and the geological survey results with bore-hole and the existing tunnels. The red dashed rectangles and dashed black circle are same manners as in Fig. 41.

made cover at 60m and 40m depth, respectively. It has been demonstrated that the peak amplitude of the pressure shockwave was significantly reduced outside the cover for the imploded glass bulb and thus could not cause a chain reaction.

Location

One of technical challenges of the project is to realize a gigantic underground cavern for the Hyper-K detector. In order to pin down the candidate place, seismic prospecting by using artificially generated elastic wave was performed at the area of $(400\,\text{m})^3$. Receivers or sensors, called 'geophones,' which detect the elastic wave, were installed in six tunnels at 111 locations with three geophones to capture triaxial components of the elastic wave for each. A seismic source is set in the tunnels and generated the elastic wave at 738 points.

The data obtained in the seismic survey were analyzed with two methods, seismic tomography and reflection imaging. Figure 41 shows the results of reflection imaging overlaid with known faults and fracture zones. The study identified the known faults as expected, while there was no new faults found at the central region. Figure 42 is rock class distribution made by combining the results of seismic tomography, reflection imaging, and the past geological survey. In both figures, the red dashed rectangle denotes a region which has the best rock quality and the least uneven rock over the entire Hyper-K candidate site. We successfully found the candidate place that is suitable for the gigantic cavern construction.

Physics

Hyper-K will be able to measure the magnitude of the CP violation with high precision, which could explain the baryon asymmetry in the Universe. Figure 43 shows an expected significance of the CP violation discovery by ten years operation. Hyper-K covers the 76% of δ_{CP} parameter space with 3σ or more significance, and 57% of the parameter space with 5σ or more. Hyper-K will go beyond 7σ significance if $\delta_{CP} = -90°$ as suggested by T2K[2] and NOνA[3] results. Figure 44

shows the discovery significance for the case of $\delta_{CP} = -90°$ as a function of year. The US-based program LBNF/DUNE [6] plans to start its beam in 2026 and it is critical for Hyper-K to start its construction and operation on time.

A proton decay $p \to e^+\pi^0$ is an important signal favored by many Grand Unified Theory models with a prediction close to the current limit of the proton decay life time. Figure 45 shows the 3σ discovery potential for the $p \to e^+\pi^0$ mode as a function of year. Hyper-K is an only realistic proposal which can go beyond the proton lifetime of 1×10^{35} years.
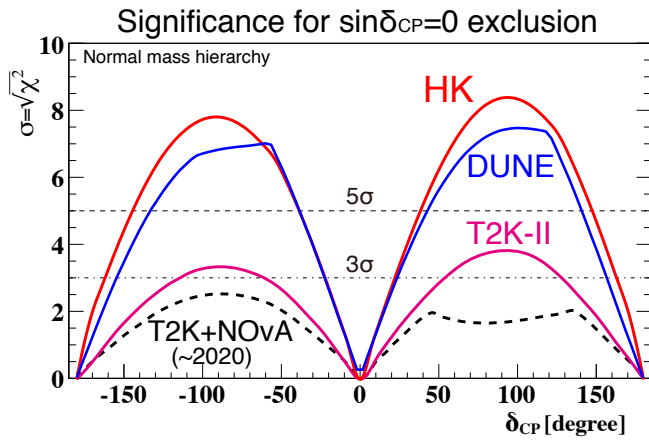
Fig. 43. Significance of the CP violation discovery in lepton sector with a 10-year observation in Hyper-K (HK) as a function of the unknown CP phase. The normal neutrino mass hierarchy is assumed. Ongoing and planned long baseline experiments are superimposed[4, 5].
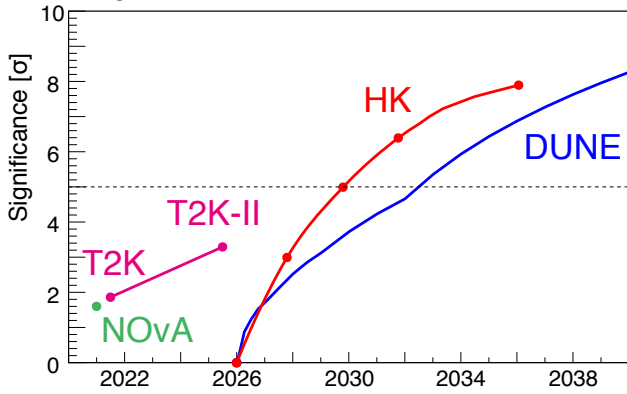
Fig. 44. Discovery potential of the CP violation in lepton sector as a function year. The normal neutrino mass hierarchy is assumed. Ongoing and planned long baseline experiments are superimposed [4, 5].

Fig. 45. The $p \rightarrow e^+ \pi^0$ discovery reach in proton lifetime with 3σ significance as a function of year. It shows Hyper-K (HK) planing to start in 2026, superimposed with the ongoing Super-K (SK) and planned DUNE experiments. The DUNE project assumes 10 kton operation from 2024, toward full 40 kton by increasing 10 kton every year[6].
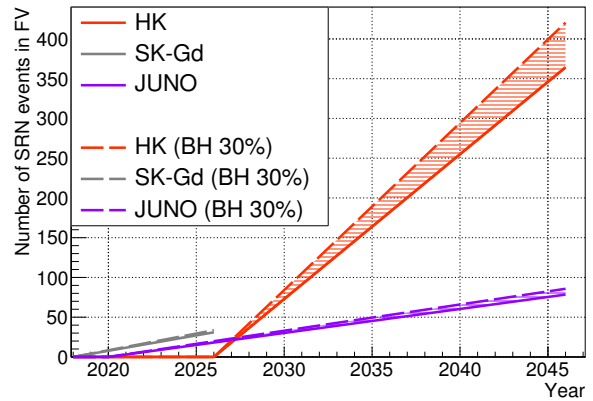
Fig. 46. The accumulated number of supernova relic neutrino events as a function of year. The JUNO experiment and SK-Gd are also plotted [7, 8, 9, 10]. Effective temperature of neutrinos inside supernova is assumed to be 6 MeV. The solid line assumes no black hole formation while the dashed line assumes that 30% of core–collapse stars form a black hole.

As well as the supernova burst neutrino that was successfully observed in Kamiokande at once, undiscovered supernova relic neutrinos, accumulated by past all supernovae since the beginning of the universe, are interesting events to explore the history of heavy elements and the onset of stellar formation. Figure 46 shows the expected number of events as a function of year.

Community support and Organization

In January 2015, ICRR and the Institute of Particle and Nuclear Studies (IPNS) of KEK signed a memorandum of understanding (MoU) for cooperation on the Hyper-K project.

In accordance of the MoU, the Hyper-K Advisory Committee (HKAC) has been formed under the directors of ICRR and KEK-IPNS. The HKAC is composed of international members outside the Hyper-K proto-collaboration, and its mandate is to advise on the scientific, technical and managerial strategy of the Hyper-K project with a view to further developing a highly effective neutrino programme based in Japan. Two rounds of the HKAC meetings were held so far,

the first in winter 2015-2016 and the second in summer 2017. In the official report by the HKAC, the committee endorses Hyper-K as a very important experiment for Japan and for the world-wide program of fundamental science, and encourages ICRR and IPNS to fully support it.

The Hyper-K project are strongly supported by research communities. The Japan Association of High Energy Physicists (JAHEP) and the Cosmic Ray Researchers Congress (CRC) in Japan endorse Hyper-K as the main future project. KEK Project Implementation Plan (KEK-PIP) released in June 2016 [11] has put the first priority to the upgrade of the J-PARC accelerator for the Hyper-K experiment. The ICRR Future Project Committee has concluded in March 2017 that Hyper-K should be the laboratory's next main project.

The Hyper-K project is listed in "Roadmap 2017" by Min-

istry of Education, Culture, Sports, Science and Technology (MEXT) as one of the seven highest-priority large-scale projects in Japan. This is a golden opportunity to get the approval of the construction budget.

In October 2017, the University of Tokyo launched Next-Generation Neutrino Science Organization (NNSO), where ICRR, Kavli IPMU, and the School of Science cooperate for pioneering the future of neutrino physics through the development of neutrino research techniques and detector technologies. In particular, it aims to promote what will become its flagship facility, the Hyper-Kamiokande project. The development of the organization framework for the Hyper-K detector construction centered on NNSO is starting.

Bibliography

[1] "Hyper-Kamiokande Design Report,"
arXiv: 1805.04163

[2] K. Abe *et al.* [T2K Collaboration],
Phys. Rev. Lett. 118, 151801.

[3] P. Adamson *et al.* [NOνA Collaboration],
Phys. Rev. Lett. 118, 231801.

[4] K. Abe *et al.* [The T2K Collaboration],
arXiv:1609.04111 [physics.ins-det].

[5] K. Abe *et al.* [The T2K Collaboration],
PTEP **2015**, no. 4, 043C01 (2015).

[6] R. Acciarri *et al.* [The DUNE Collaboration],
arXiv:1601.05471 [physics.ins-det].

[7] H. Sekiya [Super-K Collaboration],
PoS(ICHEP2016) 982 (2016).

[8] ICRR News (2016), http://www.icrr.u-tokyo.ac.jp/2016/06/30101400.html.

[9] F. An *et al.* [JUNO Collaboration],
J. Phys. G **43**, no. 3, 030401 (2016).

[10] Yu-Feng LI, Presentation at "Workshop on Supernova at Hyper-Kamiokande" (2017).

[11] KEK Roadmap (Project Implementation Plan),
https://www.kek.jp/ja/About/Organization Overview/Assessment/Roadmap/KEK-PIP.pdf (2016).

HIGH ENERGY COSMIC RAY DIVISION

Overview

There are three major experimental research activities in the High Energy Cosmic Ray Division, the study of high energy gamma rays and the development of the next generation gamma-ray telescopes by the Cherenkov Cosmic Gamma Ray group, the study of extremely high energy cosmic rays by the Telescope Array (TA) group, and the study of very high energy cosmic rays and gamma rays by the Tibet ASγ group.

Other activities, such as experiments utilizing the Akeno observatory, the Norikura observatory, the Mt. Chacaltaya observatory (jointly operated with Bolivia) are closely related to inter-university joint research programs. Also an all-sky high resolution air-shower detector (Ashra) is in partial operation on the Hawaii island. The High Energy Astrophysics group created in the fiscal year 2009 aims to explore various high energy astrophysical phenomena, through theoretical and observational approaches.

The CANGAROO telescopes had been in operation in South Australia since 1992, with a 3.8 m small telescope and then with four 10 m telescopes. The major scientific objective was the study of Very High Energy (VHE) gamma-ray sources in our galaxy in the southern hemisphere. The mission of these telescopes was completed and the CANGAROO observation site was closed in 2011.

For further development of VHE gamma-ray astronomy, the Cherenkov Cosmic Gamma Ray group is working on the design study and development of the next generation international ground-based gamma-ray observatory CTA which will offer an order of magnitude better sensitivity than currently running Cherenkov telescopes, three times better angular resolution, and wider energy coverage from 20 GeV to 100 TeV or higher.

At the Akeno observatory, a series of air shower arrays of increasing geometrical sizes were constructed and operated to observe extremely high energy cosmic rays (EHECRs). The Akeno Giant Air Shower Array (AGASA) was operated from 1991 to January 2004 and covered the ground area of 100 km^2 as the world largest air shower array. In 13 years of operation, AGASA observed a handful of cosmic rays exceeding the theoretical energy end of the extra-galactic cosmic rays (GZK cutoff) at 10^{20} eV.

The Telescope Array (TA), a large plastic scintillator array with air fluorescence telescopes, has been constructed in Utah, USA, which succeeds AGASA and measures the EHECRs with an order of magnitude larger aperture than that of AGASA for the further study of EHECRs. The full-scale TA is accumulating data as the largest array viewing the northern sky and observed the energy spectrum with high statistics, which is in good agreement with the GZK suppression.

An air shower experiment aiming to search for celestial gamma-ray point sources started in 1990 with Chinese physicists at Yangbajing (Tibet, 4,300 m a.s.l.). This international collaboration is called the Tibet ASγ Collaboration. An extension of the air shower array was completed in 1995 and an emulsion chamber has been combined with this air shower array since 1996 to study the primary cosmic rays around the knee energy region. After successive extensions carried out in 1999, 2002 and 2003, the total area of the air shower array amounts to 37,000 m^2. The sun's shadow in cosmic rays affected by the solar magnetic field was observed for the first time in 1992, utilizing its good angular resolution at multi-TeV energy region. The group is planning to construct a new air shower array to cover the sky in the Southern hemisphere.

The High Energy Astrophysics group is conducting theoretical researches on fundamental processes responsible for non-thermal particle acceleration in various astrophysical environments, including first-order diffusive shock acceleration, second-order stochastic acceleration in shock downstream regions, modification of shock structure by pick-up interstellar neutrals, as well as injection processes of suprathermal particles. In addition to these theoretical works, R/D studies for radio observations of pulsars and cosmic ray air showers are also being made.

Cherenkov Cosmic Gamma-Ray Group

CTA Project (Cherenkov Telescope Array)

CTA-Japan Consortium
[Spokespersons : M.Teshima and H.Kubo]

Collaboration list:

Institute for Cosmic Ray Research, The University of Tokyo, Chiba, Japan; Department of Physics, Aoyama Gakuin University, Tokyo, Japan; Department of Physics, Hiroshima University, Hiroshima, Japan; Hiroshima Astrophysical Science Center, Hiroshima University, Hiroshima, Japan; Faculty of Science, Ibaraki University, Ibaraki, Japan; Institute of Particle and Nuclear Studies, High Energy Accelerator Research Organization (KEK), Ibaraki, Japan; Department of Physics, Konan University, Hyogo, Japan; Faculty of Medical Engineering and Technology, Kitasato University, Kanagawa, Japan; Graduate School of Science and Technology, Kumamoto University, Kumamoto, Japan; Department of Physics, Kyoto University, Kyoto, Japan; Department of Applied Physics, University of Miyazaki, Miyazaki, Japan; Department of Physics, Nagoya University, Aichi, Japan; Solar-Terrestrial Environment Laboratory, Nagoya University, Aichi, Japan; Kobayashi-Maskawa Institute, Nagoya University, Aichi, Japan; Department of Earth and Space Science, Osaka University, Japan; Department of Physics, Kinki University, Osaka, Japan; Astrophysical Big Bang laboratory, RIKEN, Wako, Japan; Department of Physics, Rikkyo University, Tokyo, Japan; Department of Physics, Saitama Uni-
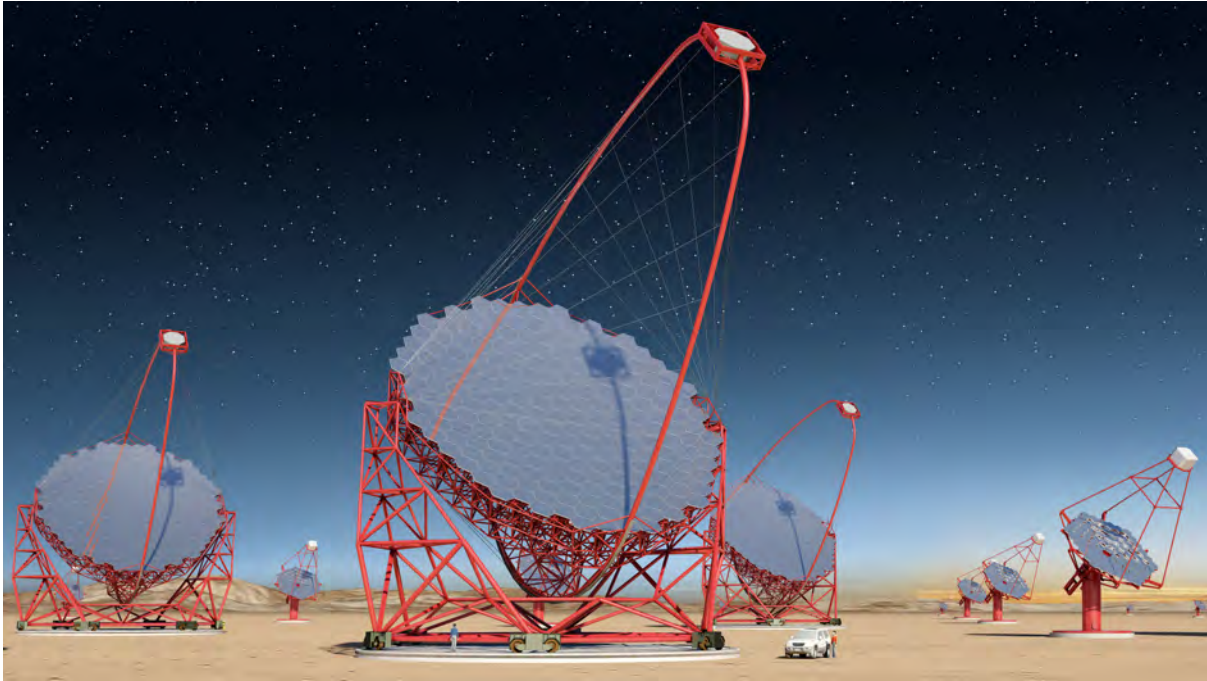
Fig. 1. Artist view of the CTA observatory. CTA consists of three types of telescopes, Large Size Telescopes (23m diameter), Mid Size Telescopes (12m) and Small Size Telescopes (4m), and covers the broad energy band from 20GeV to 100TeV.

versity, Saitama, Japan; Institute of Space and Astronautical Science, JAXA, Kanagawa, Japan; Department of Physics, Tokai University, Kanagawa, Japan; Faculty of Integrated Arts and Sciences, The University of Tokushima; Department of Astronomy, The University of Tokyo, Tokyo, Japan; Department of Physics, The University of Tokyo, Tokyo, Japan; Faculty of Science and Engineering, Waseda University, Tokyo, Japan; Department of Physics, Yamagata University, Yamagata, Japan; Faculty of Management Information, Yamanashi Gakuin University, Yamanashi, Japan; Center for Cosmology and AstroParticle Physics, Ohio State University, Ohio, USA; Max-Planck-Institute for Physics, Munich, Germany [1].

CTA Project

During the past several years, Very High Energy (VHE) gamma-ray astronomy has made spectacular progress and has established itself as a vital branch of astrophysics. To advance this field even further, we propose the Cherenkov Telescope Array (CTA) [6], the next generation VHE gamma ray observatory, in the framework of a worldwide, international collaboration. CTA is the ultimate VHE gamma ray observatory, whose sensitivity and broad energy coverage will attain an order of magnitude improvement above those of current Imaging Atmospheric Cherenkov Telescopes (IACTs). By observing the highest energy photons known, CTA will clarify many aspects of the extreme Universe, including the origin of the highest energy cosmic rays in our Galaxy and beyond, the physics of energetic particle generation in neutron stars and black holes, as well as the star formation history of the Universe. CTA will also address critical issues in fundamental physics, such as the identity of dark matter particles and the nature of space and time.

VHE gamma rays from 100GeV to 10TeV can be observed with ground-based IACTs. The history of VHE gamma ray astronomy began with the discovery of VHE gamma rays from the Crab Nebula by the Whipple Observatory in 1989. To date, the current generation IACTs featuring new technologies, such as H.E.S.S., MAGIC, and VERITAS have discovered more than 200 Galactic and extragalactic sources of various types.

CTA is designed to achieve superior sensitivity and performance, utilizing established technologies and experience gained from the current IACTs. The project is presently in its pre-construction (prototyping) phase, with international efforts from Japan, US, and EU countries. It will consist of several 10s of IACTs of three different sizes (Large Size Telescopes, Mid Size Telescopes, and Small Size Telescopes). With a factor of 10 increase in sensitivity (1m Crab $\sim 10^{-14} erg\ s^{-1}\ cm^{-2}$), together with a much broader energy coverage from 20GeV up to 300TeV, CTA will bring forth further dramatic advances for VHE gamma ray astronomy. The discovery of more than 1000 Galactic and extragalactic sources is anticipated with CTA.

CTA will allow us to explore numerous diverse topics in physics and astrophysics. The century-old question of the origin of cosmic rays is expected to be finally settled through detailed observations of supernova remnants and other Galactic objects along with the diffuse Galactic gamma ray emission, which will also shed light on the physics of the interstellar medium. Observing pulsars and associated pulsar wind nebulae will clarify physical processes in the vicinity of neutron stars and extreme magnetic fields. The physics of accretion onto supermassive black holes, the long-standing puzzle of the origin of ultra-relativistic jets emanating from them, as well as their cosmological evolution, will be addressed by extensive studies of active galactic nuclei (AGN). Through ded-

icated observing strategies, CTA will also elucidate many aspects of the mysterious nature of gamma ray bursts (GRBs), the most energetic explosions in the Universe. Detailed studies of both AGNs and GRBs can also reveal the origin of the highest energy cosmic rays in the Universe, probe the cosmic history of star formation including the very first stars, as well as provide high precision tests of theories of quantum gravity. Finally, CTA will search for signatures from elementary particles constituting dark matter with the highest sensitivity yet. Realisation of the rich scientific potential of CTA is very much feasible, thanks to the positive experience gained from the current IACTs.

The CTA-Japan consortium [1] is aiming at contributing in particularly to the construction of the Large Size Telescopes (LSTs) and is involved in their development. The LST covers the low energy domain from 20GeV to 1000GeV and is especially important for studies of high redshift AGNs and GRBs. The diameter and area of the mirror are 23m and 400m^2, respectively, in order to achieve the lowest possible energy threshold of 20GeV. All optical elements/detectors require high specifications, for example, high reflectivity, high collection efficiency, high quantum efficiency and ultra fast digitisation of signal, etc. For this purpose, CTA-Japan is developing high quantum efficiency photomultipliers, ultrafast readout electronics and high precision segmented mirrors. On the strength of their experience gained from construction of the MAGIC telescope, the Max-Planck-Institute for Physics in Munich is responsible for the design of the 23m diameter telescope structure, based on a carbon fiber tube space frame. The LSTs require very fast rotation (180 degrees/20seconds) for promptly observing GRBs. The first LST will be built in the CTA North, La Palma, Spain in 2018 and three more LSTs will be built during 2019 to 2021, then four more LSTs in the CTA South are expected to built in the ESO site in Paranal, Chile. The location of the LST array in the CTA North will overlap with MAGIC telescopes, which will allow us to operate CTA-LSTs and MAGIC telescopes together in the early phase of the construction.

The Cherenkov Cosmic Gamma Ray group is also operating the MAGIC Telescopes [10] on La Palma, Canary Islands. This facility is used not only for scientific observations but also for technological development toward the future observatory CTA.

Bibliography

[1] CTA Consortium website: http://www.cta-observatory.jp/ and http://www.cta-observatory.org/.

[2] Science with the Cherenkov Telescope Array, arXiv:1709.07997

[3] The Cherenkov Telescope Array potential for the study of young supernova remnants, Astropart. Phys. 62 (2015) 152-164.

[4] Introducing the CTA concept, The CTA Consortium, Astropart. Phys. 43 (2013) 3-18.
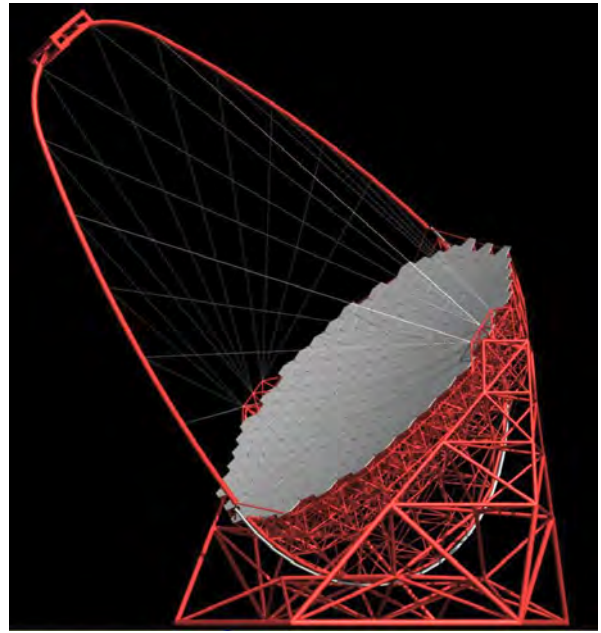
Fig. 2. Large Size Telescope (23m diameter) designed by Max–Planck-Institute for Physics. CTA Japan is contributing to the design and prototyping of the imaging camera at the focal plane, ultrafast readout electronics, and high precision segmented mirrors.

Fig. 3. Camera cluster for the Large Size Telescope (LST) developed by CTA-Japan. This cluster consists of seven high quantum efficiency photomultipliers (R11920-100), CW High Voltages, pre-amplifier, Slow Control Board, DRS4 Ultra fast waveform recording system and Trigger. The LST camera can be assembled with 265 of these clusters, cooling plates and camera housing.

Fig. 4. The high precision segmented mirrors for the Large Size Telescope (LST) developed by CTA-Japan in cooperation with Sanko Co.LTD. The mirror is made of a 60mm thick aluminum honeycomb sandwiched by 3mm thin glass on both sides. A surface protection coat consisting of the materials SiO2 and HfO2 is applied to enhance the reflectivity and to elongate the lifetime.

Fig. 5. The Large Size Telescope prototype (LST-1) under construction at Observatory de Roque de los Muchachos. The diameter of dish and mirror surface area are 23m and 400m^2.

[5] Gamma-ray burst science in the era of the Cherenkov Telescope Array, S. Inoue et al., Astropart. Phys. 43 (2013) 252-275.

[6] Design Concepts for The Cherenkov Telescope Array, The CTA Consortium, Exper. Astron. 32 (2011) 193-316.

[7] Status of Very High Energy Gamma Ray Astronomy and Future Prospects, M. Teshima, The Astronomical Herald, 104 (2011) 333-342.

[8] Design Study of a CTA Large Size Telescope, Proc. of ICRC2012 at Beijing China, M. Teshima, arXiv:1111.2183.

[9] Introducing the CTA Concept, B. Acharya et al., Astroparticle Physics, 34 (2013) 3.

[10] MAGIC Collaboration website: http://magic.mppmu.mpg.de/.

MAGIC

The MAGIC Collaboration has built in 2002 / 2003 a first large atmospheric imaging Cherenkov telescope, MAGIC-I, with a mirror surface of 236 sq.m. and equipped with photomultiplier tubes of optimal efficiency. In 2009, a second telescope of essentially the same characteristics was added; MAGIC-II was installed at a distance of 85m from MAGIC-I. With the accent of these instruments on large mirror surface and best light collection, cosmic gamma-rays at an energy threshold lower than any existing or planned terrestrial gamma-ray telescope have become accessible. So far achieved has been a threshold of 25 GeV. The Japanese group has joined the MAGIC collaboration since 2010, and contributed to the operation, observations and data analysis. The MAGIC telescopes are upgraded with new cameras, electronics and partially new mirrors in 2012, and are now operated with an unprecedented sensitivity by an international collaboration of 17 institutes from 8 countries.

The recent highlights from MAGIC are, 1) Observation of sub-TeV gamma rays from the IceCube170922A [1], [2] , 2)

Fig. 6. MAGIC Stereo System with two Cherenkov telescopes of 17m diameters, so far achieved the threshold energy of 25GeV. It locates near the mountain top of the Roque de los Muchachos on the Canary Island of La Palma. Two telescopes are located with the distance of 85 meters.
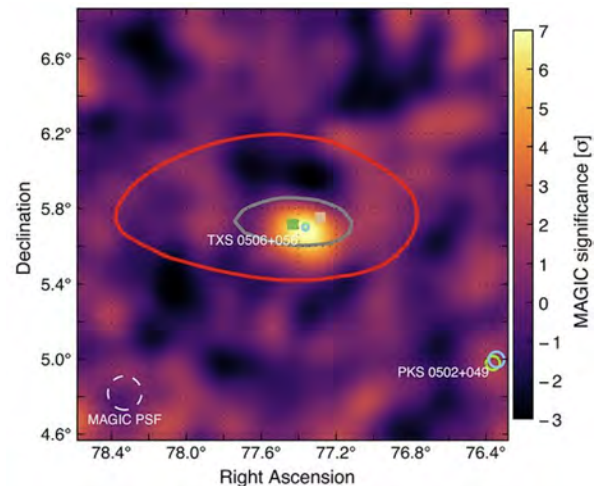
Fig. 7. Sky position of IceCube-170922A in the equatorial coordinate with contour of 50% and 90% confidence level overlaying the gamma-ray colour contour map observed by MAGIC (7 sigma in the peak).

the successful observation of pulsed gamma ray signal from the Crab pulsar up to TeV regime [3], 3) the discoveries of the most distant blazers 3S 0218 + 35 with the redshift of 0.944 [4] and PKS 1441 + 25 with the redshift of 0.939 [5], 4) the observation of the very fast flare of 1min time scale from the blazar inside Perseus cluster, IC310 [6]. These results brought new questions on the pulsar emission mechanism, the EBL energy density, and gamma ray emission mechanism from the supermassive blackholes or vicinity of them.

Bibliography

[1] First-time detection of VHE gamma rays by MAGIC from a direction consistent with the recent EHE neutrino event IceCube-170922A, ATel #10817.

[2] Multimessenger observations of a flaring blazar coincident with high-energy neutrino IceCube-170922A, Science 12 July 2018, Science.eaat1378.

[3] Phase-resolved energy spectra of the Crab pulsar in the range of 50-400 GeV measured with the MAGIC telescopes, the MAGIC Collaboration, Aleksić et al. A&A 540 (2012) A69.

Fig. 8. Akeno atmospheric Cherenkov telescope of 3 m diameter, located in the Akeno Observatory.

[4] ATEL 6349.

[5] ATEL 7416.

[6] Black hole lightning due to particle acceleration at sub-horizon scales, the MAGIC collaboration, Science 346 (2014) 1080-1084.

Other Activities

As a test bench for domestic R & D activities of future ground-based gamma-ray observatory projects, an old atmospheric Cherenkov telescope of 3 m diameter was repaired and then placed at the Akeno Observatory in November 2010. This telescope shown in Figure 8 (Akeno telescope, hereafter) is currently the only atmospheric Cherenkov telescope located in Japan [1]. We have developed an R & D imaging camera system with the Akeno telescope since 2009, the purpose of which is to make a battery-powered data acquisition system for a future mobile imaging atmospheric Cherenkov telescope array [2]. The system consists of 32 PMTs, of which detected Cherenkov light signals are read out by only four GHz-sampling analog memory ASICs.

After test observations of atmospheric Cherenkov light events in 2016, we performed observations of the Crab Nebula using this system in 2017. The Crab Nebula is the standard candle in the TeV gamma-ray energy region and utilized for checking performance of telescope systems. We could accumulate about 10 hr Crab data after two observation periods of about one week each. The data will be analyzed for detecting the gamma-ray signal from the Crab and for estimating performance of the system.

Bibliography

[1] M. Ohishi et al., Proc. of 33rd Internat. Cosmic Ray Conf. (Rio de Janeiro), 587 (2013).

[2] T. Yoshikoshi et al., Proc. of 34th Internat. Cosmic Ray Conf. (The Hague), 887 (2015).

TA: Telescope Array Experiment

[Spokespersons (Dec. 2011 - Dec. 2017: H. Sagawa[1], G. B.Thomson[2]]
[Spokespersons (Dec. 2017 - : S. Ogio[3], C.C.H. Jui[2]]

1 : ICRR, The Univ. of Tokyo, Kashiawa, Chiba 277-8582
2 : Dept. of Physics, University of Utah
3 : Graduate School of Science, Osaka City University

Collaborating Institutions:

Chiba Univ., Chiba, Japan; Chubu Univ., Kasugai, Japan; Earthquake Research Institute, Univ. of Tokyo, Tokyo, Japan; Ehime Univ., Matsuyama, Japan; Ewha W. Univ., Seoul, Korea; Hiroshima City Univ., Hiroshima, Japan; Hanyang Univ., Seoul, Korea; ICRR, Univ. of Tokyo, Kashiwa, Japan; INR, Moscow, Russia; Inst. of Phys, Czech Acad. of Sci., Prague, Czech; IPMU, Univ. of Tokyo, Kashiwa, Japan; Kanagawa Univ., Yokohama, Japan; KEK/ IPNS, Tsukuba, Japan; Kindai Univ., Higashi-Osaka, Japan; Kochi Univ., Kochi, Japan; Kyushu Univ., Fukuoka, Japan; Moscow M.V. Lomonosov State University; Moscow, Russia, Nat. Inst. of Rad. Sci., Chiba, Japan; Osaka Electro-Comm. Univ. Osaka, Japan Osaka City Univ., Osaka, Japan; RIKEN, Wako, Japan; Ritsumeikan Univ., Kusatsu, Japan; Rutgers Univ., Piscataway, NJ, USA; Saitama Univ., Saitama, Japan; Shinshu Univ., Nagano, Japan; SKKU, Suwon, Korea, Tokyo City Univ., Tokyo, Japan; Tokyo Inst. of Tech., Tokyo, Japan; Tokyo Univ. of Science, Noda, Japan; ULB, Brussels, Belgium; UNIST, Ulsan, Korea; Univ. of Utah, Salt Lake City, USA; Univ. of Yamanashi, Kofu, Japan; Waseda Univ., Tokyo, Japan; Yonsei Univ., Seoul, Korea

Introduction

The Telescope Array (TA) is the largest Ultra-High Energy Cosmic Ray (UHECR) observatory in the northern hemisphere. The main aim of TA is to explore the origin and nature of UHECRs by measuring the energy spectrum, arrival direction distribution and mass composition. The TA collaboration consists of researchers from US, Russia, Korea, Belgium and Japan.

The TA detector consists of a surface array of 507 plastic scintillator detectors (SD) and three stations of fluorescence detectors (FD). It is located in the desert of Utah in USA. The SDs were deployed on a squre grid with 1.2-km spacing, and the SD array covers ~700 km^2. Each SD has two layers of 1.2-cm-thick scintillator of 3 m^2. The full operation of SDs started in March 2008. The duty cycle is greater than 95%. The FDs view 3° - 31° or 33° above horizon. All three FD stations started the observation in November 2007, and have duty cycles of approximately 10%.

The TA Low-Energy extension (TALE) enables detailed studies of the energy spectrum and composition from $\sim 10^{16}$ eV upwards. The main aim of TALE is to clarify the expected transition from galactic cosmic rays to extragalactic cosmic rays and the comparison of the data with Monte Carlo (MC) simulation that takes into account the results of the LHC experiments. The TALE detector is located north of the TA site. The TALE FD views $31°$ - $59°$ in elevation angle. The TALE SD is described later.

We report the results from TA below.

Energy Measurement
TA energy spectrum

The preliminary result of cosmic-ray spectrum for nine years of the TA SD data is shown in Fig. 9 [1]. TA confirmed the ankle at $10^{18.7}$ eV and the flux suppression above $10^{19.8}$ eV. The statistical significance of having the same spectral index above the ankle (no suppression) is $\sim 7\sigma$.
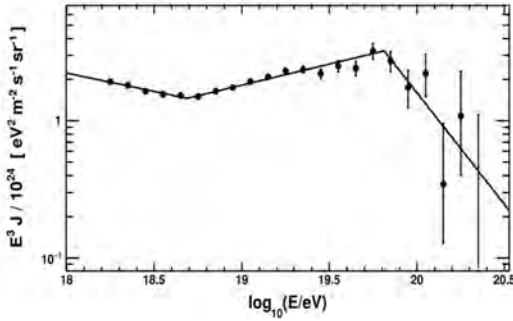
Fig. 9. The preliminary TA cosmic-ray flux multiplied by E^3 for TA SD nine-year data. The solid line shows the fit of the TA data to a broken power law.

Fig. 10 shows the TA and Pierre Auger Observatory (Auger) energy spectra with energy shifts by -5.2% and +5.2%, respectively. Significant discrepancy is seen above around $10^{19.5}$ eV, whereas good agreement is seen below $10^{19.5}$ eV. The TA and Auger collaborations formed a working group, and compared the TA and Auger spectra in the common declination (δ) band (from -15.7° to +24.8°) as shown in Fig. 11a. The cutoff energies agree at 0.5σ level. Based on this study, we compared TA energy spectra above $\delta > 25.8°$ and $\delta < 25.8°$ and found the difference of the cutoff energies as shown in Fig. 11b. The chance probability of obtaining this difference is $3.5\ \sigma$ [2].
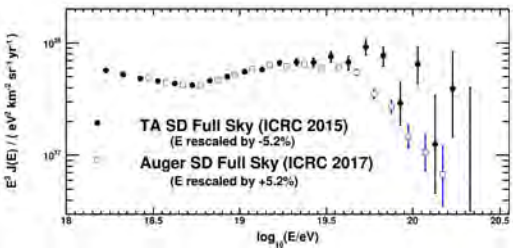
Fig. 10. The TA and Auger energy spectra with energy shifts by -5.2% and +5.2%, respectively.
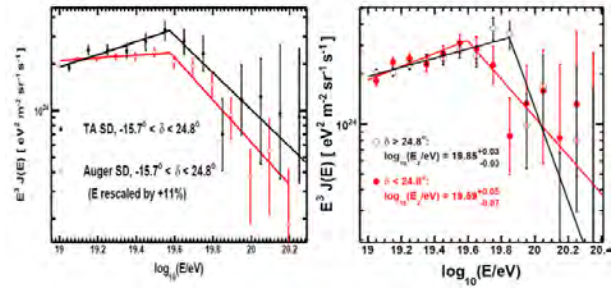
Fig. 11. a) The TA (black) and Auger (red) energy spectra of UHECR events in the common declination band after energy shift. b) The TA energy spectra for the declination angles below 24.8° in red and above 24.8° in black

TALE energy spectrum

The energy spectrum using the TALE FD data between ~ 2 PeV and 100 PeV is shown in Fig. 12 [3]. The events observed with the TALE FD are placed into three subsets: Cherenkov dominated events, fluorescence dominated events, and mixed signal events. We see two clear breaks at $10^{16.22}$ eV and $10^{17.04}$ eV. We possibly see the knee feature at around $10^{15.6}$ eV. It becomes of great importance to measure the composition precisely using hybrid events by adding the TALE SD array to understand this spectral feature. The TALE SD is described later.
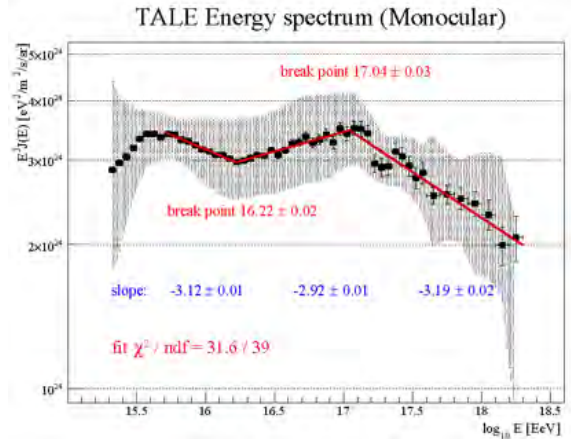
Fig. 12. a) TALE cosmic-ray energy spectrum. The gray band indicates the size of the systematic uncertainties.

Mass Composition
X_{max}

The result of the depth of shower maximum X_{max} using the first 8.5 years of hybrid events was published [4]. Fig. 13 shows the evolution of the average X_{max} as a function of energy together with MC expectations. The result is in agreement with light composition within systematic uncertainty.

We checked the shape of X_{max} distributions, too. After allowing for systematic shfting of the data X_{max} and performing the likelihood test on the data and MC distributions, we find that we fail to reject QGSJet II-04 protons as being compatible with the data for all energy bins at the 95% confidence level as shown in Fig. 14. QGSJet II-04 helium, nitrogn and iron are rejected for $\log_{10}(E) < 19.0$, 19.2, and 19.4, respectively. For

$\log_{10}(E) > 19.0$, TA has insufficient statistics to distinguish the difference between different composition.

The TA and Auger composition working group reported on a comparison of X_{max} distributions measured by the Auger and TA observatories [5]. A direct comparison of the measured X_{max} distributions is not correct due to different detector acceptances and resolutions as well as different analsysis techniques. A set of showers compatible to the composition measured by the Auger detectors was simulated and reconstructed using the official TA software chain. The TA data is within the systematic uncertainties compatible to a mixed composition as the one measured by the Auger detectors.

Fig. 15. Average atomic mass $< lnA >$ in comparison with the TA hybrid results.
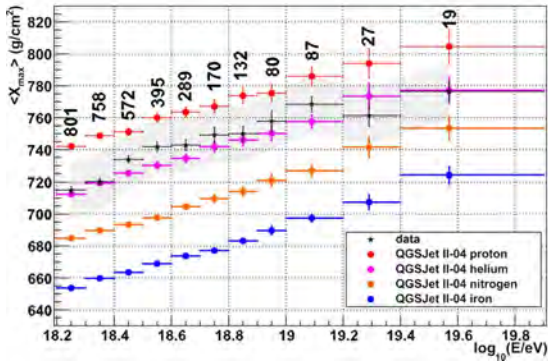
Fig. 13. The average reconstructed X_{max} as a function of energy. The black, red, magenta, orange and blue colors denote the data, pure proton, helium, nitrogen and iron QGSJet II-04 predictions, respectively.
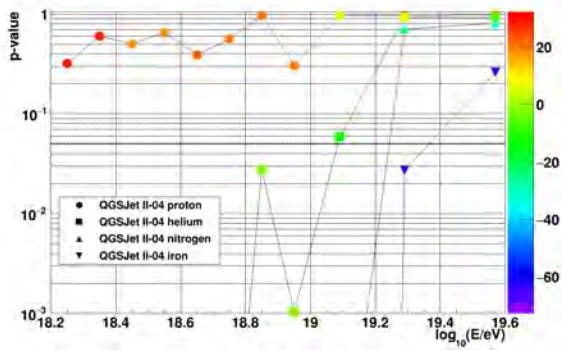
Fig. 14. Unbinned maximum likelihood test on observed and simulated QGSJet II-04 X_{max} distributions after systematic shifting of the data to find the best log likelihood.

TA SD composition

The result on UHECR mass composition obtained with the TA SD is presented [6] using the boosted decision tree multivariate analysis based on 14 observables sensitive to the properties of the shower front and the lateral distribution function. The multivariate classifier is trained with MC simulations with the QGSJET II-03 model. The average atomic mass corresponds to $< lnA >= 1.52 \pm 0.08$ (stat.) ± 0.36 (syst.). The obtained composition is qualitatively consistent with the TA hybrid results as shown in Fig. 15.

TA muon studies

The number of muons in inclined air showers observed with water Cherenkov surface detectors at the Pierre Auger Observatory is approximately 1.8 times that of the proton prediction with QGSJET II-03 model at 10^{19} eV [7]. We studied muons in air showers using seven years of the TA SD data [8, 9]. Air shower events are classified using θ, ϕ and R parameters to search for the condition of high purity of muons. Here θ is the zenith angle of the shower axis, ϕ is the azimuthal angle of the location of a surface detector around the shower core on the ground, and R is the distance of the location of the surface detector from the shower axis. The direction of zero degrees of ϕ is opposite to the cosmic-ray incident direction projected onto the ground. The counterclockwise direction is positive. The condition ($30° < \theta < 45°$ and $150° < |\phi| < 180°$ (the older shower side in an inclined shower), 2000 m $< R < 4000$ m) gives muon purity of $\sim$65% from the MC expectation at E $\sim$10 EeV. Typical ratios of charge densities of the data to those of the MC are 1.72 ± 0.10 (stat.) $\pm$ 0.40 (syst) at 1910 m $< R < 2160$ m and 3.14 ± 0.36 (stat.) $\pm$ 0.72 (syst) at 2760 m $< R < 3120$ m for QGSJET II-03 model together with other hadronic models as shown in Fig. 16. A similar excess is seen in comparison with other hadronic models.

Search for EeV photons

We present the search for photons using the first nine years of the TA SD data, employing multivariate analysis with the classifier based on the Boosted Decision Tree [10]. There are no photon candidates found in the data set for $10^{18.0}$, $10^{18.5}$, $10^{19.0}$ and $10^{19.5}$ eV, and the diffuse flux limits for photons are compared to the results of other experiments as shown in Fig. 17.

Arrival Directions of UHECRs
TA hotspot for the highest-energy cosmic rays

We have searched for intermediate-scale anisotropy of 72 cosmic-ray events above 5.7×10^{19} eV using the first five years of the TA SD data [11]. We reported a cluster of events that we call the hotspot, found by oversampling using circles 20° in radius. The hotspot has a Li-Ma pre-trial statistical significance of 5.1σ. The probability of such a hotspot appearing
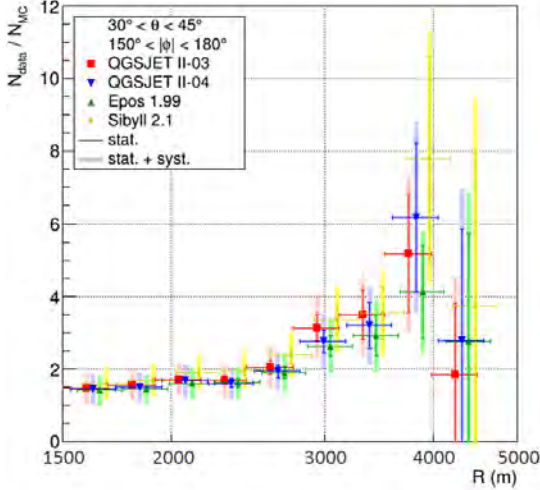
Fig. 16. The ratios of the average charge densities of the data to MC simulations as a function of core distance for $30° < \theta < 45°$, $150° < |\phi| < 180°$ and $1500 \, m < R < 4500 \, m$. The red, blue, green and yellow represent QGSJET II-03, QGSJET II-04, EPOS1.99 and SIBYLL2.1, respectively.
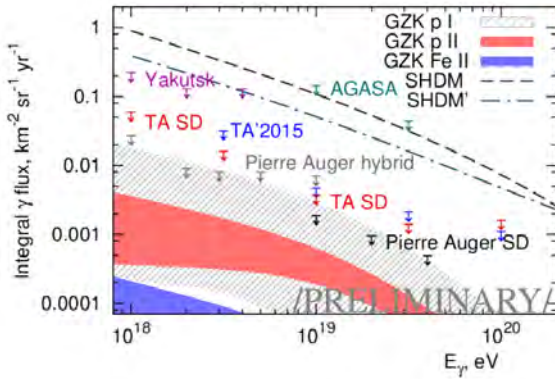
Fig. 17. Preliminary TA photon flux limits (red) compared with the results from AGASA (green), Auger SD (black) and hybrid data (grey), Yakutsk (magenta) and TA result at ICRC2015 (blue) and the predictions of certain models.

Fig. 18. Aitoff projection of Li-Ma significance map using cosmic-ray events above 5.7×10^{19} eV for the first nine years of the TA SD data in equatorial coordinates. Our FoV is defined as the region above the dashed curve at decl. = -10°.

$10^{19.75}$ eV and an excess above $10^{19.75}$ eV as shown in Fig. 19. The post-trial probability of this energy anisotropy, appearing by chance anywhere on isotropic sky, is found to be 9×10^{-5} (3.74σ) by MC simulation.
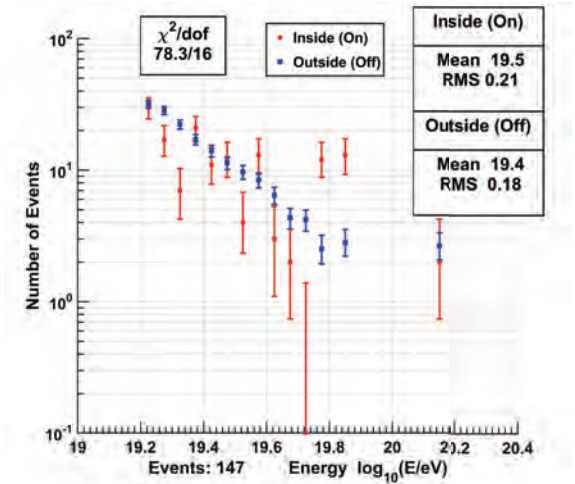
Fig. 19. The histogram of energies of events inside the spherical cap bin of radius 28.43° (red) at the maximum pre-trial significance. It's compared to the histogram of expected (normalized outside) energies (blue).

by chance in an isotropic cosmic-ray sky is estimated to be 3.4σ. For the first nine years of the TA data, 143 events above 5.7×10^{19} eV were observed. We scanned by circles with different radii and obtained the maximum Li-Ma pre-trial significance of $\sim 5\sigma$ at right ascension of $144.3°$ and declination of $+40.3°$ with oversmpling using circles with a radius of 25°. The Li-Ma significance plot is shown in Fig. 18. The chance probability of this occurance was $\sim 3\sigma$ [1].

Hot/cold spot

An energy dependent intermediate-scale anisotropy was studied using UHECRs above $10^{19.2}$ eV for seven years of the TA SD data [12]. The energy distributions inside oversampled circles are compared to that outside using the Poisson Likelihood Ratio test. The maximum pre-trial significance was obtained to be 6.17σ at right ascension of $139°$ and declination of $45°$. The energy distribution within the circle at the center of maximum significance shows a deficit of events below

Spectrum anisotropy with respect to the supergalactic plane

In the cosmic-ray energy region above 10 EeV, the shape of cosmic-ray energy spectrum may carry an imprint of the distribution of the cosmic-ray source density. The Super-Galactic plane (SGP) consists of local galactic clusters containing more nearby objects. By considering the effect of the loss of UHECRs due to attenuation during the propagation in the universe, the energy spectrum of UHECRs in the area near the SGP (On-source area) is expected to be different from that in the area far from the SGP (Off-source area) containing less nearby objects. Here the On-source area is defined as the area within $\pm 30°$ from the SGP latitude of $0°$ and the Off-source area is defined as the area that is the rest in the sky. We found that the Off-source spectrum has a break at lower energy for the first five years of TA SD data as shown in Fig. 20. The chance probability of obtaining such or larger difference in statistically equivalent distributions is estimated

to be $6.2\pm1.1\times10^{-4}$ (3.2σ) by a MC simulation [13]. The observed difference in the spectra is in a reasonable quantitative agreement with a simplified model assuming that the UHECR sources trace the galaxy distribution from the 2MRS catalogue, primary particles are protons and the magnetic deflections are neglected.
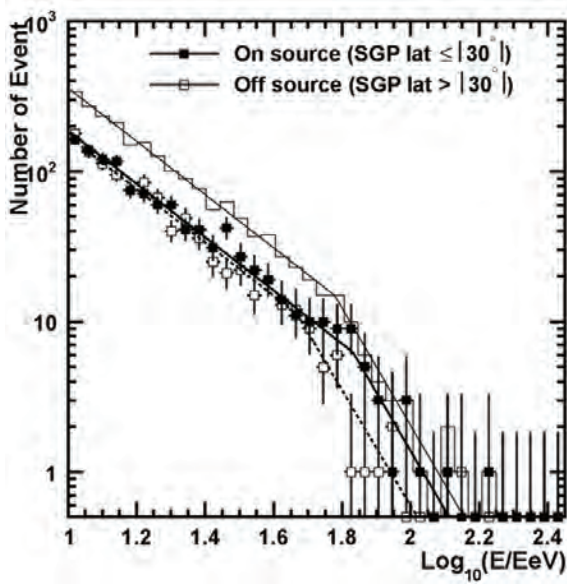
Fig. 20. The energy distributions of UHECR events observed with the TA SDs. The histogram shows the distribution of all events. Closed and open symbols show energy distributions observed in On- and Off-source areas respectively.

Interdisciplinary research
TA SD burst events in coincdence with lightning

The TA SD observed several short-time bursts of air shower like events for the first five years. The expectation of chance coincidence is less than 10^{-4}. We found evidence for correlations between these bursts of the TA SD events and powerful lightning data obtained with the National Lightning Detection Network in timing and position [14]. After installting a 3-D lightning mapping array and electric field change instrument at the TA SD site, detailed features were observed [15].

TA extension
TAx4

As mentioned above, TA found evidence for intermediate-scale anisotropy of arrival directions of cosmic rays with greater than 5.7×10^{19} eV. With enhanced statistics, we expect to observe the structure of the hotspot along with other possible excesses and point sources along with the correlations with extreme phenomena in the nearby universe. We proposed to quadruple the area of the TA SD aperture including the existing TA SD array by installing additional 500 counters of the current TA SD design, which will be deployed on a square grid with wider, 2.08-km spacing between each [16, 17]. The new array would need two FD stations overlooking it to increase the number of hybrid events for the measurement of X_{max} and to confirm the energy scale. These FDs will be formed using additional refurbished HiRes telescopes. The layout of four
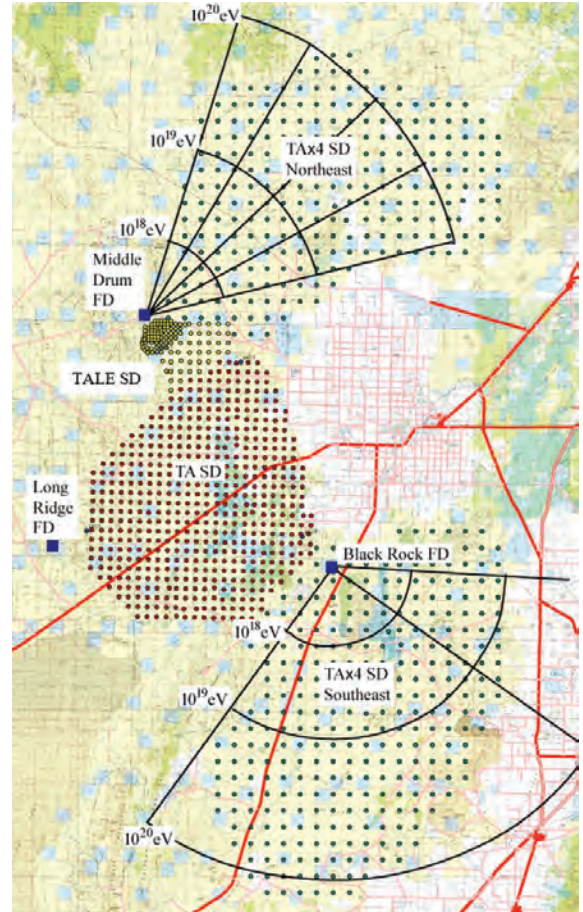
Fig. 21. The layout of the proposed TAx4. The array of 507 SDs (red filled circles on the left) is the current TA SD array. There are three TA FD stations (MD to the north, LR to the west, and BRM to the east of the TA SD array). The array of surface detectors to the north of the TA SD array is the TALE SD array. Additional two sub-arrays of 500 surface detectors in total (green filled circles) for TAx4 are located to the northeast and southeast of the TA SD array. Additional two FD stations with refurbished HiRes telescopes for the TAx4 are located at the MD and BRM FD sites and view to the northeast and southeast as denoted each by the black frame of the fan.

times TA, which we call TAx4, is shown in Fig. 21 together with TALE.

The proposal of the SD part of TAx4 that was approved for the Japan Society for the Promotion of Science (JSPS) Grant-in-Aid for Scientific Research on Specially Promoted Research in Japan in 2015 as a five-year project. In 2017 the TAx4 scintillator counters were assembled at the Akeno Observtory as shown in Fig. 22. The assembled counters were sent to Utah, and the final assembly of the TAx4 SDs was partially performed at the Cosmic Ray Center in Delta city near the TA site. The SD deployment would start in early 2019. The FD part of TAx4 was approved by NSF in the USA in 2016. The TAx4 FD at the northern site was completed and started the stable operation in February of 2018. The TAx4 FD at the southern site is under construction as of summer in 2018.

Fig. 22. Assembly of a plastic scintillator counter at the assembly hall of the Akeno Observatory

Fig. 23. An example of the footprint of a TALE SD event

TALE

The layout of TALE is shown in Fig. 21. The TALE FD operation was commenced in the spring of 2013. We saw two clear breaks in the energy spectrum measured with the TALE FD as shown in Fig. 12. It is of importance to measure X_{max} precisely adding timing information of surface detectors near the shower core on the ground. The TALE SD array consists of 103 plastic scintillation counters, which are identical to those of the TA SD array. These counters have graded spacings, ranging from 400 m near the FD to 600 m further away, which merge into the TA SD array with 1200-m spacing at its northwestern corner. The 35 TALE SDs were firstly deployed in 2013. Therefore we proposed to complete the full TALE SD array. The proposal of adding remaining SDs in the TALE SD array was approved for the JSPS Grant-in-Aid for Scientific Research (S) in 2015 as a five-year project. The full TALE SDs were deployed in February of 2017. The TALE SD array is in stable operation [18]. Fig. 23 is an example of the footprint of a TALE SD event.

The observation of cosmic rays with energies down to 10^{15} eV, called the Non-Imaging CHErenkov (NICHE) array [19], was proposed. The plan is to install an array of simple Cherenkov counters of PMTs each three inches in diameter on the ground looking upwards within the TALE SD array. The part of the NICHE with 15 PMTs, called jNICHE, was constructed by the JSPS Grant-in-Aid for Young Scientists (A) that was approved in 2014.

R&D for future detectors

To collect much larger statistics at the highest energies, observatories of significantly larger aperture are needed to identify sources via anisotropy studies. Because of the prohibitive cost, it may be difficult to build a sufficiently large detector using existing technologies. Hence, it is important to develop new detectors. The TA site is used worldwidely for R&D of future detectors.

The JEM-EUSO is a new type of observatory that will utilize very large volumes of the earth's atmosphere as a detector of the highest-energy cosmic rays from the universe. K-EUSO [20] employs the technologies developed for the JEM-EUSO mission and will be mounted to the International Space Station (ISS) . K-EUSO is a wide-field (40°), fast, and large telescope, and observes brief UV flashes in the earth's atmosphere caused by the highest-energy cosmic rays. The advantage is its rather uniform and huge aperture in the whole sky. EUSO-TA, which is a EUSO prototype installed at the TA BRM FD site in 2013, has been tested occasionally. The first result from EUSO-TA for laser shots, star images, and UHE-CRs in association with those observed with the BRM FD was published in [21].
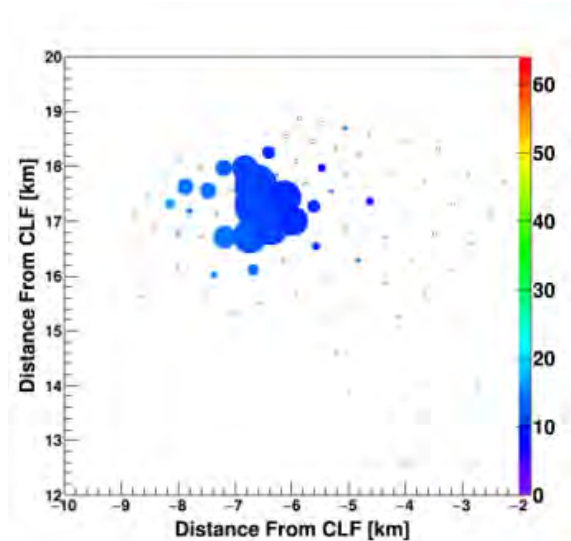
New types of fluorescence detector were proposed for large area and low-cost detection of UHECRs such as FAST with reflecting mirrors [22] and CRAFFT with fresnel lenses [23]. They were installed at the BRM FD site, and the observations of UHECRs are being performed.

Summary

TA confirmed the ankle at $10^{18.7}$ eV and the flux suppression above $10^{19.8}$ eV. The statistical significance of having the same spectral index above the ankle (no suppression) is $\sim 7\sigma$.

We confirmed the breaks at $10^{16.2}$ eV and $10^{17.0}$ eV in the energy spectrum measured with the TALE FD.

The X_{max} measurement above $10^{18.2}$ eV is consistent with light composition. We need more statistics to clarify the feature above 10^{19} eV.

We obtained 143 cosmic-ray events above 5.7×10^{19} eV in the nine years of the TA SD data. By scanning the sizes of circles for oversampling these events, we found maximum Li-Ma significance at $\sim 5\sigma$. Its significance appearing in an isotropic cosmic-ray sky is $\sim 3\sigma$. Evidence for some features of spectral anisotropy is seen.

In order to confirm the TA hotspot and understand its feature, we are constructing TAx4, which would quadruple the TA SD aperture and would add two FD stations. The assembly of the TAx4 SDs is under way. One of the TAx4 FDs at two sites was completed and started its operation in February, 2018.

The TALE SDs were fully deployed at the TALE site, and the data acquisition system is been checked. TA, TAx4,

TALE, TAx4 and NICHE will provide important measurements of energy spectrum, composition, and arrival directions of UHECRs from the knee region up to the highest-energy region of over five to six decades in energy.

The TA BRM FD site is used for R&D of future detectors with larger aperture. The prototype (EUSO-TA) of JEM-EUSO has been tested occasionally since 2013. The first result from EUSO-TA was summarized in [21]. New types of fluorescence telescope consisting of a small number of PMTs that aim at a future large and low-cost detector of UHECRs such as FAST and CRAFFT are tested.

Bibliography

[1] J.N. Matthews, "Highlights from the Telescope Array", The 35th International Cosmic Ray Conference (ICRC2017), 2017/7/17 (invited).

[2] R.U. Abbasi *et al.*, "Evidence for Declination Dependence of Ultrahigh Energy Cosmic Ray Spectrum in the Northern Hemisphere", submitted to Astrophys. J., arXiv:1801.07820.

[3] R.U. Abbasi *et al.* "Cosmic-Ray Energy Spectrum between 2 PeV and 2 EeV Observed with the TALE detector in monocular mode", accepted for Astrophys. J., arXiv:1803.01288.

[4] R.U. Abbasi *et al.*, "Depth of Ultra HIgh Energy Cosmic Ray Induced Air Shower Maxima Measured by the Telescope Array Black Rock and Long Ridge FADC Fluorescence Detectors and Surace Array in Hybrid Mode", Astrophys. J., 858:76 (2018).

[5] V. de Souza, "Testing the agreement between the X_{max} distributions measured by the Pierre Auger and Telescope Array Observatories", ICRC2017, 2017/7/18 (oral).

[6] R.U. Abassi *et al.*, "Mass composition of ultra-high-energy cosmic rays with the Telescope Array Surface Detector Data", submitted to Phys. Rev. D., arXiv:1808.03680.

[7] A. Aab *et al.*, (Pierre Auger Collaboration), Phys. Rev. D 91 032003 (2015).

[8] R. Takeishi, "Study of muons from ultra-high energy cosmic ray air showers measured with the Telescope Array experiment", University of Tokyo (2016).

[9] R.U. Abbasi *et al.*, "Study of muons from ultra-high energy cosmic ray air showers measured with the Telescope Array experiment", Phys. Rev. D 98, 022002 (2018).

[10] . G. Rubtsov, "Telescope Array search for EeV photons and neutrinos", ICRC2017, 2017/7/17 (oral).

[11] R.U. Abbasi *et al.*, "INDICATIONS OF INTERMEDIATE-SCALE ANISOTROPY OF COSMIC RAYS WITH ENERGY GREATER THAN 57 EeV IN THE NORTHERN SKY MEASURED WITH THE SURFACE DETECTOR OF THE TELESCOPE ARRAY EXPERIMENT", Astrophys. J. Lett. 790:L21 (2014).

[12] R.U. Abbasi. *et al.*, "Evidence of Intermediate-scale Energy Spectrum Anisotropy of Cosmic Rays E $\geq 10^{19.2}$ eV with the Telescope Array Surface Detector", Astrophys. J. 862:91 (2018).

[13] R.U. Abbasi *et al.*, "Search for Anisotropy in the Ultra High Energy Cosmic Ray Spectrum using the Telescope Array Surface Detector", submitted to Phys. Rev. Lett., arXiv:1707.04967.

[14] R.U. Abbasi *et al.* "The bursts of high energy events observed by the telescope array surface detector", Phys. Lett., A381 (2017) 2565-2572.

[15] R.U. Abbasi *et al.*, "Gamma Ray Showers Observed at Ground Level in Coincidence With Downward Lightning Leaders", J. Geophys. Res: Atmos., 123 (2018).

[16] H. Sagawa, "The plan of the Telescope Array Experiment for the Next Five Years", ICRC2013, 2013/7/2-7/9 (poster).

[17] E. Kido, "The TAx4 experiment", ICRC2017, Busan, Korea, 2017/7/15 (oral).

[18] S. Udo, "The Telescope Array Low-energy Extension", ICRC2017, Busan, Korea, 2017/7/15 (oral).

[19] D. Bergman, "j-NICHE: Prototype detectors of a non-imaging Cherenkov array at the Telescope Array site", ICRC2017, Busan, Korea, 2017/7/17 (oral)

[20] M. Casolino "KLYPVE-EUSO: Science and UHECR observational capabilities", ICRC2017, Busan, Korea (2017)

[21] G. Abdellaoui et al., JEM-EUSO Collaboration, "EUSO-TA - First results from a ground-based EUSO telescope", Astrop. Phys. 102 (2018) 98-111.

[22] T. Fujii, "First results from the full-scale prototype for the Fluorescence detector Array of Single-pixel Telescopes", ICRC2017, Busan, Korea, 2017/7/17 (oral)

[23] Y. Tameda, "The Cosmic Ray Air Fluorescence Fresnel lens Telescope (CRAFFT) for the next generation UHECR obsevatory", ICRC2017, Busan, Korea, 2017/7/18 (poster)

Tibet ASγ Project

[Spokesperson: M. Takita]

ICRR, The Univ. of Tokyo, Kashiwa, Chiba 277-8582

1. Experiment

The Tibet air shower experiment has been successfully operated at Yangbajing (90°31′ E, 30°06′ N; 4300 m above sea level) in Tibet, China since 1990. It has continuously made a wide field-of-view (approximately 2 steradian) observation of cosmic rays and gamma rays in the northern sky.

The Tibet I array was constructed in 1990 and it was gradually upgraded to the Tibet II by 1994 which consisted of 185 fast-timing (FT) scintillation counters placed on a 15 m square grid covering 36,900 m^2, and 36 density (D) counters around the FT-counter array. Each counter has a plastic scintillator plate of 0.5 m^2 in area and 3 cm in thickness. All the FT counters are equipped with a fast-timing 2-inch-in-diameter photomultiplier tube (FT-PMT), and 52 out of 185 FT counters are also equipped with a wide dynamic range 1.5-inch-in-diameter PMT (D-PMT) by which we measure up to 500 particles which saturates FT-PMT output, and all the D-counters have a D-PMT. A 0.5 cm thick lead plate is put on the top of each counter in order to increase the counter sensitivity by converting gamma rays into electron-positron pairs in an electromagnetic shower. The mode energy of the triggered events in Tibet II is 10 TeV.

In 1996, we added 77 FT counters with a 7.5 m lattice interval to a 5,200 m^2 area inside the northern part of the Tibet II array. We called this high-density array Tibet HD. The mode energy of the triggered events in Tibet HD is a few TeV.

In the late fall of 1999, the array was further upgraded by adding 235 FT-counters so as to enlarge the high-density area from 5,200 m^2 to 22,050 m^2, and we call this array and further upgraded one Tibet III. In 2002, all of the 36,900 m^2 area was covered by the high-density array by adding 200 FT-counters more. Finally we set up 56 FT-counters around the 36,900 m^2 high density array and equipped 8 D-counters with FT-PMT in 2003. At present, the Tibet air shower array consists of 761 FT-counters (249 of which have a D-PMT) and 28 D-counters as in Fig. 24.

The performance of the Tibet air shower array has been well examined by observing the Moon's shadow (approximately 0.5 degrees in diameter) in cosmic rays. The deficit map of cosmic rays around the Moon demonstrates the angular resolution to be around 0.9° at a few TeV for the Tibet III array. The pointing error is estimated to be better than ~0.01°, as shown in Fig. 25, by displacement of the shadow center from the apparent center in the north-south direction, as the east-west component of the geomagnetic field is very small at the experimental site. On the other hand, the shadow center displacement in the east-west direction due to the geomagnetic field enables us to spectroscopically estimate the energy
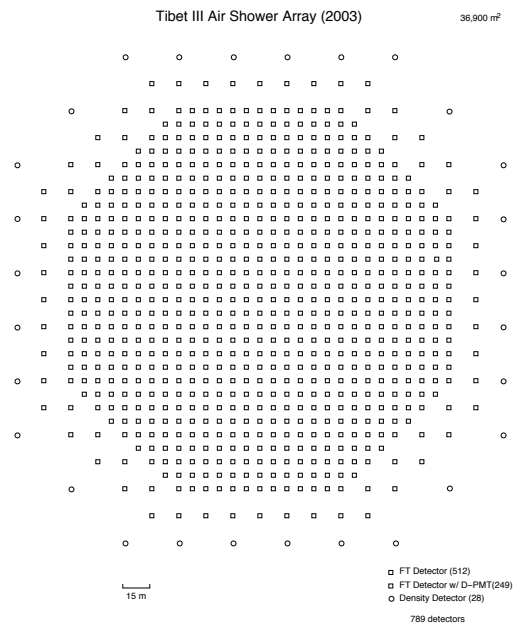
Fig. 24. Schematic view of Tibet III.

Fig. 25. From [1]. The Moon's shadow center displacement from the apparent position in the north-south direction as a function of energy, observed by Tibet III.

scale uncertainty at ± 12 % level, as shown in Fig. 26. Thus, the Tibet air shower experiment introduces a new method for energy scale calibration other than the conventional estimation by the difference between the measured cosmic-ray flux by an air shower experiment and the higher-energy extrapolation of cosmic-ray flux measured by direct measurements by balloon-borne or satellite experiments.
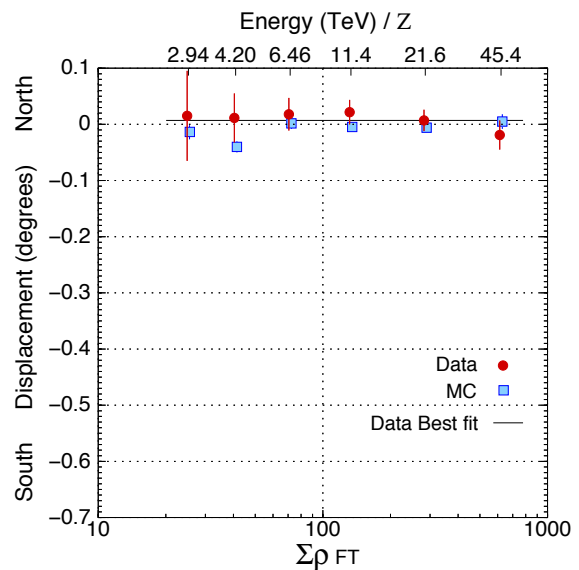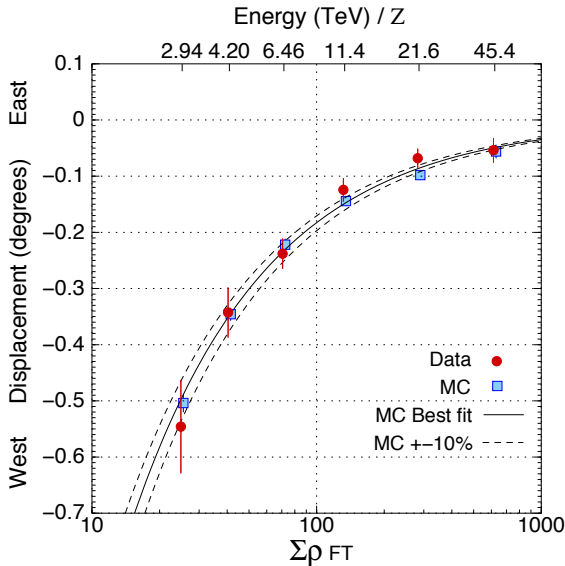
Fig. 26. From [1]. The Moon's shadow center displacement from the apparent position in the east-west direction as a function of energy, observed by Tibet III.

2. Physics Results

Our current research theme is classified into 4 categories:

(1) TeV celestial gamma-ray point/diffuse sources,

(2) Chemical composition and energy spectrum of primary cosmic rays in the knee energy region,

(3) Cosmic-ray anisotropy in the multi-TeV region with high precision,

(4) Global 3-dimensional structure of the solar and interplanetary magnetic fields by observing the Sun's shadow in cosmic rays.

We will introduce a part of the results obtained in this fiscal year.

Cosmic rays arriving at the Earth from the direction of the Sun are shielded by the Sun and the Sun casts a shadow in cosmic rays. Cosmic rays are positively charged particles made up of hydrogen and helium nuclei mostly and the trajectory of cosmic rays is deflected by the magnetic field between the Sun and Earth which depends on the magnetic field strength and the rigidity of cosmic rays. The Tibet air shower array has observed the Sun's shadow around the 10 TeV energy region. We have confirmed, for the first time, the effect of the solar magnetic field on the shadow. The observed deficit in the cosmic-ray intensity in the Sun's shadow indicates a clear 11-year anti-correlation with the solar activity. From the numerical simulations, which reproduce the observed features of the Sun's shadow quantitatively, we now know that more cosmic rays arriving from the direction around the solar limb are scattered by the strong magnetic field in the solar corona during the solar maximum period and they are observed at the Earth from the optical disc direction of the Sun, reducing the intensity deficit in the Sun's shadow.

The strong coronal magnetic field affects the cosmic-ray deficit in the shadow, however, the interplanetary magnetic field (IMF) between the Sun and the Earth deflects trajectories of TeV cosmic rays little. The deflection has actually been observed by some air shower experiments as the North-South displacement of the Sun's shadow center from the optical center of the Sun. We can utilize the observed features of the Sun's shadow as a probe of the solar magnetic field. The solar magnetic field on the photosphere has constantly been monitored by optical measurements employing the Zeeman effect, while the local IMF at the Earth has been directly observed by an near-Earth satellite. However, the observation of the average IMF between the Sun and the Earth is still difficult. As the deflection angle of cosmic rays is proportional to the magnetic field strength, the observed Sun's shadow can be used for evaluating the IMF strength averaged over the distance between the Sun and the Earth.

We develop Monte Carlo (MC) simulations of the Sun's shadow, tracing trajectories of anti-particle cosmic rays shot back to the Sun in the model magnetic field between the Sun and Earth and the dipole geomagnetic field, for comparison with our data. For the solar magnetic field in the MC simulations, the potential field model (PFM) called the current sheet source surface (CSSS) model is employed. The PFM is unique in the sense that it provides the coronal and interplanetary magnetic field together, based on the observed photospheric magnetic field. The CSSS model includes three free parameters, the radius R_{ss} of the source surface (SS), the radius R_{cp} ($<$ R_{ss}) of the spherical surface where the magnetic cusp structure in the helmet streamers shows up, and the length scale l_a of the horizontal electric currents in the corona. In the MC simulations, we set R_{cp} and l_a to 1.7 and 1.0 solar radii, respectively. Also, R_{ss} is set to 10 solar radii which is recently supported by some observed evidences. The MC simulations with the CSSS model reproduces the observed 11-year-period variation of D_{obs}. The magnetic field components are calculated at each point in the solar corona between the solar radius and R_{ss} by the spherical harmonic functions derived from the photospheric magnetic field observations with the spectro-magnetograph of the National Solar Observatory at Kitt Peak (KPVT/SOLIS) for every Carrington rotation period (approximately 27.3 days). The radial coronal field on the SS is subsequently extrapolated to the interplanetary space assuming the simple Parker-spiral IMF..

We use cosmic-ray data recorded during the period between the year 2000 and the year 2009 by the Tibet-III air shower array for the analysis of the Sun's shadow. The configuration of the Tibet-III air array consists of 789 scintillation detectors which cover an effective area of 37,000 m^2. The observed air shower events are divided into seven energy bins (representative energies: 4.9, 7.7, 13, 22, 43, 90, and 240 TeV), according to the shower size $\Sigma\rho_{FT}$ which is the sum of the number of particles per 1 m^2 as a measure of energy of a primary cosmic-ray particle.

The number of on-source events (N_{on}) is defined as the number of air shower events coming from the direction within a circle of Δd radius centered at a given point on the celestial sphere. The number of background, namely, off-source events (N_{off}) is calculated by averaging the number of events

within each of the eight off-source windows located at the same zenith angle as the on-source one. Subsequently, the flux deficit relative to the number of background events is estimated as $D_{obs} = (N_{on} - N_{off})/N_{off}$ at every $0.1°$ grid of the Geocentric Solar Ecliptic (GSE) longitude and latitude.

The IMF sector polarity is allocated to each day in reference to the daily-averaged GSE-x and GSE-y components of the IMF (B_x, B_y) observed by the near-Earth satellite and the average D_{obs} in "Away" and "Toward" sectors is separately calculated. The "Away" ("Toward") sector polarity is allocated to a day when the IMF observed two days later satisfies $B_x<0$ and $B_y>0$ ($B_x>0$ and $B_y<0$). The sector polarity in the solar corona is carried out by the solar wind with an average velocity of approximately 400 km/s and observed at the Earth roughly four days behind. For our assignment of the IMF sector polarity to a day under consideration, therefore, we use the IMF data observed at the Earth two days later as an average along the Sun- Earth line on the day. The average contour maps of D_{obs} in % observed with all the air shower events in "Away" and "Toward" sectors are shown in Fig. 27, together with each projection on the North-South (N-S) and East-West (E-W) axes. In Fig. 27, we notice that the shadow center displaces from the optical center of the Sun located at the origin in the map. The shadow center shifts northward (southward) in "Away" ("Toward") sector as expected from the deflection in the average positive (negative) B_y along the Sun-Earth direction. In the meanwhile, the shadow center deviates westward irrelevant to the IMF sector polarity, because positively charged cosmic rays are deflected in the geomagnetice field.

The average N-S and E-W displacement angles in "Away" and "Toward" sectors are calculated for each energy bin and plotted as functions of cosmic ray rigidity in Fig. 28. We convert the representative energy of each energy bin to the average rigidity of the Sun's shadow by considering the energy spectra and chemical composition of primary cosmic rays based on the direct measurements. As expected from the magnetic deflection of charged particles, the observed displacement angles displayed by black solid circles are reasonably fitted by a function $\alpha/(R/10\text{TV})$ of rigidity R in TV with a fitting parameter α standing for the deflection angle at 10 TV.

In the N-S displacement in Fig. 28(a) and 28(b), we see that the magnitudes of the expected shift (broken curves) are smaller than the magnitudes of the observed one (solid curves) in both sectors, implying an underestimation by the MC simulations. On the other hand, the expected E-W shifts in Figure 2(c) and 2(d), are consistent with the observation, which indicates the E-W shifts are mainly caused by the deflection of cosmic-ray trajectories in the geomagnetic field. It is cofirmed that α in the E-W shifts averaged over "Away" and "Toward" sectors is -0.212 ± 0.034 ($\pm 0.023_{stat} \pm 0.025_{sys}$) and consistent with the E-W shiftss in the Moon's shadow. The IMF strength observed at the Earth is compared with the MC simulations in Fig. 29(a) and 29(b). We find a systematic tendency that the magnitudes of the expected B_x and B_y are smaller than the observations. Based on the calculation of the yearly averaged B_x and B_y each as a function of Carrington longitude between the year 2000 and the year 2009, the correlations between the observed and expected B_x and B_y are checked,
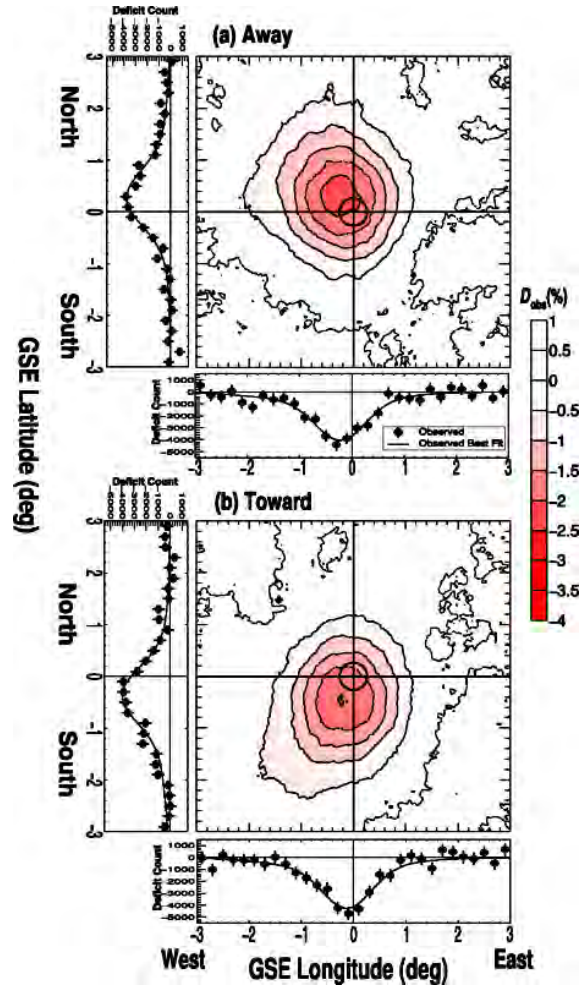
Fig. 27. From Ref. [2]. Two dimensional maps of D_{obs} in the away (a) and toward (b) sectors in 2000-2009. Each panel shows a two dimensional contour of Dobs deduced from AS events with $\Sigma\rho$FT 10 corresponding to the modal primary energy of ~3 TeV and Δd = 0.9°. In each panel, a small circle centered on the origin indicates the optical solar disk. The significance at the maximum deficit point derived with the Li-Ma formula in the away (toward) sector is -23.9 σ (-22.1 σ). The projections of D_{obs} on the horizontal and vertical axes are also attached to each panel.
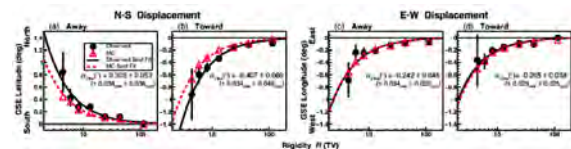
Fig. 28. From Ref. [2]. The rigidity dependence of the N-S [(a), (b)] and E-W [(c), (d)] displacements of the center of the Sun's shadow in away and toward sectors. Black solid circles and red open triangles in each panel show the observed and simulated displacements, respectively, each as a function of the rigidity (R) on the horizontal axis. The error bar of each solid circle indicates the statistical error. Black solid and red broken curves display the function of $\alpha/(R/10$ TV) best fitting to black solid circles and red open triangles, respectively. The best-fit parameter α to the observed data is indicated in each panel with systematic errors estimated from the systematic error of the primary energy in our analyses of the Moon's shadow.
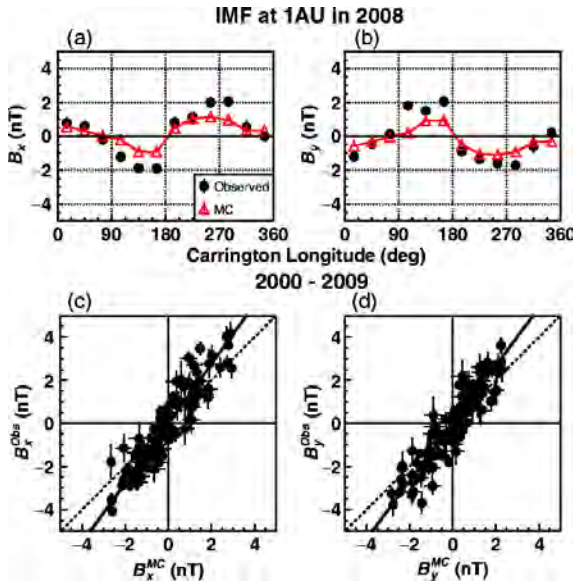
Fig. 29. From Ref. [2]. Comparison between the observed and simulated IMF components at Earth. Black solid circles (red open triangles) in the upper panels display the observed (simulated) B_x (a) and B_y (b), respectively, each as a function of the Carrington longitude. The lower panels show the correlations between the observed and simulated B_x (c) and B_y (d). The regression coefficient (slope of the black solid line) is significantly larger than 1 (slope of the dashed line).

Fig. 30. From Ref. [2]. The parameter α obtained from simulations by changing the multiplication factor f (see text). Red open triangles in (a) and (b) show α in the away and toward sectors, respectively, each as a function of f. The horizontal black line in each panel shows the observed α, while the vertical blue line indicates f deduced from the observed and simulated B_{IMF} at 1 AU. The shaded area in each panel indicates the 1σ region of f allowed by the observed α.

as is shown in Fig. 29(c) and 29(d). The correlation coefficients between the expected and observed magnetic field components are 0.93 and 0.92 for B_x and B_y, in the figure, respectively, which implies that high correlations, the regression coefficients are 1.38 ± 0.03 for B_x and 1.34 ± 0.03 for B_y, significantly larger than 1.00. This indicates that the underestimation of the expected B_x and B_y on the horizontal axes. The underestimation is observed every year, however, the magnitude of B_x or B_y changes in a positive correlation with the solar activity. Meanwhile, the obseved average B_z is negligible in both sectors as expected from the Parker-spiral IMF. The N-S shifts of the Sun's shadow center is relevant to the average magnetic field along the cosmic-ray trajectories between the Sun and the Earth, while B_x and B_y in Fig. 29 are the local field components at the Earth. Hence, it is suggested that the underestimation of the N-S shifts in Fig. 28 should be caused by the underestimation of the average field strength between the Sun and the Earth.

For the purpose quantitatively estimating the underestimation, the expedted magnetic field strength is simply multiplied by a constant factor f uniformly in the space outside the geomagnetic field. Then, we repeat the MC simulations by changing f and calculate $\alpha(f)$ best fit to each expected shift. We see $\alpha(f)$ represented by open triangles with linear best-fit curves, in Fig. 30, each as a function of f. From the intersection between the solid curves and solid lines showing α for the observed N-S shift in Fig. 28, f best fitting the observed shift is evaluated to be $1.54 \pm 0.21_{\text{stat}} \pm 0.20_{\text{sys}}$ ($1.62 \pm 0.15_{\text{stat}} \pm 0.22_{\text{sys}}$) in the "Away" ("Toward") sector. The result is consistent with the regression coefficient, 1.38 ± 0.03 (1.34 ± 0.03) in the "Away" ("Toward") sector, estimated from the expected

and observed IMF strengths at the Earth.

3. Other Activities

The emulsion-pouring facilities can meet the demands for making any kind of nuclear emulsion plates which are used for cosmic ray or accelerator experiments. The thermostatic emulsion-processing facilities are operated in order to develop nuclear emulsion plates or X-ray films. Using these facilities, it is also possible to make and develop emulsion pellicle in 600-micron thickness each. In this way, these facilities have been open to all the qualified scientists who want to carry out joint research programs successfully. Of recent, however, the shrinking demand for the facilities let us decide that we should suspend calls for joint research programs to utilize the emulsion-pouring facilities, starting from 2012.

Fig. 31. YAC2 set up at Yangbajing.

Fig. 32. The 5 shaded squares represent the constructed 5 MD pools.

4. Ongoing Plans

(1)Chemical composition of primary cosmic rays making the knee in the all-particle energy spectrum

We have measured the energy spectra of primary cosmic-ray protons, helium, all particles around the knee energy region. The main component responsible for making the knee structure in the all particle energy spectrum is heavier nuclei than helium. The next step is to identify the chemical component making the knee in the all particle energy spectrum. We have a plan to install an Yangbajing Air shower Core detector array (YAC) near the center of Tibet III to distinguish the chemical component making the knee. We completed construction of YAC2 (124 detectors over ∼500m^2 in area), as is shown in Fig. 31, and started data-taking in 2014. YAC2 aims at mainly studying the energy spectra of proton and helium components in the knee energy region.

(2) Gamma-ray astronomy in the 100 TeV region

For the purpose of detecting high-energy cosmic gamma rays with an air shower array, a large underground muon detecter[3] is very effective to reduce cosmic-ray background.

We decided to add a large (∼4,000 m^2 × 1.5m deep) underground (∼ 2.5 m soil+concrete overburden) water Cherenkov muon detector array (Tibet MD) under the present Tibet air shower array (Tibet AS). By Tibet AS + MD, we aim at background-free detection of celestial point-source gamma rays around 100 TeV with the world-best sensitivity and at locating the origins (PeVatrons) of cosmic rays accelerated up to the knee (PeV) energy region in the northern sky. The measurement of cut off energies in the energy spectra of such gamma rays in the 100 TeV region may contribute significantly to understanding of the cosmic- ray acceleration limit at SNRs. Search for extremely diffuse gamma-ray sources by Tibet AS + MD, for example, from the galactic plane or from the Cygnus region may be very intriguing as well. Above 100 TeV, the angular resolution of Tibet AS with 2-steradian wide field of view is 0.2° and the hadron rejection power of Tibet MD is 1/1000.
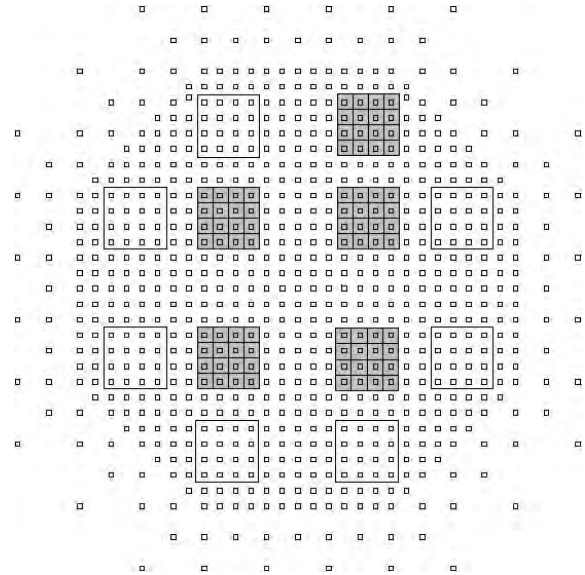
In addition to unknown point-like sources, we expect to detect established sources in the 100 TeV region: TeV J2032+4130, HESS J1837-069, Crab, MGRO J2019+37, MGRO J1908+06, Milagro candidate sources, Mrk421, Mrk501 are sufficiently detectable and Cas A, HESS J1834-087,LS I+63 303, IC443 and M87 are marginal.

Furthermore, our integral flux sensitivity to diffuse gamma rays will be very high. We hope that the diffuse gamma rays from the Cygnus region reported by the Milagro group and also diffuse gamma-rays from the galactic plane will be detected. Diffuse gamma-rays of extragalacitic origin may be an interesting target as well.

In 2007, a prototype 100-m^2 underground water Cherenkov muon detector was successfully constructed in Tibet to demonstrate the technical feasibility, cost estimate, validity of our Monte Carlo simulation. Data analyses demonstrate that our MC simulation reproduces real data quite reasonably.

In 2014, construction of the ∼4,000 m^2 MD, as is shown in Fig. 32, was successfully completed and data-taking started. We have accumulated approximately three-year data. One of the detector cell filled with water is demonstrated in Fig. 33.

Development of Monte Carlo simulation is under way for comparison with real data. Various analysis tools are also extensively being developed. According to the simulation, the sensitivity of the current configuration (Tibet AS + MD) is demonstrated in Fig. 34.

Bibliography

Papers in refereed journals

[1] "Multi-TeV Gamma-Ray Observation from the Crab Nebula Using the Tibet-III Air Shower Array Finely Tuned by the Cosmic-Ray Moon's Shadow", M. Amenomori *et al.*, Astrophysical Journal, **692** , 61-72 (2009).
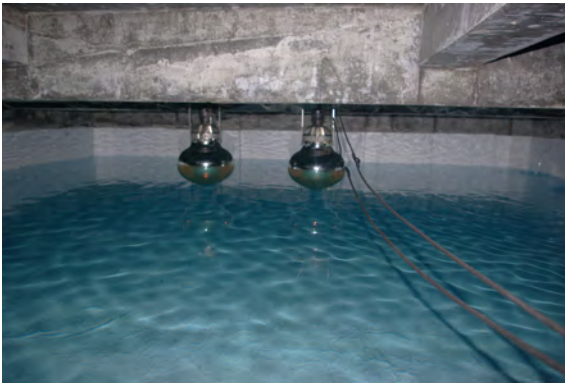
Fig. 33. PMTs mounted in a MD cell filled with water.
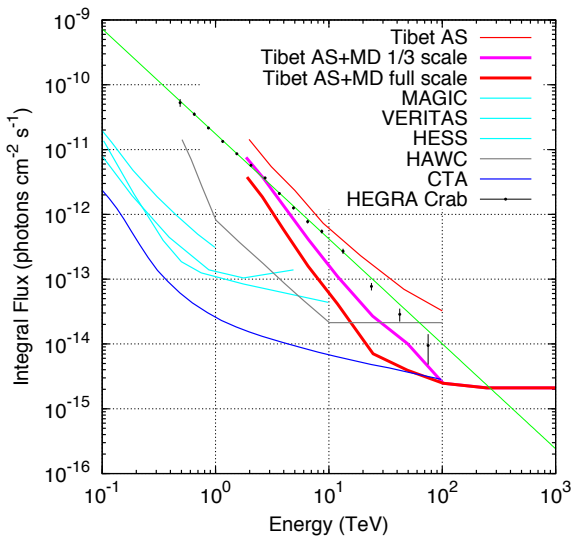
Fig. 34. Sensitivity to point-like gamma-ray sources with Tibet AS+MD (see,Tibet AS+MD 1/3 scale) by pink curve.

[2] "Evaluation of the Interplanetary Magnetic Field Strength Using the Cosmic-Ray Shadow of the Sun", M. Amenomori *et al.*, Physical Review Letters, **120** , 031101-1-7 (2018).

[3] "Exploration of a 100 TeV gamma-ray northern sky using the Tibet air-shower array combined with an underground water-Cherenkov muon-detector array", T.K. Sako *et al.*, Astroparticle Physics, **32** , 177-184 (2009).

The Tibet ASγ Collaboration

M. Amenomori,[1] X. J. Bi,[2] D. Chen,[3] T. L. Chen,[4] W. Y. Chen,[2] S. W. Cui,[5] Danzengluobu,[4] L. K. Ding,[2] C. F. Feng,[6] Zhaoyang Feng,[2] Z. Y. Feng,[7] Q. B. Gou,[2] Y. Q. Guo,[2] H. H. He,[2] Z. T. He,[5] K. Hibino,[8] N. Hotta,[9] Haibing Hu,[4] H. B. Hu,[2] J. Huang,[2] H. Y. Jia,[7] L. Jiang,[2] F. Kajino,[10] K. Kasahara,[11] Y. Katayose,[12] C. Kato,[13] K. Kawata,[14] M. Kozai,[13,15] Labaciren,[4] G. M. Le,[16] A. F. Li,[17,6,2] H. J. Li,[4] W. J. Li,[2,7] C. Liu,[2] J. S. Liu,[2] M. Y. Liu,[4] H. Lu,[2] X. R. Meng,[4] T. Miyazaki,[13] K. Mizutani,[11,18,*] K. Munakata,[13] T. Nakajima,[13] Y. Nakamura,[13] H. Nanjo,[1] M. Nishizawa,[19] T. Niwa,[13] M. Ohnishi,[14] I. Ohta,[20] S. Ozawa,[11] X. L. Qian,[6,2] X. B. Qu,[21] T. Saito,[22] T. Y. Saito,[23] M. Sakata,[10] T. K. Sako,[14,24] J. Shao,[2,6] M. Shibata,[12] A. Shiomi,[25] T. Shirai,[8] H. Sugimoto,[26] M. Takita,[14] Y. H. Tan,[2] N. Tateyama,[8] S. Torii,[11] H. Tsuchiya,[27] S. Udo,[8] H. Wang,[2] H. R. Wu,[2] L. Xue,[6] Y. Yamamoto,[10] K. Yamauchi,[12] Z. Yang,[2] A. F. Yuan,[4] T. Yuda,[14,*] L. M. Zhai,[3] H. M. Zhang,[2] J. L. Zhang,[2] X. Y. Zhang,[6] Y. Zhang,[2] Yi Zhang,[2] Ying Zhang,[2] Zhaxisangzhu,[4] X. X. Zhou[7]

[1]*Department of Physics, Hirosaki University, Hirosaki 036-8561, Japan*
[2]*Key Laboratory of Particle Astrophysics, Institute of High Energy Physics, Chinese Academy of Sciences, Beijing 100049, China*
[3]*National Astronomical Observatories, Chinese Academy of Sciences, Beijing 100012, China*
[4]*Department of Mathematics and Physics, Tibet University, Lhasa 850000, China*
[5]*Department of Physics, Hebei Normal University, Shijiazhuang 050016, China*
[6]*Department of Physics, Shandong University, Jinan 250100, China*
[7]*Institute of Modern Physics, SouthWest Jiaotong University, Chengdu 610031, China*
[8]*Faculty of Engineering, Kanagawa University, Yokohama 221-8686, Japan*
[9]*Faculty of Education, Utsunomiya University, Utsunomiya 321-8505, Japan*
[10]*Department of Physics, Konan University, Kobe 658-8501, Japan*
[11]*Research Institute for Science and Engineering, Waseda University, Tokyo 169-8555, Japan*
[12]*Faculty of Engineering, Yokohama National University, Yokohama 240-8501, Japan*
[13]*Department of Physics, Shinshu University, Matsumoto 390-8621, Japan*
[14]*Institute for Cosmic Ray Research, University of Tokyo, Kashiwa 277-8582, Japan*
[15]*Institute of Space and Astronomical Science, Japan Aerospace Exploration Agency (ISAS/JAXA), Sagamihara, Kanagawa 252-5210, Japan*
[16]*National Center for Space Weather, China Meteorological Administration, Beijing 100081, China*
[17]*School of Information Science and Engineering, Shandong Agriculture University, Taian 271018, China*
[18]*Saitama University, Saitama 338-8570, Japan*
[19]*National Institute of Informatics, Tokyo 101-8430, Japan*
[20]*Sakushin Gakuin University, Utsunomiya 321-3295, Japan*
[21]*College of Science, China University of Petroleum, Quingdao 266555, China*
[22]*Tokyo Metropolitan College of Industrial Technology, Tokyo 116-8523, Japan*
[23]*Max-Planck-Institut für Physik, München D-80805, Deutschland*
[24]*Escuela de Ciencias Física y Nanotechnologia, Yachay Tech, Imbabura 100115, Ecuador*
[25]*College of Industrial Technology, Nihon University,*

Narashino 275-8576, Japan
[26]*Shonan Institute of Technology, Fujisawa 251-8511, Japan*
[27]*Japan Atomic Energy Agency, Tokai-mura 319-1195, Japan*
*Deceased

ALPACA Project

[Spokesperson: M. Takita]

ICRR, The Univ. of Tokyo, Kashiawa, Chiba 277-8582

Cosmic rays are supposed to be accelerated up to the knee energy (PeV) region at supernova remnants (SNRs) in our galaxy. Therefore, we naturally expect gamma rays at 100 TeV energies, which originate in π^0 decays produced by the accelerated cosmic rays interacting with matter surrounding the SNRs. However, on-going experiments focus on measuring gamma rays in the 1 - 10 TeV region. The gamma-ray emission of electron origin might be highly suppressed above 10 TeV due to rapid decrease of inverse-Compton cross section by the Klein-Nishina effect as well as synchrotron radiation energy loss in the strong magnetic field around the SNRs. The detection and spectral measurement of gamma rays in the 100 TeV region from their celestial sources, together with multi-wavelength (radio, X-ray, gamma-ray) observations, will be an important experiment enabling us to discriminate between the two processes (cosmic-ray/electron origins), to locate the acceleration site (PeVatron which accelerate cosmic rays up to PeV energies) of cosmic rays and to verify the standard acceleration model of cosmic rays. Furthermore, diffuse gamma rays from the Fermi bubbles recently reported by the Fermi-LAT group and sub-PeV neutrino events[1] detected by IceCube suggests that the Fermi bubbles be a PeVatron candidate. Similarly, the energy spectrum of diffuse gamma rays from the extended region around the galactic center marginally measured by HESS up to approximately 10 TeV also strongly indicates existence of PeVatron[2], from which we expect to detect gamma rays at 100 TeV energies. Thus, a wide field-of-view gamma-ray imaging at 100 TeV energies in the southern sky, where the HESS sources, the Fermi bubbles and the galactic center are located within field of view, will be a key experiment.

1.   Experiment

The ALPACA[3],[4] (Andes Large area PArticle detector for Cosmic ray physics and Astrophysics) is a cosmic-ray experiment with a large surface air shower array with a large underground muon detector array The experimental site (approximately 500 m×500 m ∼250,000 m^2 in total area) is located on a flat high land called Cerro Estuqueria (4,740 m above sea level, 16°23' S, 68°08' W), as shown in Fig. 1, around Mount Chacaltaya, near La Paz, Bolivia. In some part in this area, our detectors will be set up.

We plan to set up a 5,400 m^2 underground (approximately one to a few meters) muon detector array (MD) and

Fig. 1. From Ref.[3]. Experimental site for the ALPACA experiment, Cerro Estuqueria (4,740 m above see level, 16°23' S, 68°08' W), near Mount Chacaltaya, in Bolivia.

an 83,000 m^2 air shower array (AS), shown in Fig. 2. MD of water Cherenkov type is composed of eight pools with each pool (approximately 1 m deep) containing twelve 56 m^2 unit detectors. AS is made up of 401 1 m^2 plastic scintillation counters at 15 m spacing.

The AS field of view is roughly 2 steradian. The expected angular resolution of AS is approximately 1 degree at 5 TeV and 0.2 degrees around 100 TeV for gamma rays. For 100 TeV gamma rays, the AS energy resolution is estimated to be ∼20-25 %. The hadron rejection power of MD is more than 99.9 % at 100 TeV, while keeping most of gamma-ray events. Long-term detector stability, angular resolution, pointing accuracy and energy scale can be calibrated by the cosmic-ray shadow in the Moon as well as by some of the bright stable TeV gamma ray sources in the southern sky.

2.   Covered Physics

Our reserch target is divided into four in ALPACA:

1. Measurement of high-energy (5 TeV – 1 PeV) cosmic gamma rays.

2. Measurement of cosmic ray energy spectra around the Knee energy region (100 TeV – 100 PeV)

3. Measurement of cosmic ray anisotropy > 5 TeV at sidereal time frame.

4. Measurement of the Sun shadow in cosmic rays > 5 TeV.

We aim at low-background detection of celestial gamma rays in the 100 TeV region with the world-best sensitivity (an order of magnitude better than any previous/existing experiments) and at locating the origins of cosmic rays accelerated up to the knee energy region in the southern sky. Presuming a Crab-like gamma-ray source extending up with power-law index -2.6 located in the southern sky, the ALPACA experiment is sensitive to the source with ∼15 % Crab intensity during one calendar year, as is demonstrated in Fig. 3.

The AS + MD in the southern hemisphere will be a
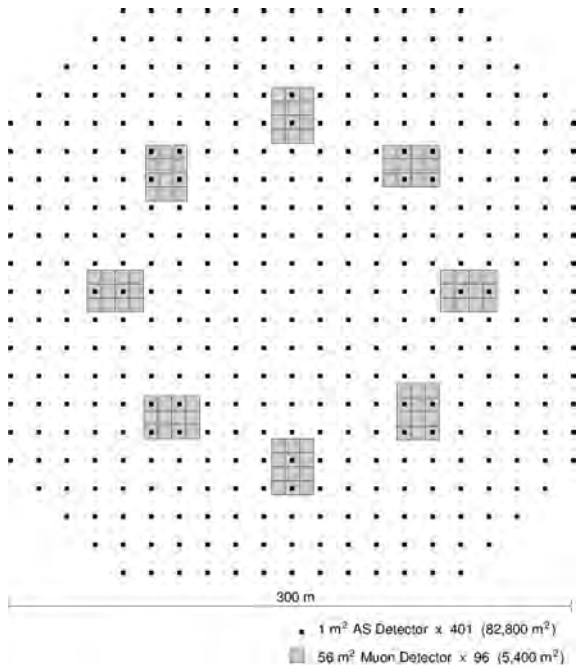
Fig. 2. From Ref.[3]. Schematic view of the ALPACA experiment. The small black squares indicate 401 1 m² plastic scintillarion detectors, forming an air shower array with 83,000 m² in area.The grey rectangles indicate eight underground muon detector pools, each of which contains twelve 56 m² muon detector units. The total area of the underground muon detector array is 5,400 m².
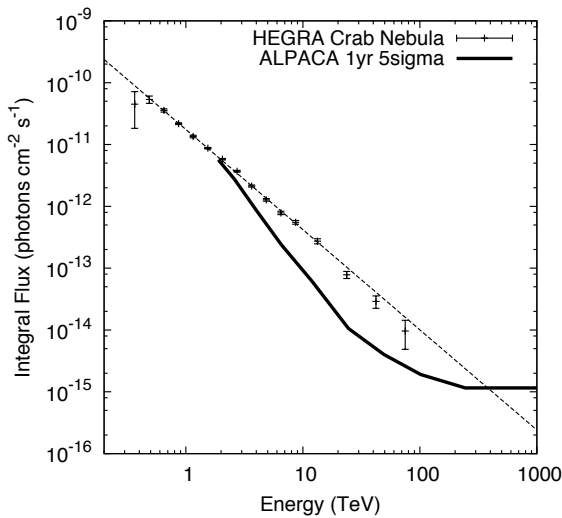
Fig. 3. From Ref.[3]. Sensitivity of ALPACA to high-energy gamma-ray point source. The experimental points are from Ref.[5]. The ALPACA sensitivity is evaluated from Ref.[6].

unique/complementary experiment to on-going experiments (FERMI, HESS, VERITAS, MAGIC, CALET, Tibet ASγ, HAWC) and future projects (LHAASO, CTA) in this field, which are either located in the northern hemisphere or aiming at gamma-ray astronomy below 10 TeV region, or having narrow field-of-view. Thus, the new energy window in the 100 TeV region observing gamma rays with wide field-of-view will be opened first in the southern sky by the ALPACA experiment. We expect to detect established more than a dozen of sources, i.e., young SNRs (SN1006, RX J1713.7-

3946, RX J0852.0-4622), Pulsar Wind Nebulae, the galactic center, etc) in the 100 TeV region, some of which may be cosmic-ray PeVatron candidates. Furthermore, our wide field-of-view sensitivity to diffuse gamma rays allows us to study extremely diffuse gamma-ray sources which are difficult to detect by IACTs. The diffuse gamma rays from the Fermi bubbles recently reported by the Fermi-LAT group may be clearly detected, if they extend up to the 100 TeV region. Similarly, detection of diffuse gamma rays above 100 TeV from extended region from the galactic center is promising, where the gamma-ray energy spectrum strongly suggests existence of PeVatron. Detection and spectral measurement of gamma rays in the 100 TeV region from these celestial sources, together with multi-wavelength (radio, X-ray, gamma-ray) observations, are key points enabling us to discriminate between the two processes (cosmic-ray/electron origins), to locate the acceleration site of cosmic rays and to examine the standard acceleration model of cosmic rays. In astronomical point of view, we pioneer the ultra-high energy (above 100 TeV) gamma-astronomy in the southern sky. Besides, gamma-ray emission from near-by extragalactic sources, e.g. M87, Cen A, gamma rays of dark matter origin, those from the Sun disk recently obseved by Fermi[7] may be interesting subjects.

We also aim at measuring energy spectra of proton, helium and iron components separately around the knee energy region with the new AS + MD. The standard cosmic-ray acceleration model at SNR predicts the knee energy of each nucleus component being proportional to Z (atomic number). We can discriminate proton and iron components by MD, as an iron nucleus produces approximately 2 times more muons than a proton with the same energy. Thus, the cosmic-ray acceleration scenario (SNR shock acceleration) will be verified by observing the linearly Z(atomic number)-dependent knee(=bent) positions of proton, helium, iron components around the knee energy region.

Precise cosmic-ray anisotropy measurement at sidereal time frame in the TeV energy region in the southern sky provides unique data for the community to understand the magnetic field structure in the heliosphere. The ALPACA experiment gives complementary data in the TeV region to those from IceCube above a few tens of TeV.

Furthermore, measurement of the Sun shadow in cosmic rays above the TeV energy region in the southern hemisphere also helps understand the modeling of the magnetic fields between the Sun and the Earth, complementary to the observations in the northern hemisphere.

3. ALPAQUITA

As a proto-type experiment, the ALPAQUITA[8] air shower array without MD, which is ~10 % of the ALPACA air shower array in area will be constructed at the experimental site, Cerro Estuqueria, in 2018.

Bibliography

Papers and references

[1] C. Lunardini et al., PRD, **92**, 021301-1-5 (2015).

[2] A. Abramoswski et al., Nature, **531**, 476 (2016).

[3] M. Takita for the ALPACA Collaboration, THE EURO-PEAN PHYSICAL JOURNAL, **145**, 01002-1-3, (2017).

[4] T. Asaba et al, Proc. of ICRC2017, ID=827, Busan, Korea, July 12-20, (2017).

[5] F. Aharonian et al., ApJ, **614**, 897 (2004)

[6] T. K. Sako et al., Astroparticle Physics, **32**, 177 (2009).

[7] C. Y. Kenny et al., arXiv:1508.06276v1.

[8] T. Asaba et al, Proc. of ICRC2017, ID=437, Busan, Korea, July 12-20, (2017).

The ALPACA Collaboration

T. Asaba,[a] K. Hibino,[b] N. Hotta,[c] M. Kataoka,[a] Y. Katayose,[a] C. Kato,[d] K. Kawata,[e] H. Kojima,[fg] R. Mayta,[h] P. Miranda,[i] K. Munakata,[d] Y. Nakamura,[d] M. Nishizawa,[j] S. Ogio,[h] M. Ohnishi,[e] A. Oshima,[k] M. Raljevich,[i] H. Rivera,[i] T. Saito,[l] T. Sako,[e] T. K. Sako,[me] T. Sasaki,[a] S. Shibata,[k] A. Shiomi,[n] M. Subieta,[i] M. Suzuki,[a] N. Tajima,[o] M. Takita,[e] Y. Tameda,[p] K. Tanaka,[q] R. Ticona,[i] H. Tsuchiya,[r] Y. Tsunesada,[h] S. Udo[b] and M. Wakamatsu[a] (The ALPACA Collaboration)

[a]Faculty of Engineering, Yokohama National University, Japan

[b]Faculty of Engineering, Kanagawa University, Japan

[c]Faculty of Education, Utsunomiya University, Japan

[d]Department of Physics, Shinshu University, Japan

[e]Institute for Cosmic Ray Research, The University of Tokyo, Japan

[f]Faculty of Engineering, Aichi Institute of Technology, Japan

[g]Chubu Innovative Astronomical Observatory, Japan

[h]Graduate School of Science, Osaka City University, Japan

[i]Instituto de Investigaciones Físicas, Universidad Mayor de San Andrés, Bolivia

[j]National Institute of Informatics, Japan

[k]College of Engineering, Chubu University, Japan

[l]Tokyo Metropolitan College of Industrial Technology, Japan

[m]Escuela de Ciencias Físicas y Nanotechnología, Yachay Tech, Ecuador

[n]College of Industrial Technology, Nihon University, Japan

[o]RIKEN, Japan

[p]Faculty of Engineering, Osaka Electro-Communication University, Japan

[q]Graduate School of Information Sciences, Hiroshima City University, Japan

[r]Japan Atomic Energy Agency, Japan

High Energy Astrophysics Group

[Spokesperson: K. Asano]
ICRR, The Univ. of Tokyo, Kashiwa, Chiba 277-8582

Overview

The high energy astrophysics group has been making theoretical and observational studies of violent astrophysical phenomena, in which nonthermal cosmic ray particles are being accelerated. Targets of the group's study include high energy astrophysical objects such as supernova remnants/pulsar magnetospheres, giant flares and repeating bursts of magnetars, a giant galactic explosion called 'Fermi bubble', black hole/neutron star merger events, fast radio bursts (FRBs), jets from active galactic nuclei (AGN), as well as mysterious gamma ray bursts (GRBs). Research works on the origin of ultra high energy cosmic rays (UHECRs) are also within the coverage of the group.

Research Topic 1: Temporal Evolution of Non-thermal Emission from Shock

Shock propagating in the interstellar medium (ISM) accelerates electrons and protons. The shock produced by an explosive phenomemon gradually decelerates. As the shock speed changes, the particle energy distribution in the post shock region also evolves with time. This leads to temporal evolution of emission from accelerated particles.

We numerically simulate the gamma-ray burst (GRB) afterglow emission with a one-zone time-dependent code. The temporal evolutions of the decelerating shocked shell and energy distributions of electrons and photons are consistently calculated. The photon spectrum and light curves for an observer are obtained taking into account the relativistic propagation of the shocked shell and the curvature of the emission surface. We find that the onset time of the afterglow is significantly earlier than the previous analytical estimate. The analytical formulae of the shock propagation and light curve for the radiative case are also different from our results. Our results show that even if the emission mechanism is switching from synchrotron to synchrotron self-Compton (SSC), the gamma-ray light curves can be a smooth power law, which agrees with the observed light curve and the late detection of a 32 GeV photon in GRB 130427A. We discuss the uncertainty of the model parameters obtained with the analytical formula, especially in connection with the closure relation between spectral index and decay index.

The binary neutron star merger detected as gravitational wave event GW170817 by the Advanced LIGO and Virgo accompanied a weak short gamma-ray burst, GRB 170817A (Abbott et al. 2017b). Furthermore, follow-up observations with UV, optical, and infrared telescopes found a kilonova emitting from the mildly relativistic ejecta as expected in advance. The ejected material will form a shock propagating in the circumbinary medium (CBM), and electromagnetic signals on a timescale of a few years have been predicted.
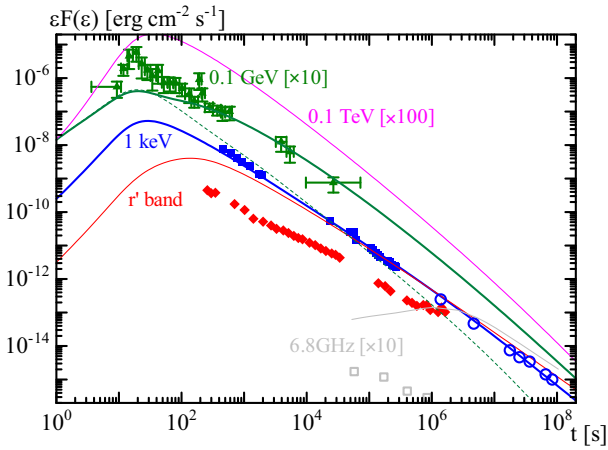
Fig. 1. Light curves for GRB 130427A. The model light curves are plotted with solid purple (0.1 TeV), green (0.1 GeV), blue (keV), red (r' band), and gray (6.8 GHz) lines. The thin black line represents a 0.1 GeV light curve with the same parameters but with a lower maximum energy of electrons. The green dashed line is also the 0.1 GeV light curve but switching off the SSC emission artificially.
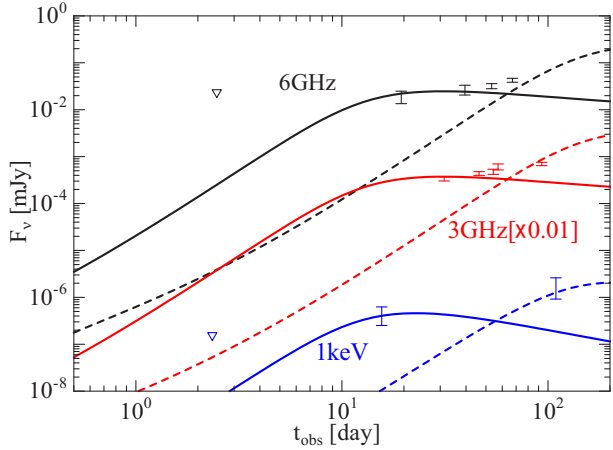
Fig. 2. Model light curves for 6 GHz (black), 3 GHz (red), and X-ray (1 keV; blue) for the afterglow of GW170817. The solid and dashed lines correspond to the emission due to the fast ($0.77c$) and slow ($0.59c$) ejecta, respectively.

This event provides a unique opportunity to investigate the particle acceleration at a mildly relativistic shock propagating in the circumbinary medium. We simulate the nonthermal emission from electrons accelerated by the shock induced by the kilonova ejecta with a time-dependent method. The initial velocity and mass of the ejecta in the simulations are obtained from the kilonova observations in GW170817. If the ambient density is high enough ($\geq 10^{-2}$ cm^{-3}), radio, optical/IR, and X-ray signals will be detected in a few years, though the off-axis short gamma-ray burst models, accounting for the X-ray/radio counterpart detected at .10 days after the merger, imply low ambient density. We also demonstrate that the additional low-mass ($10^{-5}\,M_\odot$) component with a velocity of 0.5c–0.8c can reproduce the early X-ray/radio counterpart (see Fig. 2). This alternative model allows a favorably high density to detect the nonthermal emission due to the kilonova

ejecta. Even for a low ambient density such as $\sim 10^{-3}$ cm^{-3}, depending on the microscopic parameters for the electron acceleration, we can expect a growth of radio flux of ~ 0.1 mJy in a few years.

Research Topic 2: Particle Acceleration by Turbulence in Pulsar Wind Nebulae

The relativistic outflow from a pulsar, called the pulsar wind, interacts with external SN ejecta and forms a termination shock. We observe non-thermal radiation from the particles accelerated at the termination shock as pulsar wind nebulae (PWNe). However, the spectrum of the "radio-emitting particles" is too hard to be explained by the diffusive shock acceleration. The other problem is that the radio-emitting particles dominate in the particle number inside PWNe and are higher than the estimated number of particles supplied by the pulsar wind.

We propose a possible resolution for the particle energy distribution in PWNe; the radio-emitting particles are not accelerated at the pulsar wind termination shock but are stochastically accelerated by turbulence inside PWNe. We upgrade our past one-zone spectral evolution model to include the energy diffusion, i.e., the stochastic acceleration, and apply the model to the Crab Nebula. A fairly simple form of the energy diffusion coefficient is assumed for this demonstrative study. The electron–positron energy distribution is evolved as shown in Fig. 3. The observed broadband spectrum and the decay of the radio flux are reproduced by tuning the amount of the particle injected to the stochastic acceleration process (Fig. 4). The acceleration timescale and the duration of the acceleration are required to be a few decades and a few hundred years, respectively. Our results imply that some unveiled mechanisms, such as back reaction to the turbulence, are required to make the energies of stochastically and shock-accelerated particles comparable.
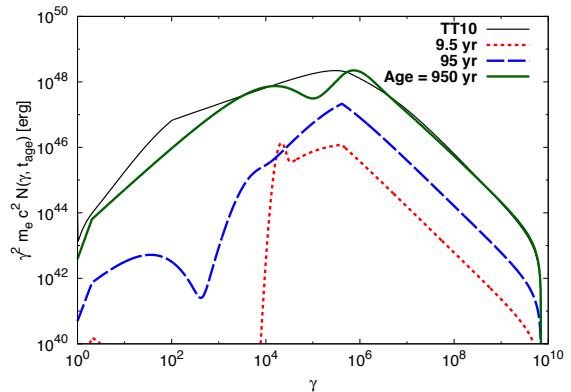
Fig. 3. Evolution of the particle spectra from 9.5 years (dotted red) to 950 years (thick green) in Crab PWN.

Research Topic 3: Spatial Profile of Pulsar Wind Nebulae

The observed radial profiles of the X-ray emission from PWNe have been claimed to contradict the standard 1D steady model. However, the 1D model has not been tested to simultaneously reproduce the volume-integrated spectrum and the ra-
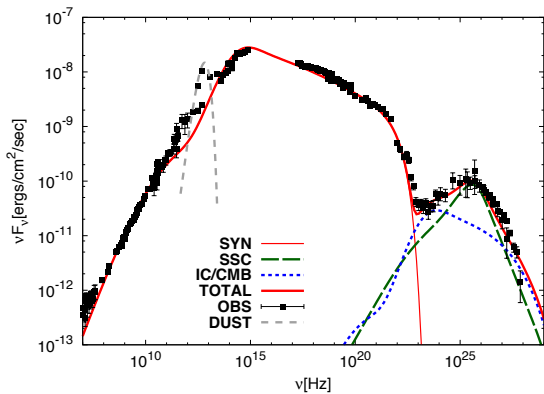
Fig. 4. The current photon spectrum with the observational data of Crab PWNe.

of PWNe.

Fig. 6. Radial profiles of the surface brightness in various frequencies for G21.5–0.9. The thick lines are the X-ray surface brightnesses for the broadband (red solid) and alternative (blue dashed) models.

dial profile of the surface brightness. We revisit the 1D steady model and apply it to PWNe 3C 58 and G21.5–0.9. We find that the parameters of the pulsar wind, the radius of the termination shock r_s, and magnetization σ greatly affect both the photon spectrum and radial profile of the emission. We have shown that the parameters constrained by the entire spectrum lead to an X-ray nebula smaller than the observed nebula (see red lines in Figs. 5 and 6).

Fig. 5. Entire photon spectra for G21.5–0.9. While the red solid lines represent the broadband models, the blue dashed lines represent the alternative models, in which the radio/IR data are disregarded

We have also tested the case that reproduces only the observations in X- and gamma-rays, ignoring the radio and optical components (see blue lines in Figs. 5 and 6). In this case, there are parameter sets that reproduce both the spectrum and emission profile, but the advection time to the edge of the nebula becomes much smaller than the age. Our detailed discussion clarifies that the standard 1D steady model has severe difficulty to simultaneously reproduce both the volume-integrated spectrum and the surface brightness. This implies that the model should be improved by taking into account extra physical processes such as spatial diffusion of particles. Additionally, we calculate the surface brightness profile of the radio, optical, and TeV gamma-rays. The future observations in these wavelengths are also important to probe the spatial distributions of the relativistic plasma and the magnetic field

Research Topic 4: Cosmological Evolution of Long Gamma-ray Burst Rate

The long GRBs may arise from the core collapse of massive stars. However, the derived redshift evolution of the GRB rate does not follow the star formation rate (SFR) especially at high redshift. The black hole (BH) and accretion disk system in the core collapse of massive stars has been considered to be the central engine of long GRBs. In order to make the accretion disk around the BH, the progenitor star just before the collapse must have a high angular momentum. However, massive stars generally lose a lot of angular momentum via the stellar wind mass loss.

We consider the binary merger progenitor model, a Wolf–Rayet star and a giant star system or two giant stars merge during the common-envelope (CE) phase. After the merger, a rapidly rotating naked helium star remains, because the star obtains a lot of angular momentum from the orbital angular momentum at the merger. Such a compact and highly rotating star is ideal to induce a GRB. With this scenario, we estimate the GRB rate by the population synthesis method with the metallicity evolution. It is easier for low metallicity binaries to become long GRB progenitors than those of solar metallicity due to the weak wind mass loss and the difference in the stellar evolution. In our results, the long GRB rate roughly agrees with the observed rate, and shows a similar behavior to the observed redshift evolution (see Fig. 7).

Research Topic 5: CALET Project

We have joined CALET, CALorimetric Electron Telescope, which is a mission for the Japanese Experiment Module-Exposed Facility (JEM-EF) on the International Space Station. The CALET mission aims at revealing unsolved problems in high energy phenomena of the Universe by carrying out accurate measurements of high energy spectra of electrons, gamma-rays and nuclei. HTV5 equipped with CALET was successfully launched by the H-IIB at 8:50:49 p.m. on August 19 2015 (JST) from the Tanegashima Space Center, and CALET is observeing cosmic rays without apparent problems.
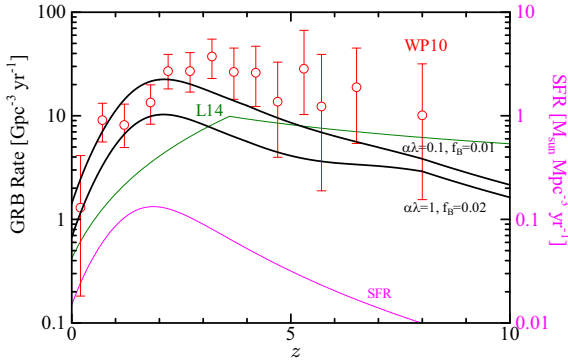
Fig. 7. Apparent long GRB rates in our model (black lines). The upper solid line is the result for the CE parameter $\alpha lambda = 0.1$ and the beaming factor $f_B = 0.01$, while the lower solid lines show the case of $\alpha lambda = 1$ and $f_B = 0.02$. The estimated rates from the Swift samples are also shown by the red data points (WP10) and the green line (L14). The purple line (see the right axis) shows the SFR.

Major scientific objectives are to search nearby cosmic ray sources and dark matter signatures by carrying out accurate measurements of cosmic ray electrons in 1 GeV – 20 TeV and gamma-rays in 4 GeV – 10 TeV. Since proton background is very large, high proton rejection power is mandatory for high energy electron and gamma-ray measurements. CALET has an imaging and deep calorimeter with 30 radiation length for electromagnetic particles, which provides high proton rejection and excellent energy resolution.

First CALET results of a cosmic-ray electron and positron spectrum from 10 GeV to 3 TeV is presented in Fig. 8. Nearly a half million electron and positron events are included in the analysis. The observed energy spectrum over 30 GeV can be fit with a single power law with a spectral index of -3.152 ± 0.016 (stat + syst). Possible structure observed above 100 GeV requires further investigation with increased statistics and refined data analysis.
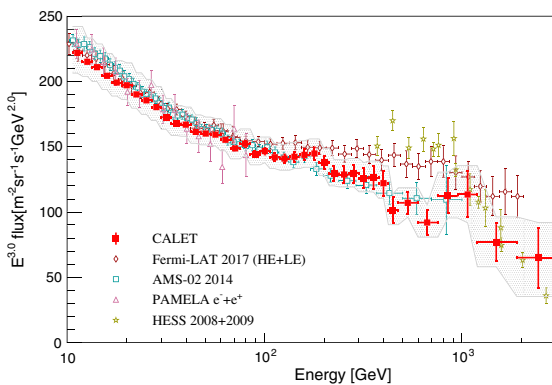
Fig. 8. Cosmic-ray all-electron spectrum measured by CALET from 10 GeV to 3 TeV, where systematic errors (not including the uncertainty on the energy scale) are drawn as a gray band. Also plotted are measurements in space and from ground-based experiments.

Bibliography
Papers in refereed journals

1. Wataru Ishizaki, Shuta J. Tanaka, Katsuaki Asano, Toshio Terasawa "Broadband Photon Spectrum and its Radial Profile of Pulsar Wind Nebulae", Astrophys. J., 838, 142(14pp) (2017).

2. F. Acero, R. Aloisio, J. Amans, et al. "Prospects for CTA Observations of the Young SNR RX J1713.7–3946", Astrophys. J., 840, 74(14pp) (2017).

3. Shuta J. Tanaka, Katsuaki Asano "On the Radio-emitting Particles of the Crab Nebula: Stochastic Acceleration Model", Astrophys. J., 841, 78(11pp) (2017).

4. Takuma Fukushima, Sho To, Katsuaki Asano, Yutaka Fujita "Temporal Evolution of the Gamma-ray Burst Afterglow Spectrum for an Observer: GeV–TeV Synchrotron Self-Compton Light Curve", Astrophys. J., 844, 92(11pp) (2017).

5. G. Abdellaoui, S. Abe, A. Acheli, et al. "Meteor Studies in the Framework of the JEM-EUSO Program", Planetary and Space Science, 143, 245-255 (2017).

6. Akinobu Miyamoto, Tomoya Kinugawa, Takashi Nakamura, Nobuyuki Kanda "How to Confirm the Existence of Population III Stars by Observations of Gravitational Waves", Phys. Rev. D, 96, 064025(10pp) (2017).

7. O. Adriani, Y. Akaike, K. Asano, et al. "Energy Spectrum of Cosmic-ray Electron and Positron from 10 GeV to 3 TeV Observed with the Calorimetric Electron Telescope on the International Space Station", Phys. Rev. Lett., 96, 064025(10pp) (2017).

8. Tomoya Kinugawa, Katsuaki Asano "Long Gamma-ray Burst Rate in the Binary Merger Progenitor Model", Astrophys. J., 849, L29(5pp) (2017).

9. B. P. Abbott, et al. "Multi-messenger Observations of a Binary Neutron Star Merger", Astrophys. J., 848, L12(59pp) (2017).

10. Katsuaki Asano, and Sho To "Subsequent Nonthermal Emission due to the Kilonova Ejecta in GW170817", Astrophys. J., 852, 105(5pp) (2018).

11. Y. Asaoka, S. Ozawa, S. Torii, O. Adriani, Y. Akaike, K. Asano, et al. "On-orbit Operations and Offline Data Processing of CALET onboard the ISS", Astropart. Phys., 100, 29-37 (2018).
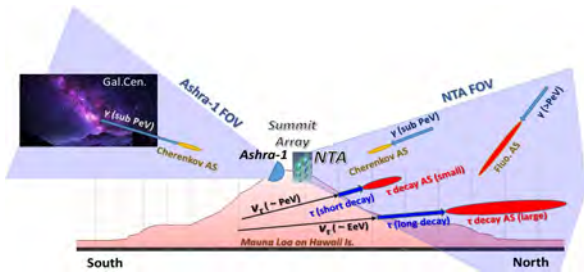
Fig. 9. Concept of imaging observation of PeV ν's, γ-rays, and nuclei with Ashra NTA summit array. Simultaneously 6 Ashra-1 light collectors watch our galactic bulge. NTA can check the coincidence with gamma-ray events by Ashra-1.
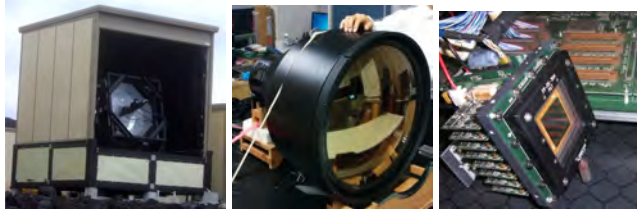
Fig. 10. Ashra-1 light collector (*left*), photo-electric lens imaging tube fabricated in 2016 (*center*) and local exposure/readout fine sensor with trigger (*right*).

Fig. 11. Effective area for ES-ν_τ's as changing energies with NTA in comparison with all flavor ν's with IceCube, IceCube Gen2, and ARA-100.
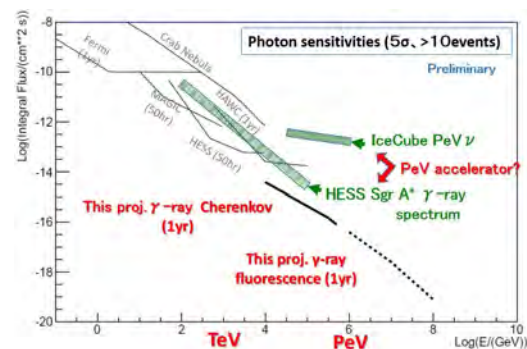
Fig. 12. Integral flux sensitivity limits (5σ or more than 10 events) for γ's versus the energies with NTA (1yr observation) and other detectors.

Other Activities

Ashra NTA

[Spokesperson: Makoto Sasaki]

ICRR, Univ. of Tokyo, Kashiwa, Chiba 277-8582

Combined detection of PeV ν's and γ's from an accelerator provides indispensable identification of the location and the physics mechanism i.e. $p + \gamma \to \Delta^+ \to \pi^0 + p$, $\pi^+ + n$; $p + \text{nucleus} \to \pi^{\pm,0} + X$, which can clearly reveal the long-standing unresolved origin(s) of cosmic rays. Recently several suggestive observations have been independently made [1, 2, 3]. Such a "multi-particle" paradigm [4] can be performed by Ashra NTA with the single unique detector system [5].

In 2002, Sasaki *et al.* presented the distinctive potential of the Earth-skimming tau ν (ES-ν_τ) technique [6]. It enjoys a large target mass by detecting air-showers (ASs) produced by τ decays in the air. The τ's, produced by ν_τ's that interact with the Earth matter, traverse, and emerge out of a mountain or the ground decaying and generating ASs. Adding to the good detection sensitivity for for ν's, the advantages are perfect shielding of cosmic ray secondaries, precise arrival direction determination, and negligible background from atmospheric ν's [7]. The Ashra detector can efficiently image AS Cherenkov (CE) and fluorescence (FL) light generated from ES-ν_τ and γ ASs in the effective volume of air in the field of view (FOV) (Figure 9).

The unique point is the resolution better than 0.1° yielding strong hadron rejection as selecting γ's both with FL and CE light.

The Ashra Phase 1 (Ashra-1) [8] light collector (LC) (Figure 10) achieves the total resolution of ~ 3 arcminutes covering 42° FOV. The key feature is the use of electrostatic rather than optical lenses to generate convergent beams with the 20 inch Photoelectric Lens Imaging tube (PLI) [9] (Figure 10) demagnifying to 1 inch at focal surface, enabling high resolution over a wide FOV [10]. The following trigger readout Photoelectric Image Pipeline (PIP) [11] can image and read out three independent phenomena on different time scales, i.e. AS CE emission (ns), AS FL (μ's), and starlight (s), without sacrificing the S/N ratios. The demonstration phase has been operated since 2008 at the Mauna Loa Observation Site at 3300 m asl. on Hawaii Island. With alert for GRB081203A given by SWIFT satellite, Ashra-1 succeeded in the first search for PeV-EeV ν_τ's originating from a GRB [12] with the ES-ν_τ technique setting stringent fluence limits. The updated ES-ν_τ limits from 1863 hours observation will be published soon.

Based on Ashra-1 performance, we have planned a new extension, i.e. Ashra Neutrino Telescope Array (NTA), which is an AS imaging ν and γ observation system for the aim/scientific goal [5]: *Clear Discovery and Identification of Nonthermal Hadronic Processes in the Universe, be it Galactic, Extragalatic, or Cosmogenic* .

By optimizing the layout of the NTA stations to enhance
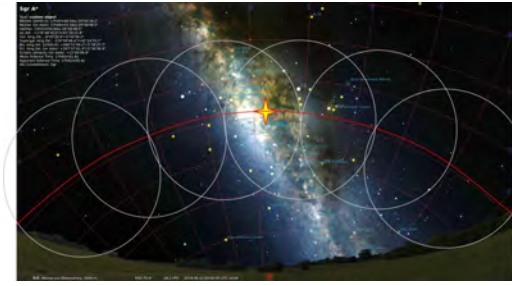
Fig. 13. Simulated southern sky at the Mauna Loa site at 0:00 on June 23, 2019. The cross star indicates the location of the galactic center(GC). The track of GC (arc) and the FOV of the rearranged Ashra-1 light collectors (circles) are also shown.

the detection sensitivity for ES-ν_τ's around 1 PeV from the detailed simulation studies [5, 7], four NTA stations are to be deployed on Mauna Loa at 3000 - 3500 m asl (NTA Summit Array), watching the air volume surrounding Mauna Loa including the surface of Mauna Loa, the largest volcano, to efficiently detect CE and FL light generated from τ ASs with both short and long decay lengths and γ ASs (Figure 9). The reconstructed AS images with fine resolution is powerful not only in the determination of point sources of PeV ν_τ's but also FL observation for γ ASs above PeV with the large effective area (Figure 9). Figure 11 shows NTA achieves the effective area similar with that of IceCube at 3 PeV and larger than it above 30 PeV by 10-100 times and larger than either of Ice-Cube Gen2 or ARA-100 in the 30 PeV-30 EeV region. The sensitivity for ES-ν_τ's with observing CE light can enhance more the discovery potential around PeV or lower energy region. Figure 12 shows the integral flux sensitivity limits for γ's with NTA for one year observation time comparing with those of other detectors. The unique combination among CE and FL observations for both ES-ν_τ's and γ with NTA will truly identify Pevatron(s) and open up new types of search for ν's and γ's in the wide energy range.

The combination between Ashra-1 light collectors and new NTA detector units is useful to realize the comprehensive observation both with TeV-PeV γ-rays and PeV ν's. Six Ashra-1 LCs will be realigned for the FOV centers to be on the arc of the Galactic Center trajectory maximizing the stereoscopic observation efficiency as shown in Figure 13. Therefore we will arrange the fields of view so that their fields of view overlap by half of the field of view of adjacent telescopes as shown in Figure 13. As a result, the total rate of the stereoscopic observation can be more than 70% of the trajectory in the sky. We estimate the annual observable time to be 1150 hours $\times \varepsilon_w$ during nights without moon in the south, where the weather efficiency $\varepsilon_w \sim 90\%$ according to the Ashra-1 experience, which is more than 50 times better than HESS achieved i.e. 227 hours for Sgr A* in 10 years [2].

The series of 6 Ashra-1 LC FOVs can monitor AS CE light of γ-rays arrived from the galactic bulge (GB) or central region. Another interest of the detection of γ-rays is the large zenith-angle method. The GB trajectory experiences the zenith angle larger than 50 degrees (70 degrees), which corresponds to the distance to the shower max larger than 9 km (26 km) and the threshold energies higher than 16 TeV (240 TeV). This situation is useful to check the cut-off energy

in the γ-ray spectrum in the galactic bulge or central region. Once the northward NTA units detect ν's from the same direction as γ-rays, we can discuss the physics of the occurrence of γ-rays and ν's more concretely than ever.

Bibliography

[1] M. Aartsen *et al.*, PRL **113**, 101101 (2014).

[2] HESS Collaboration, Nature **531**, 476 (2016).

[3] IceCube Collaboration, Science **361**, 147 (2018).

[4] M. Sasaki, ICRR2000 Sat. Sympo., 109 (2000).

[5] M. Sasaki, G. Hou, arXiv:1408.6244 (2014).

[6] M. Sasaki, *et al.*, Astropart. Phys. **19**, 37 (2003).

[7] Y. Asaoka, M. Sasaki, Astropart. Phys. **41**, 7 (2013).

[8] M. Sasaki, Prog. Theo. Phys. Suppl. **151**, 192 (2003).

[9] Y. Asaoka, M. Sasaki, NIMA **647**, 34 (2011).

[10] M. Sasaki, *et al.*, NIMA **492**, 49 (2002).

[11] M. Sasaki *et al.*, NIMA **501**, 359 (2003).

[12] Y. Aita *et al.*, ApJ Lett. **736**, L12 (2011).

γI Group

γI Project

γI Consortium
[Spokesperson : R.Enomoto]
Collaboration list:
ICRR, The University of Tokyo, Chiba, Japan; College of Science, Ibaraki University, Ibaraki, Japan; Faculty of Medical Engineering and Technology, Kitasato University, Kanagawa, Japan; Department of Radiological Sciences, Tokyo Metropolitan University, Tokyo, Japan; National Institute of Technology, Sendai College, Miyagi, Japan IPNS, High Energy Accelerator Research Organization, Ibaraki, Japan; National Cancer Center, East, Chiba, Japan;

Remote measurement of urinary radioactivity in ^{18}F-FDG PET patients using Compton camera for accurate evaluation of standardized uptake value

Generally, the evaluation method of treatment effects in solid tumors is based on systematic assessments of tumor size using morphological images obtained from X-ray computed tomography (CT).[1] Recently, with developments in chemotherapy, a new evaluation method using functional images obtained from positron emission tomography (PET)[2] as well as X-ray CT has been widely used. The most commonly used estimate of sugar metabolic activity in clinical ^{18}F-fluorodeoxyglucose (^{18}F-FDG)-PET is standardized uptake

value (SUV; semiquantitative evaluation).[3] SUV calculations are performed using corrections based on injected dose, weight, and other such parameters to estimate the capturing amount of FDG. During the uniform distribution of a tracer throughout the body, SUV equals 1 everywhere. Reportedly, SUV evaluation is imprecise and not easily replicable because SUV is affected by factors, such as patient stress,[4] uptake time,[5] blood glucose level,[6] region-of-interest (ROI) definition,[7] patient motion or breathing,[8] and urinary FDG excretion[1, 9, 10] Of note, several studies were conducted to improve SUV.[11, 12, 13, 14, 15, 16, 17, 18, 19]

Therefore, the injected dose warrants correction by assessment of urinary radioactivity in patients before PET to enhance the accuracy of FDG calculation. However, this is not typically performed in clinical practice owing to secondary effects of radioactive contamination in hospitals and radiation exposure risk to the attending staff. Therefore, we aimed to develop a remote method for the measurement of urinary radioactivity in FDG-PET patients. Urinary radioactivity was estimated in a toilet bowl using gamma-ray distribution obtained with a Compton camera (γI detector: [20, 21]) as shown in Fig.14.
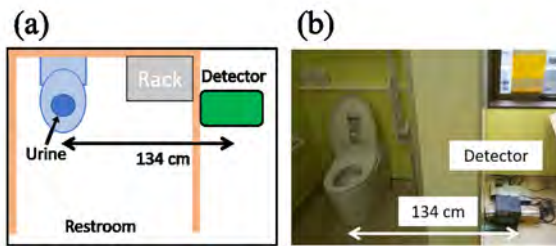
Fig. 14. a, Top, schematic of the measurement set-up of urinary radioactivity in the PET facility. b, photograph of the set-up. The detector was placed outside a toilet, with a wall between the toilet bowl and the detector, and the distance between the toilet bowl and the detector was 134 cm. The center of the toilet bowl was set in the forward direction of the detector.

The gamma-ray events from the toilet bowl per unit time (5 s) facilitated radioactivity calculation. The gamma-ray image is shown in Fig.15a. Between 0 and 40 MBq, deviation of our detector from the linearity for radioactivity was <8.3% as shown in Fig.15b. The accuracy of radioactive assessment was 11% for a 5-s measurement of 19.7 MBq ^{18}F-FDG.

Overall, we obtained 75 samples (45 males and 30 females). The results are shown in Fig.16. Our results revealed that excretion of FDG in the urine per person varied between 1.9% and 15.6% of the injected dose (range, 225–305 MBq).

Fig.17 indicates the typical time variation of radioactivity every 5 s. When a patient entered the toilet, radioactivity increased due to the effects from other parts of the body; however, the measurement value became stable after the patient left the toilet, and only urinary radioactivity was measured. If automatic flushing of the toilet is set in a manner that it flushes 1 min after closing the toilet lid, it then becomes unnecessary for the medical staff to manually flush the toilet after 1 min. Alternatively, the angular resolution of the detector could be improved by suppressing the contamination from other body parts of the patients. The detector should comprise smaller
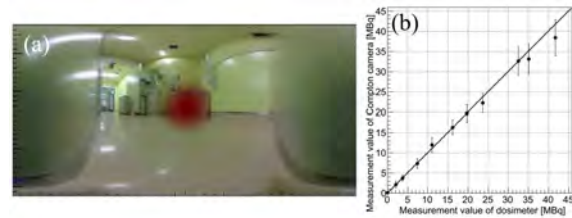
Fig. 15. a, The omnidirectional image of 511-keV gamma rays superimposed on the optical image of the restroom in the PET facility. ^{18}F-FDG at 19.7 MBq was placed in the toilet bowl. To superimpose it on the optical image, the red map was plotted only for over 75% of the peak value. The horizontal axis represents the azimuthal direction; the vertical axis represents the elevation direction. The measurement time was 5 s. The peak in the reconstructed image was consistent with the toilet bowl direction. b, linearity of our detector. The horizontal axis, the measurement values by dosimeter; the vertical axis, the average measurement values by a 5-s measurement by our detector where vertical bars for several points show 1 standard deviation; solid line, the line of y = x. The deviation from the linearity of our detector for radioactivity was within 8.3% between 0 and 40 MBq. The standard deviation of radioactive measurement was 11% by a 5-s measurement for 19.7 MBq ^{18}F-FDG.
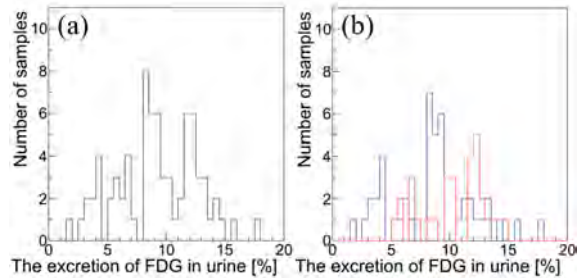
Fig. 16. The distributions of radioactivity in urine samples measured with our detector. a, the total radioactivity in the urine samples. The horizontal axis represents the excretion of radioactivity in the urine regarding injected radioactivity (range, 225-305 MBq); the vertical axis represents the number of samples. b, same as (a). Blue and red lines indicate male and female samples, respectively.

scintillators with the distance among the neighboring scintillators set to be constant.

Urinary radioactivity can be evaluated before PET using a Compton camera. SUV determination in clinical context could be enhanced by considering urinary radioactivity for corrections caused by individual differences in radioactivity. The detail can be found in [22]. We intend to improve the angular resolution of the detector to suppress the contamination from other body parts of patients for the system to be more automatic. Clinically, the determination of FDG can be improved to use urinary radioactivity for corrections.

Bibliography

[1] E A Eisenhauer, Therasse P, Bogaerts J, Schwartz L H, Sargent D, Ford R, Dancey J, Arbuck S, Gwyther S, Mooney M, Rubinstein L, Shankar L, Dodd L, Kaplan R, Lacombe D, Verweij J 2009 New response evaluation criteria in solid tumors: Revised RECIST guideline (version 1.1) Eur. J. Cancer. 45 228-47

56
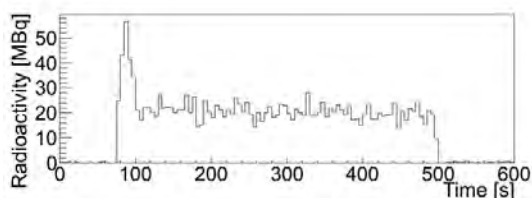
Fig. 17. A typical time variation of the radioactivity every 5 s. The horizontal axis represents the time; the vertical axis represents the measurement value of the Compton camera. When a patient entered the restroom, the radioactivity increased because of the contamination from other parts of the body. After the patient left the restroom, the measurement value stabilized, indicating that only radioactivity in the urine was assessed. The radioactivity was not detected in the durations before the patient entered the restroom and after the toilet was flushed.

[2] R L Wahl, Jacene H, Kasamon Y, Lodge MA From RE-CIST to PERCIST: Evolving considerations for PET response criteria in solid tumors 2009 J. Nucl. Med. 50 122S-150S

[3] J A Thie 2004 Understanding the standardized uptake value, its methods, and implications for usage J. Nucl. Med. 45 1431-4

[4] Y Sugawara, Zasadny K R, Neuhoff A W, Wahl R L 1999 Reevaluation of the standardized uptake value for FDG: variations with body weight and methods for correction. Radiology. 213 521-5

[5] V J Lowe, DeLong D M, Hoffman J M, Coleman R E 1995 Optimum scanning protocol for FDG-PET evaluation of pulmonary malignancy J. Nucl. Med. 36 883-7

[6] J F Eary, Mankoff D A 1998 Tumor metabolic rates in sarcoma using FDG PET J. Nucl. Med. 39 250-4

[7] M Westerterp, Pruim J, Oyen W, Hoekstra O, Paans A, Visser E, van Lanschot J, Sloof G, Boellaard R 2007 Quantification of FDG PET studies using standardized uptake values in multi-center trials: effects of image reconstruction, resolution and ROI definition parameters Eur. J. Nucl. Med. Mol. Imaging. 34 392-404

[8] Y E Erdi, Nehmeh S A, Pan T, Pevsner A, Rosenzweig K E, Mageras G, Yorke ED, Schoder H, Hsiao W, Squire OD, Vernon P, Ashman JB, Mostafavi H, Larson SM, Humm JL 2004 The CT motion quantitation of lung lesions and its impact on PET-measured SUVs J. Nucl. Med. 45 1287-92

[9] Bach-Gansmo T, Dybvik J, Adamsen T, Naum A 2012 Variation in urinary excretion of FDG, yet another uncertainty in quantitative PET Acta. Radiol. Short. Rep. 1 26-8

[10] R Boellaard 2009 Standards for PET image acquisition and quantitative data analysis J. Nucl. Med. 50 11S-20S

[11] K Miyashita, Takahashi N, Oka T, Asakawa S, Lee J, Shizukuishi K, Inoue T 2007 SUV correction for injection errors in FDG-PET examination Ann. Nucl. Med. 21 607-13

[12] M C Adams, Turkington T G, Wilson J M, Wong T Z 2010 A systematic review of the factors affecting accuracy of SUV measurements AJR. Am. J. Roentgenol. 195 310-20

[13] T H Jochimsen, Schulz J, Busse H, Werner P, Schaudinn A, Zeisig V, Kurch L, Seese A, Barthel H, Sattler B, Sabri O 2015 Lean body mass correction of standardized uptake value in simultaneous whole-body positron emission tomography and magnetic resonance imaging Phys. Med. Bio. 60 4651-64

[14] H Lindholm, Staaf J, Jacobsson H, Brolin F, Hatherly R, Crespo A S 2014 Repeatability of the maximum standard uptake value (SUVmax) in FDG PET Mol. Imaging. Radionucl. Ther. 23 16-20

[15] A K Tahari, Chien D, Azadi J R, Wahl R L 2014 Optimum lean body formulation for correction of standardized uptake value in PET imaging J. Nucl. Med. 55 1481-4

[16] F Gallivanone, Canevari C, Gianolli L, Salvatore C, Della Rosa P A, Gilardi M C, Castiglioni I 2013 A partial volume effect correction tailored for 18F-FDG-PET oncological studies Biomed. Res. Int. 780458

[17] B F Holman, Cuplov V, Miller L, Hutton B F, Maher T M, Groves A M, Thielemans K 2015 Improved correction for the tissue fraction effect in lung PET/CT imaging. Phys. Med. Bio. 60 7387-402

[18] R T H Leijienaar, Nalbantov G, Carvalho S, Elmpt WJCV, Troost EGC, Boellaard R, Aerts H J, Gillies R J, Lambin P 2015 The effect of SUV discretization in quantitative FDG-PET radiomics: the need for standardized methodology in tumor texture analysis Sci. Rep. 5 11075

[19] M A Lodge, Chaudhry M A, Wahl R L 2012 Noise considerations for PET quantification using maximum and peak standardized uptake value J. Nucl. Med. 53 1041-7

[20] Kagaya M, Katagiri H, Enomoto R, Hanafusa R, Hosokawa M, Itoh Y, et al. Development of a low-cost-high-sensitivity Compton camera using CsI(Tl) scintillators (γI). Nucl Instrum Methods Phys Res Sect A. 2015;804:25-32.

[21] Watanabe T, Enomoto R, Muraishi H, Katagiri H, Kagaya M, Fukushi M, et al. Development of an omnidirectional gamma-ray imaging Compton camera for low-radiation-level environmental monitoring. Jpn J Appl Phys. 2018;57;026401.

[22] Watanabe.T, Kano.D, Enomoto.R Muraishi.H et al., Remote measurement of urinary radioactivity of 18F-FDG

PET patients using Compton camera for improved ac-
curacy of the standardized uptake value. submitted for
publication.

ASTROPHYSICS AND GRAVITY DIVISION

Overview

Astrophysics and Gravity Division consists of Gravitational Wave Group, The Observational Cosmology Group, Primary Cosmic Ray Group and Theory Group.

The Gravitational Wave Group conducts experimental research of gravitational wave with researchers of gravitational wave experiment and theory in Japan. The main items are the construction of the large scale cryogenic interferometer(KAGRA) at Kamioka underground and the operation of CLIO. For this purpose, KAGRA observatory was established at the beginning of the fiscal year of 2016 to assist the construction of KAGRA gravitational wave telescope.

The Observational Cosmology Group studies the cosmic history based on deep multi-wavelength observations in collaboration with worldwide researchers. This group has started a new optical deep survey project with the wide-field imager of Hyper Suprime-Cam mounted on the Subaru telescope.

Theory Group conducts both theoretical study of the Universe and astroparticle physics.
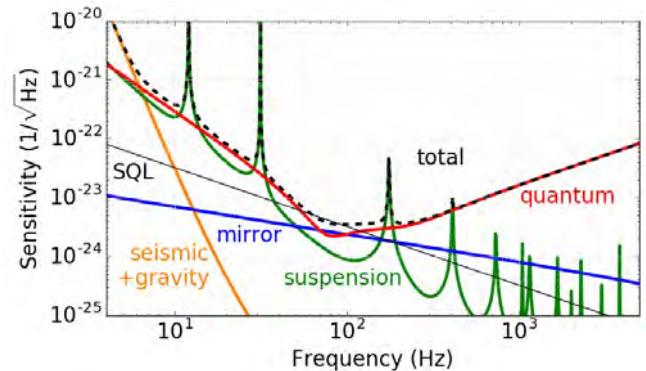
Fig. 1. Ultimate sensitivity limit of KAGRA. "SQL", "seismic+gravity", "mirror", "suspension", and "quantum" mean standard quantum limit, seismic noise and gravity gradient noise, mirror thermal noise, suspension thermal noise, and quantum noise, respectively. Observation range for an in-spiral and merger of neutron-star binary with the ultimate sensitivity limit of KAGRA is about 152 Mpc with the same definition of the observation range as LIGO and Virgo.

Gravitational Wave Group

KAGRA Project Status

[Spokesperson : Takashi UCHIYAMA]

ICRR, The Univ. of Tokyo, Hida, Gifu 506-1205

Overview

KAGRA, Large-scale Cryogenic Gravitational wave Telescope, aims at detecting gravitational waves and developing gravitational wave astronomy, which was established by the first detection of gravitational waves by LIGO. KAGRA employs a 3 km L-shaped laser interferometer with a cryogenic mirror system placed underground at Kamioka. The KAGRA development is divided into two stages: the initial KAGRA (iKAGRA) and baseline KAGRA (bKAGRA). The iKAGRA detector is a simple Michelson interferometer with a 2-Watt laser, room-temperature mirrors, and a simple seismic isolation system. We completed the iKAGRA detector with a test run in March 2016. Then we proceed to bKAGRA. The bKAGRA detector will employ a Resonant Sideband Extraction (RSE) interferometer with 180-Watt laser, cryogenic Sapphire mirrors, and an advanced Seismic Attenuation System (SAS). The bKAGRA detector should attain the sensitivity high enough for the detection of gravitational waves with the help of the high power laser and RSE interferometer to reduce the quantum noise, the cryogenic Sapphire mirrors to reduce the thermal noise, and the SAS to reduce the seismic noise. We plan to operate the cryogenic 3 km Michelson interferom-

eter as bKAGRA Phase 1 in May 2018, and then install other necessary bKAGRA subsystems to attain the target sensitivity.

Figure 1 shows the estimated ultimate sensitivity limits of KAGRA, where incoherent sum of the fundamental noise sources is assumed. Observation range for an in-spiral and merger of neutron-star binary with the ultimate sensitivity limit of KAGRA is about 152 Mpc with the same definition of the observation range as LIGO and Virgo.

In FY2017 we continued several installation and upgrade works toward the bKAGRA Phase 1. Fig. 2 and 3 shows optical layout of bKAGRA Phase 1 and vibration isolation systems, respectively. We have installed mirrors of PRM, PR2, BS, ETMX, and ETMY in FY2017. ETMX is the sapphire mirror. ETMY is a spare sapphire mirror. PRM, PR2, and BS are made of fused silica. PRM, PR2 have been suspended Type-Bp vibration isolation systems. We have also upgraded the vibration isolation system for PR3 from Type-Bp' to Type-Bp. BS has been suspended by a Type-B vibration isolation system. ETMX and ETMY have been suspended Type-A vibration isolation systems. ETMY has been cooled 18 K. All the optics needed for bKAGRA Phase 1 have been installed in FY2017 and we have successfully operated the cryogenic 3 km Michelson interferometer from 28 April of 2018.

There are progress reports in this annual report from Vacuum subgroup, Input Output Optics subgroup, Cryogenic subgroup, Digital control System subgroup, Analogue Electronics subgroup, Detector Characterization subgroup, Mirror subgroup, and Data analysis subgroup. Here shows some photos about vibration isolation systems and mirrors installed in FY2017.

We also enhanced the international collaborations with the
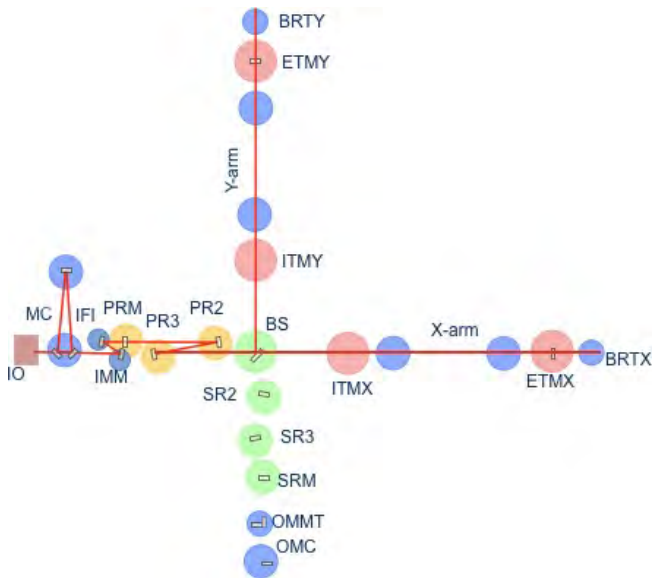
Fig. 2. Optical layout of bKAGRA Phase1. Purpose of bKAGRA Phase 1 is operation of the cryogenic 3 km Michelson interferometer. A laser source is placed in IO and laser beam is input into vacuum systems from MC. Each mirror is suspended by a vibration isolation system. Solid lines indicate laser beams.
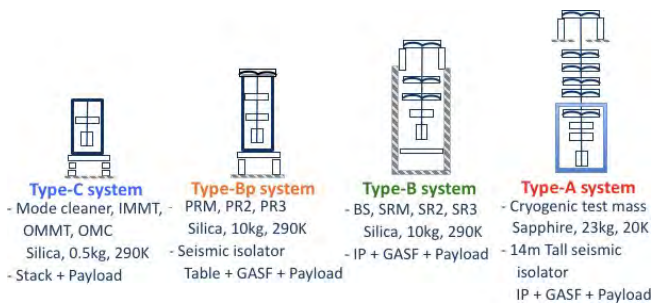
Fig. 3. KAGRA vibration isolation systems. KAGRA equips four kinds of vibration isolation systems such as Type-A, Type-B, Type-B, and Type-Bp. We have installed PRM, PR2, BS, ETMX, and ETMY in FY2017. We have also upgraded the vibration isolation system for PR3 from Type-Bp' to Type-Bp.

Einstein Telescope (ET) project, LIGO, Virgo, Korean and other Asian groups mainly based on the JSPS core-to-core program.

The rapidly progressing status of KAGAR were presented in many international conferences. Many papers about the progress of KAGRA were also published [1], [2], [3]. We also presented activities on our web-page.[4]

Bibliography

[1] "Construction of KAGRA: an underground gravitational-wave observatory", The KAGRA collaboration, Prog. Theor. Exp. Phys. 2018, 013F01 (2018)

[2] "Mirror actuation design for the interferometer control of the KAGRA gravitational wave telescope", Yuta Michimura, Tomofumi Shimoda, Takahiro Miyamoto, Ayaka Shoda, Koki Okutomi, Yoshinori Fujii, Hiroki Tanaka, Mark A. Barton, Ryutaro Takahashi, Yoichi Aso, Tomotada Akutsu, Masaki Ando, Yutaro Enomoto, Raffaele Flaminio, Kazuhiro Hayama, Eiichi Hirose, Yuki Inoue, Takaaki Kajita, Masahiro Kamiizumi, Seiji Kawamura, Keiko Kokeyama, Kentaro Komori, Rahul Kumar, Osamu Miyakawa, Koji Nagano, Masayuki Nakano, Naoko Ohishi, Ching Pin Ooi, Fabian Erasmo Pena Arellano, Yoshio Saito, Katsuhiko Shimode, Kentaro Somiya, Hiroki Takeda, Takayuki Tomaru, Takashi Uchiyama, Takafumi Ushiba, Kazuhiro Yamamoto, Takaaki Yokozawa, Hirotaka Yuzurihara, Classical and Quantum Gravity 34, 225001(2017)

[3] "Design and operation of a 1500-m laser strainmeter installed at underground site in Kamioka", Akito Araya, Akiteru Takamori, Wataru Morii, Kouseki Miyo, Masatake Ohashi, Kazuhiro Hayama, Takashi Uchiyama, Shinji Miyoki and Yoshio Saito, Earth, Planets and Space 69, 77 (2017)

[4] http://gwcenter.icrr.u-tokyo.ac.jp/en/

Fig. 4. Type-B vibration isolation system for beam splitter.
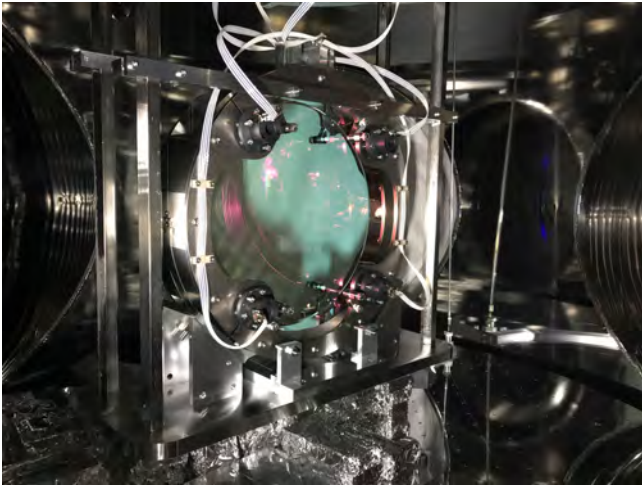
Fig. 5. Beam splitter suspended in a vacuum chamber.
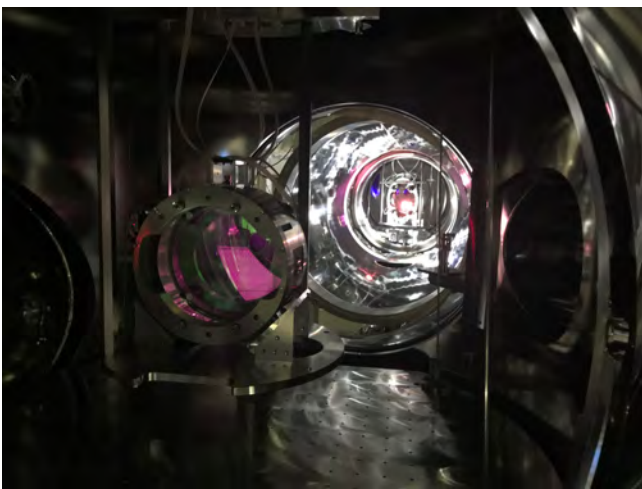
Fig. 6. PR2 mirror suspended in a vacuum chamber. There is beam splitter behind the PR2 mirror.

Fig. 7. A part of Type-A vibration isolation system.

Vacuum system for KAGRA

[Spokesperson : Takashi UCHIYAMA]

ICRR, The Univ. of Tokyo, Hida, Gifu 506-1205

We firstly pumped six vacuum chambers those are IFI, IMM, PRM, PR3, PR2, and BS and vacuum pressure achieved order of 10^{-5} Pa. We made control boxes for seven large gate valves those are GVmc between MCF and IFI, GVbsx between BS and IXC, GVitmx between IXA and the X-arm tube, GVetmx between the X-arm and EXA, GVbsy between BS and IYC, GVitmy between IYA and the Y-arm tube, and GVetmy between the Y-arm and EYA. The control boxes has open/close control buttons and indicators. The GVs will be controlled by remotely via KAGRA machine control system which has Programable Logic Circuits through the control boxes.

Input and Output Optics

[Spokesperson : Keiko KOKEYAMA]

ICRR, The Univ. of Tokyo, Hida, Gifu 506-1205

The input and output optics of KAGRA consists of the pre-stabilization system for the laser, auxiliary locking system, input optics chain, output optics chain, and detectors. The pre-stabilization system includes the frequency stabilization system, intensity stabilization system, pre-mode cleaner, and modulation system for the main interferometer. The auxiliary locking system includes the phase locking system for the green beam, the fiber system, and the locking system for the arm cavity. The input optics chain includes the input mode cleaner, input Faraday isolator, and input mode matching telescope. The output optics chain includes the output mode matching telescope, output Faraday isolator, and output mode cleaner. The detectors are for the symmetric, antisymmetric, and pick-off ports.

In the fiscal year 2017, major developments towards the bKAGRA phase-1 operation, planned in the spring of 2018, were conducted. The reference cavity was installed on the optical table where the laser source is placed. The reference cavity consists of a cylindrical spacer made of a ultra-low expansion glass, and two mirrors attached on the both side of the cylinder. The length of the cavity is extremely stable, therefore works as a frequency reference for the laser. The frequency of the laser was successfully stabilized, with an acousto-optic modulator installed as the frequency actuator. The input mode cleaner, which had been operating since the iKAGRA operation, was re-commissioned as a part of the frequency stabilization system. At the low frequency, the cavity length of the input mode cleaner is controlled by actuating

one of the three mode-cleaner mirrors, whereas the high frequency feedback is applied to the acousto-optic modulator for the frequency stabilization. The cross over frequency of the control was 3 Hz. In addition, the operation procedure was automated. For the intensity stabilization system, the main optical components were installed in the laser room, and the loop was closed. The performance of the intensity stabilization did not reach the goal stability yet, and to be improved in the next fiscal year.

There are two input mode-matching telescopes downstream of the input mode cleaner, where is upstream of the main interferometer. The input mode-matching telescopes are the curved mirrors, hung by the double pendulum, for matching the spacial mode of the beam to the main interferometer mode. The installation of the suspensions had been finished in the previous fiscal year, and in 2017, the fused silica mirrors (diameter 100 mm) were hung from the suspensions. The beam profile after the second input mode-matching telescope was measured, and the beam shape was confirmed to be as designed.

In November, KAGRA hosted the commissioning workshop in Kamioka. Researchers working at the LIGO and VIRGO sites visited the KAGRA site to accelerate the KAGRA experiments. The input and output optics group provided the topics to study in the workshop. Particularly, the noise couplings on the input mode cleaner and laser system were investigated, and useful findings and suggestions were obtained.

The interferometric tilt sensors, developed by Sogang university and tested at the KAGRA site in 2016, was upgraded. The upgraded tilt sensor can sense the orthogonal two degrees of freedom, pitch and yaw motions of a target. The performance was compared with the currently-used sensors (optical levers), and found to be as good in the lower frequencies, and to be better at the frequencies higher than 10 Hz. The tilt sensor was installed permanently at one of the mirrors of the input mode clear.

Cryogenic system
[Spokesperson : Takafumi USHIBA]
ICRR, The Univ. of Tokyo, Kashiwa, Chiba 277-8582

A key feature of KAGRA is to cool four sapphire mirrors, which are used for constitution of two arm cavity, to 20 K. Members working for a cryogenic system, which plays an important role for achieving this unique characteristics, is mainly constituted by that of ICRR, KEK, and the University of Toyama. Here, we summarize the activity of members of ICRR in FY 2017.

Cryogenic payload A KAGRA sapphire mirror is suspended by 9-stage suspension and its bottom 4 stages that include sapphire mirror is called cryogenic payload. The first cryogenic payload with a sapphire mirror was installed at Kamioka in November, 2017. Figure 8 shows the cryogenic payload installed at KAGRA site. This payload was cooled down after installation and reached about 18 K, which is below the target temperature of KAGRA, 20 K.

Performance evaluation of sensors and actuators was performed at the site after cooling. It was then confirmed that all sensors and actuators on the cryogenic payload worked even at cryogenic temperature. Damping feedback system for the suspension eigenmode was also implemented, which is significant to operate KAGRA as an interferometer.
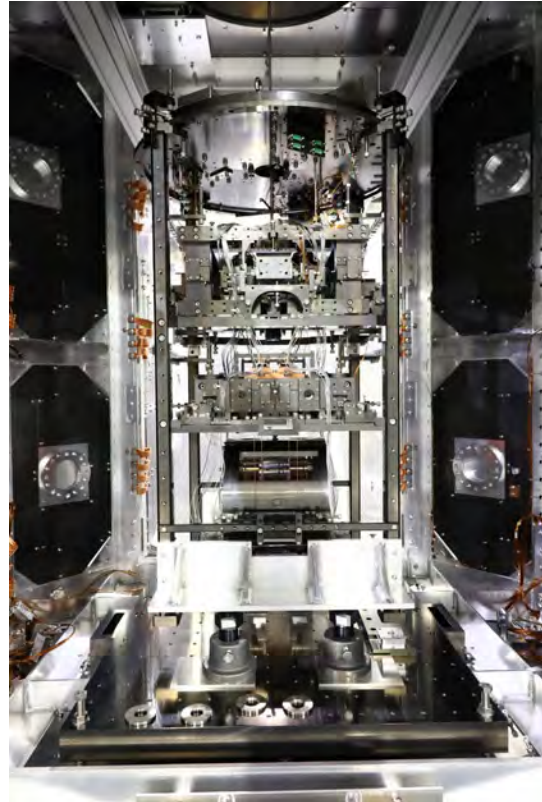
Fig. 8. Cryogenic payload installed into the cryostat at KAGRA site

Pure aluminum heat conductor In order to cool the mirror down to 20 K, it is necessary to utilize a high thermal-conductive heat conductor because at cryogenic temperature, especially below 100 K, thermal radiation becomes small and cannot cool the mirror effectively. However, these heat conductors can easily induce vibration that worsens the KAGRA sensitivity. It is therefore important for the heat conductor to have flexibility enough to reduce the vibration transmission via itself. To realize high thermal conductivity and flexibility, Stranded cables made of pure aluminum of 99.9998% (5N8 aluminum) are used for KAGRA heat conductor.

In FY 2017, thermal conductivity and flexibility measurement of the heat conductor were performed. Then, we measured a thermal conductivity of 1.85×10^4 W/m/K at 10 K, which is high sufficiently for applying to heat conductors for KAGRA. We also measured a spring constant of stranded heat conductor and compared with that of a single aluminum wire. Then, we confirmed that a spring constant of this stranded aluminum heat conductor is 43 times smaller than that of the single one.

Vibration measurement inside the cryostat   We should use huge cryostat (roughly saying, diameter and hight are both 4 m) in order to install the cryogenic payload and two-layer radiation shields. The resonant frequency of vibration modes of such huge structures is several tens of hertz, which covers KAGRA observation band. So, it is important to make a research for eigenmodes of the cryostat and implement their damping.

An interferometric accelerometer that can be fundamentally used even at the cryogenic temperature was developed. vibration level measurement inside the cryostat under the room temperature condition by using this accelerometer was performed. Then, we found that there is 1000 times lager vibration around 30 Hz than typical ground vibration of KAGRA site. We also confirmed vibration from the cryocoolers are slightly larger than the ground vibration as well.

Magnetic field measurement   Coil magnet actuators are adopted to control the cryogenic payload, and sapphire mirror has a small magnet on its AR side. So, fluctuation of magnetic field around the payload make some force to the mirror and shake it. Magnetic field of the earth is small enough but there are many devices around the payload such as cryocoolers, vacuum pump, and so on. So, magnetic field generated by these devices should be well studied.

We compared the magnetic field when the cryocoolers are working with that when they are not working. As a result, we confirmed that there are several periodic magnetic field generated by the cryocoolers. Further investigation for these magnetic field issue is promoting.

Master theses   Two Master thesis, *Vibration Analysis of Cryostat on KAGRA Site* and *A Study of the KAGRA Cryogenic Payload System and its Conduction Cooling*, were accepted in FY 2017.

Integrated DAQ/control system using real time computers

[Spokesperson : Osamu MIYAKAWA]

ICRR, The Univ. of Tokyo, Hida, Gifu 506-1205

KAGRA is a huge plant which consists of a large number of subsystems. We need to connect the subsystems and the KAGRA should work as a whole combined device for gravitational wave detections. We are using many computers running under the realtime operating system to establish feedback control loops among many subsystems. Synchronized computers connected by low latency network work as a controller for whole KAGRA detector. In the last fiscal year, we increased the number of the real-time computers with an increment of the number of vibration isolation systems and additional other subsystems. This system can remotely control the KAGRA detector from the surface building at Mozumi area. Nobody needs to enter into the mine once observations started, so we can operate KAGRA independently from the noise due to human activities.

On the other hand, manual controls by a person for such a complicated system can easily introduce mistakes. We have implemented a script management program called Guardian which manages many scripts for slow control loops. The Guardian can establish automatic operations for each subsystem. We actually implemented several automatic controls for some subsystems, for example moving states among a safe mode, a finding lock mode, and an operation mode or so.

Also we had a big progress on evaluating the accuracy of timing synchronization for each device. Computers and ADCs/DACs which require timing synchronizations are placed everywhere in the KAGRA laboratory area. It means that each device can be separated in 3 km long between the center area and the end area. Timing delays in the long distance have been actually measured and it was confirmed that the relative timing among all devices are compensated when the device is booted. It has an accuracy within 15ns independently from the distance. An absolute accuracy of the master clock has been also measured and it was found that the master clock has some delay from UTC by 187 ns±61 ns. This offset of 187 ns might be shifted in order of hundred micro seconds in the long term. As a result of these measurements, it was turned out that the current data acquisition system has a sufficient accuracy to determine the arrival time of the gravitational waves.

This control system also has an important role as a data acquisition system. We increased the size of local data storage to prepare for the full-scale observation, so that we can stably store a large amount of data. Recently we locked the Michelson interferometer with a low temperature mirror and performed one-week long operations. In the year between 2018-2019, we have many commissioning works for a full configuration interferometer. It is expected that this DAQ/control system performs a stable automatic operations for the KAGRA interferometer.

Core Optics for KAGRA

[Spokesperson : Eiichi HIROSE]

ICRR, The Univ. of Tokyo, Kashiwa, Chiba, 277-8582

MIR subgroup is responsible for all core optics in the KAGRA detectors in terms of both fabrication and quality assurance. As of the end of FY 2016, a set of Input Test Mass (ITM) mirrors was not completed. These are made of sapphire substrates that we developed with a domestic crystal maker introduced in the last report. Unfortunately, it took longer than expected to polish one of the crystals, which resulted in postponing coating process of the second substrate (ITMY). Characterization of the ITMX revealed that the round trip loss in the Fabry-Perot cavity should be about 50ppm. Which is half of the requirement (RTL < 100ppm), and we confirmed that all specifications were met to realize the cryogenic KAGRA gravitational wave detector. The detail of the sapphire mirrors will be reported elsewhere. As for fused silica mirrors,
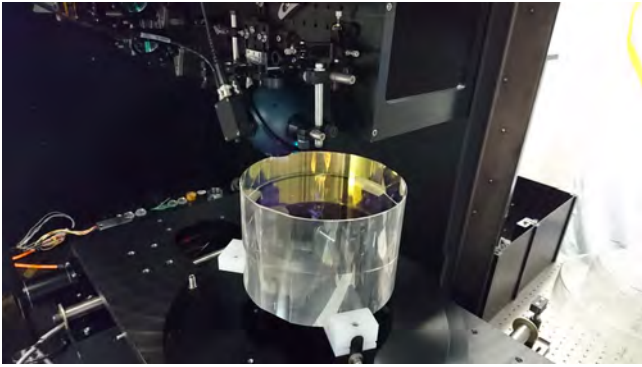
Fig. 9. Sapphire ETM mirror during characterization.

we completed OMMT1 & 2 and started preparation of new surrogate 2-inch Signal Recycling Mirrors (SRM, the original and final one with 250mm in diameter already exists) for early phase operation. As of June 2018, fabrication of both the ITMY and SRMs have been completed.

Data Analysis

[Spokesperson : Hideyuki Tagoshi]

ICRR, The Univ. of Tokyo, Kashiwa, Chiba, 277-8582

As a common data analysis tool for KAGRA, the data analysis library, KAGALI, has been developed. Currently, KAGALI is written mainly in C. In this year, the parameter estimation pipeline for compact binary coalescence signals based on the Markov Chain Monte Carlo method has been developed. This activity will be continued in 2018. A search pipeline for coalescing compact binaries has also been developed which were used to analyze iKAGRA data which was taken in March-April 2016. In this year, we summarized the results of the search for coalescing binary neutron stars in iKAGRA data. The search method is the standard matched filtering method supplemented with chi-square statistic. The mass range are set to $1 - 3M_\odot$ and spin-less TaylorF2 waveforms are used as templates. We derived an upper limit to the event rate. We also analyzed investigated the non-linear correlation between matched filter trigger time and auxiliary channel data of KAGRA detector. The method is based on Maximum Information Coefficient method. We found non-linear correlatin between the control signal of input mode cleaner and main interferometer data. This result will be used to reduce non-stationary noise of the detector.

We are also performing some projects by using open data of LIGO. We investigated optimal strategy for follow-up observations by 1-3 m class optical/infrared telescopes which target optical/infrared counterparts of gravitational wave events detected with two laser interferometric gravitational wave detectors. The probability maps of transient sources, such as coalescing neutron stars and/or black holes, determined by two laser interferometers generally spread widely. They include the distant region where it is difficult for small aperture telescopes to observe the optical/infrared counterparts. For small telescopes, there is a possibility that it is more advantageous to search for nearby region even if the probability inferred by two gravitational wave detectors is low. We showed that in the case of the first three events of advanced LIGO, the posterior probability map, derived by using a distance prior restricted to a nearby region, is different from that derived without such restriction. This suggests that the optimal strategy for small telescopes to perform follow-up observation of LIGO's first three events are different from what has been searched so far. We also show that, when the binary is nearly edge-on, it is possible that the true direction is not included in the 90% posterior probability region.

Ref. Tatsuya Narikawa, Masato Kaneyama, Hideyuki Tagoshi, Physical Review D 96, 084067 (2017).

Observational Cosmology Group

[Spokesperson : Yoshiaki Ono]

ICRR, The Univ. of Tokyo, Kashiwa, Chiba 277-8582

Great Optically Luminous Dropout Research Using Subaru HSC (GOLDRUSH). I. UV Luminosity Functions at $z \sim 4 - 7$ Derived with the Half-Million Dropouts on the 100 deg^2 Sky [1]

In collaboration with the members of The University of Tokyo, Carnegie Observatories, Mahidol University, Saint Mary's University, National Research Council Canada, Universite Lyon, Tohoku University, University of Geneva, National Astronomical Observatory of Japan, Academia Sinica, Ehime University, European Southern Observatory, Kavli Institute for the Physics and Mathematics of the Universe, and The Open University of Japan.

We study the UV luminosity functions (LFs) at $z \sim 4$, 5, 6, and 7 based on the deep large-area optical images taken by the Hyper Suprime-Cam (HSC) Subaru Strategic Program (SSP). On the 100 deg^2 sky of the HSC SSP data available to date, we make enormous samples consisting of a total of 579565 dropout candidates at $z \sim 4 - 7$ by the standard color selection technique, 358 out of which are spectroscopically confirmed by our follow-up spectroscopy and other studies. We obtain UV LFs at $z \sim 4 - 7$ that span a very wide UV luminosity range of $\sim 0.002 - 100 L^*_{UV}$ ($-26 < M_{UV} < -14$ mag) by combining LFs from our program and the ultra-deep *Hubble Space Telescope* legacy surveys. We derive three parameters of the best-fit Schechter function, ϕ^*, M^*_{UV}, and α, of the UV LFs in the magnitude range where the AGN contribution is negligible, and find that α and ϕ^* decrease from $z \sim 4$ to 7 with no significant evolution of M^*_{UV}. Because our HSC SSP data bridge the LFs of galaxies and AGNs with great statistical accuracy, we carefully investigate the bright end of the galaxy UV LFs that are estimated by the subtraction of the AGN contribution either aided with spectroscopy or the best-fit AGN UV LFs (Figure 10). We find that the bright end of the galaxy

UV LFs cannot be explained by the Schechter function fits at $> 2\sigma$ significance, and require either double power-law functions or modified Schechter functions that consider a magnification bias due to gravitational lensing.

Bibliography

[1] Ono, Y., Ouchi, M., Harikane, Y., Toshikawa, J., Rauch, M., Yuma, S., Sawicki, M., Shibuya, T., Shimasaku, K., Oguri, M., Willott, C., Akhlaghi, M., Akiyama, M., Coupon, J., Kashikawa, N., Komiyama, Y., Konno, A., Lin, L., Matsuoka, Y., Miyazaki, S., Nagao, T., Nakajima, K., Silverman, J., Tanaka, M., & Wang, S.-Y. 2018, Publications of the Astronomical Society of Japan, 70, S10

GOLDRUSH. II. Clustering of galaxies at $z \sim 4-6$ revealed with the half-million dropouts over the 100 deg^2 area corresponding to 1 Gpc^3 [2]

In collaboration with the members of Max Planck Institute for Astrophysics, University of California Berkeley, Kavli Institute for the Physics and Mathematics of the Universe, The University of Tokyo, Academia Sinica, Tohoku University, University of Geneva, National Astronomical Observatory of Japan, and Nagoya University.

We present clustering properties from 579492 Lyman-break galaxies (LBGs) at $z \sim 4-6$ over the 100 deg^2 sky (corresponding to a 1.4 Gpc^3 volume) identified in early data of the Hyper Suprime-Cam (HSC) Subaru Strategic Program survey. We derive angular correlation functions (ACFs) for the HSC LBGs with unprecedentedly high statistical accuracies at $z \sim 4-6$, and compare them with the halo occupation distribution (HOD) models. We clearly identify significant ACF excesses in $10 < \theta < 90$, the transition scale between one- and two-halo terms, suggestive of the existence of the non-linear halo bias effect. Combining the HOD models and previous clustering measurements of faint LBGs at $z \sim 4-7$, we investigate the dark matter halo mass (M_h) of the $z \sim 4-7$ LBGs and its correlation with various physical properties including the star formation rate (SFR), the stellar-to-halo mass ratio (SHMR), and the dark matter accretion rate ($\dot{M}_h$) over a wide mass range of $M_h/M_\odot = 4 \times 10^{10} - 4 \times 10^{12}$. We find that the SHMR increases from $z \sim 4$ to 7 by a factor of ~ 4 at $M_h \simeq 1 \times 10^{11} M_\odot$, while the SHMR shows no strong evolution in the similar redshift range at $M_h \simeq 1 \times 10^{12} M_\odot$. Interestingly, we identify a tight relation of SFR/$\dot{M}_h - M_h$ showing no significant evolution beyond 0.15 dex in this wide mass range over $z \sim 4-7$ (Figure 11). This weak evolution suggests that the SFR/$\dot{M}_h - M_h$ relation is a fundamental relation in high-redshift galaxy formation whose star formation activities are regulated by the dark matter mass assembly. Assuming this fundamental relation, we calculate the cosmic star formation rate densities (SFRDs) over $z = 0-10$ (a.k.a. the Madau–Lilly plot). The cosmic SFRD evolution based on the fundamental relation agrees with the one obtained by observations, suggesting that the cosmic SFRD increase from $z \sim 10$ to $4-2$ (decrease from $z \sim 4-2$ to 0) is mainly driven by the increase of the halo abundance (the decrease of the accretion rate).

Bibliography

[2] Harikane, Y., Ouchi, M., Ono, Y., Saito, S., Behroozi, P., More, S., Shimasaku, K., Toshikawa, J., Lin, Y.-T., Akiyama, M., Coupon, J., Komiyama, Y., Konno, A., Lin, S.-C., Miyazaki, S., Nishizawa, A. J., Shibuya, T., & Silverman, J., 2018, Publications of the Astronomical Society of Japan, 70, S11

GOLDRUSH. III. A Systematic Search of Protoclusters at $z \sim 4$ Based on the $> 100 \deg^2$ Area [3]

In collaboration with the members of National Astronomical Observatory of Japan, National Observatory of Brazil, The University of Tokyo, Academia Sinica, Ehime University, Tohoku University, and National Tsing Hua University.

We conduct a systematic search for galaxy protoclusters at $z \sim 3.8$ based on the latest internal data release (S16A) of the Hyper Suprime-Cam Subaru strategic program (HSC-SSP). In the Wide layer of the HSC-SSP, we investigate the large-scale projected sky distribution of g-dropout galaxies over an area of $121 \deg^2$, and identify 216 large-scale overdense regions ($> 4\sigma$ overdensity significance) that are likely protocluster candidates. Of these, 37 are located within 8 arcmin (3.4 physical Mpc) from other protocluster candidates of higher overdensity, and are expected to merge into a single massive structure by $z = 0$. Therefore, we find 179 unique protocluster candidates in our survey. A cosmological simulation that includes projection effects predicts that more than 76% of these candidates will evolve into galaxy clusters with halo masses of at least $10^{14} M_\odot$ by $z = 0$. The unprecedented size of our protocluster candidate catalog allows us to perform, for the first time, an angular clustering analysis of the systematic sample of protocluster candidates. We find a correlation length of $35.0 h^{-1}$ Mpc. The relation between correlation length and number density of $z \sim 3.8$ protocluster candidates is consistent with the prediction of the ΛCDM model, and the correlation length is similar to that of rich clusters in the local universe (Figure 12). This result suggests that our protocluster candidates are tracing similar spatial structures to those expected from the progenitors of rich clusters, and enhances the confidence that our method for identifying protoclusters at high redshifts is robust. In years to come, our protocluster search will be extended to the entire HSC-SSP Wide sky coverage of $\sim 1400 \deg^2$ to probe cluster formation over a wide redshift range of $z \sim 2-6$.

Bibliography

[3] Toshikawa, J., Uchiyama, H., Kashikawa, N., Ouchi, M., Overzier, R., Ono, Y., Harikane, Y., Ishikawa, S., Kodama, T., Matsuda, Y., Lin, Y.-T., Onoue, M., Tanaka, M., Nagao, T., Akiyama, M., Komiyama, Y., Goto, T., & Lee, C.-H. 2018, Publications of the Astronomical Society of Japan, 70, S12
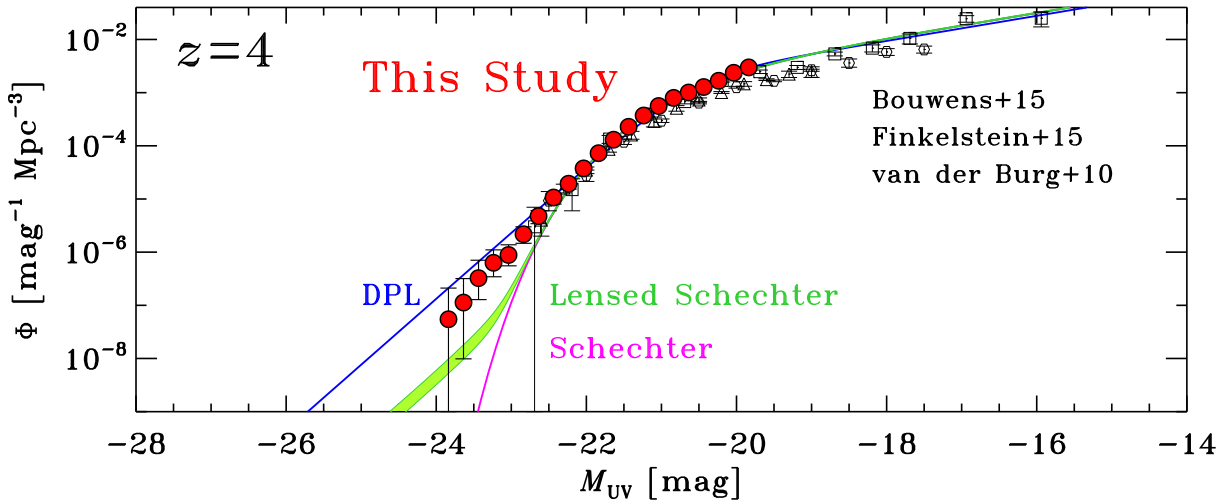
Fig. 10. Rest-frame UV luminosity functions of galaxies that take into account quasar contamination correction at $z \sim 4$. The green shaded region corresponds to the best-fit Schechter functions that take into account the effect of gravitational lensing with the two cases of the optical depth estimates. The magenta curve is the best-fit Schechter function without considering the lensing effect and the blue curve is the best-fit DPL function. For comparison, we also show previous results for galaxies taken from the literature.
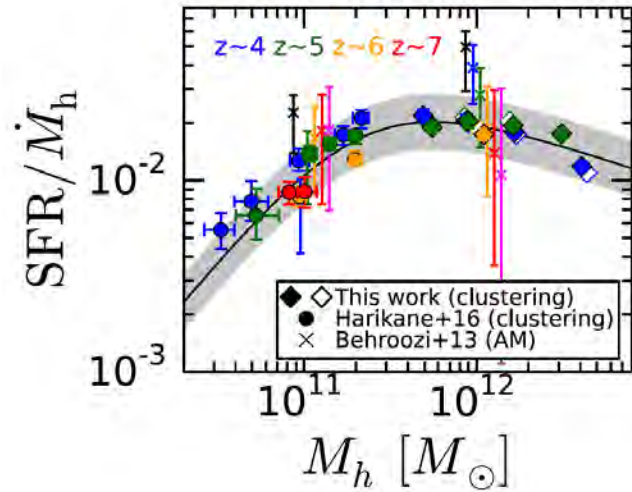
Fig. 11. SFR/$\dot{M}_h$ as a function of the halo mass. The filled blue, green, orange, and red diamonds (circles) denote the ratio of the extinction-corrected SFR to the dark matter accretion rate at $z \sim 4$, 5, 6, and 7, respectively, in this work The statistical errors for our data are smaller than the symbols (diamonds). We also plot SFR/$\dot{M}_h$ at $z \sim 0$, 4, 5, 6, 7, and 8 in the literature with the black, blue, green, orange, red, and magenta crosses for comparison. The black solid curve is the fitting formula for the SFR/$\dot{M}_h - M_h$ relation for $z \sim 4 - 7$, and the gray shaded region represents the typical scatter (0.15 dex) of the data points. For reference, we also plot the results for the subsamples with the magnitude cut of $m_{UV}^{cut} = 20.0$ mag with the open diamonds.

Fig. 12. Comoving number density, n, versus correlation length, r_0, for protocluster candidates at $z \sim 3.8$ (red star, this study), distant clusters at $z \sim 1.5$ (blue circles), local clusters at $z = 0.1 - 0.3$ (black squares), and X-ray-selected clusters at $z < 0.2$ (green triangles). The dashed line indicates the expected relation between n and r_0 from ΛCDM.

Systematic Identification of LAEs for Visible Exploration and Reionization Research Using Subaru HSC (SILVERRUSH). I. Program Strategy and Clustering Properties of ~ 2000 ***Lyα Emitters at*** $z = 6 - 7$ ***over the*** $0.3 - 0.5$ ***Gpc^2 Survey Area*** [4]

In collaboration with the members of The University of Tokyo, The Open University of Japan, Kure College, Ehime University, Osaka Sangyo University, University of Tsukuba, Nagoya University, National Astronomical Observatory of Japan, European Southern Observatory, University of Hyogo, and Academia Sinica.

We present the SILVERRUSH program strategy and clustering properties investigated with ~ 2000 Lyα emitters at $z = 5.7$ and 6.6 found in the early data of the Hyper Suprime-Cam (HSC) Subaru Strategic Program survey exploiting the carefully designed narrowband filters (Figure 13). We derive angular correlation functions with the unprecedentedly large samples of LAEs at $z = 6 - 7$ over the large total area of $14 - 21$ deg^2 corresponding to $0.3 - 0.5$ comoving Gpc^2. We obtain the average large-scale bias values of $b_{avg} = 4.1 \pm 0.2$ (4.5 ± 0.6) at $z = 5.7$ $(z = 6.6)$ for $\gtrsim L^*$ LAEs, indicating a weak evolution of LAE clustering from $z = 5.7$ to 6.6. We compare the LAE clustering results with two independent theoretical models that suggest an increase of an LAE clustering signal by the patchy ionized bubbles at the epoch of reionization (EoR), and estimate the neutral hydrogen frac-

tion to be $x_{\mathrm{HI}} = 0.15^{+0.15}_{-0.15}$ at $z = 6.6$. Based on the halo occupation distribution models, we find that the $\gtrsim L^*$ LAEs are hosted by the dark-matter halos with an average mass of $\log(\langle M_{\mathrm{h}} \rangle / M_\odot) = 11.1^{+0.2}_{-0.4}$ $(10.8^{+0.3}_{-0.5})$ at $z = 5.7$ (6.6) with a Lyα duty cycle of 1 % or less, where the results of $z = 6.6$ LAEs may be slightly biased, due to the increase of the clustering signal at the EoR. Our clustering analysis reveals the low-mass nature of $\gtrsim L^*$ LAEs at $z = 6 - 7$, and that these LAEs probably evolve into massive super-L^* galaxies in the present-day universe.

Bibliography

[4] Ouchi, M., Harikane, Y., Shibuya, T., Shimasaku, K., Taniguchi, Y., Konno, A., Kobayashi, M., Kajisawa, M., Nagao, T., Ono, Y., Inoue, A. K., Umemura, M., Mori, M., Hasegawa, K., Higuchi, R., Komiyama, Y., Matsuda, Y., Nakajima, K., Saito, T., & Wang, S.-Y. 2018, Publications of the Astronomical Society of Japan, 70, S13

SILVERRUSH. II. First Catalogs and Properties of $\sim$ 2000 Lyα Emitters and Blobs at $z \sim 6 - 7$ Identified over the $14 - 21$ deg^2 Sky [5]

In collaboration with the members of The University of Tokyo, The Open University of Japan, Kure College, Ehime University, National Astronomical Observatory of Japan, National Tsing Hua University, European Southern Observatory, Academia Sinica, and Mahidol University.

We present an unprecedentedly large catalog consisting of $2230 \gtrsim L^*$ Lyα emitters (LAEs) at $z = 5.7$ and 6.6 on the 13.8 and 21.2 deg^2 sky, respectively, that are identified by the SILVERRUSH program with the first narrowband imaging data of the Hyper Suprime-Cam (HSC) survey. We confirm that the LAE catalog is reliable on the basis of 96 LAEs whose spectroscopic redshifts are already determined by this program and the previous studies. This catalogue is also available online. Based on this catalogue, we derive the rest-frame Lyα equivalent-width distributions of LAEs at $z \simeq 5.7 - 6.6$ that are reasonably explained by the exponential profiles with the scale lengths of $\simeq 120 - 170 \,\text{Å}$, showing no significant evolution from $z \simeq 5.7$ to $z \simeq 6.6$. We find that 275 LAEs with large equivalent widths (LEWs) of > 240 Å are candidates of young-metal poor galaxies and AGNs. We also find that the fraction of LEW LAEs to all LAEs is 4% and 21% at $z \simeq 5.7$ and $z \simeq 6.6$, respectively. Our LAE catalog includes 11 Lyα blobs (LABs) that are LAEs with spatially extended Lyα emission whose profile is clearly distinguished from those of stellar objects at the $\gtrsim 3\sigma$ level. The number density of the LABs at $z = 6 - 7$ is $\sim 10^{-7} - 10^{-6}$ Mpc^{-3}, being $\sim 10 - 100$ times lower than those claimed for LABs at $z \simeq 2 - 3$, suggestive of disappearing LABs at $z \gtrsim 6$, albeit with the different selection methods and criteria for the low and high-z LABs (Figure 14).

Bibliography

[5] Shibuya, T., Ouchi, M., Konno, A., Higuchi, R., Harikane, Y., Ono, Y., Shimasaku, K., Taniguchi, Y.,

Kobayashi, M. A. R., Kajisawa, M., Nagao, T., Furusawa, H., Goto, T., Kashikawa, N., Komiyama, Y., Kusakabe, H., Lee, C.-H., Momose, R., Nakajima, K., Tanaka, M., Wang, S.-Y., & Yuma, S. 2018, Publications of the Astronomical Society of Japan, 70, S14

SILVERRUSH. III. Deep Optical and Near-Infrared Spectroscopy for Lyα and UV-Nebular Lines of Bright Lyα Emitters at $z = 6 - 7$ [6]

In collaboration with the members of The University of Tokyo, Carnegie Observatories, Mahidol University, National Astronomical Observatory of Japan, University of California Santa Barbara, The Open University of Japan, Kure College, Ehime University, National Tsing Hua University, European Southern Observatory, and Academia Sinica.

We present Lyα and UV-nebular emission line properties of bright Lyα emitters (LAEs) at $z = 6 - 7$ with a luminosity of $\log L_{\mathrm{Ly}\alpha}/[\text{erg s}^{-1}] = 43 - 44$ identified in the 21-deg^2 area of the SILVERRUSH early sample developed with the Subaru Hyper Suprime-Cam (HSC) survey data. Our optical spectroscopy newly confirms 21 bright LAEs with clear Lyα emission, and contributes to making a spectroscopic sample of 96 LAEs at $z = 6 - 7$ in SILVERRUSH. From the spectroscopic sample, we select 7 remarkable LAEs as bright as Himiko and CR7 objects, and perform deep Keck/MOSFIRE and Subaru/nuMOIRCS near-infrared spectroscopy reaching the 3σ-flux limit of $\sim 2 \times 10^{-18}$ erg s^{-1} for the UV-nebular emission lines of He II$\lambda 1640$, C IV$\lambda\lambda 1548, 1550$, and O III]$\lambda\lambda 1661, 1666$. Except for one tentative detection of C IV, we find no strong UV-nebular lines down to the flux limit, placing the upper limits of the rest-frame equivalent widths (EW_0) of $\sim 2 - 4$ Å for C IV, He II, and O III] lines. We also investigate the VLT/X-SHOOTER spectrum of CR7 whose 6σ detection of He II is claimed by Sobral et al. Although two individuals and the ESO-archive service carefully re-analyze the X-SHOOTER data that are used in the study of Sobral et al., no He II signal of CR7 is detected, supportive of weak UV-nebular lines of the bright LAEs even for CR7. The spectral properties of these bright LAEs are thus clearly different from those of faint dropouts at $z \sim 7$ that have strong UV-nebular lines shown in the various studies. Comparing these bright LAEs and the faint dropouts, we find anti-correlations between the UV-nebular line EW_0 and UV-continuum luminosity, which are similar to those found at $z \sim 2 - 3$ (Figure 15).

Bibliography

[6] Shibuya, T., Ouchi, M., Harikane, Y., Rauch, M., Ono, Y., Mukae, S., Higuchi, R., Kojima, T., Yuma, S., Lee, C.-H., Furusawa, H., Konno, A., Martin, C. L., Shimasaku, K., Taniguchi, Y., Kobayashi, M. A. R., Kajisawa, M., Nagao, T., Goto, T., Kashikawa, N., Komiyama, Y., Kusakabe, H., Momose, R., Nakajima, K., Tanaka, M., & Wang, S.-Y. 2018, Publications of the Astronomical Society of Japan, 70, S15
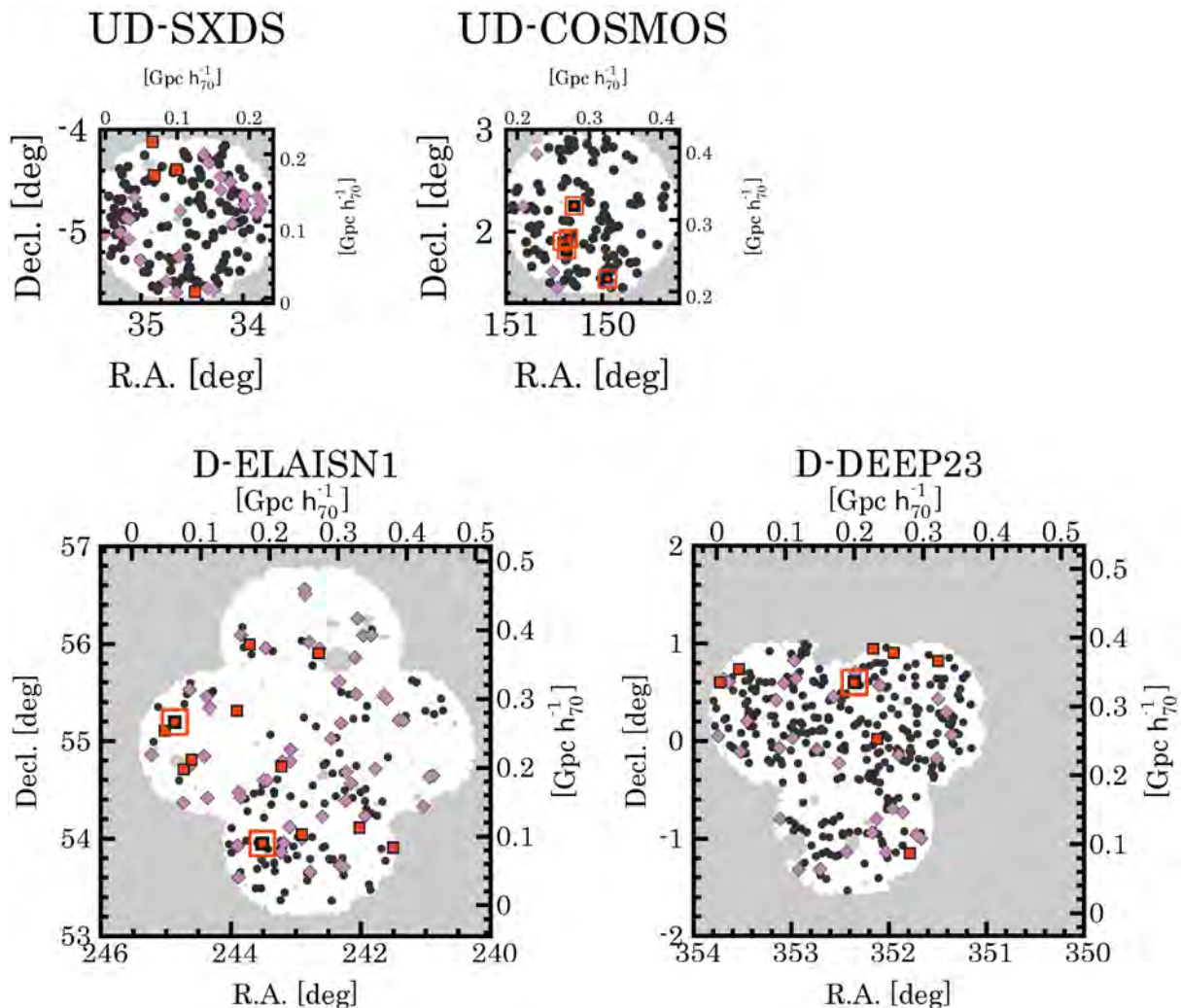
Fig. 13. Sky distribution of the LAEs at $z = 5.7$. The red squares, magenta diamonds, and black circles represent positions of narrowband bright (< 23.5 mag), medium-bright ($23.5 - 24.0$ mag), and faint ($24.0 - 25.0$ mag) LAEs, respectively. The large red open square indicates the LAEs with spatially extended Lyα emission. The gray shades denote either the areas with no HSC data or the masked regions with a bad data quality. The scale on the map is marked in angles (degrees) and the projected distances (comoving megaparsecs).

SILVERRUSH. IV. Lyα Luminosity Functions at $z = 5.7$ and 6.6 Studied with ~ 1300 LAEs on the $14 - 21$ deg^2 Sky [7]

In collaboration with the members of The University of Tokyo, The Open University of Japan, Ehime University, Kure College, National Astronomical Observatory of Japan, Osaka Sangyo University, National Tsing Hua University, European Southern Observatory, and Academia Sinica.

We present the Lyα luminosity functions (LFs) at $z = 5.7$ and 6.6 derived from a new large sample of 1266 Lyα emitters (LAEs) identified in total areas of 14 and 21 deg^2, respectively, based on the early narrowband data of the Subaru/Hyper Suprime-Cam (HSC) survey. Together with careful Monte Carlo simulations that account for the incompleteness of the LAE selection and the flux estimate systematics in the narrowband imaging, we determine the Lyα LFs with unprecedentedly small statistical and systematic uncertainties in a wide Lyα luminosity range of $10^{42.8-43.8}$ erg s^{-1} (Figure 16). We obtain the best-fit Schechter parameters of $L^*_{\mathrm{Ly}\alpha} = 1.6^{+2.2}_{-0.6}$ ($1.7^{+0.3}_{-0.7}$) $\times$ 10^{43} erg s^{-1}, $\phi^*_{\mathrm{Ly}\alpha} = 0.85^{+1.87}_{-0.77}$ ($0.47^{+1.44}_{-0.44}$) $\times 10^{-4}$ Mpc^{-3}, and $\alpha = -2.6^{+0.6}_{-0.4}$ ($-2.5^{+0.5}_{-0.5}$) at $z = 5.7$ (6.6). We confirm that our best-estimate Lyα LFs are consistent with the majority of the previous studies, but find that our Lyα LFs do not agree with the high number densities of LAEs recently claimed by Matthee/Santos et al.'s studies that may overcorrect the incompleteness and the flux systematics. Our Lyα LFs at $z = 5.7$ and 6.6 show an indication that the faint-end slope is very steep ($\alpha \simeq -2.5$), although it is also possible that the bright-end LF results are enhanced by systematic effects such as the contribution from AGNs, blended merging galaxies, and/or large ionized bubbles around bright LAEs. Comparing our Lyα LF measurements with four independent reionization models, we estimate the neutral hydrogen fraction of the IGM to be $x_{\mathrm{HI}} = 0.3 \pm 0.2$ at $z = 6.6$, which is consistent with the small Thomson scattering optical depth obtained by *Planck* 2016.
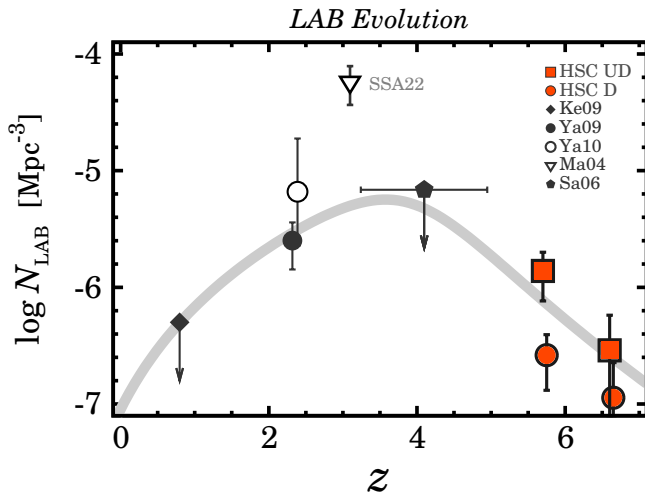
Fig. 14. Redshift evolution of the LAB number density. The filled red squares and filled red circles denote the LABs selected in the HSC UD and D fields, respectively. The error bars are given by Poisson statistics from the LAB number counts. The black symbols show LABs found in the literature All the measurements are based on LABs identified down to the surface brightness limit of $\simeq 5 \times 10^{-18}$ erg s^{-1} cm^{-2} arcsec^{-2}. The gray solid curve represents the best–fit formula to the data points expect for the measurement in the SSA22 proto-cluster region.

Bibliography

[7] Konno, A., Ouchi, M., Shibuya, T., Ono, Y., Shimasaku, K., Taniguchi, Y., Nagao, T., Kobayashi, M. A. R., Kajisawa, M., Kashikawa, N., Inoue, A. K., Oguri, M., Furusawa, H., Goto, T., Harikane, Y., Higuchi, R., Komiyama, Y., Kusakabe, H., Miyazaki, S., Nakajima, K., & Wang, S.-Y. 2018, Publications of the Astronomical Society of Japan, 70, S16

Theory Group

Overview

The theory group is active in elementary particle physics focusing on particle phenomenology, and in astroparticle physics focusing on particle cosmology. In particle physics, the main topics are theoretical studies of dark matter, inflation and extensions of the standard model. In astroparticle physics, the main topics are theoretical studies of inflation, thermal history of the early universe, dark matter, baryogenesis and big-bang nucleosynthesis.

Recently, the LHC accumulated around 40 fb^{-1} at the center of mass energy of 13 TeV. Many of the observed intriguing anomalies turned out to be statistical fluctuations. However, a large part of the results with 13TeV data will be released in the coming year, which may include interesting anomalies.

Since the LIGO detectors detected the first confirmed gravitational waves (GWs) from colliding black holes on September 14, 2015, new era of GW astronomy began. So far, six GW events were detected by LIGO. Among them is the first detection of GW from binary neutron star. The discovery
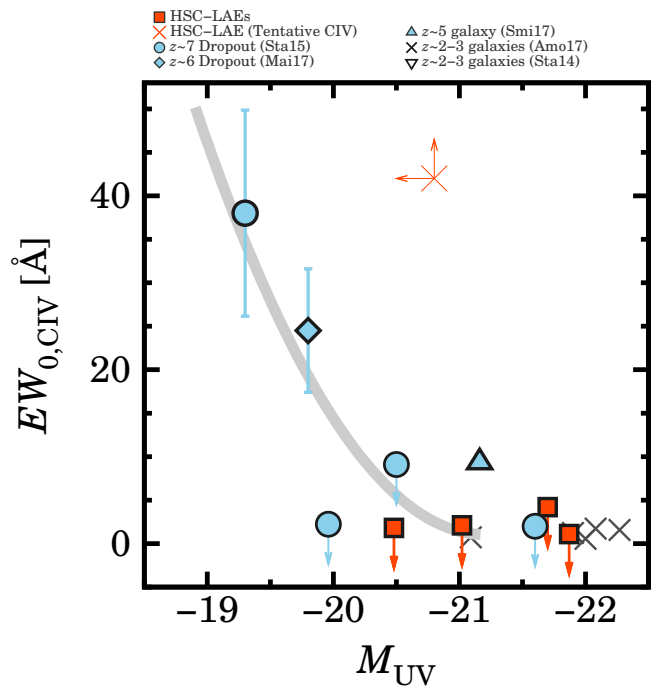
Fig. 15. Line equivalent widths of C IV as a function of UV magnitude, M_{UV}. The red filled squares denote our four bright LAEs with an upper limit of UV-nebular line EW. The red cross represents the LAEs whose C IV emission is tentatively detected. The cyan filled symbols denote high-z dropout galaxies in the literature. The gray symbols indicate $z \simeq 2-3$ galaxies. The gray curves represent the best-fit quadratic functions to the data points of $z \simeq 6-7$ dropouts and our LAEs. The data points without a UV-nebular line detection indicate 2σ upper limits.

suggested strongly the existence of kilonova which can produce r-process elements. If they continue to find GW events from black holes and neutron stars, their origin becomes one of the most interesting topics.

The supersymmetric (SUSY) extension of the standard model (SM) in the particle physics is considered to be one of the most promising models beyond the standard model. It solves the naturalness problem for the Higgs boson mass term in the standard model, and it is also compatible with the grand unified theories (GUTs). Our group has been studying phenomenological and cosmological aspects of the SUSY models.

Recent cosmological observations including the Planck data determine precisely the mean densities of matter and baryon in the Universe, and existence of non-baryonic dark matter is established. Weakly interacting massive particles (WIMPs) are considered to be good candidates of the dark matter. They act as the cold dark matter in the structure formation of the universe. Our group has been studying model building for dark matter and detectability in direct and indirect search experiments.

For understanding of the early universe, a role of the elementary particle physics is crucial. Recent progress in the particle physics such as grand unification theories and supersymmetry leads us to a more deeper insight into the fundamental aspects of the early universe. In the inflationary universe, the quantum fluctuations of the scalar field which drives the inflation become the density fluctuations and lead to formation of
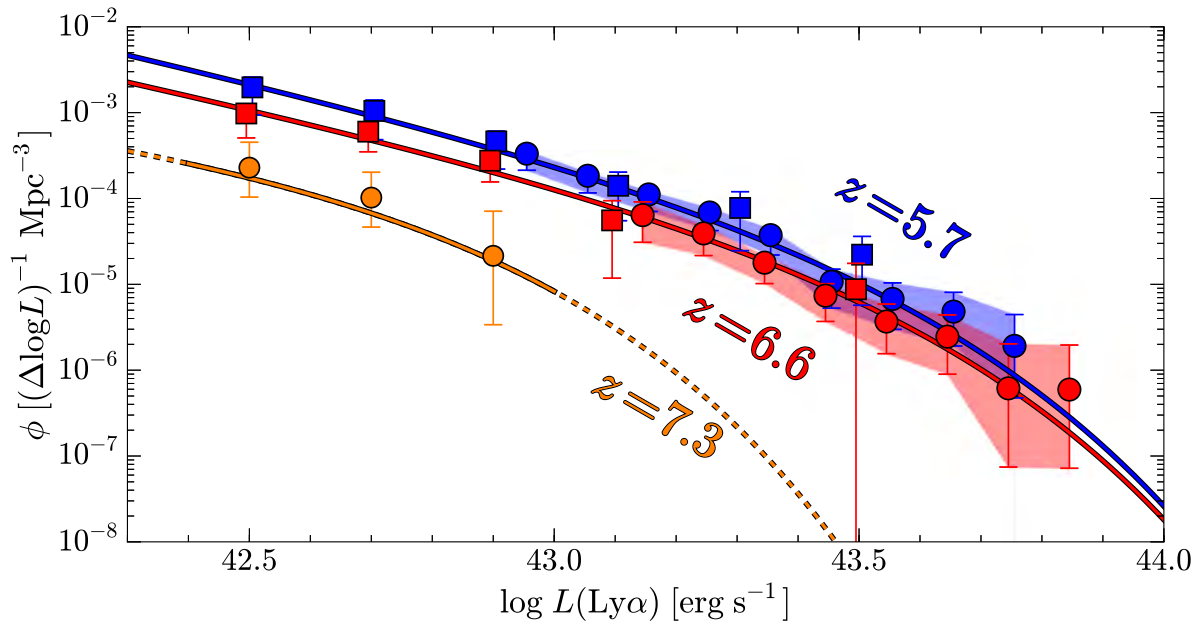
Fig. 16. Evolution of the Lyα LFs. The blue and red filled circles are our $z = 5.7$ and 6.6 Lyα LF measurements, respectively, which are derived from the HSC SSP data. The blue and red filled squares denote the $z = 5.7$ and 6.6 Lyα LF measurements with the Subaru/Suprime-Cam data in the literature. The best-fit Schechter function for the Lyα LF at $z = 5.7$ (6.6) is shown with the blue (red) solid curve, which are derived for the luminosity range of $\log L(\mathrm{Ly}\alpha)$ [erg s^{-1}] $= 42.4 - 44.0$. The orange circles represent the Lyα LF at $z = 7.3$ derived in the literature.

the structure observed in the present universe. On the other hand cosmology and astrophysics are used to test new theories in particle physics. Such particle cosmology is one of main subjects of our group.

Big Bang Nucleosynthesis (BBN) is one of the most important subjects in modern cosmology. Predicted abundances of the light elements are very sensitive to the cosmological scenario. On the other hand, physics beyond the standard model predicts the new particles which would have existed at the BBN epoch. Such particles may spoil the success of BBN, which leads to constraints on the new particles and the particle physics models.

The grand unified theories predict that our universe undergoes several vacuum phase transitions. In the course of phase transitions topological defects (monopoles, cosmic strings and domain walls) are generally produced depending on symmetries of the vacua. Our group has studied evolution of various topological defects.

Particle Phenomenology

[Spokesperson : M. Ibe]

ICRR, The Univ. of Tokyo, Kashiwa, Chiba 277-8582

Beyond the Standard Model, Collider Phenomenology

● Decay Rate of Electroweak Vacuum in the Standard Model and Beyond

In collaboration with the members of the University of Tokyo.

We perform a precise calculation of the decay rate of the electroweak vacuum in the standard model as well as in models beyond the standard model. We use a recently-developed technique to calculate the decay rate of a false vacuum, which provides a gauge invariant calculation of the decay rate at the one-loop level. We give a prescription to take into account the zero modes in association with translational, dilatational, and gauge symmetries. We calculate the decay rate per unit volume, γ, by using an analytic formula. The decay rate of the electroweak vacuum in the standard model is estimated to be $\log_{10} \gamma \times \mathrm{Gyr}\,\mathrm{Gpc}^3 = -582^{+40}_{-45}{}^{+184}_{-329}{}^{+144}_{-218}{}^{+2}_{-1}$, where the 1st, 2nd, 3rd, and 4th errors are due to the uncertainties of the Higgs mass, the top quark mass, the strong coupling constant and the choice of the renormalization scale, respectively. The analytic formula of the decay rate, as well as its fitting formula given in this paper, is also applicable to models that exhibit a classical scale invariance at a high energy scale. As an example, we consider extra fermions that couple to the standard model Higgs boson, and discuss their effects on the decay rate of the electroweak vacuum.

● State-of-the-Art Calculation of the Decay Rate of Electroweak Vacuum in the Standard Model

In collaboration with the members of the University of Tokyo.

The decay rate of the electroweak (EW) vacuum is calculated in the framework of the standard model (SM) of particle physics, using the recent progress in the understanding of the decay rate of metastable vacuum in gauge theories. We give a manifestly gauge-invariant expression of the decay rate. We also perform a detailed numerical calculation of the decay rate. With the best-fit values of the SM parameters, we find that the decay rate of the EW vacuum per unit volume is about $10^{-554}\mathrm{Gyr}^{-1}\mathrm{Gpc}^{-3}$.
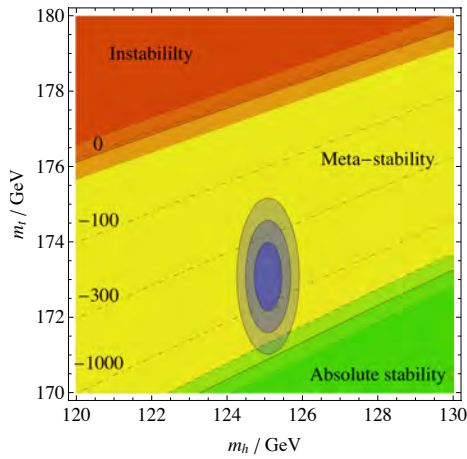
Fig. 17. The stability of the EW vacuum in the SM. The red region is unstable, the yellow region is meta-stable, and the green region is absolutely stable. The dashed, solid, and dotted lines correspond to $\alpha_s = 0.1192$, 0.1181, and 0.1170, respectively. The black dot–dashed lines indicate $\log_{10}\left[\gamma \times \mathrm{Gyr\ Gpc}^3\right] = 0$, -100, -300, and -1000 with the central value of α_s. The blue circles indicate 68, 95, and $99\ \%$ C.L. constraints on the Higgs mass vs. top mass plane assuming that their errors are independently Gaussian.

• False Vacuum Decay in Gauge Theory

In collaboration with the members of the University of Tokyo.

The decay rate of a false vacuum is studied in gauge theory, paying particular attention to its gauge invariance. Although the decay rate should not depend on the gauge parameter ξ according to the Nielsen identity, the gauge invariance of the result of a perturbative calculation has not been clearly shown. We give a prescription to perform a one-loop calculation of the decay rate, with which a manifestly gauge-invariant expression of the decay rate is obtained. We also discuss the renormalization necessary to make the result finite, and show that the decay rate is independent of the gauge parameter even after the renormalization.

Gauged Peccei-Quinn Symmetry - A Case of Simultaneous Breaking of SUSY and PQ Symmetry

In collaboration with the members of ICRR and IPMU

Recently, a simple prescription to embed the global Peccei-Quinn (PQ) symmetry into a gauged $U(1)$ symmetry has been proposed. There, explicit breaking of the global PQ symmetry expected in quantum gravity are highly suppressed due to the gauged PQ symmetry. In this paper, we apply the gauged PQ mechanism to models where the global PQ symmetry and supersymmetry (SUSY) are simultaneously broken at around $\mathcal{O}(10^{11-12})$ GeV. Such scenario is motivated by an intriguing coincidence between the supersymmetry breaking scale which explains the observed Higgs boson mass by the gravity mediated sfermion masses, and the PQ breaking scale which evades all the astrophysical and the cosmological constraints. As a concrete example, we construct a model which consists of a simultaneous supersymmetry/PQ symmetry breaking sector based on $SU(2)$ dynamics and an addi-
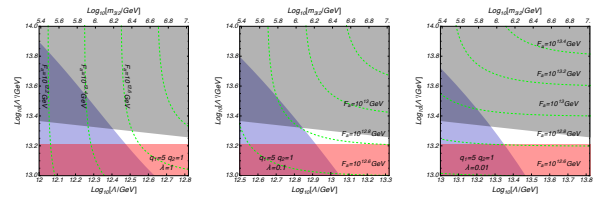
Fig. 18. The constraints on the parameter regions for given PQ charges, q_1 amd q_2. The gray region is excluded as $\theta_{\mathrm{eff}} < 10^{-10}$ is not satisfied. The perturbative unification is not achieved in the blue region. The red regions are excluded by $m'_{\mathrm{KSVZ}} \gtrsim 750$ GeV. The green lines are the contours of the effective decay constant F_a.

tional PQ symmetry breaking sector based on $SU(N)$ dynamics. We also show that new vector-like particles are predicted in the TeV range in the minimum model, which can be tested by the LHC experiments.

Dynamical Clockwork Axions

In collaboration with the members of ICRR and U. Montpellier

The clockwork mechanism is a novel method for generating a large separation between the dynamical scale and interaction scale of a theory. We demonstrate how the mechanism can arise from a sequence of strongly-coupled sectors. This framework avoids elementary scalar fields as well as ad hoc continuous global symmetries, both of which are subject to serious stability issues. The clockwork factor, q, is determined by the consistency of the strong dynamics. The preserved global U(1) of the clockwork appears as an accidental symmetry, resulting from discrete or U(1) gauge symmetries, and it is spontaneously broken by the chiral condensates. We apply such a dynamical clockwork to construct models with an effectively invisible QCD axion from TeV-scale strong dynamics. The axion couplings are determined by the localisation of the Standard Model interactions along the clockwork sequence. The TeV spectrum includes either coloured hadrons or vector-like quarks. Dark matter can be accounted for by the axion or the lightest neutral baryons, which are accidentally stable.

Bibliography

[1] S. Chigusa, T. Moroi and Y. Shoji, arXiv:1803.03902 [hep-ph].

[2] S. Chigusa, T. Moroi and Y. Shoji, Phys. Rev. Lett. **119**, no. 21, 211801 (2017) doi:10.1103/PhysRevLett.119.211801 [arXiv:1707.09301 [hep-ph]].

[3] M. Endo, T. Moroi, M. M. Nojiri and Y. Shoji, JHEP **1711**, 074 (2017) doi:10.1007/JHEP11(2017)074 [arXiv:1704.03492 [hep-ph]].

[4] H. Fukuda, M. Ibe, M. Suzuki and T. T. Yanagida, arXiv:1803.00759 [hep-ph].

[5] R. Coy, M. Frigerio and M. Ibe, JHEP **1710**, 002 (2017) doi:10.1007/JHEP10(2017)002 [arXiv:1706.04529 [hep-ph]].

Dark Matter Search

• Foreground effect on the *J*-factor estimation of ultra-faint dwarf spheroidal galaxies

In collaboration with the members of ICRR, IPMU and Peking U.

Dwarf spheroidal galaxies (dSphs) are promising targets for the gamma-ray dark matter (DM) search. In particular, DM annihilation signal is expected to be strong in some of the recently discovered nearby ultra-faint dSphs, which potentially give stringent constraints on the $\mathscr{O}(1)$ TeV WIMP DM. However, the various non-negligible systematic uncertainties complicate the estimation of the astrophysical factors relevant for the DM search in these objects. Among them, the effects of foreground stars particularly attract attention because the contamination is unavoidable even for the future kinematical survey. In this article, we assess the effects of the foreground contamination on the astrophysical *J*-factor estimation by generating mock samples of stars in the four ultra-faint dSphs and using a model of future spectrographs. We investigate various data cuts to optimize the quality of the data and apply a likelihood analysis which takes member and foreground stellar distributions into account. We show that the foreground star contaminations in the signal region (the region of interest) can be estimated with statistical uncertainty by interpolating the foreground star distribution in the control region where the foreground stars dominate the member stars. Such regions can be secured at future spectroscopic observations utilizing a multiple object spectrograph with a large field of view; e.g. the Prime Focus Spectrograph mounted on Subaru Telescope. The above estimation has several advantages: The data-driven estimation of the contamination makes the analysis of the astrophysical factor stable against the complicated foreground distribution. Besides, the uncertainties of the astrophysical factor are treated statistically.

• Migdal Effect in Dark Matter Direct Detection Experiments

In collaboration with the members of ICRR

The elastic scattering of an atomic nucleus plays a central role in dark matter direct detection experiments. In those experiments, it is usually assumed that the atomic electrons around the nucleus of the target material immediately follow the motion of the recoil nucleus. In reality, however, it takes some time for the electrons to catch up, which results in ionization and excitation of the atoms. In previous studies, those effects are taken into account by using the so-called Migdal's approach, in which the final state ionization/excitation are treated separately from the nuclear recoil. In this paper, we reformulate the Migdal's approach so that the "atomic recoil" cross section is obtained coherently, where we make transparent the energy-momentum conservation and

the probability conservation. We show that the final state ionization/excitation can enhance the detectability of rather light dark matter in the GeV mass range via the nuclear scattering. We also discuss the coherent neutrino-nucleus scattering, where the same effects are expected.

Bibliography

[1] K. Ichikawa, S. i. Horigome, M. N. Ishigaki, S. Matsumoto, M. Ibe, H. Sugai and K. Hayashi, doi:10.1093/mnras/sty1387 arXiv:1706.05481 [astro-ph.GA].

[2] M. Ibe, W. Nakano, Y. Shoji and K. Suzuki, JHEP **1803**, 194 (2018) doi:10.1007/JHEP03(2018)194 [arXiv:1707.07258 [hep-ph]].

Particle Cosmology

[Spokesperson : M. Kawasaki]
ICRR, The Univ. of Tokyo, Kashiwa, Chiba 277-8582

Inflation, Baryogenesis, Dark Matther

• Oscillating Affleck-Dine condensate and its cosmological implications

In collaboration with the members of ICRR

We study the dynamics of the Affleck-Dine field after inflation in more detail. After inflation, the Affleck-Dine field inevitably oscillates around the potential minimum. This oscillation is hard to decay and can cause accidental suppression of the consequential baryon asymmetry. This suppression is most effective for the model with nonrenormalizable superpotential $W_{AD} \sim \Phi 4$ (Φ: Affleck-Dine field). It is found that the Affleck-Dine leptogenesis in high-scale inflation, which suffers from serious gravitino overproduction, becomes workable, owing to this effect.

• Gravitino problem in inflation driven by inflaton-polonyi Kahler coupling

In collaboration with the members of ICRR, The Univ, of Tokyo, KEK, Stanford Univ.

We discuss the cosmological gravitino problem in inflation models in which the inflaton potential is constructed from Kahler potential rather than superpotential: a representative model is $\overline{D3}$-induced geometric inflation. A critical ingredient in this type of models is the coupling of the inflaton and Polonyi (supersymmetry-breaking) field in the Kahler potential, which is needed to build the inflaton potential. We point out the same coupling let the inflaton dominantly decay into a pair of inflatino and gravitino causing the gravitino problem. We propose some possible solutions to this problem.

• Inflaton fragmentation in E-models of cosmological α-attractors

In collaboration with the members of ICRR

Cosmological α-attractors are observationally favored due to the asymptotic flatness of the potential. Since its flatness induces the negative pressure, the coherent oscillation of the inflaton field could fragment into quasistable localized objects called I-balls (or "oscillons"). We investigated the possibility of I-ball formation in E models of α-attractors. Using the linear analysis and the lattice simulations, we found that the instability sufficiently grows against the cosmic expansion and the inflaton actually fragments into the I-balls for $\alpha \lesssim 10^{-3}$.

● Oscillons from Pure Natural Inflation

In collaboration with the members of ICRR and Kavli IPMU

We examine the oscillon formation in a recently proposed inflation model of the *pure natural inflation*, where the inflaton is an axion that couples to a strongly-coupled pure Yang-Mills theory. The plateau of the inflaton potential, which is favored by recent observations, drives the fragmentation of the inflaton and can produce spatially localized oscillons. We find that the oscillons are formed for $F \lesssim \emptyset(0.1)M_{\text{pl}}$, with F the effective decay constant of the model. We also comment on observational implications of the oscillons.

● Gauged Q-ball Decay Rates into Fermions

In collaboration with the members of ICRR and Kavli IPMU

We derive the decay rate of a gauged Q-ball into fermions, applying the leading semi-classical approximation. We find that more particles come out from the surface of a gauged Q-ball, compared to the case of a global Q-ball, due to the electric repulsion. We show that, however, the decay rate of a gauged Q-ball is bounded from above due to the Pauli blocking at the surface of the Q-ball, just as in the case of a global Q-ball. We also find that there is a further suppression due to the Coulomb potential outside the Q-ball, which we find to play the role of a potential barrier for the fermions coming from the inside the Q-ball.

Bibliography

[1] F. Hasegawa and M. Kawasaki, Phys. Rev. D **96**, no. 6, 063518 (2017) doi:10.1103/PhysRevD.96.063518 [arXiv:1706.08659 [hep-ph]].

[2] F. Hasegawa, K. Nakayama, T. Terada and Y. Yamada, Phys. Lett. B **777**, 270 (2018) doi:10.1016/j.physletb.2017.12.038 [arXiv:1709.01246 [hep-ph]].

[3] F. Hasegawa and J. P. Hong, Phys. Rev. D **97**, no. 8, 083514 (2018) doi:10.1103/PhysRevD.97.083514 [arXiv:1710.07487 [astro-ph.CO]].

[4] J. P. Hong, M. Kawasaki and M. Yamazaki, arXiv:1711.10496 [astro-ph.CO].

[5] J. P. Hong and M. Kawasaki, Phys. Rev. D **96**, no. 10, 103526 (2017) doi:10.1103/PhysRevD.96.103526 [arXiv:1706.01651 [hep-ph]].

Axion Cosmology

● Domain wall and isocurvature perturbation problems in a supersymmetric axion model

In collaboration with the members of ICRR and Kavli IPMU.

The axion causes two serious cosmological problems, domain wall and isocurvature perturbation problems. Linde pointed that the isocurvature perturbations are suppressed when the Peccei-Quinn (PQ) scalar field takes a large value $\sim M_{\text{pl}}$ (Planck scale) during inflation. In this case, however, the PQ field with large amplitude starts to oscillate after inflation and large fluctuations of the PQ field are produced through parametric resonance, which leads to the formation of domain walls. We consider a supersymmetric axion model and examine whether domain walls are formed by using lattice simulation. It is found that the domain wall problem does not appear in the SUSY axion model when the initial value of the PQ field is less than $10^3 \times v$ where v is the PQ symmetry breaking scale.

● Cosmologically allowed regions for the axion decay constant F_a

In collaboration with the members of ICRR and Kavli IPMU.

If the Peccei-Quinn symmetry is already broken during inflation, the decay constant F_a of the axion can be in a wide region from 10^{11} GeV to 10^{18} GeV for the axion being the dominant dark matter. In this case, however, the axion causes the serious cosmological problem, isocurvature perturbation problem, which severely constrains the Hubble parameter during inflation. The constraint is relaxed when Peccei-Quinn scalar field takes a large value $\sim M_p$ (Planck scale) during inflation. In this letter, we point out that the allowed region of the decay constant F_a is reduced to a rather narrow region for a given tensor-to-scalar ratio r when Peccei-Quinn scalar field takes $\sim M_p$ during inflation. For example, if the ratio r is determined as $r \gtrsim 10^{-3}$ in future measurements, we can predict $F_a \simeq (0.1 - 1.4) \times 10^{12}$ GeV for domain wall number $N_{\text{DW}} = 6$.

● QCD axion dark matter from long-lived domain walls during matter domination

In collaboration with the members of ICRR and University of California, Berkeley.

The domain wall problem of the Peccei-Quinn mechanism can be solved if the Peccei-Quinn symmetry is explicitly broken by a small amount. Domain walls decay into axions, which may account for dark matter of the universe. This scheme is however strongly constrained by overproduction of axions unless the phase of the explicit breaking term is tuned. We investigate the case where the universe is matter-dominated around the temperature of the MeV scale and domain walls decay during this matter dominated epoch. We show how the viable parameter space is expanded.

• Adiabatic suppression mechanism and axions

In collaboration with the members of ICRR , Tohoku University and Tufts University.

The string theory predicts many light fields called string axions and moduli, which are problematic in cosmology due to the overproduction of their coherent oscillation after inflation. One of the prominent solutions is an adiabatic suppression mechanism, where the light field follows its time-dependent minimum which moves slowly compared with the cosmological time scale. This can be achieved if the potential receives a large effective mass term which decreases as a function of time. In this paper, we provide a method to calculate the abundance of coherent oscillation in a generic situation under the adiabatic suppression mechanism. Then we apply our calculation to some examples, including the one where a string axion acquires an effective mass due to the Witten effect in the presence of monopoles of hidden $U(1)_H$ gauge theory.

Bibliography

[1] M. Kawasaki and E. Sonomoto, Phys. Rev. D **97** (2018) 083507 [arXiv:1710.07269 [hep-ph]].

[2] M. Kawasaki, E. Sonomoto and T. T. Yanagida, Phys. Lett. B **782** (2018) 181-184 [arXiv:1801.07409 [hep-ph]].

[3] K. Harigaya and M. Kawasaki, Phys. Lett. B **782**, 1 (2018) doi:10.1016/j.physletb.2018.04.056 [arXiv:1802.00579 [hep-ph]].

[4] M. Kawasaki, F. Takahashi and M. Yamada, JHEP **1801**, 053 (2018) doi:10.1007/JHEP01(2018)053 [arXiv:1708.06047 [hep-ph]].

Primodial Black Holes

• Primordial Black Holes for the LIGO Events in the Axion-like Curvaton Model

In collaboration with the members of ICRR, Kavli IPMU and DESY.

We revise primordial black hole (PBH) formation in the axion-like curvaton model and investigate whether PBHs formed in this model can be the origin of the gravitational wave (GW) signals detected by the Advanced LIGO. In this model, small-scale curvature perturbations with large amplitude are generated, which is essential for the PBH formation. On the other hand, large curvature perturbations also become a source of primordial GWs by their second-order effects. Severe constraints are imposed on such GWs by pulsar timing array (PTA) experiments. We also check the consistency of the model with these constraints. In this analysis, it is important to take into account the effect of non-Gaussianity, which is generated easily in the curvaton model. We see that, if there are non-Gaussianities, the fixed amount of PBHs can be produced with a smaller amplitude of the primordial power spectrum.
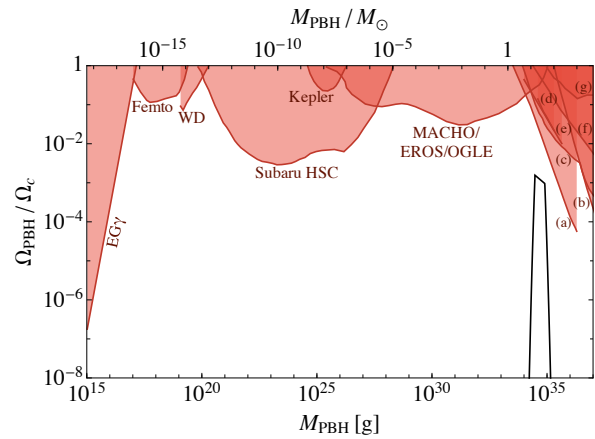
Fig. 19. *Mass spectrum of PBHs. The Black line shows the predicted PBH formed by the axion-like curvaton model which can reproduce the features of GW signals detected by the Advanced LIGO. The red shaded regions are the observational constraints on the PBH mass fraction to dark matter.*

• Primordial black holes and uncertainties on choice of window function

In collaboration with the members of ICRR.

Primordial black holes (PBHs) can be produced by the perturbations which exit the horizon during inflationary phase. While inflation models predict the power spectrum of the perturbations in Fourier space, the PBH abundance depends on the probability distribution function (PDF) of density perturbations in real space. In order to estimate the PBH abundance in a given inflation model, we must relate the power spectrum in Fourier space to the PDF in real space by coarse-graining the perturbations with a window function. However, there are uncertainties on what window function should be used, which could change the relation between the PBH abundance and the power spectrum. This is particularly important in considering PBHs with mass $30M_\odot$ which account for the LIGO events because the required power spectrum is severely constrained by the observations. In this paper, we investigate how large influence the uncertainties on the choice of a window function have over the power spectrum required for LIGO PBHs. As a result, it is found that the uncertainties most significantly affect the prediction for the stochastic gravitational waves (GWs) induced by the second order effect of the perturbations. In particular, the pulsar timing array constraints on the produced GWs could disappear for the real-space top-hat window function.

• Double Inflation as a single origin of PBHs for all dark matter and LIGO

In collaboration with the members of ICRR, IPMU, and DESY

Primordial Black Hole (PBH) is one of the leading non-particle candidates for dark matter (DM). Although several observations severely constrain the amount of PBHs, it is recently pointed out that there is an uncertainty on the mi-
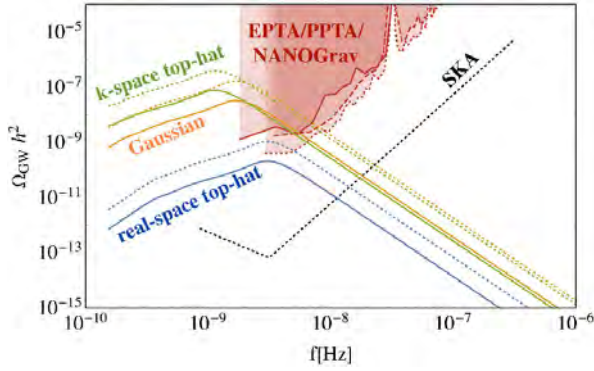
Fig. 20. *Energy density parameters of the GWs induced by the curvature perturbations. The colored solid and dashed lines indicate the different window functions. The red shaded region is excluded by the current PTA observations. The black dashed line denotes the future prospects of SKA.*

Fig. 21. *Mass spectrum of PBHs. The blue and brown solid lines show the predicted PBH as dark matter stemmed from double inflation theory. This model can also reproduce the features of GW signals detected by the Advanced LIGO. The red shaded regions show the observational constraints on the monochromatic mass function. The red dotted line denotes the uncertain constraint of HSC because of the wave effect. The orange regions show the constraint from the existence of white dwarfs in our galaxy.*

crolensing constraints below $\sim 10^{-10} M_\odot$ which was ignored originally but may weaken the constraints significantly. In this paper, facing this uncertainty, we investigate the possibility that PBHs can make up all DM in a broad mass spectrum. Moreover, we propose a concrete inflation model which can simultaneously produce PBHs for all DM in a broad mass spectrum around $\mathcal{O}(10^{-13}) M_\odot$ and PBHs for LIGO events in a sharp mass spectrum at $\mathcal{O}(10) M_\odot$.

$\mathcal{O}(10) M_\odot$ primordial black holes and string axion dark matter

In collaboration with the members of ICRR, IPMU, IAP and Sorbonne University

LIGO-Virgo collaboration has found black holes as heavy as $M \sim 30 M_\odot$ through the detections of the gravitational waves emitted during their mergers. Primordial black holes (PBHs) produced by inflation could be an origin of such BHs. While it is tempting to presume that these PBHs constitute all Dark Matter (DM), there exist a number of constraints for PBHs with $\mathcal{O}(10) M_\odot$ which contradict with the idea of PBHs as all DM. Also, it is known that weakly interacting massive particle (WIMP) that is a common DM candidate is almost impossible to coexist with PBHs. These observations motivate us to pursue another candidate of DM. In this paper, we assume that the string axion solving the strong CP problem makes up all DM, and discuss the coexistence of string axion DM and inflationary PBHs for LIGO events.

• Cogenesis of LIGO Primordial Black Holes and Dark Matter

In collaboration with the members of ICRR

We propose a novel scenario which simultaneously explains $\mathcal{O}(10) M_\odot$ primordial black holes (PBHs) and dark matter in the minimally supersymmetric standard model. Gravitational waves (GWs) events detected by LIGO-Virgo collaboration suggest an existence of black holes as heavy as $\sim 30 M_\odot$. In our scenario, as seeds of the PBHs, we make

use of the baryon number perturbations which are induced by the special type of Affleck-Dine mechanism. Furthermore, the scenario does not suffer from the stringent constraints from CMB μ-distortion due to the Silk damping and pulsar timing. We find the scenario can explain not only the current GWs events consistently, but also dark matter abundance by the non-topological solitons formed after Affleck-Dine mechanism, called Q-balls.

Bibliography

[1] K. Ando, K. Inomata, M. Kawasaki, K. Mukaida and T. T. Yanagida, Model," [arXiv:1711.08956 [astro-ph.CO]].

[2] K. Ando, K. Inomata and M. Kawasaki, " [arXiv:1802.06393 [astro-ph.CO]].

[3] K. Inomata, M. Kawasaki, K. Mukaida and T. T. Yanagida, Phys. Rev. D **97**, no. 4, 043514 (2018) doi:10.1103/PhysRevD.97.043514 [arXiv:1711.06129 [astro-ph.CO]].

[4] K. Inomata, M. Kawasaki, K. Mukaida, Y. Tada and T. T. Yanagida, Phys. Rev. D **96**, no. 12, 123527 (2017) doi:10.1103/PhysRevD.96.123527 [arXiv:1709.07865 [astro-ph.CO]].

[5] F. Hasegawa and M. Kawasaki, arXiv:1711.00990 [astro-ph.CO].

Big-Bang nucleosynthesis

• Revisiting Big-Bang Nucleosynthesis Constraints on Long-Lived Decaying Particles

In collaboration with the members of ICRR, The University of Tokyo, Okayama University and KEK.

We study effects of long-lived massive particles, which decay during the big-bang nucleosynthesis (BBN) epoch, on the primordial abundances of light elements. Compared to the previous studies, (i) the reaction rates of the standard BBN reactions are updated, (ii) the most recent observational data of light element abundances and cosmological parameters are used, (iii) the effects of the interconversion of energetic nucleons at the time of inelastic scatterings with background nuclei are considered, and (iv) the effects of the hadronic shower induced by energetic high energy anti-nucleons are included. We compare the theoretical predictions on the primordial abundances of light elements with latest observational constraints, and derive upper bounds on relic abundance of the decaying particle as a function of its lifetime. We also apply our analysis to unstable gravitino, the superpartner of the graviton in supersymmetric theories, and obtain constraints on the reheating temperature after inflation.

Bibliography

[1] M. Kawasaki, K. Kohri, T. Moroi and Y. Takaesu, Phys. Rev. D **97**, no. 2, 023502 (2018) doi:10.1103/PhysRevD.97.023502 [arXiv:1709.01211 [hep-ph]].

OBSERVATORIES and
A RESEARCH CENTER

Location of the Institute and the Observatories in Japan

Norikura Observatory

Location:	Norikuradake, Nyukawa-cho, Takayama-shi, Gifu Prefecture 506-2100
	N 36°06′, E 137°33′, 2770 m a.s.l.
Telephone (Fax):	+81-50-3730-3809
Telephone (satellite):	+81-90-7721-5674
Telephone (car):	+81-90-7408-6224

Akeno Observatory

Location:	5259 Asao, Akeno-machi, Hokuto-shi, Yamanashi Prefecture 408-0201
	N 35°47′, E 138°30′, 900 m a.s.l.
Telephone / Fax:	+81-551-25-2301 / +81-551-25-2303

Kamioka Observatory

Location:	456 Higashi-mozumi, Kamioka-cho, Hida-shi, Gifu Prefecture 506-1205
	N 36°25′26″, E 137°19′11″, 357.5 m a.s.l.
Telephone / Fax:	+81-578-85-2116 / +81-578-85-2121

KAGRA Observatory

Location:	238 Higashi-mozumi, Kamioka-cho, Hida-shi, Gifu Prefecture 506-1205
	N 36°25′26″, E 137°19′11″, 350 m a.s.l.
Telephone / Fax:	+81-578-85-2343 / +81-578-85-2346

Research Center for Cosmic Neutrinos

Location:	5-1-5 Kashiwanoha, Kashiwa, Chiba Prefecture 277-8582
Telephone / Fax:	+81-4-7136-3138 / +81-4-7136-3115

NORIKURA OBSERVATORY

Introduction

Norikura Observatory (36.10°N and 137.55°E) was founded in 1953 and attached to ICRR in 1976. It is located at 2770 m above sea level, and is the highest altitude manned laboratory in Japan. Experimental facilities of the laboratory are made available to all the qualified scientists in the field of cosmic ray research and associated subjects. The AC electric power is generated by the dynamo and supplied throughout the observatory. In 1996, two dynamos of 70 KVA each were replaced with the new ones. The observatory can be accessed easily by car and public bus in summer (July-September). The 50th anniversary of Norikura Observatory was celebrated in 2003.

Fig. 2. A dynamo of 115KV.

Fig. 1. Norikura Observatory.

The feasibility of the automatic operation of Norikura Observatory during winter period has been tested since winter 2004 in order to study the possibilities to reduce maintenance and labor costs without seriously damaging to the use of researches. A long-distance (∼40km) wireless LAN system (11M bps) was set up in 2003. Two new easy-to-handle and easy-to-maintain dynamos of 115 KVA each were installed in 2004 as well. The unmanned operation of Norikura Observatory has been mostly successful in winter, during which the battery backed-up solar panels and/or wind power generators kept supplying the electricity to the wireless LAN and on-going cosmic-ray experiments. The 60th anniversary of Norikura Observatory was celebrated in 2013.

Present major scientific interests of the laboratory is focused on the modulation of high energy cosmic rays in the interplanetary space associated with the solar activity and the generation of energetic particles by the solar flares, both of which require long-term monitoring. This research has been carried out by the group of universities, where ICRR provides them with laboratory facility. A part of the facility has been open for the environmental study at high altitude such as

aerosol-related mechanism in the atmosphere, observation of total ozone and UV solar radiation, for botanical study in the high-altitude environment, etc.

Cosmic Ray Physics

A neutron monitor has been continuously operated to study the correlation of solar activities and cosmic ray flux for a long time. It is the only active one in Japan now. The neutron monitor data are open to researchers worldwide as a world observation network point (WDC). In addition, space weather observation is actively made by a 25 m^2 muon hodoscope at Norikura Observatory[1], [2], [3], [4], [5], [6], [7], [8], [9].

The anisotropy observed with the global muon detector network (GMDN) provides us with a unique information of the spatial gradient of the GCR density which reflects the large-scale magnetic structure in the heliosphere. The solar cycle variation of the gradient gives an important information on the GCR transport in the heliosphere, while the short-term variation of the gradient enables us to deduce the large-scale geometry of the magnetic flux rope and the interplanetary coronal mass ejection (ICME). Real-time monitoring of the precursory anisotropy which has often been observed at the Earth preceding the arrival of the ICME accompanied by a strong shock may provide us with useful tools for forecasting the space weather with a long lead time. By using a self-supporting power system utilizing the solar panels and batteries, we keep a 25 m^2 muon hodoscope running at the Mt. Norikura Cosmic Ray Observatory as an important component detector of the GMDN. The total power consumption of this detector has been suppressed as low as 36 Watt by replacing all amplifier boards with those using CMOS ICs and by introducing a new recording system using the FPGA. This new system, in which the observation has been automatically car-

ried out by a PC connected with the internet, also enabled us to monitor the data on the real-time basis for the space weather study.

The Sun is the nearest site to the Earth capable of accelerating particles up to high energies. When the Sun becomes active, flares are frequently observed on its surface. The flare accelerates the proton and ion to high energy and they are detected on the Earth soon after the flare. Among the particles generated by the flare, high energy neutrons provide the most direct information about the acceleration mechanism as they come straight from the flare position to the Earth without deflected by the magnetic field.

Observation of solar neutron has been conducted at the Norikura Observatory since 1990. Neutron is used to clarify the acceleration mechanism of high energy particles in association with solar flares, because the neutron is not reflected by the interplanetary magnetic field. The $64m^2$ solar neutron telescope was constructed in 1996, which is one of 7 solar neutron telescopes deployed at different longitudes to make up a network of 24 hour observation of solar neutrons. The Norikura $64m^2$ solar neutron telescope has been operated by solar batteries and windmills since 2004.

This collaborative work has started since fiscal 2007 succeeding to the previous project titled 'Observation of solar neutrons by using a new method.' Although solar cycle 24 has started since 2008, the solar activity has continued to be inactive, and no new solar neutron event has been detected by the network since 2006. The last solar neutron event was on September 7, 2005. This event is unique because it indicates ions were accelerated or trapped at the acceleration region longer than electrons. The summary of 11 solar neutron events detected until 2005 shows that it may not be probable that a very efficient acceleration such as the shock acceleration works for ions at solar flares. This is given by deriving the energy spectrum of neutrons at the solar surface for each solar neutron event with a power law. Power law indices obtained span from 3 to 7. The energy spectrum of the original ions is softer than that of neutron. Therefore an efficient acceleration has not been detected by the observation of solar neutrons so far.This work continues in solar cycle 24 to accumulate more events to obtain definite results related with particle acceleration at the solar surface.

Another effort aiming at observation of highest-energy solar cosmic rays started at the Norikura Observatory. The Sun is an accelerator of protons and electrons in the universe. In association with large solar flares, protons and electrons are accelerated into high energies. It is known that protons are accelerated over 50 GeV in the largest solar flares[24]. These high energy particles produce the Ground Level Enhancement (GLE).

In order to understand the acceleration mechanism of protons, we have prepared several solar neutron telescopes at the high altitude laboratories in the world. They are located at Gornergrat (3,135m), Mt. Aragats in Armenia (3,200m), Tibet (4,200m), Mauna-Kea in Hawaii (4,200m), Mt. Chacaltaya in Bolivia (5,250m), and at Mt. Sierra Negra in Mexico (4,900m). We have constructed a solar neutron telescopes at Mt. Norikura Cosmic Ray Observatory (2,770m) in 1990 and operated it until 2004[21]. However due to the lack of power supply during the winter time since 2005, the first solar neutron telescope ($36 m^2$) has not been operated.

From 2008 to 2009, we have decided to make a new solar neutron telescope to utilize the large amount of the plastic scintillator ($0.5m^3$), as shown in Fig.3, left at the observatory.

Fig. 3. 0.5-m^2 plastic scintillation counter for a new neutron telescope.

The new solar neutron telescope with use of the recycled plastic scintillator consists of main target where neutrons are converted into protons and of the anti-counters surrounding the target. The signals of neutrons converted into protons are observed by using one photomultiplier from bottom side to reduce the electric power. Furthermore a lead plate with the thickness of 1cm is located over the target and the lead plate is sandwiched by two layers of the plastic scintillator to identify gamma-rays from neutrons.

The new solar neutron telescope has a function to reject charged particles with an efficiency of 90%. Therefore the new solar neutron telescope has capability of 1/3 of the $64m^2$ large solar neutron telescope located at the same place. We are waiting large solar flares over our detectors.

In addition to the long-term cosmic-ray observations mentioned above, various kinds of short-dated experiments are carried out every year taking an advantage of the high altitude of the observatory.

High-energy radiations from thunderstorms have been ob-

served by flight measurement, high-mountain observations and ground-based measurement. There are two types of those radiations associated with thunderstorms. One is short-duration radiations with duration of 1 ms or less. The other is long-duration emissions lasting for a few seconds to a few minutes, or a few tens of minutes on rare occasions. It is believed that both emissions originate from electrons accelerated in strong electric fields formed in lightning and thunderclouds. However, compared with the former, the latter has remained less understood due to lack of a large sample of observations.

To investigate production mechanism of long-duration emissions and the relevant electron acceleration, we installed at Norikura Cosmic-ray Observatory a radiation detection system and environmental sensors to measure light and electric fields during 2008−2010. The radiation system consists of a spherical NaI scintillator and a thin plastic scintillator that is placed just above the NaI counter. During the period, the system detected one long-duration bursts as well as five short-duration events.

Fig. 4 (top) shows the long-duration event observed during thunderstorms on 2008 September 20th [25]. The event lasted for 90 sec. Fig.4 (bottom) represents an observed photon spectrum extending from 10 keV to 10 MeV. This indicates that electrons can be accelerated to at least 10 MeV in a quasi-stable thundercloud electric field. In addition, we compared the observed spectrum with model ones, and concluded that a gamma-ray source is located 60 m−130 m (at 90% confidence level) apart from our detector. Given these results, the observed emission was found to consist of not only gamma rays but also electrons. This was the first simultaneous observation of gamma rays and electrons in long-duration bursts.

Observation of night sky background is carried out at Mt. Norikura for basic study of ultra high energy cosmic-ray physics.

The JEM-EUSO mission is going on in order to study ultra high energy cosmic rays (UHECRs), especially above 10^{20}eV. A 2.5m telescope with 60° FoV will be attached to the International Space Station in 2017 and detect fluorescence in near UV band from extensive air showers induced by UHECRs. Observation of UHECRs from a satellite orbit has not been done yet, so that the knowledge of background light intensity is important to realize the observation. We have measured it from a balloon altitude, but the opportunity is limited. We started the background measurement at Mt. Norikura.
Two 1 inch multi-anode photomultipliers (MAPMTs) developed for EUSO was used with UV filters. The center wavelengths of the filters were 337, 350, 358, 370, 380, 391, 400nm with 10nm band width. In addition BG3 filter was used to detect light in wider range from 330nm to 430nm. The MAPMTs were collimated to 7° FoV. The data was taken with the photon counting method.
We have observed several nights for three years. The intensity at zenith was almost constant at 600-800 photons/ns∼sr m^2 for BG3 filter. The spectral intensity was about 1.5-2 times larger than those measured at La Palma and Namibia. The estimated portion of star light and zodiacal light was ∼30% and artificial light and nightglow at upper atmosphere may be the main components at Mt.Norikura.
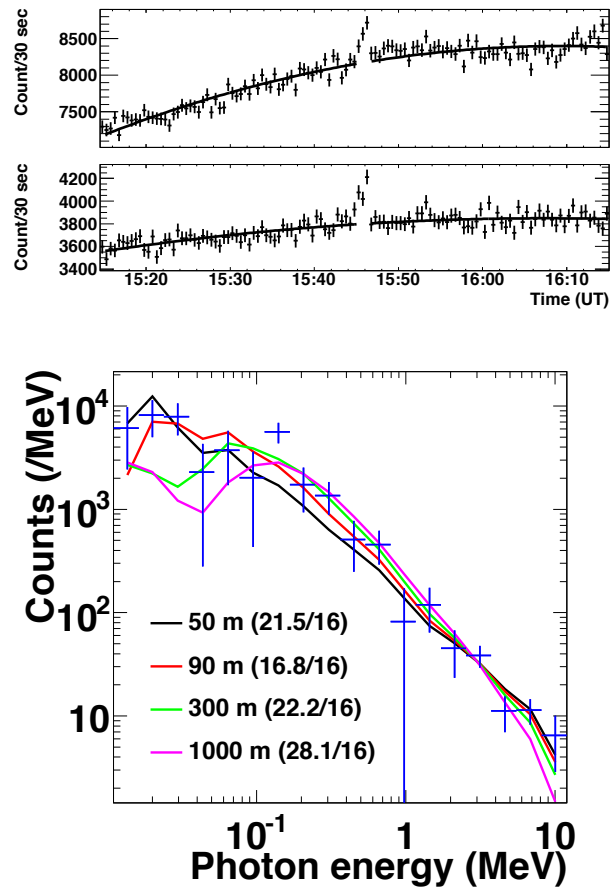
Fig. 4. (Top) Count rates per 30 sec observed by the >10 keV NaI scintillator (upper) and > 100 keV plastic one (lower). (Bottom) The photon spectrum observed by the NaI scintillator.
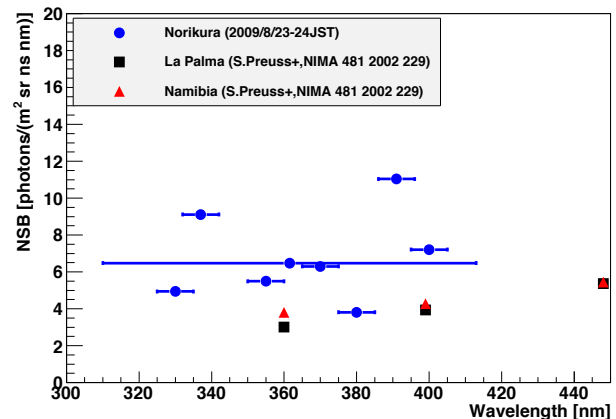
Fig. 5. Spectrum of night sky background measured at Mt.Norikura compared with those at La Palma and Namibia.

Environmental Study

One of the interesting topics is atmospheric environment especially relating with atmospheric aerosol particles and water soluble gases. The cosmic ray observatory at Mt. Norikura provides us very unique opportunity for the observations of atmosphere at free-tropospheric conditions with its high altitude, AC power supply at the site, accommodation facility,

and easy accessibility. From year 2000 to 2007, we conducted continuous monitoring (mostly mid-May to mid-October) of meteorological parameters, number-size distribution of aerosols, aerosol chemical composition, ozone and radon concentrations, and column amount of aerosols from sky radiometer and ceilometers. We also collected rain, fog, water-condensed aerosol samples. These samples combined with other observed parameters were used in publications in the following subjects [26, 27, 28]:

(1) Polluted air pumping effects over central Japanese Alps in summer
(2) Seasonal variation of aerosol chemistry in free troposphere
(3) Vertical profiles of aerosols and clouds near the top of the atmospheric boundary layer.

Ceilometer (lidar with small output energy) was installed in summer 2002, and was operated in 6 summer seasons. The aerosol and cloud profiles near the top of the atmospheric boundary layer have been observed. Some events of Asian dust were detected.

Observations of total ozone and UV solar radiation with Brewer spectrophotometer on the Norikura mountains are also made[29, 30, 31].

Aerological Observatory started "Observations of total ozone and UV solar radiation with Brewer spectrophotometer at Norikura mountains" as a joint project with Institute for Cosmic Ray Research (ICRR), University of Tokyo at the Norikura Observatory of ICRR (Brewer site: 36.11 N, 137.56 E, 2,772 m a.s.l.), locating at the Northern Japanese Alps in every summer seasons from 2009 (Ito *et al.*: 2011). Purpose of this study is based on the concept of developing Regional Brewer Calibration Centre in Asia and study of total ozone, total sulfur oxide and global/diffuse UV included solar radiation on the high mountains. Observation results by using Brewer spectrophotometers and other instruments for the observation period of three summer seasons of recent three years between 2009 to 2011 are summarized as follows;

(1) Daily means of ds O_3 (total ozone) at Norikura for the observation periods were approx. 280 to 290 m atm-cm and were running on the lower values of approx. -3 to -6% compared to the value at Tsukuba (36.06 N, 140.13 E, 39 m a.s.l.) at almost same latitude. Day-to-day variations at Norikura were also small against Tsukuba. On the other hand, daily mean of ds SO_2 (total sulfur oxide) values were not recognized at Norikura.

(2) Absolute calibration of Brewers for ds O_3 and ds SO_2 observations could be carried out within the range of air mass from 7.928 (maximum) to 1.028 (minimum) at Norikura in the clear day. O_3 and SO_2 Extra-Terrestrial Coefficients (=ETC) of Brewers could be produced as about 10 samples satisfying the condition of "$R^2 > 0.9997$" by the calibrations. As an example of the calibration in 2011, the average of O_3 ETC of Brewers was identical within 1% to the currently used coefficient.

(3) In comparison to the data acquired at Tsukuba, the average of daily total GL_{UV} (global UV, e.g. CIE) for the observation periods indicated the intensities of approx. +23 % in 2009 to -6 % in 2011. The low intensity in 2011 was due to the bad weather on the Norikura Mountain. In the case of clear days, the GL_{UV} at Norikura indicated high intensities of approx. +35 to +52 % against the values at Tsukuba. On the other hand, the GL_{UV} increased in the short wavelength range at Norikura against the average at Tsukuba. The altitudinal increasing rate of GL_{UV} in the clear day indicated the calculated amounts of approx. +13 to +18 % per 1,000 m.

This joint project had been clarifying the low total O_3, high UV in clear day, low turbidity and etc. at Norikura against the value at Tsukuba. Those environmental conditions are useful for the intercomparison and the absolute calibrations with Brewers. The continuous observations with Brewers and other instrument are very important for the clarification of the seasonal variation and the coefficient trends.

Botanical Study

Effects of snow cover on pine shrub Pinus pumila in the alpine region of Mt. Norikura

High mountainous habit is one of the most severe habits for plant life and sometimes dwarf shrubs cannot survive. In the alpine regions of Japan, the dwarf shrub Pinus pumila (Japanese name : Haimatsu) forms communities together with small alpine plants, whereas dwarf shrubs occur only in the transition zone between the alpine region and the subalpine forest in Europe and North America. This characteristic of alpine vegetation is considered to be owing to winter heavy snow in the alpine regions of Japan. The purpose of this study is to elucidate how snow cover protects Haimatsu from winter environmental stresses in the alpine region of Mt. Norikura.

Study site
Tree height of Haimatsu and snow depth differ greatly as a result of slight difference in topography. Two site of the study area were selected. (i) site P (wind-protected) and (ii) site E (wind-exposed). At site P, mean tree height was 1.1 m. There was a lot of snow accumulation and Haimatsu was almost entirely covered with snow during the winter. Needle browning and death occurred rarely. At site E, mean tree height was 0.4 m. Snow accumulation was minimal, and Haimatsu was not entirely covered with snow. Needle browning and death was observed frequently.

Winter needle death in Haimatsu[32]
At site E, the browning and death of needles of Haimatsu occurred mainly in early spring at the point where the shoot protrudes from the snowpack. They are thought to be caused by excessive water loss due to mechanical damage to the cuticle and/or to a thinner cuticle. However, needle browning and death in Haimatsu were not related to mechanical damage of the cuticle but might be due to changes in the quality and structure of the cuticle wax and resultant increase in water loss from needle cells.

Photosynthetic capacity in Haimatsu[33]

At site E, needles of Haimatsu had lower biomass, nitrogen, Rubisco (enzyme) and cell wall per unit area, and had higher photosynthetic capacity and shorter needle life-span than Haimatsu at site P. These results suggest that Haimatsu at wind-exposed site produces needles at low cost with high productivity to compensate for a short leaf life-span which may be imposed by wind stress when needles appear above the snow surface in winter.

Bibliography

[1] K. Munakata, S. Yasue, C. Kato, J. Kota, M. Tokumaru, M. Kojima, A. A. Darwish, T. Kuwabara and J. W. Bieber, "On the cross-field diffusion of galactic cosmic rays into the magnetic flux rope of a CME", *Advances in Geosciences*, 2, 115-124, eds. W. H. Ip and M. Duldig (World Scientific Publishing Co., USA), (2006).

[2] T. Kuwabara, J. W. Bieber, J. Clem, P. Evenson, R. Pyle, K. Munakata, S. Yasue, C. Kato, S. Akahane, M. Koyama, Z. Fujii, M. L. Duldig, J. E. Humble, M. R. Silva, N. B. Trivedi, W. D. Gonzalez and N. J. Schuch, "Real-time cosmic ray monitoring system for space weather", *Space Weather*, 4, S08001-1 10, (2006).

[3] M. R. Da Silva, A. Dal Lago, E. Echer, A. de Lucas, W. D. Gonzalez, N. J. Schuch, K. Munakata, L. E. A. Vieira, and F. L. Guarnieri, "Muon and neutron observations in connection with the corotating interaction regions", *Adv. Space Res.*, 40, pp348-352, (2007).

[4] Y. Okazaki, A. Fushishita, T. Narumi, C. Kato, S. Yasue, T. Kuwabara, J. W. Bieber, P. Evenson, M. R. Da Silva, A. Dal Lago, N. J. Schuch, Z. Fujii, M. L. Duldig, J. E. Humble, I. Sabbah, J. Kóta and K. Munakata, "Drift effects and the cosmic ray density gradient in a solar rotation period: First observation with the Global Muon Detector Network (GMDN)", *Astrophys. J.*, 681, 693-707, (2008).

[5] T. Kuwabara, J. W. Bieber, P. Evenson, K. Munakata, S. Yasue, C. Kato, A. Fushishita, M. Tokumaru, M. L. Duldig, J. E. Humble, M. R. Silva, A. Dal Lago, and N. J. Schuch, "Determination of ICME Geometry and Orientation from Ground Based Observations of Galactic Cosmic Rays", *J. Geophys. Res., 114*, A05109-1 10, doi:10.1029/2008JA013717, (2009).

[6] A. Fushishita, T. Kuwabara, C. Kato, S. Yasue, J. W. Bieber, P. Evenson, M. R. Da Silva, A. Dal Lago, N. J. Schuch, M. Tokumaru, M. L. Duldig, J. E. Humble, I. Sabbah, H. K. Al Jassar, M. M. Sharma, and K. Munakata, "Precursors of the Forbush Decrease on 2006 December 14 observed with the Global Muon Detector Network (GMDN)", *Astrophys. J.*, 715, 1239-1247, (2010).

[7] A. Fushishita, Y. Okazaki, T. Narumi, C. Kato, S. Yasue, T. Kuwabara, J. W. Bieber, P. Evenson, M. R. Da Silva, A. Dal Lago, N. J. Schuch, M. Tokumaru, M. L. Duldig, J. E. Humble, I. Sabbah, J. Kóta, and K. Munakata, "Drift effects and the average features of cosmic ray density gradient in CIRs during successive two solar minimum periods", *Advances in Geosciences*, eds. W. H. Ip and M. Duldig (World Scientific Publishing Co., USA), 21, 199-210, (2010).

[8] M. Tokumaru, M. Kojima, K. Fujiki, K. Munakata, T. Kuwabara and K. Marubashi, "Relation between loop-shaped interplanetary disturbances and the magnetic flux rope", *Advances in Geosciences*, eds. W. H. Ip and M. Duldig (World Scientific Publishing Co., USA), 21, 21-32, (2010).

[9] M. Rockenbach, A. Dal Lago, W. D. Gonzalez, K. Munakata, C. Kato, T. Kuwabara, J. W. Bieber, N. J. Schuch, M. L. Duldig, J. E. Humble, H. K. Al Jassar, M. M. Sharma, and I. Sabbah, "Geomagnetic Storms Precursors Observed from 2001 to 2007 with the Global Muon Detector Network GMDN", *Geophys. Res. Lett.*, 38, L16108-1 4, doi:10.1029/2011GL048556, (2011).

[10] "Solar neutron events of October-November 2003", Watanabe, K. *et al.*, Astrophys. J., **636**, 1135–1144, 2006.

[11] " Solar neutron events in association with large solar flares in November 2003", Watanabe, K. *et al.*, Adv. Space Res., **38**, 425–430, 2006.

[12] "Long-lived solar neutron emission in comparison with electron-produced radiation in the 2005 September 7 solar flare", Sako, T. *et al.*, Astrophys. J., **651**, L69–L72, 2006.

[13] " Highly significant detection of solar neutrons on 2005 September 7", Watanabe, K. *et al.*, Adv. Space Res., **39**, 1462–1466, 2007.

[14] " A solar neutron telescope in Tibet and its capability examined by the 1998 November 28th event", Muraki, Y. *et al.*, Astroparticle Phys., **28**, 119–131, 2007.

[15] " Simultaneous detection of high-energy solar neutrons and protons at Chacaltaya observatory on April 15, 2001", Muraki, Y. *et al.*, in Proc. 30th Int. Cosmic Ray Conf, Merida, **1**, 25–28, 2007.

[16] " Search for solar neutrons associated with series of X-class flares during the declining period of solar cycle 23", Matsubara, Y. *et al.*, in Proc. 30th Int. Cosmic Ray Conf, Merida, **1**, 29–32, 2007.

[17] " Ion acceleration and neutral emission mechanisms for 2005 September 7 flare", Watanabe, K. *et al.*, in Proc. 30th Int. Cosmic Ray Conf, Merida, **1**, 45–48, 2007.

[18] " Emission profile of solar neutrons obtained from the ground-based observations for the 7 September 2005 event", Sako, T. *et al.*, in Proc. 30th Int. Cosmic Ray Conf, Merida, **1**, 53–56, 2007.

[19] " Energy spectrum for the solar neutron event of September 7 2005, derived from the SNT at Sierra Negra", Gonzalez, L. X. *et al.*, in Proc. 30th Int. Cosmic Ray Conf, Merida, **1**, 57–60, 2007.

[20] " Status of the world-wide network of solar neutron telescopes in solar cycle 24", Matsubara, Y. *et al.*, in Proc. 31st Int. Cosmic Ray Conf, Lodz, **1**, On Conference homepage, 2009.

[21] " Detection of high-energy solar neutrons and protons by ground level detectors on April 15, 2001", Muraki, Y. *et al.*, Astropart. Phys., **29**, 229–242, 2008.

[22] " Solar neutron events as a tool to study particle acceleration at the Sun", Valdes-Galicia, J. F. *et al.*, Adv. Space Res., **43**, 565–572, 2009.

[23] " Physics of ion acceleration in the solar flare on 2005 September 7 determines γ-ray and neutron production", Watanabe, K. *et al.*, Adv. Space Res., **44**, 789–793, 2009.

[24] " Observation of solar neutrons associated with the large flare on 1991 June 4", Muraki, Y. *et al.*, ApJ, **400**, L75-L78 , 1992.

[25] " Observation of an energetic radiation burst from mountain-top thunderclouds", H. Tsuchiya *et al.*, Phys. Rev. Lett. **102**, 255003 (2009), Citation Index:13.

[26] Nishita, C., K. Osada, K. Matsunaga, Y. Iwasaka, e, J. Geophys. Res., **113**, D06202, doi:10.1029/2007JD009302, 2008.

"Nucleation mode particles in up-slope valley winds at Mt. Norikura, Japan: implications for the vertical extent of new particle formation events in the lower tropospher", Nishita, C., K. Osada, K. Matsunaga, Y. Iwasaka, J. Geophys. Res., **113**, D06202, doi:10.1029/2007JD009302, 2008.

[27] "Temporal variation of water-soluble ions of free tropospheric aerosol particles over central Japan", Osada, K., Kido, M., Nishita, C., Matsunaga, K., Iwasaka, Y., Nagatani, M., Nakada, H., Tellus, **59B**, 742-754, 2007.

[28] "Number-size distributions of free tropospheric aerosol particles at Mt. Norikura, Japan: effects of precipitation and air-mass transportation pathways", Nishita, C., K. Osada, K. Matsunaga, Y. Iwasaka, J. Geophys. Res., 112, doi:10.1029/2006JD007969, 2007.

[29] " Observations of total ozone and UV solar radiation with Brewer spectrophotometers on the Norikura mountains in 2009.", Ito, M., M. Takano, H. Oguri, M. Takita, H. Shimodaira and H. Ishitsuka, Jour. of the Aerological Observatory, **69**, 41-54 2011.

[30] " Observations of total ozone and UV solar radiation with Brewer spectrophotometers on the Norikura mountains, Northern Japanese Alps, from 2009.", Ito, M., S. Shimizu, Y. Noto, T. Shimamura, M. Takano, M. Takita, H. Shimodaira and H. Ishitsuka, The 13th WMO Biennial Brewer Workshop, Beijing, China in 2011, 2011.

[31] " Total ozone and UV solar radiation with Brewer spectrophotometers at Norikura of Northern Japanese Alps, in recent three years.", Ito, M., S. Shimizu, Y. Noto, T. Shimamura, M. Takita, H. Shimodaira and H. Ishitsuka, Jour. of the Aerological Observatory, **70**, in contribution.

[32] "Needle browning and death in Pinus pumila in the alpine region of central Japan were not related to mechanical damage of cuticle and cuticle thickness.", Nakamoto A., Ikeda T., Maruta E., Can. J. For. Res. 42, 167-178 (2012).

[33] "Needle traits of an evergreen, coniferous shrub growing at wind-exposed and protected sites in a mountain region: does Pinus pumila produce needles with greater mass per area under wind-stress conditions?", Nagano S., Nakano T., Hikosaka K and Maruta E., Plant Biology 11(Suppl.1), 94-100, (2009).

AKENO OBSERVATORY

Introduction

The Akeno Observatory is situated in Akeno of Hokuto-city, 20 km northwest of Kofu and 130 km west of metropolitan Tokyo. The location is at the longitude of 138.5°E and the latitude of 35.8°N. The altitude is ∼900 m above sea level. It was established in 1977 as a research center for air shower studies in the very high energy region, and it has been administered by the ICRR as a facility of joint-university-use.

The 40th anniversary of the Akeno Observatory

The lectures and the ceremony to celebrate the 40th anniversary of the Akeno Observatory were held at a hotel in Kofu in Yamanashi Prefecture on September 8th.

About 120 people attended the lectures and the ceremony including guests, companies, local residents and researchers who have contributed to the construction of the observatory and to the research at the observatory.

Before the lectures and the ceremony, a tour of the observatory was held. A ground detector that has bee used in Akeno, TAx4 ground detectors that have just assembled in the observatory were exhibited in the experimental hall together with related photographs including CTA for gamma-ray astronomy that is under construction in Lapalma. And the atmospheric Cherenkov telescope installed in the observatory campus and muong ground station just outside the campus were exhibited for the visitors.

After the tour, the lectures were given at the hotel by Prof. Kifune, Prof. Kakimoto and Prof. Teshima about the background of the founding and researches of the observatory. Following the lectures, the ceremony was held, where Norio Matsuki, Executive Director/Excecutive Vice-President of the University of Tokyo, Tomonori Nishii, Section Chief, Division of Academic Institutions of Ministry of Education, Culture, Science and Technology (MEXT), and Hitoshi Obi Akeno General Branch Office Manager of Hokuto city, gave congratulatory addresses. Then the letters of thanks were given by the ICRR Director Kajita to Hokuto City, Toko district, Asaohara district and a local resident who contributed to the Akeno Observatory. After the cremony, the celebration was held.

Akeno Air Shower Experiments

The Akeno Air Shower Experiment started in 1979 with an array covering 1 km² area (the 1 km² array, see Fig.1). The array was enlarged to 20 km² in 1984 and was gradually expanded to Akeno Giant Air Shower Array (AGASA) of approximately 100 km² area by 1990. The AGASA was built to detect Ultra-High Energy Cosmic Rays (UHECRs) in the energy range of 10^{20} eV.

Fig. 1. Aerial View of Akeno Observatory and 1 km² Array Area

One of the distinctive features of Akeno experiments is that the measurements were made over five decades of energies well covering 10^{15} eV - 10^{20} eV by using both the surface detector for electromagnetic component, and the shielded detector for muon component (Fig.2). The wide energy coverage was accomplished by the arrays of scintillation detectors of various inter-detector spacings from 3 m to 1 km and with different triggering conditions. This feature of Akeno air shower measurement is well demonstrated in Fig.3, in which the spectra from Akeno 1 km² array for $10^{14.5}$ eV - $10^{18.8}$ eV [3] and AGASA for $10^{18.5}$ eV - $10^{20.3}$ eV [4] are plotted.

Fig. 2. One of the muon detector housings with concrete shielding.

[3] M. Nagano et al., J. Phys. **G10**, 1295 (1984); M. Nagano et al., J. Phys. **G18**, 423 (1992).
[4] M. Takeda et al., Astropart. Phys. **19**, 447 (2003).
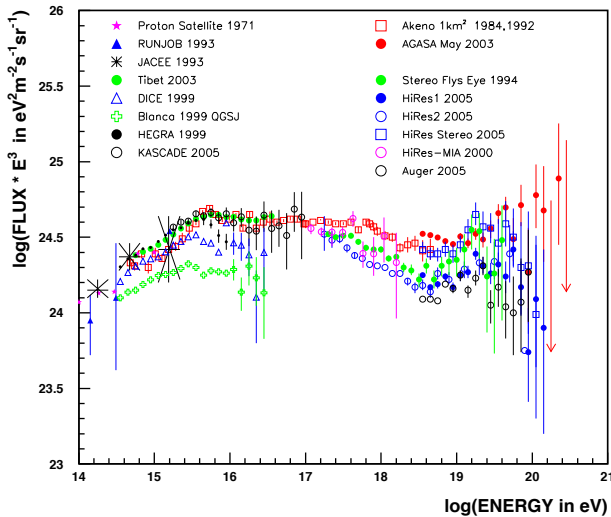
Fig. 3. Akeno energy spectrum measurements for 10^{15} eV - 10^{20} eV.

AGASA

The AGASA was composed of 111 surface detectors, each with plastic scintillator of 2.2 m^2 area and 5 cm thickness. The counters were deployed with ∼1 km spacing covering the ground area of about 100 km^2 in the suburban area of Akeno, outside of the observatory campus. All counters were connected with optical fibers for the timing measurement and digital data transfer to the observatory. The AGASA served as the largest air shower array in the world since its commissioning in 1990 until it stopped data taking in January 2004, when the construction of the succeeding experiment, Telescope Array (TA), started in Utah. The AGASA was dismantled in 2007 together with other Akeno air shower arrays.

An exposure of 5.8×10^{16} m^2 s sr above 10^{19} eV was accumulated by AGASA in 13 years of operation. Extensive air showers with zenith angles smaller than 45° and with core locations inside the array area were used for the analysis. The AGASA reported an extension of the energy spectrum beyond the predicted Greisen-Zatsepin-Kuzmin (GZK) cutoff in 1998 [5] and a total of eleven UHECR events were observed above 10^{20} eV by 2003.

Measurement of UHECRs

Since the AGASA measurement in 1998, High Resolution Fly's Eye (HiRes) [6], Pierre Auger Observatory (PAO) [7], and Telescope Array (TA) [8] measured the energy spectra of UHE-CRs with higher statistics.

The HiRes observed the UHECR using the fluorescence telescope. The PAO and the TA measure the energy spectra using the surface array consisting of either water tanks (PAO) or plastic scintillators (TA), but the energy scale of the array is determined by the fluorescence telescope using a subset of

events observed by the fluorescence telescope and surface array at the same time. The adoption of the energy scale by the fluorescence telescopes is based on its small dependence on the air shower simulation.

The energy spectra above 10^{18} eV by AGASA and other experiments are compiled and compared by the working group represented by UHECR experiments in the UHECR2012 symposium held at CERN for Feb. 13th - 16th, 2012 [9]. The result is plotted in Fig.4 with the energy scale of each experiment adjusted to a reference energy, which is set halfway between PAO and TA/HiRes. Following factors were applied for the energy scale; ×1.10 for PAO, ×0.91 for TA and HiRes, ×0.65 for AGASA and ×0.56 for Yakutsk.
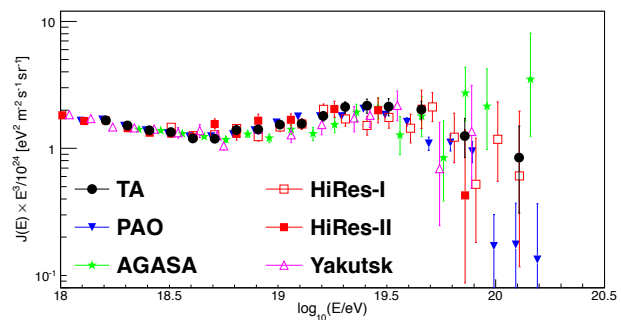
Fig. 4. Compilation of UHECR energy spectra (UHECR2012). The energy scale of each experiment is adjusted as described in the text.

As seen in Fig.4, the overall agreement between experiments is good, and a "dip" structure was seen around $10^{18.7}$ eV by all experiments. The HiRes, PAO and TA confirmed a strong flux suppression above approximately $10^{19.7}$ eV. Although the AGASA spectrum does not demonstrate the cutoff structure, the number of events above 10^{20} eV became only two after the energy rescaling, making the claim of the extended spectrum statistically insignificant. The estimate of systematic uncertainty of the energy measurement is approximately 20% for all the experiments, and rescalings for the TA/HiRes and PAO are within this limit. Rescaling of the surface array energy, ×0.65 for AGASA and ×0.56 for Yaktsuk, indicates that there exist larger systematic uncertainties than originally estimated by running the air shower simulation. This difference of energy scale obtained by the surface array and by the fluorescence telescope remains as a basic question in the understanding of the air shower phenomena. The recent detailed feature of energy spectra by PAO and TA with more statistics are described in the section of TA in this annual report.

Recent Research Activities

The study of UHECRs by AGASA in Akeno was succeeded by the TA experiment in Utah, USA since 2008. After the cessation of AGASA, the Akeno Observatory has been used for small scale cosmic ray experiments, astrophysical observations and as a test and maintenance facility of TA by the

*5 M. Takeda et al., Phys. Rev. Lett. **81**, 1163 (1998).
*6 R.U. Abbasi et al., Phys. Rev. Lett. **100**, 101101 (2008).
*7 J. Abraham et al., Phys. Lett. **B685**, 239 (2010).
*8 T. Abu-Zayyad et al., Astrophys. J. **768**, L1 (2013).
*9 http://indico.cern.ch/conferenceDisplay.py?confId=152124

ICRR and university researchers. Fig.5 shows a recent photograph of the main site of the Akeno Observatory.

Fig. 5. The main site of the Akeno Observatory. There are the movable tent for a small atmospheric Cherenkov telescope, the large experimental hall, the research building and the lodging facility from the left.

Research and development for the Telescope Array observation in Utah by the TA collaboration

All the TA fluorescence imaging cameras were assembled in the Akeno Observatory by the TA collaboration team. The detectors were tested in Akeno and shipped to the Utah observation site for the installation. All the unit mirrors of the TA fluorescence telescope were tested in Akeno and the atmospheric monitoring lidar of TA using YAG laser was developed in Akeno. In JFY 2015, the R&D of the surface detectors were performed in the large experimental hall of the Akeno Observatory for the TAx4 project that quadruples the TA surface detector array in Utah. In August in 2016, and 2017 the TAx4 scintillator counters were assembled.

Observation by the multi-color imager for transients, survey and monstrous explosions (MITSuME) by N. Kawai (Tokyo Institute of Technology) et al.

One of the three MITSuME robotic telescopes was installed in the Akeno Observatory in 2003 (Fig. 6). The telescope has an aperture of 50 cm, an FOV of 28' $\times$ 28' and is equipped with a tricolor CCD camera capable of $g'R_CI_C$-bands photometry (g':400$\sim$550 nm, Rc:570$\sim$730 nm, Ic:730$\sim$ 850 nm). It is operated remotely from the Tokyo Tech at the Ookayama Campus using dedicated ADSL connections. Upon receiving a GRB alert from Swift or Fermi satellite, it quickly directs the telescope (9°/s maneuverability) toward the GRB direction, and makes a prompt observation of the GRB and its afterglow.

The following is the status as of December in 2017. For GRB afterglow observation, MITSuME identified 4 objects in the period between 2016/12/01 and 2017/11/30, and performed continuous multi-coloro observation of GRB 161017A. MITSuME joined J-GEM and GROWTH, and performed follow-up observation of gravitational wave events for GW170105 and GW170817 with visible light. In November of 2017, the two MITSuME at the Akeno Observatory and the Okayama Astrophysical Observatory started cooperation for efficient follow-up observation of burst phenomena.
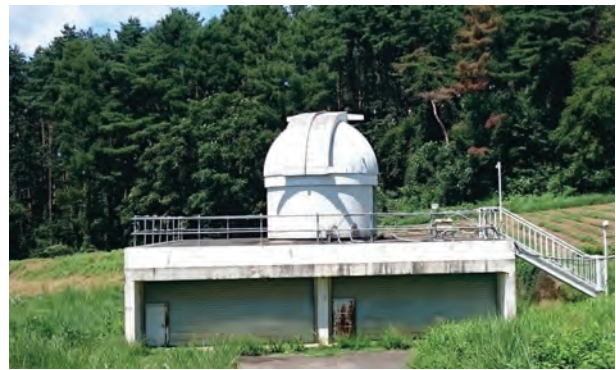
Fig. 6. The dome in which the MITSuME telescope was installed in Akeno.

Observation of galactic cosmic rays by large area muon telescope by A. Oshima (Chubu University) et al.

Four layers of proportional counter telescopes, each with 25 m^2 area, were installed in three muon houses in Akeno and have been continuously measuring the cosmic ray muons since 2003. Fig. 2 shows one of the muon houses. The mode energy of the primary cosmic rays is approximately 2.5 GeV corresponding to 2m thick concrete ceiling of the muon house at the latitude of the Akeno Observatory. The measurement in Akeno is combined with a simultaneous measurement by the GRAPES-3 experiment at Ooty in India, and the modulation effects of galactic cosmic rays by the solar activity such as the Forbush decrease and its precursor have been continuously monitored [10]. In JFY 2017, bad proportional counters were identified and repaired, and the work for long-term stable observation was done.

Research and development for a small atmospheric Cherenkov telescope at the Akeno Observatory by T. Yoshikoshi (ICRR) et al.

An alt-azimuth telescope with an aperture of three meters (Fig. 7) is being setup in the Akeno Observatory for various prototype tests with atmospheric Cherenkov observations of gamma rays on the ground [11]. This telescope is the only telescope to observe atmospherice Cherenkov light emitted from air showers induced by TeV gamma rays in Japan. In JFY2016, an atmospheric cherenkov light event was firstly observed with this telescope. By the observation of the Crab Nebula that is a standard object in TeV gamma-ray region in JFY2017, the data of the Crab Nebula of less than ten hours and the similar amount of background data were taken. The data would be analyzed in JFY2018.

Other research

A part of the large experimental hall was used for the support for the research on low frequency anti-vibration system of KAGRA: acceptance of devices, temporary storage and partial assembly before the installation in KAGRA. Remaining gasl filters for low-temperature mirrors, top filters and inverted

*[10] T. Nonaka.et al, Proc. of the 29th ICRC, **1**, 363-366 (2005).
*[11] M. Ohishi et al., 33rd ICRC, (Rio deJaneiro), **9**, in press (2013).

Fig. 7. The Cherenkov telescope at the tour of the 40th anniversary of the Akeno Observatory.

pendulums that have been stored in Akeno were shipped to the Kamioka Observatory.

Other tests using facilities or detectors in the Akeno Observatory were also performed.

KAMIOKA OBSERVATORY

Kamioka observatory is located at 1000 m underground (2700 m water equivalent) in the Kamioka Mine, Gifu prefecture, about 200 km west of Tokyo. The observatory was established in 1995 in order to operate Super-Kamiokande experiment (SK). The underground laboratories are located under Mt.Ikeno-yama and accessible to the experimental site through a 1.7 km horizontal tunnel. The observatory also has surface research buildings and a dormitory located at the distance of 15 minutes drive from the entrance of the underground laboratories.

The Super-Kamiokande experiment had discovered neutrino oscillations through the observations of atmospheric and solar neutrinos (see the section for Neutrino and Astroparticle Division). The atmospheric neutrino oscillation was confirmed by the long baseline neutrino oscillation experiment, K2K, using accelerator neutrino beam, which was conducted between 1999 and 2004. A new long baseline neutrino oscillation experiment (the T2K experiment) using a high intensity beam, 50 times of the K2K neutrino beam, by the J-PARC proton accelerator has started in 2009. In 2011, the experiment has observed 6 ν_e appearance events indicating non-zero θ_{13} which was as yet determined the last neutrino oscillation parameter. Anti-neutrino beam data was taken from 2014 to 2016 in order to search for CP violation. Based on the whole data taken until 2016, T2K presented the first CP violation search result in August 2016.

The low cosmic ray flux and low seismic noise environ-ment in the underground site enables us to conduct various researches. There is a 100 m long laser interferometer, which is a proto-type of the 3 km gravitational wave antenna (KAGRA). Using the low radioactive background environment in the Kamioka Mine, a dark matter experiment, called XMASS is operated in Lab-C. The XMASS group constructed a 800kg liquid xenon detector and started data taking from 2010. The detector has been improved and searches for dark matter interactions and rare phenomena in luquid xenon have been conducted in the last few years. The R&D study of a tracking type detector for dark matter detection led by the Kobe University group (the NEWAGE experiment) has also been performed in Lab-B. A double beta decay experiment using ^{48}Ca (the CANDLES experiment) led by the Osaka University group has been running in Lab-D. The study to improve the neutrino detection sensitivity by adding gadolinium to Super-Kamiokande (called SK-Gd project) has been performed at Lab-E. A 200 ton test tank dedicated for the R&D study of the SK-Gd project was constructed and a feasibility study has been performed. In order to support those experiments and also related R&D works, the Observatory is equipped with low background Germanium detector in Lab-1 and Lab-A, ICP-MS and so on to measure extremely low radioactive backgrounds. Lab-G area was newly excavated in 2015 and the SK-Gd equipments which include a Gd dissolving system, a pre-treatment system and a Gd-water circulation system were installed in 2016.
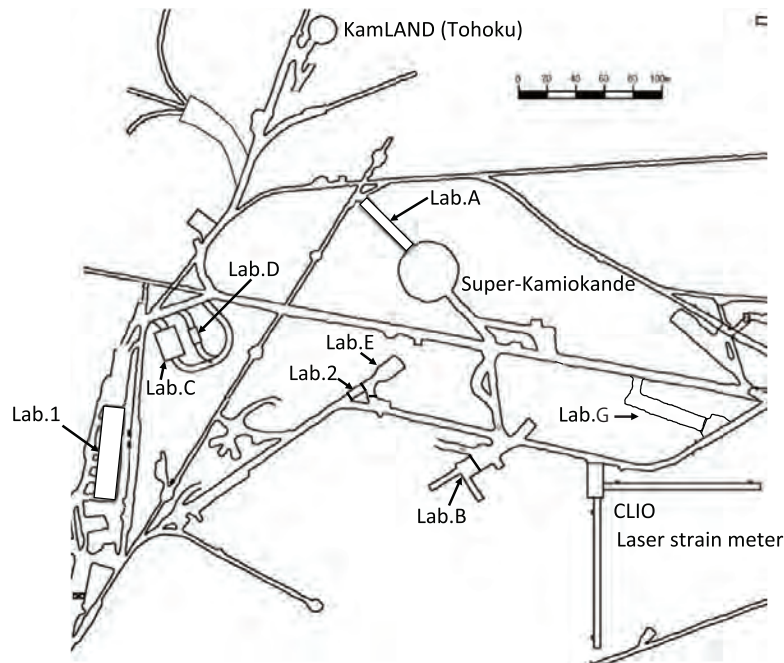
Fig. 1. Kamioka Underground Observatory.

KAGRA OBSERVATORY

KAGRA observatory is located in the Ikenoyama-mountain on the border between Gifu and Toyama prefecture, about 35 km south of Toyama city in Japan. The observatory was established in 2016 in order to operate Large -scale Cryogenic Gravitational Wave Telescope (nicknamed "KAGRA"). KAGRA itself has a L-shape tunnel facility, and it is located more than 200m under Mt.Ikeno-yama. The corner station of the L-shape tunnel is accessible through a 500-m horizontal access tunnel from Atotsu area. The observatory has its own surface research buildings and rental space in the community center of Hida city located about 5km away from the Atotsu entrance of KAGRA.

KAGRA aims to observe several gravitational waves (GWs) per a year with its designed sensitivity as one of observatories of the world GW detection network including Advanced-LIGO, Advanced-Virgo and planned LIGO-India. KAGRA project (formerly named LCGT) was partially approved in 2010 as one of Leading-edge Research Infrastructure Program, and also supported by Program for Promoting Large-scale Science Projects, Subsidy for Facilities Expense and Grants-in-Aid for Scientific Research from Ministry of Education, Culture, Sports, Science and Technology (MEXT).

In KAGRA project, Institute for Cosmic Ray Research plays a role of a host promoting institute, and National Astronomical Observatory in Japan (NAOJ) and High Energy Accelerator Research Organization (KEK) are the main support organizations, then more than 280 researchers in 87 institutes and universities in the world are collaborating for construction and data analysis of KAGRA.

The tunnel excavation started in May 2012, and finished in March 2014. After that, the basic laboratory environment was prepared until September 2015. A Michelson interferometer with 3km arm (iKAGRA) was demonstrated in March 2016, and the first engineering run was performed until May 2016. At present (June 2018) all interferometer components are being installed to complete KAGRA observatory that adopts a power recycled Fabry-Perot Michelson type interferometer with resonant sideband extraction technique. We hope to start KAGRA observatory operation around March 2019 and start joint observation with LIGO and Virgo within 2019.

Fig. 1. Surface Research Building.

Fig. 2. Atotsu Entrance of KAGRA.

RESEARCH CENTER FOR COSMIC NEUTRINOS

The Research Center for Cosmic Neutrinos (RCCN) was established in April 1999. The main mission of this center is to promote researches related to neutrinos based on data from various observations and experiments, and we have provided the occasion to discuss theoretical ideas and experimental results on neutrino physics. Members of this center have been involved in the Super-Kamiokande and T2K experiments, and contributing precise measurements of neutrino oscillations. Also, we have been involved in Hyper-Kamiokande project, and worked on the calculation of the atmospheric neutrino flux to have better predictions of the neutrino flux.

RCCN, together with the computer committee, oversees the operation of the central computer system in ICRR (Fig 1). The computer facility has high performance to analyze huge amount of data, and has been operated without any serious trouble since it was upgraded in 2014. Since 2004, RCCN has been accepted inter-university programs related to activities in the low-background underground facility also (Fig 2). In FY2017, we accepted 8 programs related to these facilities.

RCCN has been organizing domestic neutrino-related workshop since it was established. On February 24, 2018, we hosted one neutrino workshop on "High Energy Neutrino and CP". Thirty-three physicists participated in this meeting. We have also contributed holding public lectures. Since JFY2009, ICRR and the Kavli Institute for the Physics and Mathematics of the Universe (Kavli-IPMU) have co-sponsored two public lectures each year. The public lecture held in Spring is co-organized by RCCN and the Public Relation Office of ICRR. The Spring public lecture in FY2017 was held on April 15, 2017. Two scientists lectured on the latest result of the highest energy comic ray observations and the study of the Calabi-Yau manifold.

Fig. 1. Photo of the central computer faciilty in ICRR upgraded in 2014.

Fig. 2. Photo of the low-background underground facility in ICRR.

APPENDICES

A. ICRR Workshops and Ceremonies

B. ICRR Seminars

C. List of Publications

    (a) Papers Published in Journals

    (b) Conference Papers (Proceedings)

    (c) ICRR Report

D. Doctoral Theses

E. Public Relations

    (a) ICRR News

    (b) Public Lectures

    (c) Visitors

F. Inter-University Research Activities

G. List of Committee Members

    (a) Board of Councillors

    (b) Advisory Committee

    (c) Inter University Research Advisory Committee

H. List of Personnel

A. ICRR Workshops and Ceremonies

Inauguration Ceremony of Next-Generation Neutrino Science Organization for the Hyper-Kamiokande Nucleon Decay and Neutrino Experiment
Date: Nov. 8, 2017
Place: Kamioka Observatory

Outline: On October 1, 2017, The University of Tokyo launched Next-Generation Neutrino Science Organization (NNSO), where the Institute for Cosmic Ray Research, the Kavli Institute for the Physics and Mathematics of the Universe (Kavli IPMU), and the School of Science cooperate for pioneering the future of neutrino physics through the development of neutrino research techniques and detector technologies. In particular, it aims to promote what will become its flagship facility, the Hyper-Kamiokande project. To mark the occasion, an inaugural ceremony was held on November 8, 2017 in Kamioka Observatory, Japan.

Professor Takaaki Kajita, Director of NNSO and Nobel laureate, stated the importance of the major objectives of the organization in his opening remarks. Professor Masashi Haneda, Executive Vice President of The University of Tokyo, greeted attendees. The ceremony was followed by congratulatory speeches from Tomonori Nishii, Section Chief, Division of Academic Institutions of Ministry of Education, Culture, Science and Technology (MEXT), and addresses by Prof. Hiroyuki Takeda, Dean of School of Science and Prof. Hitoshi Murayama, Director of Kavli IPMU.

The ceremony was attended by about 100 people from MEXT, The University of Tokyo, KEK, local government and community, Kamioka mining and smelting company, and collaborating scientists. At the end, all attendees got together to take a group photo and celebrated the start of the new organization for promotion of neutrino physics and Hyper-Kamiokande project.

Participants: 100 participants.

Fig. 1. Inauguration Ceremony of Next-Generation Neutrino Science Organization.

Extreme Universe viewed with High Energy Gamma Rays
Date: Dec 18-19, 2017
Place: Media Hall, Kashiwa Library, The University of Tokyo

Outline: This workshop invited the talks on high-energy astrophysics, and provided the place of discussion to make future strategies for TeV Gamma-Ray astronomy to play a role in multi-messenger astronomy, working with high-energy neutrino observations and gravitational wave observations. The current status on science and construction of CTA Large Size Telescope, promoted by JSPS Grants-in-Aid for Scientific Research, was also reported.

Participants: 60 participants.

Tokyo Spring Cosmic Lyman-Alpha Workshop

Date: Mar 26 - Mar 30, 2018
Place: Koshiba Hall, School of Science, The University of Tokyo

Outline: This conference aims to discuss progresses in recent observational and theoretical studies of Lyα emission and absorption, and to explore the next generation of Lyα studies with forthcoming large facilities and technologies, such as the James Webb Space Telescope. More specifically, the following three topics and the relevant scientific results and projects were discussed:

- Lyα emission as a probe of galaxy formation and evolution

- Lyα emission and absorption as a probe of the ISM/CGM/IGM/LSS

- Lyα emission as a probe of reionization

Participants: 120 participants.

Fig. 2. Tokyo Spring Cosmic Lyman-Alpha Workshop.

B. ICRR Seminars

1. April 14, 2017: Dr. Tsuguo Aramaki (SLAC), "Hunting for Dark Matter With SuperCDMS" (ICRR & IPMU joint seminar)

2. April 28, 2017: Dr. Ryo Namba (McGill University), "Magnetic fields of primordial origin" (ICRR & IPMU joint seminar)

3. May 9, 2017 : Dr. Hang Bae Kim (Hanyang University), "Where is cosmology going?"

4. June 5, 2017 : Dr. Ellis Owen (University College London), "The implications of cosmic ray heating in and around the interstellar medium of high-redshift starbursts"

5. June 28, 2017 : Dr. Hideyuki Tagoshi (ICRR), "Challenges to Gravitational Wave Physics and Astronomy"

6. July 11, 2017 : Dr. Elena Aprile (Columbia University), "First Results from the XENON1T Dark Matter Experiment"

7. July 26, 2017 : Dr. Markus Holler (Innsbruck, Austria), "After the H.E.S.S. I Legacy - Challenges and Prospects for the First Hybrid IACT Array"

8. August 4, 2017: Dr. Christophe Bronner (ICRR), "T2K neutrino oscillation results with data up to 2017 Summer"

9. August 9, 2017: Dr. Laszlo Olah (Earthquake Research Institute, The University of Tokyo), "Application of new variant of gaseous tracking detectors for CR detection and muography"

10. October 20, 2017: Dr. Anatoly Lagutin (Altai state university, Russia), "Anomalous diffusion of cosmic rays in the Galaxy"

11. October 25, 2017: Dr. Stefan Schlenstedt (DESY Zeuthen and ICRR, U-Tokyo), "The Medium Size Telescopes for CTA"

12. November 10, 2017: Dr. Andrew J Long (University of Chicago), "Topics in Axion Cosmology" (ICRR-IPMU joint seminar)

13. December 12, 2017: Dr. Julian Sitarek (University of Lodz), "Observations of Flat Spectrum Radio Quasars with MAGIC"

14. January 12, 2018 : Dr. Toshikazu Ebisuzaki (RIKEN), "M82 starburst galaxy: possible object of the northern hotspot"

15. January 16, 2018 : Dr. Kevin McFarland (University of Rochester), "Recent Results on GeV Neutrino Interactions" (ICRR-IPMU joint seminar)

16. January 19, 2018 : Dr. Yuzuru Yoshii (ICRR)

C. List of Publications

(a) Papers Published in Journals

1. "Measurement of radon concentration in Super-Kamiokande's buffer gas", Y. Nakano, H. Sekiya, S. Tasaka, Y. Takeuchi, R.A. Wendell, M. Matsubara, M. Nakahata, Nuclear Inst. and Methods in Physics Research, A **867** (2017) 108-114.

2. "Search for solar Kaluza-Klein axions by annual modulation with the XMASS-I detector", N. Oka et al. (XMASS Collaboration), Prog. Theor. Exp. Phys. **2017**, 103C01.

3. "Determination of trace levels of uranium and thorium in high purity gadolinium sulfate using the ICP-MS with solid-phase chromatographic extraction resin", S. Ito, Y. Takaku, M. Ikeda, Y. Kishimoto, Progress of Theoretical and Experimental Physics, Volume **2017**, Issue 11.

4. "Identification of ^{210}Pb and ^{210}Po in the bulk of copper samples with a low-background alpha particle counter", K. Abe et al. (The XMASS Collaboration), Nuclear Inst. and Methods in Physics Research, A**884** (2018) 157-161.

5. "Search for nucleon decay into charged antilepton plus meson in 0.316 megaton· years exposure of the Super-Kamiokande water Cherenkov detector", Super-Kamiokande Collaboration, Phys. Rev. D **96**, 012003.

6. "Search for an Excess of Events in the Super-Kamiokande Detector in the Directions of the Astrophysical Neutrinos Reported by the IceCube Collaboration", The Super-Kamiokande Collaboration, Astrophys. J. **850**, 166 (2017).

7. "Towards a unified model of neutrino-nucleus reactions for neutrino oscillation experiments", S X Nakamura, H Kamano, Y Hayato, M Hirai, W Horiuchi, S Kumano, T Murata, K Saito, M Sakuda, T Sato, Rept.Prog.Phys. **80** (2017) no.5, 056301 .

8. Measurement of σ_{ABS} and σ_{CX} of π^+ on carbon by the Dual Use Experiment at TRIUMF(DUET)", E.S.Pinzon Guerra et al. (DUET collaboration), Phys. Rev. C**95**(2017) no.4, 045203.

9. "First neutrino event detection with nuclear emulsion at J-PARC neutrino beamline", T. Fukuda et al., PTEP **2017** (2017) no. 6, 063C02.

10. "First demonstration of an emulsion multi-stage shifter for accelerator neutrino experiments in J-PARC T60", Y. Yamada et al. , PTEP **2017** (2017) no.6, 063H02.

11. "Combined Analysis of Neutrino and Antineutrino Oscillations at T2K", K. Abe et al. (The T2K collaboration), Phys. Rev. Lett. **118** (2017) no.15, 151801.

12. "Search for Lorentz and CPT violation using sidereal time dependence of neutrino flavor transitions over a short baseline", K. Abe et al. (The T2K collaboration), Phys. Rev. D**95** (2017) no.11, 111101.

13. "Updated T2K measurements of muon neutrino and antineutrino disappearance using 1.5×10^{21} protons on target", K. Abe et al. (The T2K collaboration), Phys. Rev. D**96** (2017) no.1, 011102.

14. "Measurement of the single π^0 production rate in neutral current neutrino interactions on water", K. Abe et al. (The T2K collaboration), Phys. Rev. D**97** (2018) no.3, 032002.

15. "Measurement of $\bar{\nu}_\mu$ and ν_μ charged current inclusive cross sections and their ratio with the T2K off-axis near detector", K. Abe et al. (The T2K collaboration), Phys. Rev. D**96** (2017) no.5, 052001 .

16. "Measurement of neutrino and antineutrino oscillations by the T2K experiment including a new additional sample of ν_e interactions at the far detector", K. Abe et al. (The T2K collaboration), Phys. Rev. D**96** (2017) no.9, 092006.

17. "First measurement of the ν_μ charged-current cross section on a water target without pions in the final state", K. Abe et al. (The T2K collaboration), Phys. Rev. D**97** (2018) no.1, 012001.

18. "Developement of an ominidirectional gamma-ray imaging Compton camera for low-radiation-level environmental monitoring", T.Watanabe, R.Enomoto, H.Muraishi,et al., Jpn. J. Appl. Phys. **57** 026401.

19. "Indirect dark matter searches in the dwarf satellite galaxy Ursa Major II with the MAGIC telescopes", M. L..Ahnen., D.Hadasch, M.Hayashida, D.Mazin, T.Nagayoshi, K.Noda, T.Saito, M.Takahashi, M. Teshima et al., Journal of Cosmology and Astroparticle Physics.

20. "Search for very high-energy gamma-ray emission from the microquasar Cygnus X-1 with the MAGIC telescopes", M. L.. Ahnen., D.Hadasch, M.Hayashida, D.Mazin, T.Nagayoshi, K.Noda, T.Saito, M.Takahashi, M. Teshima et al., Monthly Notice of Royal Astronmical Society.

21. "A cut-off in the TeV gamma-ray spectrum of the SNR Cassiopeia A", M. L.. Ahnen., D.Hadasch, M.Hayashida, D.Mazin, T.Nagayoshi, K.Noda, T.Saito, M.Takahashi, M. Teshima et al., Monthly Notice of Royal Astronmical Society.

22. "MAGIC observations of the microquasar V404 Cygni during the 2015 outburst", M. L.. Ahnen., D.Hadasch, M.Hayashida, D.Mazin, T.Nagayoshi, K.Noda, T.Saito, M.Takahashi, M. Teshima et al., Monthly Notice of Royal Astronmical Society.

23. "Observation of the black widow B1957+20 millisecond pulsar binary system with the MAGIC telescopes", M. L.. Ahnen., D.Hadasch, M.Hayashida, D.Mazin, T.Nagayoshi, K.Noda, T.Saito, M.Takahashi, M. Teshima et al., Monthly Notice of Royal Astronmical Society.

24. "Constraining Lorentz Invariance Violation Using the Crab Pulsar Emission Observed up to TeV Energies by MAGIC", M. L.. Ahnen., D.Hadasch, M.Hayashida, D.Mazin, T.Nagayoshi, K.Noda, T.Saito, M.Takahashi, M. Teshima et al., The Astrophysical Journal Supplement Series, **232**:9, September 2017.

25. "Performance of the MAGIC telescopes under moonlight", M. L.. Ahnen., D.Hadasch, M.Hayashida, D.Mazin, T.Nagayoshi, K.Noda, T.Saito, M.Takahashi, M. Teshima et al., Astroparticle Physics.

26. "Multiband variability studies and novel broadband SED modeling of Mrk 501 in 2009", M. L.. Ahnen., D.Hadasch, M.Hayashida, D.Mazin, T.Nagayoshi, K.Noda, T.Saito, M.Takahashi, M. Teshima et al., Astronomy and Astrophysics.

27. "Multiwavelength observations of a VHE gamma-ray flare from PKS 1510-089 in 2015", M. L.. Ahnen., D.Hadasch, M.Hayashida, D.Mazin, T.Nagayoshi, K.Noda, T.Saito, M.Takahashi, M. Teshima et al., Astronomy and Astrophysics.

28. "First multi-wavelength campaign on the gamma-ray-loud active galaxy IC 310", M. L.. Ahnen., D.Hadasch, M.Hayashida, D.Mazin, T.Nagayoshi, K.Noda, T.Saito, M.Takahashi, M. Teshima et al., Astronomy and Astrophysics.

29. "MAGIC detection of very high energy γ-ray emission from the low-luminosity blazar 1ES 1741+196", M. L.. Ahnen., D.Hadasch, M.Hayashida, D.Mazin, T.Nagayoshi, K.Noda, T.Saito, M.Takahashi, M. Teshima et al., Monthly Notice of Royal Astronmical Society.

30. "Very-high-energy gamma-ray observations of the Type Ia Supernova SN 2014J with the MAGIC telescopes", M. L.. Ahnen., D.Hadasch, M.Hayashida, D.Mazin, T.Nagayoshi, K.Noda, T.Saito, M.Takahashi, M. Teshima et al., Astronomy and Astrophysics.

31. "Observations of Sagittarius A* during the pericenter passage of the G2 object with MAGIC", M. L.. Ahnen., D.Hadasch, M.Hayashida, D.Mazin, T.Nagayoshi, K.Noda, T.Saito, M.Takahashi, M. Teshima et al., Astronomy and Astrophysics.

32. "Prospects for Cherenkov Telescope Array Observations of the Young Supernova Remnant RX J1713.7-3946", F.Acero., D.Hadasch, M.Hayashida, D.Mazin, T.Nagayoshi, K.Noda, T.Saito, M.Takahashi, M. Teshima et al., Astrophysical Journal.

33. "The bursts of high energy events observed by the telescope array surface detector", R.U. Abbasi, et al., Phys. Lett. A **381** (2017) 2565-2572.

34. "Past, present, and future of UHECR observations", B R Dawson, M Fukushima, P Sokolsky, Prog. Theor. Exp. Phys. **2017**, 12A101.

35. "Measurement of anisotropy and the search for ultra high energy cosmic ray sources", O. Deligny, K. Kawata and P. Tinyakov, Prog. Theor. Exp. Phys. **2017**, 12A104.

36. "Energy determination of gamma-ray induced air showers observed by an extensive air shower array", K. Kawata, T.K. Sako, M. Ohnishi, et al., Exp. Astron. **44**:1-9.

37. "Evaluation of the Interplanetary Magnetic Field Strength Using the Cosmic-Ray Shadow of the Sun", M. Amenomori et al. (The Tibet ASγ Collaboration), Phys. Rev. Lett. **120**, 031101.

38. "Broadband Photon Spectrum and its Radial Profile of Pulsar Wind Nebulae", Wataru Ishizaki, Shuta J. Tanaka, Katsuaki Asano, and Toshio Terasawa, The Astrophysical Journal, Volume **838**, 142.

39. "On the Radio Emitting Particles of the Crab Nebula: Stochastic Acceleration Model", Shuta J. Tanaka, Katsuaki Asano, APJ**841**:78(11pp).

40. "Temporal Evolution of the Gamma-ray Burst Afterglow Spectrum for an Observer: GeV–TeV Synchrotron Self-Compton Light Curve", Takuma Fukushima, Sho To, Katsuaki Asano, and Yutaka Fujita, APJ**844**：92（2017）.

41. "Long Gamma Ray Burst Rate in the Binary Merger Progenitor Model", Tomoya Kinugawa, and Katsuaki Asano, APJL**849**:L29（2017）.

42. "How to Confirm the Existence of Population III Stars by Observations of Gravitational Waves", Akinobu Miyamoto, Tomoya Kinugawa, Takashi Nakamura, Nobuyuki Kanda, Phys. Rev. D **96**, 064025.

43. "Multi-messenger Observations of a Binary Neutron Star Merger", B. P. Abbott, et al., APJL**848**:L12（2017）.

44. "Subsequent Non-thermal Emission due to the Kilonova Ejecta in GW170817", Katsuaki Asano, and Sho To, APJ**852**:105(5pp), 2018.

45. "Energy Spectrum of Cosmic-ray Electron and Positron from 10 GeV to 3 TeV Observed with the Calorimetric Electron Telescope on the International Space Station", O. Adriani, Y. Akaike, K. Asano, et al., Phys. Rev. Lett. **119**, 181101.

46. "On-orbit Operations and Offline Data Processing of CALET onboard the ISS", Y. Asaoka, S. Ozawa, S. Torii et al., Astroparticle Physics **100**(2018)29-37.

47. "Optimal follow-up observations of gravitational wave events with small optical telescopes", Tatsuya Narikawa, Masato Kaneyama, Hideyuki Tagoshi, Physical Review D **96**, 084067.

48. "Black hole ringdown echoes and howls", Hiroyuki Nakano, Norichika Sago, Hideyuki Tagoshi, Takahiro Tanaka, Progress of Theoretical and Experimental Physics, **2017**, 071E01.

49. "Construction of KAGRA: an Underground Gravitational Wave Observatory", Akutsu, T.; Ando, M.; Araki, S.; Araya, A.; Arima, T.; Aritomi, N.; Asada, H.; Aso, Y.; Atsuta, S.; Awai, K.; Baiotti, L.; Barton, M. A.; Chen, D.; Cho, K.; Craig, K.; DeSalvo, R.; Doi, K.; Eda, K.; Enomoto, Y.; Flaminio, R.; Fujibayashi, S.; Fujii, Y.; Fujimoto, M.-K.; Fukushima, M.; Furuhata, T.; Hagiwara, A.; Haino, S.; Harita, S.; Hasegawa, K.; Hasegawa, M.; Hashino, K.; Hayama, K.; Hirata, N.; Hirose, E.; Ikenoue, B.; Inoue, Y.; Ioka, K.; Ishizaki, H.; Itoh, Y.; Jia, D.; Kagawa, T.; Kaji, T.; Kajita, T.; Kakizaki, M.; Kakuhata, H.; Kamiizumi, M.; Kanbara, S.; Kanda, N.; Kanemura, S.; Kaneyama, M.; Kasuya, J.; Kataoka, Y.; Kawaguchi, K.; Kawai, N.; Kawamura, S.; Kawazoe, F.; Kim, C.; Kim, J.; Kim, J. C.; Kim, W.; Kimura, N.; Kitaoka, Y.; Kobayashi, K.; Kojima, Y.; Kokeyama, K.; Komori, K.; Kotake, K.; Kubo, K.; Kumar, R.; Kume, T.; Kuroda, K.; Kuwahara, Y.; Lee, H.-K.; Lee, H.-W.; Lin, C.-Y.; Liu, Y.; Majorana, E.; Mano, S.; Marchio, M.; Matsui, T.; Matsumoto, N.; Matsushima, F.; Michimura, Y.; Mio, N.; Miyakawa, O.; Miyake, K.; Miyamoto, A.; Miyamoto, T.; Miyo, K.; Miyoki, S.; Morii, W.; Morisaki, S.; Moriwaki, Y.; Muraki, Y.; Murakoshi, M.; Musha, M.; Nagano, K.; Nagano, S.; Nakamura, K.; Nakamura, T.; Nakano, H.; Nakano, M.; Nakano, M.; Nakao, H.; Nakao, K.; Narikawa, T.; Ni, W.-T.; Nonomura, T.; Obuchi, Y.; Oh, J. J.; Oh, S.-H.; Ohashi, M.; Ohishi, N.; Ohkawa, M.; Ohmae, N.; Okino, K.; Okutomi, K.; Ono, K.; Ono, Y.; Oohara, K.; Ota, S.; Park, J.; Peña Arellano, F. E.; Pinto, I. M.; Principe, M.; Sago, N.; Saijo, M.; Saito, T.; Saito, Y.; Saitou, S.; Sakai, K.; Sakakibara, Y.; Sasaki, Y.; Sato, S.; Sato, T.; Sato, Y.; Sekiguchi, T.; Sekiguchi, Y.; Shibata, M.; Shiga, K.; Shikano, Y.; Shimoda, T.; Shinkai, H.; Shoda, A.; Someya, N.; Somiya, K.; Son, E. J.; Starecki, T.; Suemasa, A.; Sugimoto, Y.; Susa, Y.; Suwabe, H.; Suzuki, T.; Tachibana, Y.; Tagoshi, H.; Takada, S.; Takahashi, H.; Takahashi, R.; Takamori, A.; Takeda, H.; Tanaka, H.; Tanaka, K.; Tanaka, T.; Tatsumi, D.; Telada, S.; Tomaru, T.; Tsubono, K.; Tsuchida, S.; Tsukada, L.; Tsuzuki, T.; Uchikata, N.; Uchiyama, T.; Uehara, T.; Ueki, S.; Ueno, K.; Uraguchi, F.; Ushiba, T.; van Putten, M. H. P. M.; Wada, S.; Wakamatsu, T.; Yaginuma, T.; Yamamoto, K.; Yamamoto, S.; Yamamoto, T.; Yano, K.; Yokoyama, J.; Yokozawa, T.; Yoon, T. H.; Yuzurihara, H.; Zeidler, S.; Zhao, Y.; Zheng, L.; Agatsuma, K.; Akiyama, Y.; Arai, N.; Asano, M.; Bertolini, A.; Fujisawa, M.; Goetz, R.; Guscott, J.; Hashimoto, Y.; Hayashida, Y.; Hennes, E.; Hirai, K.; Hirayama, T.; Ishitsuka, H.; Kato, J.; Khalaidovski, A.; Koike, S.; Kumeta, A.; Miener, T.; Morioka, M.; Mueller, C. L.; Narita, T.; Oda, Y.; Ogawa, T.; Sekiguchi, T.; Tamura, H.; Tanner, D. B.; Tokoku, C.; Toritani, M.; Utsuki, T.; Uyeshima, M.; van den Brand, J. F. J.; van Heijningen, J. V.; Yamaguchi, S.; Yanagida, A., Progress of Theoretical and Experimental Physics, **2018**, 013F01.

50. "Mirror actuation design for the interferometer control of the KAGRA gravitational wave telescope", Yuta Michimura, Tomofumi Shimoda, Takahiro Miyamoto, Ayaka Shoda, Koki Okutomi, Yoshinori Fujii, Hiroki Tanaka, Mark A. Barton, Ryutaro Takahashi, Yoichi Aso, Tomotada Akutsu, Masaki Ando, Yutaro Enomoto, Raffaele Flaminio, Kazuhiro Hayama, Eiichi Hirose, Yuki Inoue, Takaaki Kajita, Masahiro Kamiizumi, Seiji Kawamura, Keiko Kokeyama, Kentaro Komori, Rahul Kumar, Osamu Miyakawa, Koji Nagano, Masayuki Nakano, Naoko Ohishi, Ching Pin Ooi, Fabián Erasmo Peña Arellano, Yoshio Saito, Katsuhiko Shimode, Kentaro Somiya, Hiroki Takeda, Takayuki Tomaru, Takashi Uchiyama, Takafumi Ushiba, Kazuhiro Yamamoto, Takaaki Yokozawa, Hirotaka Yuzurihara, Classical and Quantum Gravity, **34**, 225001.

51. "Guided lock of a suspended optical cavity enhanced by a higher-order extrapolation", Kiwamu Izumi, Koji Arai, Daisuke Tatsumi, Ryutaro Takahashi, Osamu Miyakawa, and Masa-Katsu Fujimoto, Applied Optics, **56**, 5470.

52. "Design and operation of a 1500-m laser strainmeter installed at an underground site in Kamioka, Japan", Akito Araya, Akiteru Takamori, Wataru Morii, Kouseki Miyo, Masatake Ohashi, Kazuhiro Hayama, Takashi Uchiyama, Shinji Miyoki and Yoshio Saito, Earth, Planets and Space, **69**, 77.

53. "Correlated Signatures of Gravitational-wave and Neutrino Emission in Threedimensional General-relativistic Core-collapse Supernova Simulations", Takumi Kuroda, Kei Kotake, Kazuhiro Hayama, Tomoya Takiwaki, Astrophysical Journal **851**, 62.

54. "Evolution of N/O Abundance Ratios and Ionization Parameters from z∼0 to 2 Investigated by the Direct Temperature Method", Takashi Kojima, Masami Ouchi, Kimihiko Nakajima, Takatoshi Shibuya, Yuichi Harikane, Yoshiaki Ono, Publ Astron Soc Jpn Nihon Tenmon Gakkai psx017.

55. "The infrared-dark dust content of high redshift galaxies", A. Ferrara, H. Hirashita, M. Ouchi, S. Fujimoto, MNRAS, **471**, 4.

56. "Evolution of Galatic-Scale Outflow up to z=1.5: Systematic Survey of [OII], [OIII], and Hα blobs", Suraphong Yuma, Masami Ouchi, Alyssa B. Drake, Seiji Fujimoto, Takashi Kojima, Yuma Sugahara, APJ, **841**, 2.

57. "First Data Release of the Hyper Suprime-Cam Subaru Strategic Program", Hiroaki Aihara, Robert Armstrong, Steven Bickerton, James Bosch, Jean Coupon, Hisanori Furusawa, Yusuke Hayashi, Hiroyuki Ikeda, Yukiko Kamata, Hiroshi Karoji, Satoshi Kawanomoto, Michitaro Koike, Yutaka Komiyama, Robert H. Lupton, Sogo Mineo, Hironao Miyatake, Satoshi Miyazaki, Tomoki Morokuma, Yoshiyuki Obuchi, Yukie Oishi, Yuki Okura, Paul A. Price, Tadafumi Takata, Manobu M. Tanaka, Masayuki Tanaka, Yoko Tanaka, Tomohisa Uchida, Fumihiro Uraguchi, Yousuke Utsumi, Shiang-Yu Wang, Yoshihiko Ya, Publications of the Astronomical Society of Japan, Volume **70**, Issue SP1.

58. "Evolution of Galactic Outflows at z$\sim$ 0-2 Revealed with SDSS, DEEP2, and Keck spectra", Yuma Sugahara, Masami Ouchi, Lihwai Lin, Crystal L. Martin, Yoshiaki Ono, Yuichi Harikane, Takatoshi Shibuya, Renbin Yan, APJ, **850**:51(14pp).

59. "Demonstrating A New Census of INfrared Galaxies with ALMA (DANCING-ALMA). I. FIR Size and Luminosity Relation at z = 0-6", Seiji Fujimoto, Masami Ouchi, Takatoshi Shibuya, Hiroshi Nagai, APJ, **850**:83(21pp)

60. "Small-scale Intensity Mapping: Extended Lyα, Hα and Continuum emission as a Probe of Halo Star Formation in High-redshift Galaxies", Lluís Mas-Ribas, Mark Dijkstra, Joseph F. Hennawi, Michele Trenti, Rieko Momose, Masami Ouchi, The Astrophysical Journal, Volume **841**, Number 1 .

61. "A New Constraint on Reionization by a Census of z=7.0 Lyα Emitters with a Deep and Large Sample to 0.3 L*: Evolution of Lyα Luminosity Function and Equivalent Width at z $\sim$ 6-7", Kazuaki Ota, Masanori Iye, Nobunari Kashikawa, Akira Konno, Fumiaki Nakata, Tomonori Totani, Masakazu A.R. Kobayashi, Yoshinobu Fudamoto, Akifumi Seko, Jun Toshikawa, Akie Ichikawa, Takatoshi Shibuya, Masafusa Onoue,, APJ, **844**:85(37pp).

62. "Deep submillimeter and radio observations in the SSA22 field. I. Powering sources and Lyα escape fraction of Lyα blobs", Y. Ao,et al., APJ,**850**:178(16pp).

63. "Subaru High-z Exploration of Low-Luminosity Quasars (SHELLQs). II. Discovery of 32 Quasars and Luminous Galaxies at 5.7< z< 6.8", Yoshiki Matsuoka, et al., Publ. Astron. Soc. Japan(2018) **70** (SP1), S35.

64. "Enhancement of Galaxy Overdensity around Quasar Pairs at z<3.6 based on the Hyper Suprime-Cam Subaru Strategic Program Survey", Masafusa Onoue, et al., Publ. Astron. Soc. Japan(2018) **70** (SP1), S31.

65. "Luminous Quasars Do Not Live in the Most Overdense Regions of Galaxies at z $\sim$ 4", Hisakazu Uchiyama, et al., Publ.Astron.Soc.Japan(2018) **70** (SP1,)S32.

66. "Great Optically Luminous Dropout Research Using Subaru HSC (GOLDRUSH). I. UV Luminosity Functions at z$\sim$ 4-7 Derived with the Half-Million Dropouts on the 100 deg^2 Sky", Yoshiaki Ono, et al., Publ. Astron. Soc. Japan(2018) **70** (SP1), S10.

67. "The Quasar Luminosity Function at Redshift 4 with Hyper Suprime-Cam Wide Survey", Masayuki Akiyama, et al., Publ. Astron. Soc. Japan(2018) **70** (SP1), S34 .

68. "A 16 deg^2 survey of emission line galaxies at z<1.5 in HSC-SSP DR1", Masao Hayashi, et al, Publ. Astron. Soc. Japan(2018) **70** (SP1), S17 .

69. "The Hyper Suprime-Cam SSP Survey: Overview and Survey Design", H. Aihara, et al., Publ. Astron. Soc. Japan(2018) **70** (SP1), S4.

70. "GOLDRUSH. II. Clustering of Galaxies at z$\sim$ 4-6 Revealed with the Half-Million Dropouts Over the 100 deg^2 Area Corresponding to 1 Gpc^3", Yuichi Harikane, et al., Publ.Astron.Soc.Japan(2018) **70** (SP1), S11.

71. "Systematic Identification of LAEs for Visible Exploration and Reionization Research Using Subaru HSC (SILVERRUSH). I. Program Strategy and Clustering Properties of $\sim$2,000 Lyα Emitters at z=6-7 over the 0.3-0.5 Gpc^2 Survey Area", Masami Ouchi, et al., Publ. Astron. Soc. Japan(2018) **70** (SP1), S13.

72. "SILVERRUSH. II. First Catalogs and Properties of $\sim$2,000 Lyα Emitters and Blobs at z$\sim$6-7 Identified over the 14-21 deg^2 Sky", Takatoshi Shibuya, et al., Publ.Astron.Soc.Japan(2018) **70** (SP1), S14.

73. "Clustering of quasars in a wide luminosity range at redshift 4 with Subaru Hyper Suprime-Cam wide field imaging", Wanqiu He, et al., Publ.Astron.Soc.Japan(2018) **70** (SP1), S33.

74. "SILVERRUSH. III. Deep Optical and Near-Infrared Spectroscopy for Lyα and UV-Nebular Lines of Bright Lyα Emitters at z=6-7", akatoshi Shibuya, et al, Publ.Astron.Soc.Japan(2018) **70** (SP1), S15.

75. "SILVERRUSH. IV. Lyα Luminosity Functions at z=5.7 and 6.6 Studied with $\sim$ 1,300 LAEs on the 14-21 deg^2 Sky", Akira Konno, et al, Publ.Astron.Soc.Japan(2018) **70** (SP1), S16.

76. "Stellar and Dark Matter Halo Properties of LAEs at z∼2", Haruka Kusakabe, et al, Publ. Astron. Soc. Japan(2018) **70** (1), 4 (1-31).

77. "GOLDRUSH. III. A Systematic Search of Protoclusters at z∼4 Based on the >100 deg^2 Area", Jun Toshikawa, et al, PASJ, **70**, S12.

78. "Minor Contribution of Quasars to Ionizing Photon Budget at z∼6: Update on Quasar Luminosity Function at the Faint-end with Subaru/Suprime-Cam", Masafusa Onoue, et al., APJL**847**:L15(6pp), 2017.

79. "Size-luminosity relations and UV luminosity functions at z=6-9 simultaneously derived from the complete Hubble Frontier Fields data", Ryota Kawamata, Masafumi Ishigaki, Kazuhiro Shimasaku, Masamune Oguri, Masami Ouchi, Shingo Tanigawa, APJ**855**:4(47pp), 2018.

80. "ALMA Twenty-six arcmin^2 Survey of GOODS-S at One-millimeter (ASAGAO): X-ray AGN Properties of Millimeter-Selected Galaxies", Y. Ueda et al., APJ**853**:24(11pp), 201.

81. "Inflationary primordial black holes for the LIGO gravitational wave events and pulsar timing array experiments", Keisuke Inomata, Masahiro Kawasaki, Kyohei Mukaida, Yuichiro Tada, and Tsutomu T. Yanagida, Phys. Rev. D**95**, 123510.

82. "Inflationary Primordial Black Holes as All Dark Matter", Keisuke Inomata, Masahiro Kawasaki, Kyohei Mukaida, Yuichiro Tada and Tsutomu T. Yanagida, Phys. Rev. D**96**, 043504.

83. "Relaxation leptogenesis, isocurvature perturbations, and the cosmic infrared background", Masahiro Kawasaki, Alexander Kusenko, Lauren Pearce and Louis Yang, Phys. Rev. D **95**, 103006.

84. "New-Type Charged Q-ball Dark Matter in Gauge Mediated SUSY Breaking Models", Jeong-Pyong Hong and Masahiro Kawasaki,, Phys. Rev. D**95**, 123532 (2017).

85. "On the Gauge Invariance of the Decay Rate of False Vacuum", Motoi Endo, Takeo Moroi, Mihoko M. Nojiri, Yutaro Shoji, Phys.Lett. B**771** (2017) 281-287.

86. "Dark Matter Candidates in a Visible Heavy QCD Axion Model", Hajime Fukuda, Masahiro Ibe, Tsutomu T. Yanagida, Phys.Rev. D**95** (2017) no.9, 095017.

87. "A "gauged" $U(1)$ Peccei-Quinn symmetry", Hajime Fukuda, Masahiro Ibe, Motoo Suzuki, Tsutomu T. Yanagida, Phys.Lett. B**771** (2017) 327-331 .

88. "False Vacuum Decay in Gauge Theory", Motoi Endo, Takeo Moroi, Mihoko M. Nojiri, Yutaro Shoji, J. High Energ. Phys. **(2017)** 2017: 74.

89. "Gauged Q-ball Decay Rates into Fermions", Jeong-Pyong Hong and Masahiro Kawasaki, Phys.Rev. D**96** (2017) no.10, 103526.

90. "Dynamical Clockwork Axions", Rupert Coy, Michele Frigerio, Masahiro Ibe, J. High Energ. Phys. **(2017)** 2017: 2.

91. "Oscillating Affleck-Dine condensate and its cosmological implications", Fuminori Hasegawa and Masahiro Kawasaki, Phys. Rev. D **96**, 063518.

92. "Adiabatic suppression of the axion abundance and isocurvature due to coupling to hidden monopoles", Masahiro Kawasaki, Fuminobu Takahashi and Masaki Yamada, J. High Energ. Phys. **(2018)** 2018: 53.

93. "Revisiting Big-Bang Nucleosynthesis Constraints on Long-Lived Decaying Particles", Masahiro Kawasaki, Kazunori Kohri, Takeo Moroi and Yoshitaro Takaesu, Phys. Rev. D **97**, 023502.

94. "$\mathcal{O}(10)M_\odot$ primordial black holes and string axion dark matter", Keisuke Inomata, Masahiro Kawasaki, Kyohei Mukaida, Yuichiro Tada and Tsutomu T. Yanagida, Phys. Rev. D **96**, 123527.

95. "Double Inflation as a single origin of PBHs for all dark matter and LIGO observations", Keisuke Inomata, Masahiro Kawasaki, Kyohei Mukaida and Tsutomu T. Yanagida, Phys. Rev. D **97**, 043514.

96. "Migdal Effect in Dark Matter Direct Detection Experiments", Masahiro Ibe, Wakutaka Nakano, Yutaro Shoji, Kazumine Suzuki, JHEP**03**(2018)194.

97. "State-of-the-Art Calculation of the Decay Rate of Electroweak Vacuum in the Standard Model", S. Chigusa, T. Moroi and Y. Shoji, Phys. Rev. Lett. **119**, 211801 (2017).

98. "Gravitino Problem in Inflation Driven by Inflaton-Polonyi Kähler Coupling", Fuminori Hasegawa, Kazunori Nakayama, Takahiro Terada, Yusuke Yamada, Phys.Lett.B **777** (2018)270-274.

(b) Conference Papers (Proceedings)

1. "AXEL-a high pressure xenon gas TPC for neutrinoless double beta decay search", Nakamura, Kiseki; Ichikawa, Atsuko K.; Nakaya, Tsuyoshi; Minamino, Akihiro; Ban, Sei; Yanagita, Saori; Tanaka, Shunsuke; Hirose, Masanori; Sekiya, Hiroyuki; Ueshima, Kota; Miuchi, Kentaro, 14th Vienna Conference on Instrumentation, Vienna Austria, FEB 15-19, 2016.

2. "Determination of Trace Level Thorium and Uranium in High Purity Gadolinium Sulfate Using ICP-MS with Solid-Phase Chromatographic Extraction Resins", Ito, S.; Takaku, Y.; Ikeda, M.; Kishimoto, Y., 6th International Workshop on Low Radioactivity Techniques (LRT), Seoul, Korea, MAY 23-27, 2017.

3. "Identification of ^{210}Pb and ^{210}Po in the bulk of copper samples with a low-background alpha particle counter", Kobayashi, Kazuyoshi, 6th International Workshop on Low Radioactivity Techniques (LRT), Seoul, Korea, MAY 23-27, 2017.

4. "Development of the Database for Low-Background Studies in Kamioka", Nakano, Yuuki; Takeuchi, Yasuo, 6th International Workshop on Low Radioactivity Techniques (LRT), Seoul, Korea, MAY 23-27, 2017.

5. "Radon assay and radioactivity database in Kamioka", Takeuchi, Yasuo; Tasaka, Shigeki; Nakano, Yuuki, 27th International Conference on Neutrino Physics and Astrophysics (Neutrino), London, UK, JUL 04-09, 2016.

6. "Experimental study of decoherence effect at Daya Bay", Wong, Chan-Fai (Steven); Chu, M. -C.; Dolgareva, M.; Gonchar, M.; Naumov, D.; Taichenachev, D.; Treskov, K.; Tsui, K. M.; Wang, W., 27th International Conference on Neutrino Physics and Astrophysics (Neutrino), London, UK, JUL 04-09, 2016.

7. "Annual modulation search by XMASS-I with 2.7 years of data", Masaki Yamashita for the XMASS Collaboration, XV International Conference on Topics in Astroparticle and Underground Physics, Sudbury, ON, Canada, 24-28 July 2017.

8. "Neutrino astrophysics with Hyper-Kamiokande", Takatomi Yano for Hyper-Kamiokande proto Collaboration, TAUP2015, Torino, Italy, 7-11 September, 2015.

9. "Astrophysical Neutrino at Hyper-Kamiokande", Takatomi Yano on behalf of Hyper-Kamiokande proto-collaboration, ICRC2017, Bexco, Busan, Korea, 10-20, July, 2017.

10. "Recent Solar neutrino Results from Super-Kamiokande", Yuuki Nakano for the Super-Kamiokande collaboration, XV International Conference on Topics in Astroparticle and Underground Physics, Sudbury, ON, Canada, 25-28 July 2017.

11. "Radon background study in Super-Kamiokande", Yuuki Nakano for the Super-Kamiokande collaboration, 27th International Conference on Neutrino Physics and Astrophysics (Neutrino), London UK, JUL 04-09, 2016.

12. "SuperK-Gd", Lluis Marti-Magro for the Super-Kamiokande Collaboration, ICRC2017, Busan, Korea, 10-20, July, 2017.

13. "Physics potential of Hyper-Kamiokande for neutrino oscillation measurements", C. Bronner on behalf of the Hyper-Kamiokande proto-collaboration, The 19th International Workshop on Neutrinos from Accelerators-NUFACT2017, Uppsala University, Uppsala, Sweden, 25-30 September, 2017.

14. "New solar cell and clean unit system platform (CUSP) for earth and environmental science", Ishibashi, A.; Matsuoka, T.; Enomoto, R.; Yasutake, M., 2nd International Conference on New Energy and Future Energy System (NEFES), China, SEP 22-25, 2017.

15. "The Energy Spectrum of Cosmic Rays at the Highest Energies", The Pierre Auger and Telescope Array Collaborations, 2016 International Conference on Ultra-High Energy Cosmic Rays (UHECR2016), Kyoto Research Park, 11-14 October 2016.

16. "Anisotropy Search in Energy Distribution in the Northern Hemisphere Using the Telescope Array Surface Detector Data", The Telescope Array Collaboration, 2016 International Conference on Ultra-High Energy Cosmic Rays (UHECR2016), Kyoto Research Park, 11-14 October 2016.

17. "Composition Measurements via Depth of Airshower Maximum at the Telescope Array", The Telescope Array Collaboration, 2016 International Conference on Ultra-High Energy Cosmic Rays (UHECR2016), Kyoto Research Park, 11-14 October 2016.

18. "Report of the Working Group on the Mass Composition of Ultrahigh Energy Cosmic Rays", The Pierre Auger and Telescope Array Collaborations, 2016 International Conference on Ultra-High Energy Cosmic Rays (UHECR2016), Kyoto Research Park, 11-14 October 2016.

19. "TA Anisotropy Summary", The Telescope Array Collaboration, 2016 International Conference on Ultra-High Energy Cosmic Rays (UHECR2016), Kyoto Research Park, 11-14 October 2016.

20. "Arrival Directions of Cosmic Rays at Ultra-High Energies", The Pierre Auger and Telescope Array Collaborations, 2016 International Conference on Ultra-High Energy Cosmic Rays (UHECR2016), Kyoto Research Park, 11-14 October 2016.

21. "High-Energy Particle Showers Observed at Ground Level in Coincidence with Downward Lightning Leaders at the Telescope Array Observatory", The Telescope Array and TA/LMA Collaborations, 2016 International Conference on Ultra-High Energy Cosmic Rays (UHECR2016), Kyoto Research Park, 11-14 October 2016.

22. "The TA$\times$ 4 experiment", The Telescope Array Collaboration, 2016 International Conference on Ultra-High Energy Cosmic Rays (UHECR2016), Kyoto Research Park, 11-14 October 2016.

23. "Telescope Array Low energy Extension: TALE", The Telescope Array Collaboration, 2016 International Conference on Ultra-High Energy Cosmic Rays (UHECR2016), Kyoto Research Park, 11-14 October 2016.

24. "Auger at the Telescope Array: Recent Progress Toward a Direct Cross-Calibration of Surface-Detector Stations", The Pierre Auger and Telescope Array Collaborations, 2016 International Conference on Ultra-High Energy Cosmic Rays (UHECR2016), Kyoto Research Park, 11-14 October 2016.

25. "Calibration of Photo-multiplier Tubes in Fluorescence Detectors of the Telescope Array", B.K. Shin, M. Fukushima, S. Ogio, Y. Tsunesada, 2016 International Conference on Ultra-High Energy Cosmic Rays (UHECR2016), Kyoto Research Park, 11-14 October 2016.

26. "Composition Studies with the Telescope Array Surface Detector", The Telescope Array Collaboration, 2016 International Conference on Ultra-High Energy Cosmic Rays (UHECR2016), Kyoto Research Park, 11-14 October 2016.

27. "Development of a UAV-mounted light source for fluorescence detector calibration of the Telescope Array experiment", The Telescope Array Collaboration, 2016 International Conference on Ultra-High Energy Cosmic Rays (UHECR2016), Kyoto Research Park, 11-14 October 2016.

28. "Development of the Cosmic Ray Air Fluorescence Fresnel lens Telescope for a next generation UHECR observatory", Y. Tameda, T. Tomida, M. Hayashi, M. Yamamoto, D. Ikeda, and T. Fujii, 2016 International Conference on Ultra-High Energy Cosmic Rays (UHECR2016), Kyoto Research Park, 11-14 October 2016.

29. "Development of the new DAQ system for the SD array of TA$\times$ 4 and TALE", The Telescope Array Collaboration, 2016 International Conference on Ultra-High Energy Cosmic Rays (UHECR2016), Kyoto Research Park, 11-14 October 2016.

30. "NICHE: Non-Imaging Cherenkov Light Observation at the TA Site", Y. Tsunesada, Y. Omura, B.K. Shin, D. R. Bergman, J. F. Krizmanic, and T. Nonaka, 2016 International Conference on Ultra-High Energy Cosmic Rays (UHECR2016), Kyoto Research Park, 11-14 October 2016.

31. "Night sky weather monitoring system using Fish-eye CCD", The Telescope Array Collaboration, 2016 International Conference on Ultra-High Energy Cosmic Rays (UHECR2016), Kyoto Research Park, 11-14 October 2016.

32. "Studies of muons in extensive air showers from ultra-high energy cosmic rays observed with the Telescope Array surface detector", The Telescope Array Collaboration, 2016 International Conference on Ultra-High Energy Cosmic Rays (UHECR2016), Kyoto Research Park, 11-14 October 2016.

33. "Study of Microwave Radiation from the Electron Beam at the Telescope Array Site", D. Ikeda et al., 2016 International Conference on Ultra-High Energy Cosmic Rays (UHECR2016), Kyoto Research Park, 11-14 October 2016.

34. "The Full-scale Prototype for the Fluorescence Detector Array of Single-pixel Telescopes", T. Fujii et al., 2016 International Conference on Ultra-High Energy Cosmic Rays (UHECR2016), Kyoto Research Park, 11-14 October 2016.

35. "The FAST Project - A Next Generation UHECR Observatory", Fujii, Toshihiro; Malacari, Max; Bellido, Jose A.; Horvath, Pavel; Hrabovsky, Miroslav; Jiang, Jiaqi; Mandat, Dusan; Matalon, Ariel; Matthews, John N.; Motloch, Pavel; Palatka, Miroslav; Pech, Miroslav; Privitera, Paolo; Schovanek, Petr; Thomas, Stan B.; Travnicek, Petr, 6th Roma International Conference on Astroparticle Physics (RICAP), Roma, JUN 21-24, 2016.

36. "Meteor studies in the framework of the JEM-EUSO program", G. Abdellaoui et al., 9th Meteoroids Conference, Netherlands, JUN 06-10, 2016.

37. "Ashra Neutrino Telescope Array (NTA): Combined Imaging Observation of Astroparticles", Makoto Sasaki, and Tadashi Kifune for the NTA Collaboration, 7th Int. Workshop on Very High Energy Particle Astronomy in 2014 (VHEPA2014), Media Hall, Kashiwa Library, The University of Tokyo, March 18-20, 2014.

(c) ICRR Reports

N/A

D. Doctoral Theses

1. "Search for Sub-GeV WIMP dark matter by annual modulation using XMASS-I detector",
   Masatoshi Kobayashi,
   Ph.D Thesis, Mar. 2018

2. "Baryon asymmetry and cosmological moduli/Polonyi problem",
   Taku Hayakawa,
   Ph.D Thesis, Mar. 2018

3. "Cosmological implications of non-topological solitons",
   Jeong Pyong Hong,
   Ph.D Thesis, Mar. 2018

E. Public Relations

(a) ICRR News

ICRR News is a quarterly publication written in Japanese about scientific and educational activities at ICRR. It includes:

1. reports on scientific activities of ICRR staff members and those conducted at one or more of its facilities,

2. reports of international conferences on topics relevant to ICRR's research activities,

3. reports on topics discussed at ICRR's Committees,

4. list of publications published by ICRR [ICRR-Report],

5. list of seminars held at ICRR,

6. announcements, and

7. other items of relevance.

Below lists the main topics in the issues published in FY 2017:

No.99 (2017 Spring)

- 30 years after the detection of SN1987A neutrinos, Masayuki Nakahata

- ICRR Spring School 2017 Report

- Report of the 16th ICRR/IPMU joint public lecture

- Staff Reassignment

- ICRR Seminar

No.100 (2017 Autumn)

- Q-ball, Masahiro Kawasaki

- Report of the commemoration of the 40th anniversary of Akeno Observatory

- Open Campus 2017 Report

- Awards

- Staff Reassignment

- ICRR Seminar

No.101 (2018 Spring)

- Features: Graduate students' round table talk (CTA group)

- Report: ICRR Spring School 2018 Report

- Report: Sapphire mirror installation for KAGRA

- Press Release

- Topics: ICRR Joint-Use Report Workshop

- Topics: Renovation of Hokubu Kaikan for KAGRA Observatory

- Topics: Questionnaire results of Super-Kamiokande jigsaw puzzle

- Awards

- Information: Staff Reassignment

- Information: ICRR Seminar

(b) Public Lectures

- "Public Lecture for high school students", Apr. 21, 2017, Komaba Campus, The University of Tokyo, Takaaki Kajita (ICRR, The University of Tokyo).

- "Public Lecture for JpGU-AGU Joint Meeting 2017", May. 21, 2017, Makuhari Messe, Chiba, Takaaki Kajita (ICRR, The University of Tokyo).

- "Yume Navi Live 2017", Jul. 22, 2017, Tokyo Big Sight, Tokyo, Takaaki Kajita (ICRR, The University of Tokyo).

- "Public Lecture", Jul. 31, 2017, Koganei-City, Tokyo, Takaaki Kajita (ICRR, The University of Tokyo).

- "Public Lecture for Japan Vice Principals Association of Public School", Aug. 4, 2017, Saitama Super Arena, Saitama, Takaaki Kajita (ICRR, The University of Tokyo).

- "Hida Academy", Aug. 6, 2017, Hida-City, Gifu, Takaaki Kajita (ICRR, The University of Tokyo).

- "Shinano Kizaki Kaki Digaku", Aug. 7, 2017, Omachi-City, Nagano, Takaaki Kajita (ICRR, The University of Tokyo).

- "Public Lecture for science teachers in Saitama", Aug. 9, 2017, Westa Kawagoe, Saitama, Takaaki Kajita (ICRR, The University of Tokyo).

- "Special Lecture", Aug. 18, 2017, KEK Summer Challenge 2017, Ibaraki, Takaaki Kajita (ICRR, The University of Tokyo).

- "Tohoku University Science Symposium", Aug. 19, 2017, Sendai-City, Miyagi, Takaaki Kajita (ICRR, The University of Tokyo).

- "Public Lecture for ICO-24", Aug. 24, 2017, Keio Plaza Hotel, Tokyo, Takaaki Kajita (ICRR, The University of Tokyo).

- "Public Lecture for teachers in Maniwa-City, Okayama", Aug. 25, 2017, Maniwa-City, Okayama, Takaaki Kajita (ICRR, The University of Tokyo).

- "Public Lecture", Sep. 2, 2017, Kyoto University, Kyoto, Takaaki Kajita (ICRR, The University of Tokyo).

- "Public Lecture for JPS Autumn Meeting 2017 in Utsunomiya", Sep. 18, 2017, Utsunomiya-City, Tochigi, Takaaki Kajita (ICRR, The University of Tokyo).

- "Public Lecture", Nov. 4, 2017, Kochi University of Technology, Kochi, Takaaki Kajita (ICRR, The University of Tokyo).

- "Sakae Chunichi Culture Center", Nov. 20, 2017, Nagoya-City, Aichi, Takaaki Kajita (ICRR, The University of Tokyo).

- "Science Public Lecture", Dec. 10, 2017, Asakuchi-Gun, Okayama, Takaaki Kajita (ICRR, The University of Tokyo).

- "Public Lecture for The 17th Annual Meeting of the Japanese Society for Neutron Science", Dec. 17, 2017, Fukuoka University, Fukuoka, Takaaki Kajita (ICRR, The University of Tokyo).

- "Asahi Culture Center Shinjuku", Feb. 3, 2018, Asahi Culture Center Shinjuku, Tokyo, Takaaki Kajita (ICRR, The University of Tokyo).

- "Public Lecture", Feb. 4, 2018, Discovery Park Yaizu, Shizuoka, Takaaki Kajita (ICRR, The University of Tokyo).

- "Public Lecture", Feb. 17, 2018, Matsue-City, Shimane, Takaaki Kajita (ICRR, The University of Tokyo).

- "Public Lecture", Feb. 18, 2018, Osaka Science & Technology Center, Osaka, Takaaki Kajita (ICRR, The University of Tokyo).

- "Shizuoka Kita High School", Apr. 25, 2017, Kamioka Observatory, Gifu, Jun Kameda (Kamioka Observatory, ICRR, The University of Tokyo).

- "Asahi Culture Center", May. 20, 2017, Asahi Culture Center, Tokyo, Masato Shiozawa (Kamioka Observatory, ICRR, The University of Tokyo).

- "Public Lecture for the Board of Education in Toyama City", Jul. 1, 2017, Toyama Science Museum, Toyama, Masayuki Nakahata (Kamioka Observatory, ICRR, The University of Tokyo).

- "Public Lecture for Science Teachers in Aichi Prefecture", Jul. 3, 2017, Kamioka Observatory, Gifu, Ko Abe (Kamioka Observatory, ICRR, The University of Tokyo).

- "Public Lecture", Jul. 11, 2017, Toyonaka-City, Osaka, Yasuhiro Kishimoto (Kamioka Observatory, ICRR, The University of Tokyo).

- "Matsumoto Fukashi High School", Jul. 11, 2017, Kamioka Observatory, Gifu, Masayuki Nakahata (Kamioka Observatory, ICRR, The University of Tokyo).

- "Public Lecture", Jul. 13, 2017, Chiyoda-Ku, Tokyo, Yasuhiro Kishimoto (Kamioka Observatory, ICRR, The University of Tokyo).

- "Seminar for Geo Space Adventure", Jul. 15, 2017, Kamioka Community Center, Gifu, Masato Shiozawa (Kamioka Observatory, ICRR, The University of Tokyo).

- "Geo Space Adventure", Jul. 15-16, 2017, Kamioka Observatory, Gifu, ICRR, The University of Tokyo

- "Toyama High School", Jul. 24, 2017, Kamioka Observatory, Gifu, Shigetaka Moriyama (Kamioka Observatory, ICRR, The University of Tokyo).

- "Senior High School Attached to Kyoto University of Education", Jul. 31, 2017, Kamioka Observatory, Gifu, Atsushi Takeda (Kamioka Observatory, ICRR, The University of Tokyo).

- "Hirameki Tokimeki Science", Jul. 31-Aug. 1, 2017, Kamioka Observatory, Gifu, Motoyasu Ikeda, Yasuhiro Nakajima, Masaki Yamashita, Katsuki Hiraide (Kamioka Observatory, ICRR, The University of Tokyo).

- "Ashikaga High School", Aug. 1, 2017, Kamioka Observatory, Gifu, Makoto Miura (Kamioka Observatory, ICRR, The University of Tokyo).

- "Yume-no-Tamago-Juku", Aug. 7, 2017, Hida-City, Gifu, Yasuhiro Nakajima (Kamioka Observatory, ICRR, The University of Tokyo).

- "Osaka Seiko Gakuin", Aug. 9, 2017, Kamioka Observatory, Gifu, Yoshinari Hayato (Kamioka Observatory, ICRR, The University of Tokyo).

- "Takada High School", Aug. 21, 2017, Kamioka Observatory, Gifu, Jun Kameda (Kamioka Observatory, ICRR, The University of Tokyo).

- "Ochanomizu University Senior High School", Aug. 28, 2017, Kamioka Observatory, Gifu, Hiroyuki Sekiya (Kamioka Observatory, ICRR, The University of Tokyo).

- "Public Lecture", Aug. 29, 2017, Yayoi Auditorium, The University of Tokyo, Yasuhiro Kishimoto (Kamioka Observatory, ICRR, The University of Tokyo).

- "Kariya High School", Aug. 29, 2017, Kamioka Observatory, Gifu, Shoei Nakayama (Kamioka Observatory, ICRR, The University of Tokyo).

- "Nanao High School", Sep. 19, 2017, Kamioka Observatory, Gifu, Makoto Miura (Kamioka Observatory, ICRR, The University of Tokyo).

- "Morioka Chuo High School", Sep. 26, 2017, Kamioka Observatory, Gifu, Yasuhiro Nakajima (Kamioka Observatory, ICRR, The University of Tokyo).

- "Public Lecture", Oct. 3, 2017, Kamioka Junior High School, Gifu, Ko Abe (Kamioka Observatory, ICRR, The University of Tokyo).

- "Yoshiki High School", Oct. 17, 2017, Kamioka Observatory, Gifu, Yasuhiro Kishimoto (Kamioka Observatory, ICRR, The University of Tokyo).

- "Public Lecture", Oct. 21, 2017, Hamagin Space Science Center, Kanagawa, Yasuhiro Kishimoto (Kamioka Observatory, ICRR, The University of Tokyo).

- "Science Cafe in Gifu", Oct. 21, 2017, Gifu Shinbun sha, Gifu, Yoshinari Hayato (Kamioka Observatory, ICRR, The University of Tokyo).

- "Super-Kamiokande Open House", Nov. 4, 2017, Kamioka Observatory, Gifu, ICRR, The University of Tokyo

- "Public Lecture for Super-Kamiokande Open House", Nov. 4, 2017, Kamioka Community Center, Gifu, Masayuki Nakahata (Kamioka Observatory, ICRR, The University of Tokyo).

- "Asahi Culture Center Yokohama", Nov. 18, 2017, Asahi Culture Center Yokohama, Kanagawa, Masayuki Nakahata (Kamioka Observatory, ICRR, The University of Tokyo).

- "Doshisha Junior High School", Dec. 11, 2017, Kamioka Observatory, Gifu, Yasuhiro Nakajima (Kamioka Observatory, ICRR, The University of Tokyo).

- "Public Lecture", Feb. 23, 2018, Kamisunagawa Junior High School, Hokkaido, Jun Kameda (Kamioka Observatory, ICRR, The University of Tokyo).

- "Akita High School", Aug. 3, 2017, ICRR, Kashiwa-City, Chiba, Takayuki Saito (ICRR, The University of Tokyo).

- "Public Lecture", Apr. 15, 2017, Kashiwa-City, Chiba, Hiroyuki Sagawa (ICRR, The University of Tokyo).

- "Public Lecture", Apr. 24, 2017, Omiya Kaisei High School, Saitama, Daisuke Ikeda (ICRR, The University of Tokyo).

- "Science Cafe", Nov. 5, 2017, Tamarokuto Science Center, Tokyo, Toshihiro Fujii (ICRR, The University of Tokyo).

- "Public Lecture", Jul. 22, 2017, NHK Culture Center Machida, Tokyo, Tomoya Kinugawa (ICRR, The University of Tokyo).

- "Science Cafe", Jan. 20, 2018, Tamarokuto Science Center, Tokyo, Tomoya Kinugawa (ICRR, The University of Tokyo).

- "Public Lecture", Apr. 22, 2017, NHK Culture Center Machida, Tokyo, Masami Ouchi (ICRR, The University of Tokyo).

- "Observational Studies on First Stars and Galaxies", May 27, 2017, NHK Culture Center Machida, Tokyo, Yoshiaki Ono (ICRR, The University of Tokyo).

- "First Galaxies Studied with the Large Telescopes", Jul. 8, 2017, Asahi Culture Center Shinjuku, Tokyo, Yoshiaki Ono (ICRR, The University of Tokyo).

- "First Galaxies Studied with the Large Telescopes", Nov. 8, 2017, Musashi High School, Tokyo, Yoshiaki Ono (ICRR, The University of Tokyo).

- "U-Tokyo's Open Lecture," Nov. 11, 2017, Yasuda Auditorium, The University of Tokyo, Masato Takita (ICRR, The University of Tokyo).

- "Kawasaki Public Academy," Apr. 18, 2017, Kawasaki-City, Kanagawa, Shinji Miyoki (KAGRA Observatory, ICRR, The University of Tokyo).

- "Shizuoka Kita High School," Apr. 25, 2017, Kamioka observatory, Gifu, Shinji Miyoki (KAGRA Observatory, ICRR, The University of Tokyo).

- "Kawasaki Public Academy," May. 9, 2017, Kawasaki-City, Kanagawa, Yoshio Saito (KAGRA Observatory, ICRR, The University of Tokyo).

- "Public Lecture for teachers in Aichi Prefecture," Jul. 3, 2017, Kamioka Observatory, Gifu, Yoichi Aso (KAGRA Collaborator) (Gravitational Wave Project Office, NOAJ).

- "Matsumoto Fukashi High School," Jul. 11, 2017, Kamioka Observatory, Gifu, Shinji Miyoki (KAGRA Observatory, ICRR, The University of Tokyo).

- "Toyama High School," Jul. 12, 2017, Toyama High School, Osamu Miyakawa (KAGRA Observatory, ICRR, The University of Tokyo).

- "Toyama High School," Jul. 24, 2017, KAGRA Observatory, The University of Tokyo, Osamu Miyakawa (KAGRA Observatory, ICRR, The University of Tokyo).

- "Hida Kamioka High School," Jul. 25, 2017, KAGRA Observatory, The University of Tokyo, Shinji Miyoki (KAGRA Observatory, ICRR, The University of Tokyo).

- "Preview of Yumeyakata," Aug. 1, 2017, Yumeyakata, Hida-City, Gifu, Takashi Uchiyama (KAGRA Observatory, ICRR, The University of Tokyo).

- "Hida Science Cafe," Aug. 6, 2017, Kamioka Library, Hida-City, Gifu, Masatake Ohashi, Shinji Miyoki, Takashi Uchiyama, Keiko Kokeyama (KAGRA Observatory, ICRR, The University of Tokyo).

- "Yume-no-Tamago-Juku," Aug. 6, 2017, Kamioka-Cho, Hida-City, Gifu, Hideaki Hayakawa (KAGRA Observatory, ICRR, The University of Tokyo).

- "Yoshiki High School," Aug. 7-8, 2017, Takayama-City, Gifu, Koseki Miyo, Shin Kirii (KAGRA Observatory, ICRR, The University of Tokyo).

- "Youngsters' Science Festival 2017," Aug. 19, 2017, Harbis Hall in Osaka-City, Osaka, Hideyuki Tagoshi (KAGRA Observatory, ICRR, The University of Tokyo).

- "Nanao High School," Aug. 21, 2017, Yumeyakata, Hida-City, Gifu, Shinji Miyoki (KAGRA Observatory, ICRR, The University of Tokyo).

- "JASIS2017 Science Seminar," Sep. 8, 2017, Makuhari Messe, Chiba, Seiji Kawamura (KAGRA Observatory, ICRR, The University of Tokyo).

- "KAGRA Tour for Donators to KAGRA Project," Sep. 16, 2017, KAGRA Observatory, The University of Tokyo, (KAGRA Observatory, ICRR, The University of Tokyo).

- "KAGRA Tour," Sep. 17, 2017, KAGRA Observatory, The University of Tokyo, (KAGRA Observatory, ICRR, The University of Tokyo).

- "Yoshiki High School," Oct. 17, 2017, Yumeyakata, Hida-City, Gifu, Kazuhiro Hayama (KAGRA Observatory, ICRR, The University of Tokyo).

- "ICRR/IPMU joint public lecture," Nov. 3, 2017, Ito Hall, The University of Tokyo, Seiji Kawamura (KAGRA Observatory, ICRR, The University of Tokyo).

- "Public Lecture for the Board of Education in Gifu," Nov. 10, 2017, Spirit Garden Hall in Hida-City, Gifu, Masatake Ohashi (KAGRA Observatory, ICRR, The University of Tokyo).

- "Hamagin Kids' Science," Nov. 18, 2017, Hamagin Space Science Center, Shizuoka, Shinji Miyoki (KAGRA Observatory, ICRR, The University of Tokyo).

- "Woman's career meeting, 'Yappari Butsuri-ga-Suki!'," Nov. 18, 2017, Kavli IPMU, The University of Tokyo, Keiko Kokeyama (KAGRA Observatory, ICRR, The University of Tokyo).

- "Public Lecture," Dec. 3, 2017, Kamioka Community Center, Gifu, Masatake Ohashi, Shinji Miyoki (KAGRA Observatory, ICRR, The University of Tokyo).

- "Science Public Lecture," Feb. 18, 2018, Miraikan, Tokyo, Masatake Ohashi (KAGRA Observatory, ICRR, The University of Tokyo).

- "Hida Science Cafe," Feb. 24, 2018, Hida-City, Gifu, Takaaki Yokozawa (KAGRA Observatory, ICRR, The University of Tokyo).

- "Science Cafe," Feb. 25, 2018, Toyama Astronomical Observatory, Toyama, Osamu Miyakawa (KAGRA Observatory, ICRR, The University of Tokyo).

- "J-PARC Science Cafe," Mar. 30, 2018, Tokai-Mura, Ibaraki, Takayuki Tomaru (Visiting Associate Professor, KAGRA Observatory, ICRR, The University of Tokyo).

- "Public Lecture", Aug. 26, 2017, NHK Culture Center Machida, Tokyo, Masahiro Kawsaki (ICRR, The University of Tokyo).

(c) Visitors

Kashiwa Campus (Total: 33 groups, 3,081 people)

- Elementary, Junior High and High schools: 8 groups

- Universities and Graduate schools: 4 groups

- Researchers: 0 group

- Inspections: 3 groups

- Press: 15 groups

- Others: 3 groups

KAMIOKA Observatory (Total: 230 groups, 3,346 people)

- Elementary, Junior High and High schools: 24 groups

- Universities and Graduate schools: 23 groups

- Researchers: 41 groups

- Inspections: 28 groups

- Press: 18 groups

- Others: 96 groups

KAGRA Observatory (Total: 102 groups, 1,263 people)

- Junior High and High schools: 11 groups

- Universities and Graduate schools: 15 groups

- Researchers: 17 groups

- Inspections: 15 groups

- Press: 18 groups

- Others: 26 groups

F.   Inter-University Research Activities

Numbers of Researchers

	Number of Applications	Number of Adoptions	Number of Researchers
Facility Usage			
Kamioka Observatory	42	42	926
Akeno Observatory	4	4	52
Norikura Observatory	10	10	94
Low-Level Radioisotope Measurement Facility	4	4	27
Cryogenic Laser Interferometer in Kashiwa	14	14	473
Laboratorial Facility in Kashiwa	3	3	33
Computer Facility in Kashiwa	12	12	203
Conference Facility in Kashiwa	13	13	428
Over Sea Facilities	26	26	485
Annual Sums	128	128	2,721

	Number of Applications	Number of Adoptions	Number of Researchers
Joint Research			
Neutrino and Astroparticle Research	42	42	925
High Energy Cosmic Ray Research	58	58	1,151
Astrophysics and Gravity Research	20	20	564
Research Center for Cosmic neutrinos	8	8	81
Annual Sums	128	128	2,721

Research Project Titles

1. Study of simulation for atmospheric neutrino

2. Study of atmospheric neutrino flux and neutrino oscillations

3. Studying the Neutrino Mass Hierarchy With Atmospheric Neutrinos

4. Study of flavor identification of atmospheric and beam neutrinos

5. Study of solar neutrino energy spectrum

6. Precise measurement of Day/Night effect for B8 solar neutrinos

7. Study for Supernova monitor

8. Improved measurement of solar neutrino at Super-Kamiokande and SK-Gd

9. Study of Supernova Relic Neutrinos

10. Search for proton decay via $e^+\pi^0$ mode

11. Study of proton decay $p \rightarrow \nu K^+$

12. Study in upward-going muons and high energy neutrinos

13. Sidereal daily variation of ~ 10TeV galactic cosmic ray intensity observed by the Super-Kamiokande

14. Tokai to Kamioka Long Baseline Experiment T2K

15. Neutrino interaction study using accelerator data

16. Study of the electron neutrino appearance measurement in the T2K experiment

17. Study to improve sensitivity of neutrino oscillation measurement in T2K experiment

18. Joint Oscillation Analysis With the T2K and Super-Kamiokande Experiments

19. Energy cailbration for Super-Kamiokande

20. Research and development of computer simulation of Super-Kamiokande detector.

21. Development of low concentration radon detection system

22. R&D of Megaton scale water Cherenkov Detector Hyper-Kamiokande

23. Development of the Large Aperture Photodetector for a next-generation neutrino detector

24. Development of software for the next generation neutrino detector

25. A Search for Dark Matter using Liquid Xenon Detector

26. Study of annual modulation for dark matter search with XMASS

27. Study for future XMASS detector

28. Development of calibration system for XMASS detector

29. Micro-analysis of gaserous cantamination in Xe

30. Study on neutrino physics using liquid xenon

31. Radon emanation measurement from material using dark matter search experiment.(2)

32. A study on scattering processes of scintillation photons in liquid xenon

33. Study on surface background removal in the dark matter search

34. Study of Double beta decay of 48Ca

35. Direction-sensitive dark matter search

36. Study for lowering backgrounds of radioisotopes in large volume detectors

37. Studies on the background evaluation using laser spectroscopy analysis

38. Development of a radioactivity assay system for underground experiments

39. Dark Matter Search with double-phase Argon detector

40. Integration of crustal activity observation around the Atotsugawa fault

41. Strain, tilt, seismic measurement in Kamioka-mine

42. Keeping neuclear emulsion plates in a box made of lead blacks at Kamioka Underground Lab

43. R&D for a Small Atmospheric Cherenkov Telescope in Akeno Observatory

44. Development of new surface detector for observation of ultra high energy cosmic ray at Telescope Array site

45. Development of the national control station for the fully remote operation of TA-FD

46. Multi-Color Imager for Transients, Survey and Monstrous Explosions

47. Observation of Galactic Cosmic Ray Intensities using Large Area Muon Telescopes

48. Study for cosmic ray detector with capability of indivisual particle identification and particle tracking

49. The development for the platform of advanced field measurement

50. Observation of solar neutrons in solar cycle 24

51. Space weather observation using muon hodoscope at Mt. Norikura

52. Observation of cosmogenic nuclides concentrations at Mt. Norikura

53. Study of secondary cosmic rays from Thundercloud at Mt. Norikura

54. Relativistic Electron Acceleraton in Thunderstorm Eelectric Field

55. Observational study of electron acceleration mechanism in thunderclouds

56. High-energy phenomena via interaction between cosmic-rays and thunderstorms

57. Development of high energy proton irradiation technique for devices used in spaceship

58. Investigation of alpine plants on Mt. Norikura

59. Effect of forest fragmentation on the belowground microorganisms

60. Symbiosis betweem Pinus pumila and Nucifraga caryocatactes on Mt. Norikura

61. The CTA Project

62. CTA-Japan Physics Research

63. Development of Focal Plane Instruments for the CTA Large Sized Telescope

64. Development of the readout system for the CTA large sized telescopes

65. Installation and commissioning of the first Large Size Telescope of CTA in La Palma, Canary Islands, Spain

66. Integration & Commissioning of the Slow Control Program for the Camera of the first Large Size Telescope of CTA in La Palma, Spain

67. Development of the optical system for CTA Large size telescopes

68. Development of a calibration system of the CTA-LST PMT modules

69. Development of camera for CTA small-sized telescopes

70. CTA Monte Carlo Simulation

71. Development of advanced photon counter for the future IACT

72. Study of High Energy Gamma-ray Objects with the MAGIC telescope

73. The study on simultaneous observations of gamma ray bursts by CTA and LEAP

74. Study of Extremely-high Energy Cosmic Rays by Telescope Array

75. Observation of Ultra High Energy Cosmic-Ray with New Fluorescence Detector at the Telescope Array Site

76. Timing and position calibration of surface detectors of TA$\times$4 and TALE experiment

77. Research and development of the surface detectors for the TALE experiment

78. Study of radio detection of highest energy cosmic rays

79. Research and development of a Fresnel lens air fluorescence telescope for the next generation UHECR observation

80. The observation of abnormal shower event with lightning by TA surface particle detector

81. Development of solar power system and detector protection system for the new-type fluorescent detector

82. Calibration of fluorescence detector responce and optical system with standard light source mounted on UAV

83. Development and analysis of night cloud observation by CCD camera for automatic observation of air fluorescence detector

84. Study of absolute energy calibration of air shower by a compact electron linac

85. Observation of airshower fluorescence light at the TA FD site by using an Imaging UV telescope

86. Experimental Study of High-energy Cosmic Rays in the Tibet ASγ experiment

87. Study of High Enegitic Radiation from Thundercloud in Tibet

88. Sidereal daily variation of $\sim$10TeV galactic cosmic ray intensity observed by the Tibet air shower array

89. Study of the composition of cosmic-rays at the Knee

90. A study on variation of interplanetary magnetic field with the cosmic-ray shadow by the sun.

91. Air shower observation for high-energy gamma ray and cosmic ray detections at the Chacaltaya Cosmic Ray Observatory

92. Study on High Energy Cosmic Ray Sources by Observation in Spac with CALET

93. Design study of a Compton camera for study of cosmic rays

94. Observation with Ahsra

95. Integration of the optical fiber trigger system for Ashra

96. Comparative study of astrophysical particle acceleration processes

97. The extreme Universe viewed in very-high-energy gamma rays 2017

98. Development of a new code for cosmic-ray air shower simulation

99. Cosmic ray interactions in the knee and the highest energy regions

100. YMAP symposium 2017 (Basic Part)

101. Research of Large-scale Gravitational wave Telescope (VII)

102. Research on ultra-low frequency anti-vibration system for KAGRA

103. Development of High Performance Cryogenic Mirror Control System

104. Research on cryogenic payload for KAGRA

105. Study for improving a curing time of silicate bonding by controlling gas environment.

106. Development of Very Low Vibration CryoCooler System

107. Development of ultra-low loss coating for the KAGRA sapphire mirror - 2

108. Numerical Simulation of Electro-Magnetic Wave Propagation in Gravitational wave Detector V

109. Control and automatic operation for KAGRA

110. Construction of KAGRA data transfer and storage system (3)

111. Data analysis of KAGRA detector (III)

112. R&D for the intensity stabilization of the laser system in KAGRA

113. Technical development for effects on high optical power for bKAGRA mode cleaner

114. Precise geophysical observation at the Kamioka underground site and modeling of crustal activities

115. Study of Gravitational-wave by cryogenic laser interferometer CLIO in KAMIOKA Mine

116. Development of precision profiler for mirrors of LCGT interferometer 7

117. Development of optical cavity for ultranarrow stable lasers

118. Research and development on advanced gravitational wave observatory network for KAGRA

119. Cosmic Reionization and Galaxy Formation Probed with Large Optical Near-Infrared Telescope

120. Evolution of the universe and particle physics

121. Detection of time variations for cosmogenic nucleid Be-7

122. Evaluation of the erupted radioactivities into the environment

123. Frontier of the planetary material science

124. Time profile of radioactive Cs concentration and its aerosol size distribution in local area

125. Continuous Measurement of Underground Laboratory Environment

126. Precise calculation of the atmospheric neutrino flux

127. Neutrino Workshop

128. CRC workshop for future plans in cosmic ray research

G.   List of Committee Members

(a) Board of Councillors

KAJITA, Takaaki	ICRR, The University of Tokyo
OHASHI, Masatake	ICRR, The University of Tokyo
TESHIMA, Masahiro	ICRR, The University of Tokyo
NAKAHATA, Masayuki	ICRR, The University of Tokyo
TAKEDA, Hiroyuki	The University of Tokyo
KOSEKI, Toshihiko	The University of Tokyo
TOKUSHUKU, Katsuo	KEK
AOKI, Shinya	Yukawa Institute for Theoretical Physics, Kyoto University
HAYASHI, Masahiko	National Astronomical Observatory of Japan
NAKAMURA, Takashi	Kyoto University
OKAMURA, Sadanori	Hosei University
TORII, Shoji	Faculty of Science and Engineering, Waseda University
TSUNETA, Saku	Institute of Space and Astronautical Science
MORI, Masaki	Ritsumeikan University
KOMAMIYA, Sachio	The University of Tokyo

(b) Advisory Committee

KAJITA, Takaaki	ICRR, The University of Tokyo
HISANO, Junji	Nagoya University
IOKA, Kunihito	Yukawa Institute for Theoretical Physics, Kyoto University
HAZUMI, Masashi	KEK
AOI, Nori	Research Center for Nuclear Physics, Osaka University
YOKOYAMA, Masashi	The University of Tokyo
KAWAI, Nobuyuki	Tokyo Institute of Technology
ITOW, Yoshitaka	Institute for Space-Earth Environmental Research, Nagoya University
OGIO, Shoichi	Osaka City University
KANDA, Nobuyuki	Osaka City University
NISHIJIMA, Kyoshi	Tokai University
KAWASAKI, Masahiro	ICRR, The University of Tokyo
NAKAHATA, Masayuki	ICRR, The University of Tokyo
SHIOZAWA, Masato	ICRR, The University of Tokyo
KAWAMURA, Seiji	ICRR, The University of Tokyo
TESHIMA, Masahiro	ICRR, The University of Tokyo
OHASHI, Masatake	ICRR, The University of Tokyo
SAGAWA, Hiroyuki	ICRR, The University of Tokyo

(c) Inter-University Research Advisory Committee

KANDA, Nobuyuki	Osaka City University
MUNAKATA, Kazuoki	Shinshu University
MORI, Masaki	Ritsumeikan University
YOSHIDA, Shigeru	Chiba University
TAKEUCHI, Yasuo	Kobe University
SAKO, Takashi	Institute for Space-Earth Environmental Research, Nagoya University
TOMARU, Takayuki	KEK
MASUDA, Kimiaki	Institute for Space-Earth Environmental Research, Nagoya University
NAKAHATA, Masayuki	ICRR, the University of Tokyo
TAKITA, Masato	ICRR, the University of Tokyo
SAGAWA, Hiroyuki	ICRR, the University of Tokyo
UCHIYAMA, Takashi	ICRR, the University of Tokyo
MORIYAMA, Shigetaka	ICRR, the University of Tokyo

H. List of Personnel

Director	KAJITA, Takaaki,		
Vice-Director	KAWASAKI, Masahiro,	NAKAHATA, Masayuki,	

Kamioka Observatory (Neutrino and Astroparticle Division)

Scientific Staff	ABE, Ko,	BRONNER, Christophe,	HAYATO, Yoshinari,
	HIRAIDE, Katsuki,	ICHIMURA, Koichi,	IKEDA, Motoyasu,
	KAMEDA, Jun,	KATAOKA, Yosuke,	KATO, Yo,
	KISHIMOTO, Yasuhiro,	KOBAYASHI, Kazuyoshi,	MARTI MAGRO, Lluis,
	MIURA, Makoto,	MORIYAMA, Shigetaka,	NAKAHATA, Masayuki,
	NAKAJIMA, Yasuhiro,	NAKAYAMA, Shoei,	SEKIYA, Hiroyuki,
	SHIOZAWA, Masato,	TAKEDA, Atsushi,	TANAKA, Hidekazu,
	YAMASHITA, Masaki	YANG, Byeongsu,	YANO, Takatomi,
Administrative Staff	SHIMIZU, Akihiko,		
Public Relations Staff	TAKENAGA, Yumiko,		
Technical Staff	HIGASHI, Tetsuji,	NOZAWA, Noriyuki,	OGAWA, Hiroshi,
	ONOUE, Tatsuya,		
Research Fellow	MINAKATA, Hisakazu,	NAKANO, Yuki,	PRONOST, Guillaume,
	SATO, Kazufumi,	TASAKA, Shigeki,	
Secretary	DOI, Kyoko,	FUJIMURA, Yuko,	KAMIKAWATO, Rie,

Research Center for Cosmic Neutrinos (Neutrino and Astroparticle Division)

Scientific Staff	KAJITA, Takaaki,	MASUDA, Kimiaki,	NISHIMURA, Yasuhiro,
	OKUMURA, Kimihiro,		
Technical Staff	SHINOHARA, Masanobu,		
Research Fellow	ZIEMBICKI, Marcin,		
Secretary	KITSUGI, Atsuko,	MASHIMA, Chieko,	

High Energy Cosmic Ray Division

Scientific Staff	ASANO, Katsuaki,	ENOMOTO, Ryoji,	IKEDA, Daisuke,
	KAWATA, Kazumasa,	KIDO, Eiji,	KUBO, Hidetoshi,
	MAZIN, Daniil Mihajlovic,	NODA, Koji,	NONAKA, Toshiyuki,
	OHISHI, Michiko,	OHNISHI, Munehiro,	SAITO, Takayuki,
	SAKO, Takashi,	SASAKI, Makoto,	SCHLENSTEDT, Stefan,
	SITAREK, Julian,	TAKEDA, Masahiro,	TAKITA, Masato,
	TESHIMA, Masahiro,	YAMAMOTO, Tokonatsu,	YOSHIDA, Tatsuo,
	YOSHIKOSHI, Takanori,		
Technical Staff	AOKI, Toshifumi,	INOME, Yusuke,	SEKINO, Koichi,
Research Fellow	FUJII, Toshihiro,	HADASCH, Daniela,	KINUGAWA, Tomoya,
	NAKAJIMA, Daisuke,	SAKAKI, Naoto,	SAKO, Takashi,
	TAKEISHI, Ryuji,		
Secretary	IDOMURA, Takako,	SHIRAGA, Ryoko,	SUGAHARA, Midori,

Akeno Observatory (High Energy Cosmic Ray Division)

Scientific Staff	SAGAWA, Hiroyuki,
Technical Staff	KOBAYASHI, Ryoichi,

Norikura Observatory (High Energy Cosmic Ray Division)

Technical Staff	AWAI, Kyosuke,	HAYAKAWA, Hideaki,	IMANISHI, Hidenori,
	OKAZAKI, Nao,	SHIMODAIRA, Hideaki,	TOMURA, Tomonobu,
	USHIMARU, Tsukasa,		

Astrophysics and Gravity Division

Scientific Staff	IBE, Masahiro,	KAWASAKI, Masahiro,	ONO, Yoshiaki,
	OUCHI, Masami,		
Research Fellow	SHIBUYA, Takatoshi,	SHOJI, Yutaro,	TOSHIKAWA, Jun,

KAGRA Observatory (Astrophysics and Gravity Division)

Scientific Staff	HAYAMA, Kazuhiro,	HIROSE, Eiichi,	KAWAGUCHI, Kyohei,
	KAWAMURA, Seiji,	KIMURA, Nobuhiro,	KOKEYAMA, Keiko,
	MIYAKAWA, Osamu,	MIYOKI, Shinji,	OHASHI, Masatake,
	SAITO, Yoshio,	TAGOSHI, Hideyuki,	TOMARU, Takayuki,
	UCHIYAMA, Takashi,	VOCCA, Helios,	YAMAMOTO, Kazuhiro,
	YOSHII, Yuzuru,		
Administrative Staff	OKINAKA, Mihoko,	TAKAYAMA, Kyoichi,	
Technical Staff	FURUTA, Kiyoshi,	KAMIIZUMI, Masahiro,	NAKADA, Kazuo,
	OBAYASHI, Yoshihisa,	OHOKA, Hideyuki,	SHIMODE, Katsuhiko,
	TAKAHASHI, Masahiro,	TAMORI, Yukio,	UCHIKATA, Nami,
Research Fellow	CRAIG, Kieran,	LEE, Hyung Won,	NARIKAWA, Tatsuya,
	SUZUKI, Toshikazu,	USHIBA, Takafumi,	YAMAMOTO, Takahiro,
	YOKOZAWA, Takaaki,	YUZURIHARA, Hirotaka,	
Secretary	CHIDA, Ai,	HARA, Yayoi,	IWAMATSU, Miho,
	KIKUCHI, Rie,	MAEDA, Yukari,	

Graduate Students

Doctor	AKUTSU, Ryosuke,	FUJIMOTO, Seiji,	FUKAMI, Satoshi,
	HARIKANE, Yuichi,	HASEGAWA, Fuminori,	HASEGAWA, Kunihiko,
	HAYAKAWA, Taku,	HIROSHIMA, Nagisa,	HONG, Jeong Pyong,
	INADA, Tomohiro,	INOMATA, Keisuke,	ISHIZAKI, Wataru,
	IWAMURA, Yuki,	IYOGI, Kazuki,	KOBAYASHI, Masatoshi,
	KOJIMA, Takashi,	MIYAMOTO, Takahiro,	MIYO, Koseki,
	MUKAE, Shiro,	NAGANO, Koji,	NAKANO, Masayuki,
	NAKANO, Wakutaka,	ONO, Kenji,	ORII, Asato,
	SHIN, Heungsu,	SONODA, Yutaro,	SUGAHARA, Yuma,
	SUZUKI, Motoo,	TAKAHASHI, Mitsunari,	TANAKA, Hiroki,
	TO, Sho,	TSUI, Kaming,	ZHANG, Haibin,
Master	ANDO, Kenta,	ARAI, Koya,	ARAI, Yuya,
	FUKUNAGA, Masashi,	HIGUCHI, Ryo,	HILMI, Miftahul,
	HSIEH, Bin-Hua,	IIDA, Kento,	ITO, Ryohei,
	KATO, Nobuyuki,	KIKUCHIHARA, Shotaro,	KIRII, Shin,
	KOBAYASHI, Shin,	KOZU, Ryohei,	KUMON, Taku,
	KURODA, Hayato,	MOCHIZUKI, Toshiki,	MOROZUMI, Tatsuhiko,
	NAKATSUKA, Hiromasa,	OCHI, Toshiro,	OKAMOTO, Kohei,
	OTANI, Francis,	PEDERSEN, Juan William,	SAKURAI, Shunsuke,
	SONOMOTO, Eisuke,	SUZUKI, Kazumine,	SUZUKI, Takumi,
	TAKENAKA, Akira,	WANG, Ru,	XIA, Junjie,
	YADA, Kyohei,	YAMADA, Tomohiro,	YAMAGUCHI, Soma,
	YAMAMOTO, Kohei,		

Administrative Division

Administrative Staff	AKAIDA, Yohei,	AKIYAMA, Makiko,	BOLENS, Yukari,
	FUKUHARA, Nana,	KOBAYASHI, Toyoki,	KONDO, Hitomi,
	MARUMORI, Yasuko,	NAMATAME, Kaneo,	OHURA, Kiichi,
	OKANO, Yuka,	SAITO, Akiko,	SATO, Yu,
	YAMAGUCHI, Akiko,		
Research Administrator	SATO, Ritsuko,		
Public Relations Staff	FUKUDA, Hironobu,	ITO, Yoriko,	

INSTITUTE FOR COSMIC RAY RESEARCH
THE UNIVERSITY OF TOKYO

Address   5-1-5, Kashiwanoha, Kashiwa-shi, Chiba, 277-8582 Japan

TEL   +81-4-7136-3102

FAX   +81-4-7136-3115

URL   www.icrr.u-tokyo.ac.jp